Biomechanical Information Transfer: Maximum Caliber, λ genome ejection dynamics, and the formation of otoliths in zebrafish

Thesis by

David Dah-wei Wu

In Partial Fulfillment of the Requirements

for the Degree of

Doctor of Philosophy

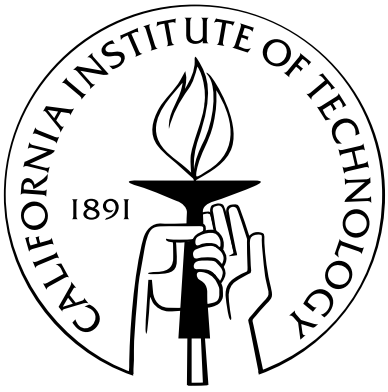

California Institute of Technology

Pasadena, California

2010

(Submitted May 19, 2010)

Acknowledgements

These past six years, recorded in part in this document, would have been impossible to complete without the help of many individuals. A preliminary note, however: collaborators and coworkers they may be, yet I consider many of them friends, and it is no exaggeration to say that this document would be considerably shortened without their cornucopia of contributions. I thank you all, wholeheartedly.

I'd like to specifically acknowledge Mandar Inamdar, Kingshuk Ghosh and Ken Dill for their help on the theory side of the Maximum Caliber part, and Heun Jin Lee for his invaluable expertise on optics. David Van Valen, Qicong Hu, Hannah Tuson, and Paul Grayson were either key advice-givers or helped complete - or completed themselves - a substantial portion of the work on phages. Julien Vermot and Jon Freund were also invaluable on the part about zebrafish. My thesis committee consisted of John Brady, Scott Fraser, Niles Pierce, Rob Phillips, and Zhen-Gang Wang, whom I would like to thank for their helpful advice.

I have had many discussions with the following individuals, whom have influenced my work in subtle, though substantial ways (in no specific order): Arbel Tadmor, Yi-Ju Chen, Effroseyni Seitaridou, Lin Han, Sarah Marzen, and Paul Grayson.

Lastly, of course, are the advisers: Rob Phillips and Scott Fraser whose support was always enlightening. I am delighted to have had the opportunity to tangentially participate in your grand schemes of Science.

Abstract

Biology is inherently a non-equilibrium process - constantly battling or co-opting the entropic enemy in order to achieve its *sine qua non*: growth, development, and reproduction. Involved in these processes is the formation of temporal and spatial order from disorder, and the transfer of information in genomic content but also in the form of physical principles.

First, I will describe a different way to analyze dynamics called Maximum Caliber, a model-free application of the Principle of Maximum Entropy to trajectories or processes, based purely on information theory. We apply Maximum Caliber to analyze particles diffusing on a dual-minima energy landscape and attempt to describe and predict the probability distribution of trajectories. Next, I will discuss our efforts in analyzing the literal transfer of information from one organism to the next: specifically, how phage lambda's DNA gets inside *Escherichia coli*. The use of counterions as a parameter to tune the force of *in vitro* ejections is clarified before performing suggestive *in vivo* injection experiments. Last, the process of building and shaping the otolith of the zebrafish (the accelerometer and hearing organ) is analyzed, with the conclusion that it is possible to generate said organ through purely physical mechanisms, suggesting that biological information transfer is not exclusively genetic.

Contents

List of Figures

List of Tables

Chapter 1

Biomechanical Information Transfer

Fundamental to life on this planet is that the ultimate originator of phenotype, i.e., the morphology or function of something, is embedded in linear sequences of nucleic acids bound to sugar molecules, and amino-acids. Both nucleic acids and amino acids are able to fold into regular (or irregular) structures that depend on long-range interactions within the molecules themselves. Predicting these structures is not trivial. Naturally, the side chains of the amino acids and sequences of nucleic acids provide the heterogeneity needed to specify a unique structure or set of structures, as the case may be. Thus we know intuitively that three-dimensional encoding is possible from a one-dimensional polymer; however, this type of encoding takes place on the nanometer length scale, as the long-range interactions are always within a single polymer chain, if we are to discount the quarternary structure of protein and protein-nucleic acid assemblies (such as ribosomes) for the moment. Yet, the structure of these multi-component assemblies is also extremely small. However, life is certainly not bound to the nanometer length scale: viruses, the smallest units of encapsulated "life" are already in the 100 nm range and consist of self-assembled units of protein and nucleic; bacteria are 10 times larger and exhibit dynamic rearrangement of protein structures and even contain molecular machines that resemble car motors. Eukaryotic organelles exist across micron scales, the cells themselves span the 10 micron to meter length scales, and multicellular organisms can span from the 1 micron length scale all the way to the 10 meter length scale (the size of a blue whale, the largest animal on earth), 6 orders of magnitude larger. The multicellular organisms, it should be noted, still maintain diversity in their structure at all length scales. Yet all the structures are dictated by the same strands of

DNA.

We know that this is not really true. The activation of the programs and subroutines inside DNA, which determines the fate of a cell, depends on a host of external factors - RNA and protein based, primarily, although there is some evidence that DNA can activate or repress itself upon looping. These chemical external cues which dictate the activated programs must have somehow been transferred into the cell at some point - and beyond physical injection, the other way is via cell division; i.e., the cells inherited the chemical factors. Thus we proceed *reductio ad infinitum* (or *absurdum*) in an unbroken chain of daughter to mother to the original cell. These epigenetic arguments of DNA functions dictate the expression levels and patterns of cells, which work together ultimately to form multicellular organisms, and, in my mind, confirm that the process of biology is indeed, one of descent.

One can think of cells as existing in certain defined morphological and functional states. Thus a question one might ask is: given some archetypal cell, how does it transition between states? This is a central goal of biology - for when we understand how this is possible, we will understand a unique aspect of life - the interplay of differentiation with evolution. One of the perhaps simplest examples of transitioning between different functional states is how lambda phage can dictate the state of an *Escherichia coli* cell. Another question one might ask is: how are the states of cells influenced by mechanical (as opposed to chemical) events? An example of this is the construction of biominerals upon which organisms are able to drape their cells in a multitude of animals. Each chapter in this thesis contains its own more detailed introduction; as one suspects from the abstract, the three topics are only loosely connected. Therefore this introduction will be brief and will only sketch the general philosophy of the scientific questions to be addressed.

In order to understand the flow of information in biology, tools that are able to discern pattern formation, or principles that enable us to discern the most likely paths in non-equilibrium systems, would be useful. That is, biology relies on the constant flux of energy in order to organize into defined patterns, yet the dominant analytical tools rely on agent based models for analysis, in the form of Langevin or Master equations. Thus, the first section will concern the use of a non-traditional metric in analyzing patterns - that of Maximum Caliber - a variational tool that can possibly be used to derive the distribution of trajectories for a dynamical process.

From an information theoretic perspective, the Principle of Maximum Entropy determines that, at equilibrium, the least biased probability distribution of a system will correspond to the largest amount of missing information. However, there is no reason why information theory cannot be applied to dynamical systems as well, and we attempt to do so for the case of a particle diffusing in a bi-minima (W-shaped) potential landscape. In Maximum Caliber, entire trajectory time-histories are considered in defining the most-likely dynamics, not just states. In considering these two-state trajectories, we arrive at new fluctuation theorems that can be validated or disproved by experiments, its predictive successes or failures scored. We also discuss the connection of the Maximum Caliber formalism for two-state trajectories to the random telegraph model.

Many of the ideas presented were initially developed by Mandar Inamdar in concert with Rob Phillips. I had much additional help on the theoretical front from Kingshuk Ghosh and Ken Dill. Heun Jin Lee and Scott Fraser provided essential support in the construction and design of a robust optical system, as well as detection electronics.

Then we turn our attention to mechanical events that influence gene expression and hence the functional state of the cell. Specifically, we will analyze the mechanical properties of DNA during bacteriophage lambda ejection that influence how phage DNA is transferred into the bacterial cell. We present preliminary data demonstrating this latter phenomenon.

Phages are only able to reproduce by hijacking hosts - they are the viruses of bacteria. Phages must deliver their genome into the cell - a not unimpressive feat given the physical constraints involved. Yet the mechanism for DNA entry is unknown for phage lambda, despite being one of the oldest biological systems studied at the molecular level. We dissect how changing the character of the counterions affects the velocity of phage DNA ejections, and quantify how much force is needed to stall ejections in the different ionic conditions. We also seek to measure the process of lambda DNA entry into bacterial cells, and present preliminary evidence suggesting that DNA entry takes place on the $\sim$100 second time scale, as compared to $\sim$10 seconds for *in vitro* ejections. By understanding the horizontal transfer of genomes from one source to another, we will gain insight into the influence of gene expression due to external sources.

The *in vitro* experiments described were performed in partnership with David Van Valen. Qicong (Russell) Hu also carried out the initial optical trapping experiments at the Physiology Course in the Marine Biological Laboratory located in Woods Hole, MA. Hannah

Tuson, another member of MBL, also devoted much of her time exploring the methodologies described in the *in vivo* section. Rob Phillips provided the impetus and guidance for these sets of experiments. We are also indebted to Paul Grayson for his wisdom and nigh-infallible technique.

Finally, we analyze the formation of the inner ear otolith of zebrafish. DNA can dictate the expression of proteins, and protein localization sequences are sometimes embedded in DNA; however, we will show that the formation and shape of the otolith relies on hydrodynamics, a mechanical process that received little input from DNA, beyond clever starting conditions.

The otolith of zebrafish, an accelerometer and hearing organ with a mushroom-top shape, is formed in an ovoid cavity by accretion of calcium carbonate, protein, and glycogen particles. In the adult fish, it sits on top of hair cells which transduce vibrations into chemical signals that are propagated to the brain. Thus, both the shape and position of the otolith is crucial for its function. The otolith forms in the presence of beating cilia, which if knocked out by genetic means, leads to malformed shapes and sizes of otoliths. We explore why this is by discussing the effects of cilia on the hydrodynamics of the cavity, and perform experiments which suggest that cilia control the shape of the otolith by hydrodynamically focusing the otolith precursor particles and locally sculpting the otolith itself.

I had extensive help from Jonathan Freund and Julien Vermot; the former helped with much of the initial formulation of Stokes flow inside a sphere, and the latter provided the zebrafish samples for study. JV was also a relentless force for seeing the project to the end. Additionally, without the sage advice from Scott Fraser, we would undoubtedly be months behind.

The three chapters of the thesis together are bound together via the theme of "biomechanical information transfer," the notion that information is critical in determining the states of cells, that we can analyze the information in a variational sense, and that this information can be transmitted literally, through direct DNA transfer, or through mechanical means, such as in otolith formation.

Chapter 2

Maximum Caliber and Two-State Trajectories

2.1 The Principle of Maximum Entropy and Maximum Caliber

In this section, we seek to formulate the dynamics of stochastic processes, which can be defined as trajectories, from a variational standpoint. That is, the usual method to understand non-equilibrium systems is to explicitly develop an agent-based model (where the actor is the random variable) in the form of differential equations - these are known as Master equations or Langevin equations; the basis of the former lies in kinetic schemes with probability conservation at their heart, whereas the latter are force-balance schemes that include stochastic forces. The use of these methods has been successful in describing a variety of phenomena. However, under conditions of equilibrium, there exists a variational principle called the Principle of Maximum Entropy that can generate distributions of the random variable from a simple maximization scheme; in deterministic dynamics, the Principle of Least Action can perform an equivalent duty, in contrast to (for example) Newton's laws that are again, agent-based. E. T. Jaynes proposed that information theory can provide a variational principle for non-equilibrium statistical systems [1], an alternative way to generating dynamics. In this first chapter of the thesis, we show that this variational principle is applicable to stochastic systems that obey Markov-type dynamics: specifically, a particle diffusing on a two-state sculpted energy landscape.

Consider the information entropy, which we describe below, in Section 2.2. The information entropy, $S = -\sum_i p_i \ln p_i$, where p_i are the the probabilities of some state i of

the system at hand, quantifies the amount of missing information - and is called the entropy in statistical mechanics, up to a multiplicative constant. Maximizing this function in equilibrium (subject, perhaps, to constraints) will produce the least-biased probability distribution for each state i. This is called the Principle of Maximum Entropy. Lurking behind the scenes is the assumption that at equilibrium, systems behave ergodically: systems are able to sample all energy states, or conversely, that entropy will be maximized.

To compute the equilibrium distribution, one constrains the information-entropy by known moments of the random variables, A_j, such that

$$S = -\sum_i p_i \ln p_i + \lambda_0 \left(\sum_i p_i - 1 \right) + \sum_j \lambda_j \sum_i A_j p_i - \langle A_j \rangle \tag{2.1}$$

and then maximizes S: $\partial S / \partial p_i = 0$. Here, the underlying dynamics that generate A_j are assumed to be stationary, and so the moments of A_j, such as $\langle A_j \rangle$, are constants in time. Only first moments are written here, although in principle any combination of higher moments can be used. λ_j are the Lagrange multipliers, multiplicative factors that effectively weight each constraint in the final probability distribution.

From an information theory perspective, $S = -\sum_i p_i \ln p_i$ is merely a quantity that describes the amount of missing information, and isn't simply a thermodynamic result, despite its formal equivalence with Gibb's form of entropy. Thus its application is not limited to equilibrium; in fact, it was proposed by E. T. Jaynes that this variational principle for generating distributions be extended to non-equilibrium processes; the constraints $\lambda_j A_j$ become $\sum_t \int d^3x dt \lambda_j (x,t) A_j (x,t)$ and so S now incorporates much more than the space of possible states, but also the history of a process - A_j is no longer generated by a stationary process, and so the Lagrange multipliers λ_j also become time (and space) dependent. It is that history whose weights must be discovered for the probability distribution to be calculated - he called these weights the *caliber* of those histories [1].

We follow in Jaynes' footsteps and study a basic process which flows through space-time in stochastic fashion. We study the trajectories of a single colloidal particle as it hops between two energy wells which are sculpted using optical traps. Whereas the dynamical behaviors of such systems are often treated by Master-equation methods that focus on *particles* as actors, we analyze them here instead using the Principle of Maximum Caliber - a *trajectory*-based variational method as described above. We show that the MaxCal

strategy accurately predicts the full dynamics that we observe in the experiments: from the observed averages, it predicts second and third moments and covariances, with no free parameters. The literature on the principles behind information theory and its use in statistical mechanics are fraught with philosophizing about the nature of probability [2] and calls to abandon "entropy" [3]. Our goal, in contrast, is simply to see if MaxCal can be used to solve problems.

2.2 The information theory perspective of statistical mechanics

2.2.1 Shannon's theorem

Information theory's origins lie in the simple question: how does one transmit information reliably at low cost [4] (much of this section follows the discussion in Ben-Naim's book, [3])? This is, perhaps, a nebulous concept, but it turns out that we don't care what the information contains, but only the size of the information. To quantify the amount of information a message contains, Shannon, the originator of information theory, required three things to compose his $H(p_i)$-function, which quantifies the amount of missing information, where $p_{i=1\ldots n}$ is the probability distribution of the i states of some random variable X:

(i) H should be continuous in all p_i.

(ii) If all p_i are equal, then H should have a maximum value and this should be a monotonic increasing function of n.

(iii) If a choice is broken down into successive choices, the quantity of H should be the weighted sum of the individual values of H.

These requirements are all reasonable, in the following senses: (i) small changes in p_i do not produce discontinuities in H. (ii) In the situation where information is at a minimum, we assign equal probabilities to everything, and so H is at a maximum. Moreover, with increasing n, H must also be larger, as the possible state space has increased. (iii) Composition law: the amount of information shouldn't depend on the way in which the information was acquired, but only on the amount of information itself. Shannon showed that the only

function that satisfies these requirements is

$$H\left(p_{i=1\ldots n}\right) = -\sum_{i=1}^{n} p_i \log p_i. \tag{2.2}$$

Proofs are located in [5] and [3], the latter of which provides an excellent treatment of information theory as it relates to statistical mechanics.

Now consider the case of maximal ignorance - given n urns and 1 ball, what is the probability of any given urn containing the ball? - the fair assignment is for each urn containing the ball to have probability $p_i = \frac{1}{n}$ and so

$$H_{max} = -\sum_{i=1}^{n} \frac{1}{n} \log \frac{1}{n} = \log n. \tag{2.3}$$

However, we could have used the method of Lagrange multipliers (briefly sketched in Section 2.1) to arrive at the same conclusion. Consider the probability normalization condition: $\sum_i p_i = 1$. Then, we can augment the missing information, H, as

$$H = -\sum_{i=1}^{n} p_i \log p_i + \lambda \left(\sum_i p_i - 1 \right) \tag{2.4}$$

where clearly the augmentation term is equal to zero, so there is no difficulty adding it to H. Variable λ is called a "Lagrange multiplier;" hence, the eponymous name of the method. Then maximizing H, $\partial H / \partial p_i = 0$, we have

$$p_i = e^{\lambda - 1}. \tag{2.5}$$

Since $\sum_i p_i = 1$, $p_i = \frac{1}{n}$, and we again arrive at $H_{max} = \log n$, equivalent to the Boltzmann entropy up to a multiplicative constant. Given the amount of information we had regarding the random variable X, $p_i = \frac{1}{n}$ is the least biased estimate for the probability of X to be in state i - since, mathematically, we are maximizing the amount of uncertainty H. If we were to replace H, the missing information, with S, the entropy, then this would be the Principle of Maximum Entropy [6], as seen in Section 2.1.

2.2.2 From missing information to entropy

Yet the question remains of how to justify the replacement of entropy with "uncertainty" or "missing information." As has been noted by others [3], just as H_{max} has the same form as the Boltzmann entropy, and Shannon's H-function the same form as the Gibbs entropy, does not mean that the concepts are interchangeable. We now must make a leap and consider just why information is a useful concept to apply to physics - statistical mechanics in particular - and not just information in the bits sense. This is conceptually straightforward. Suppose we were to guess at where, on a chess board, a piece is located - the use of H to quantify the amount of missing information is clearly appropriate - as in the ball and urn example above. But is this not the same question as: what is the location of a particle in space? Then the information entropy, H, is performing the same as Gibbs' form of entropy, S, in the Principle of Maximum Entropy!

From a physical point of view, an isolated system is ergodic and spends equal fractions of time in each of the permissible microstates [7]: this is the essence of equilibrium statistical thermodynamics. Given this ergodicity principle, it then follows that the number of occupied microstates is consistent with the external constraints and the number of occupied microstates is therefore at a maximum - consistent with our intuitive notions of a gas, say, filling an entire box. Furthermore, the logarithm of the number of microstates is also at a maximum, and at equilibrium we arrive at the notion that $S_{max} = \ln \Omega$ - but this is also the condition of maximal ignorance. Callen [7] makes an interesting argument as to the mathematical interpretation of ergodicity: at equilibrium there is detailed balance. Then

$$\frac{df_i}{dt} = -\sum_{j \neq i} f_i f_{ij} + \sum_{j \neq i} f_j f_{ji} = 0. \tag{2.6}$$

where f_{ij} is the transition probability from state i to state j and f_i is the probability of state i. Since $f_{ij} = f_{ji}$ (detailed balance), then a general solution to Equation 2.6 is $f_i = f_j$, which means that $f_i = 1/\Omega$ is an equilibrium configuration for any set of transition probabilities $\{f_{ij}\}$ for which $f_{ij} = f_{ji}$. In other words, at equilibrium, particles are likely to occupy states with equal probability. This dovetails perfectly with the concept of "maximum ignorance."

Maximizing our uncertainty about a system is the same as the Principle of Maximum Entropy in statistical mechanics for deriving ensembles, which Jaynes sums up [6]: "there is

nothing in the general laws of motion that can provide us with any additional information about the state of a system beyond what we have obtained from measurement." He goes on:

> This refers to interpretation of the state of a system at time t on the basis of measurements carried out at time t. For predicting the course of time-dependent phenomena, knowledge of the equations of motion is of course needed. By restricting our attention to the prediction of equilibrium properties ..., we are in effect deciding at the outset that the only type of initial information allowed will be values of quantities which are observed to be constant in time.

In other words, to arrive at the equilibrium distribution of our random variable, whatever that may be, we must augment our uncertainty by information regarding the average energy, number of particles, etc., quantities which are conserved in time. Particular ensembles, therefore, describe changing states of knowledge due to changing boundary conditions.

However, we are particularly concerned with dynamics at the single particle level. Then if one were to consider a trajectory of a particle in solution, its sampling of state space would be characterized by an incessant bombardment of other particles, resulting in Brownian motion. And we would furthermore expect that by maximizing H, our ignorance, that it is in fact possible to recover the dynamics of particles executing Brownian motion: the macroscopic phenomena that is called diffusion. It was recently shown by Ghosh et al., [8], that this is indeed the case. It is not altogether clear, however, how to constrain the information entropy for dynamic processes, especially for dissipative phenomena.

Below, we use the Principle of Maximum Entropy, due to its foundations in information theory, to analyze trajectories of particles; however, we now use Jaynes' phrase, the Principle of Maximum Caliber. We apply this algorithm to a dynamical system by considering trajectories as states.

2.3 Maximum Caliber of two state systems

We explore the kinetics of two-state processes, $A \leftrightharpoons B$, at the one-particle level. A more concise treatment of this was recently published [9]. Examples of single-molecule or single-particle dynamical processes that mimic two-state dynamics include DNA loop formation [10], RNA oligomer hairpin formation/destruction [11], protein folding oscillations [12],

sequence-dependent protein unfolding [13], or ion-channel opening and closing kinetics [14]. Two-state fluctuating systems having fixed rates are called *random telegraph* processes.

One way to understand two-state and random-telegraph processes is through Master equations, which are differential equations that are solved for time-dependent probability density functions [15]. For single-particle and few-particle systems, however, other convenient experimental observables are the trajectories themselves, rather than the time-dependent populations of the two states. Here, we describe an experimental model system to study such single-particle two-state stochastic trajectories. We use these experiments to test Maximum Caliber and to predict the full trajectory distributions, given certain observed mean values.

Using dual optical traps, we have "sculpted" various energy landscapes. We can control the relative time the particle spends in its two states and the rate of transitioning between them. Our method follows from earlier work on the dual trapping of colloidal particles that was used to study Kramers reaction rate theory [16]. While these experiments were previously focused on studying average rates, our interest here is in the probability distribution of trajectories.

We trap a 1 μm silica bead in a neighboring pair of optical traps, as shown in Figure 2.1. The laser, wavelength of 532 nm, power at 100 mW, produces a Gaussian shaped potential when focused by a lens. An acousto-optic deflector alternately sets up two traps close together in space, at a switching rate of 10 kHz, which is both much faster than each individual trap's corner frequency [17] and also the fastest bead hopping rate, resulting in a double Gaussian potential. The strength of each trap and the spacing between them can be controlled in order to sculpt the shape of the potential. A tracking 658 nm red laser at 1 mW was used to determine the position of the bead. The forward scattered light is imaged through a microscope condenser onto a position-sensitive detector [18]. The green trapping laser light at the detector is filtered out by a long-pass filter. The data was recorded at a rate of 20 KHz, which sets the fundamental time step, Δt, for our analysis. Trajectories were recorded for intervals ranging from 20 minutes to more than 1 hour, depending on the hopping rate. A simple threshold, following a median filter of 1 KHz width, was used to determine states in the trajectories.

As described above in Section 2.1, Maximum Caliber (MaxCal) was first proposed by E.T. Jaynes in 1980, as a variational principle that purports to predict dynamical properties

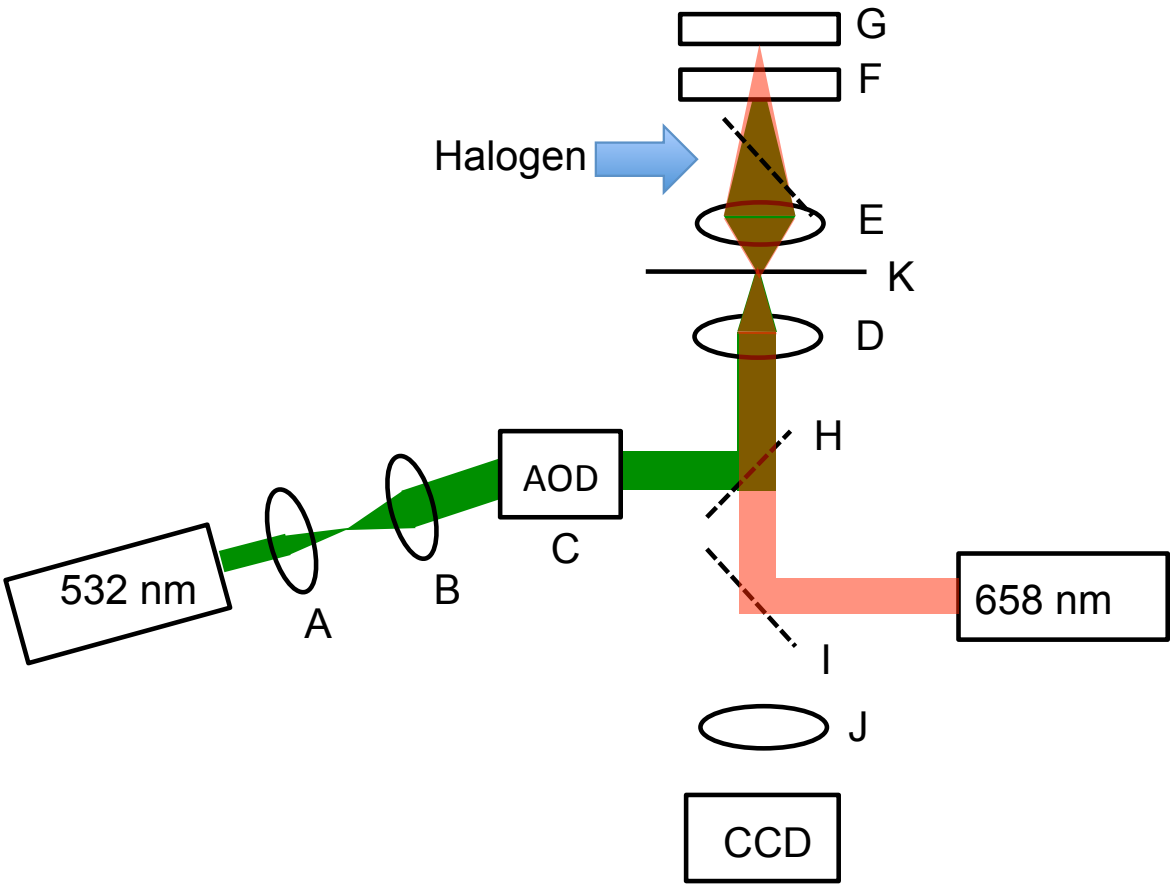

Figure 2.1: **Instrument setup for Maximum Caliber**. The instrument consists of a scanned optical trap (λ = 532 nm) together with a stationary detection beam (λ = 658 nm). The beam is expanded to fill the back aperture of the objective (**D**) through telescope (**A**) and (**B**). Computer controlled acousto-optic deflectors (**C**) scan the laser, creating the double-Gaussian potential well. The detection beam is collected by the condenser (**E**) and focused onto a position sensitive detector (**G**); a long-pass filter (**F**) blocks the trapping laser. **H** and **I**. Dichroic mirrors. **J**. Tube lens for brightfield imaging. **K**. Sample plane.

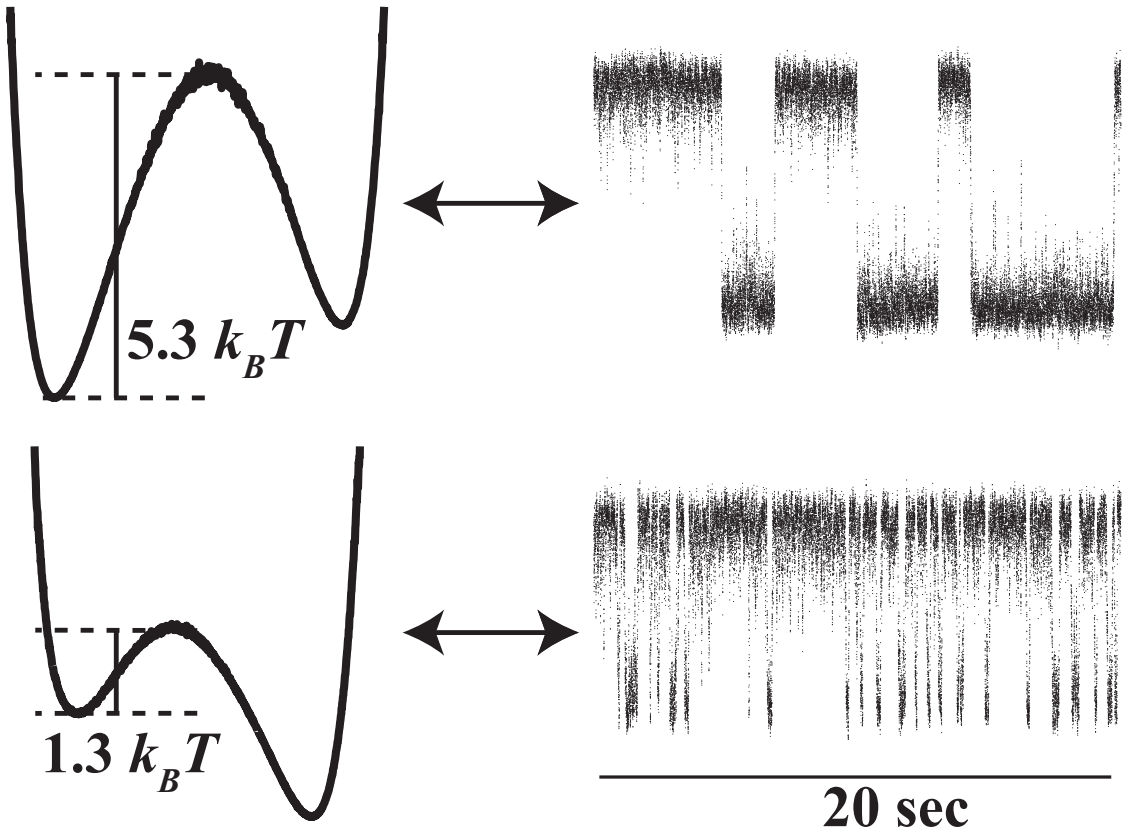

Figure 2.2: **Sculpted energy landscapes Left**. Trajectories were averaged 20 minutes, and the negative logarithm of the position histogram plotted. **Right**. The trace is raw data; states are assigned after boxcar filtering and threshold finding. **Top**: the lower state is slightly more populated; there is a high barrier (infrequent transitions). **Bottom**: the upper state is more populated; the barrier is small (frequent transitions). The distance between the two potential minima ranges from 200 nm to 700 nm.

of systems in much the same way that the Maximum Entropy (MaxEnt) approach predicts the properties of equilibrium systems; both use information theory as a basis [19]. MaxCal has been shown to be a simple and useful way to derive the flux distributions in diffusive systems, such as in Fick's Law of particle transport, Fourier's Law of heat transport, and Newton's Viscosity Law of momentum transport [20]. The Caliber, $\mathcal{C}$, is

$$\mathcal{C} = -\sum_i p_i \ln p_i, \tag{2.7}$$

where p_i denotes the probability of the ith trajectory, is augmented with moment-type quantities which are experimental observables, in the formulation described here. Maximization of the Caliber thus predicts the full distribution of trajectories.

Examples of trajectories in our system are shown in Figure 2.2. By *trajectory*, we mean one individual time sequence of events over which the particle can transition back and forth many times between states a and b. In our experiments, we divide time into discretized time intervals, Δt, set by the inverse of our sampling rate. A trajectory has N time steps, so it lasts for a total time $N\Delta t$. We aim to characterize the probability distribution for all trajectories given the known constraints on the space of possible trajectories, as defined by our first moment experimental observables.

We take a reduced view of the experimental system which will allow the solution to p_i to be analytically tractable. For each Δt time step there are four possible transitions. If the system is in state a, it can stay in state a or switch to state b. Similarly, if the system is in state b, it can stay in state b or switch to state a, as shown in Figure 2.3. Over the entirety of the ith trajectory, the total number of transition events from a to a is represented by the variable N_{aa}, with N_{ab}, N_{ba}, and N_{bb} defined similarly. In the experiments, we assert that the observables are the averages of these quantities, $\langle N_{ab} \rangle$, $\langle N_{ba} \rangle$, $\langle N_{aa} \rangle$, and $\langle N_{bb} \rangle$, taken over all the trajectories (summarized in Equations 2.12 and 2.13). Thus there are four corresponding unknown Lagrange multipliers (plus normalization) which are fully determined by the four observables. Writing down the definition of these observables, we have

$$\langle N_{jk} \rangle = \sum_i p_i N_{jk,i} \tag{2.8}$$

where j, k are either a or b. In this case, the Caliber is defined as

$$\mathcal{C} = -\sum_i [p_i \ln p_i - \lambda_0 p_i - p_i(\lambda_{aa} N_{aa,i} + \lambda_{ab} N_{ab,i} + \lambda_{ba} N_{ba,i} + \lambda_{bb} N_{bb,i})] \tag{2.9}$$

where the λs are the corresponding Lagrange multipliers (among this set of five Lagrange multipliers, there are only two independent variables (see below), so only two experimental average quantities, plus the length of a trajectory, N, are required [21]). The probabilities p_i of all the trajectories are then found by maximizing the Caliber: $\partial\mathcal{C}/\partial p_i = 0$.

The calculation of the p_is is made simple by the use of the trajectory partition function Q_d, which serves for our dynamical system very much the same role that the equilibrium partition function serves for the Boltzmann distribution law of equilibrium. For $s = 2^N$ trajectories having N time steps, Q_d is given by

$$Q_d = \sum_i^s \left(\alpha^{N_{aa,i}} \beta^{N_{bb,i}} \omega_f^{N_{ab,i}} \omega_r^{N_{ba,i}}\right), \tag{2.10}$$

and the probability of a particular trajectory labeled i is given by

$$p_i = Q_d^{-1} \alpha^{N_{aa,i}} \beta^{N_{bb,i}} \omega_f^{N_{ab,i}} \omega_r^{N_{ba,i}}. \tag{2.11}$$

We write the exponentiated Lagrange multipliers ($e^{\lambda_{jk}}$) as the "statistical weights" α, β, ω_f, and ω_r, with respect to the observables described above: α is the statistical weight that, given that the system is in state a at time t, it is also in state a at time $t+\Delta t$; β, for staying in state b at time $t + \Delta t$, given that the system was in b at time t; ω_f, for switching from a to b in the time interval Δt; and ω_r, for switching from b to a in the time interval Δt, as shown in Figure 2.3.

It is readily shown that the average quantities are simply derivatives of the partition function; for example

$$\langle N_{bb} \rangle = \left.\frac{\partial \ln Q_d}{\partial \ln \beta}\right|_{\alpha,\omega_f,\omega_r} \quad \langle N_{ab} \rangle = \left.\frac{\partial \ln Q_d}{\partial \ln \omega_f}\right|_{\alpha,\beta,\omega_r} \tag{2.12}$$

and

$$\langle N_{aa} \rangle = \left.\frac{\partial \ln Q_d}{\partial \ln \alpha}\right|_{\beta,\omega_f,\omega_r} \quad \langle N_{ba} \rangle = \left.\frac{\partial \ln Q_d}{\partial \ln \omega_r}\right|_{\alpha,\beta,\omega_f} \tag{2.13}$$

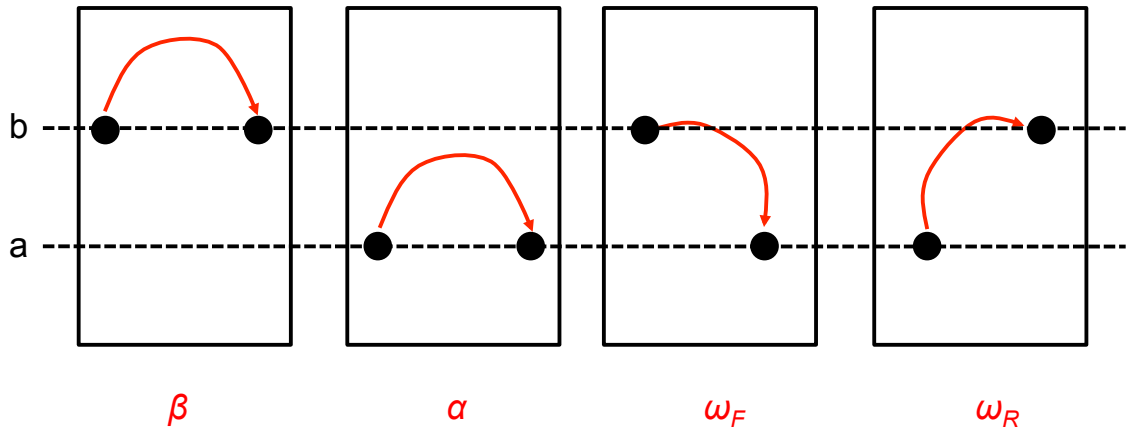

Figure 2.3: **Trajectories are composed of four statistical weights.** The colloidal particle is allowed to hop between two states a and b. We statistically weight these microtrajectories: in the next Δt, the particle will stay in the same state, resulting in the statistical weight $\alpha : a \to a$ or $\beta : b \to b$, or move to a different state, resulting the statistical weight $\omega_f : b \to a$ or $\omega_r : a \to b$.

together define the "statistical weights".

The MaxCal strategy is as follows. First, experiments give the four trajectory-averaged quantities such as $\langle N_{bb} \rangle, \langle N_{ab} \rangle$, etc. Second, substituting those measured values into Equation 2.12 and Equation 2.13 gives four equations that are solved for the four unknowns $\alpha, \beta, \omega_f, \omega_r$. This now gives all the information needed to compute Q_d and p_i for any trajectory from Equation 2.10 and Equation 2.11. Finally, taking the second and higher derivatives of Q_d results in the higher moments (i.e., the dynamical fluctuations) of the observables, such as

$$\langle N_{ba}^2 \rangle - \langle N_{ba} \rangle^2 = \left. \frac{\partial^2 \ln Q_d}{\partial \left(\ln \omega_r \right)^2} \right|_{\alpha,\beta,\omega_f} . \tag{2.14}$$

In addition, other properties of interest are readily computed. Let N_B represent the number of units of time that the system spends in state b. Then we have for each individual trajectory $N_B = N_{ab} + N_{bb} + N_{0b}$ and $N_A = N_{aa} + N_{ba} + N_{0a}$ where N_{0b} is $0(1)$ if the trajectory begins in state $a(b)$ and N_{0a} is $1(0)$ if the trajectory begins in state $a(b)$. If the number of steps is sufficiently large, the contribution from initial conditions can be ignored. Hence the variance for N_B is given by

$$\langle N_B^2 \rangle - \langle N_B \rangle^2 \simeq \left. \frac{\partial^2 \ln Q_d}{\partial \left(\ln \beta \right)^2} \right|_{\alpha,\omega_r,\omega_f} + \left. \frac{\partial^2 \ln Q_d}{\partial \left(\ln \omega_f \right)^2} \right|_{\alpha,\beta,\omega_r} + 2 \left. \frac{\partial^2 \ln Q_d}{\partial \ln \beta \partial \ln \omega_f} \right|_{\alpha,\omega_r} . \tag{2.15}$$

Mixed moments and covariances are obtained from mixed derivatives of Q_d. For example,

$$\left.\frac{\partial^2 \ln Q_d}{\partial \ln \omega_f \partial \ln \beta}\right|_{\alpha,\omega_r} = \left.\frac{\partial^2 \ln Q_d}{\partial \ln \beta \partial \ln \omega_f}\right|_{\alpha,\omega_r} \tag{2.16}$$

which leads to

$$\left.\frac{\partial \langle N_{bb}\rangle}{\partial \ln \omega_f}\right|_{\alpha,\beta,\omega_r} = \left.\frac{\partial \langle N_{ab}\rangle}{\partial \ln \beta}\right|_{\alpha,\omega_f,\omega_r} = \langle N_{ab}N_{bb}\rangle - \langle N_{ab}\rangle\langle N_{bb}\rangle. \tag{2.17}$$

Higher derivatives of Q_d give information about the higher-order fluctuations. Hence, given Q_d, all higher moments of random variables N_{jk} can be computed. More details of the theoretical approach for this problem are given in [21].

A simple way to compute Q_d is through the matrix propagator $\mathbf{G}$,

$$\mathbf{G} = \begin{pmatrix} \alpha & \omega_r \\ \omega_f & \beta \end{pmatrix}, \tag{2.18}$$

where each element of $\mathbf{G}$ represents the propagator of transitioning from some initial state during each time step. We consider here only stationary processes, for which the statistical weights are time-independent, but the MaxCal method itself is not limited to such simple dynamics. We can express $Q_d = (1 \quad 1)\,\mathbf{G}^{N-1}\,(a_0 \quad b_0)^T$, where $(a_0 \quad b_0)^T$ denotes the initial state probabilities. Thus all the higher moments of the random variables are analytically tractable since Q_d can always be expressed in terms of partial derivatives of the eigenvalues of $\mathbf{G}$. For non-stationary processes, the $\mathbf{G}$ matrix would differ for each time step.

Thus the probability of being in state a at time t is given by:

$$P(a,t) = \frac{(1 \quad 0)\,\mathbf{G}^{N-1}\,(a_0 \quad b_0)^{\mathbf{T}}}{(1 \quad 1)\,\mathbf{G}^{N-1}\,(a_0 \quad b_0)^{\mathbf{T}}}. \tag{2.19}$$

Again, $N = t/\Delta t$; this is another form of Equation 2.11. For random telegraph processes, this form of the probability of a trajectory reproduces the conventional result from master equations [15]; see below in Section 2.4. In MaxCal, the higher moments of the observables are easily accessed by taking higher derivatives of Q_d; it is unclear how to compute similar quantities from the Master equation approach.

Functional similarities between microscopic models in statistical mechanics and equa-

tions of state in thermodynamics allows assigment of undetermined Lagrange multipliers in the MaxEnt formalism to physically realizable quantities, such as $\beta \leftrightarrow T^{-1}$ [5]. We now make similar correspondences between the MaxCal-derived "statistical weights" with probabilities. The four (exponentiated) Lagrange multipliers α, β, ω_f, and ω_r in matrix $\mathbf{G}$ are reminiscent of a Markov chain propagator. Thus we choose to assign

$$\begin{aligned} \alpha &\leftrightarrow P\left(a, t+\Delta t \mid a, t\right) \\ \omega_f &\leftrightarrow P\left(b, t+\Delta t \mid a, t\right) \\ \beta &\leftrightarrow P\left(b, t+\Delta t \mid b, t\right) \\ \omega_r &\leftrightarrow P\left(a, t+\Delta t \mid b, t\right); \end{aligned} \tag{2.20}$$

each is a probability of moving between or among states in time Δt. Thus

$$\begin{aligned} \alpha + \omega_f &= 1 \\ \beta + \omega_r &= 1 \end{aligned} \tag{2.21}$$

enforces probability conservation; these conservation relations also numerically fall out of calculating the first partial derivatives of Q_d against observed first moments. The Lagrange multipliers can be interpreted as log transition probabilities, since $\lambda_{aa} = \log P\left(a, t+\Delta t \mid a, t\right)$, for example. $\mathbf{G}$ becomes $\begin{pmatrix} 1-\omega_f & \omega_r \\ \omega_f & 1-\omega_r \end{pmatrix}$ and the Master equation follows immediately. The advantage of the MaxCal approach is that Q_d readily provides information about trajectory observables not obviously accessible from Master equations.

We now show an example of a direct calculation of the moments of the trajectory random variables, starting from the transition matrix definition of Q_d, Equation 2.18. We again write the partition function, Equation 2.10 as

$$Q_d = \begin{pmatrix} 1 & 1 \end{pmatrix} \begin{pmatrix} \alpha & \omega_r \\ \omega_f & \beta \end{pmatrix}^N \begin{pmatrix} a_0 \\ b_0 \end{pmatrix}, \tag{2.22}$$

where a_0 and b_0 are initial state probabilities for a and b, respectively (it is easy to show by direct evaluation that Eqns. 2.10 and 2.22 are equivalent), and use Equations 2.23 and

2.24 to compute partial derivatives of Q_d. The eigenvectors of $\mathbf{G}$ are

$$\begin{pmatrix} 1 & 1 \\ \frac{-\alpha+\beta+\sqrt{(\alpha-\beta)^2+4\omega_f\omega_r}}{2\omega_r} & \frac{-\alpha+\beta-\sqrt{(\alpha-\beta)^2+4\omega_f\omega_r}}{2\omega_r} \end{pmatrix}, \tag{2.23}$$

and the eigenvalues of $\mathbf{G}$ are

$$\begin{pmatrix} \frac{\alpha+\beta+\sqrt{(\alpha-\beta)^2+4\omega_f\omega_r}}{2} & 0 \\ 0 & \frac{\alpha+\beta-\sqrt{(\alpha-\beta)^2+4\omega_f\omega_r}}{2} \end{pmatrix}. \tag{2.24}$$

Q_d, when expanded, becomes

$$\begin{aligned} Q_d &= \left(\frac{\alpha+\beta+\gamma}{2}\right)^{N+1}(a_0+b_0)+ \\ &\quad \left(\frac{\alpha+\beta-\gamma}{2}\right)^{N+1}\left(a_0\left(\frac{-\alpha+\beta+\gamma}{2\omega_r}\right)+b_0\left(\frac{-\alpha+\beta-\gamma}{2\omega_r}\right)\right) \end{aligned} \tag{2.25}$$

where $\gamma = \sqrt{(\alpha-\beta)^2+4\omega_f\omega_r}$.

To compute $\langle N_{ab,i}^2\rangle - \langle N_{ab,i}\rangle^2$, we evaluate $\left.\frac{\partial^2 \ln Q_d}{\partial(\ln\omega_f)^2}\right|_{\alpha,\beta,\omega_r}$ using Eqn. 2.26 and enforce conservation of probability (i.e., make the jump from information theory to physics as alluded to in Section 2.2), in Equations 2.22. The result is:

$$\begin{aligned} &\frac{\langle N_{ab,i}^2\rangle - \langle N_{ab,i}\rangle^2}{N} \\ &= -\frac{\omega_f\omega_r\left((\omega_r-1)\left(\omega_f^3+\omega_f\omega_r^2\right)-\omega_r^3+\omega_f^2\left(\frac{2}{n}-2\lambda^n-\omega_r+2\omega_r^2\right)\right)}{(\omega_f+\omega_r)^4} \end{aligned} \tag{2.26}$$

where λ is the smaller eigenvalue in Equation 2.24. Additionally, since ω_f and ω_r are positive, and much smaller than 1 (this is the result of our experimental requirement that we sample all transitions from a to b and vice versa, or that our sampling rate $\Delta t \ll \min(\tau_{ab},\tau_{ba})$ where τ_{ab} is the mean waiting time before the particle transitions from a to b), then $\lambda = (1-\omega_f-\omega_r) < 1$, and so $(1-\omega_f-\omega_r)^N \to 0$ as N becomes large. Thus, $\frac{\langle N_{ab,i}^2\rangle - \langle N_{ab,i}\rangle^2}{N}$ simplifies to:

$$\frac{\langle N_{ab,i}^2\rangle - \langle N_{ab,i}\rangle^2}{N} = \frac{\omega_r\omega_f}{\omega_r+\omega_f}\left(\frac{\omega_r^2+\omega_f^2}{(\omega_r+\omega_f)^2}-\frac{\omega_r\omega_f}{\omega_r+\omega_f}\right). \tag{2.27}$$

It can similarly be shown that

$$\begin{aligned}
\frac{\langle N_{ab,i}\rangle}{N} &= \frac{\omega_r\omega_f}{\omega_r+\omega_f} \\
\frac{\langle N_{aa,i}\rangle}{N} &= \frac{\omega_r}{\omega_r+\omega_f} - \frac{\omega_r\omega_f}{\omega_r+\omega_f} \\
\frac{\langle N_{aa,i}^2\rangle - \langle N_{aa,i}\rangle^2}{N} &= \frac{\left(-1+\omega_f\right)\omega_f\omega_r\left(2+\omega_f\left(\omega_r-1\right)+\omega_r\left(\omega_r+1\right)\right)}{\left(\omega_r+\omega_f\right)^3} \\
\frac{\langle N_{ab,i}N_{aa,i}\rangle\langle N_{ab,i}\rangle\langle N_{aa,i}\rangle}{N} &= \frac{\left(-1+\omega_f\right)\omega_f\omega_r\left(\omega_f\left(\omega_r-1\right)+\omega_r\left(\omega_r+1\right)\right)}{\left(\omega_r+\omega_f\right)^3},
\end{aligned} \tag{2.28}$$

etc. We demonstrate that the Master equation and Maximum Caliber approaches are equivalent in Section 2.4 below.

We now show tests of the MaxCal predictions. Given the first-moment averages observed for the trajectories, MaxCal predicts the second moments. Figure 2.4 shows that two such predicted second moments are strongly correlated with the experimental data.

Figure 2.5 compares one experimental third cumulant with the predicted value from Caliber obtained from the measured first moments. These predictions are also in good agreement with experiments, although, because higher cumulants involve higher derivatives and more data, the scatter is larger than for lower moments. The first moments are easy to measure with good accuracy from short trajectories, so one virtue of the Caliber approach is that all the higher predicted moments are noise-free compared to higher moments extracted from data: predicted moments are dependent on first moments only, whereas data-based higher moments are contaminated by noise from every other lower moment. This is borne out by the form of moments - higher moments always incorporate all lower moments (such as form of the third moment in Figure 2.5) - and hence require measurement of all lower moments - whereas higher moments predicted from Maximum Caliber only take into account the variability from the first moment (from Equations 2.12 and 2.13); higher moments are then simple partial derivatives with respect to the derived Lagrange multipliers.

Figure 2.5 also shows the quantity $\langle N_B N_{ab}\rangle - \langle N_B\rangle\langle N_{ab}\rangle$. These covariances, equivalent to mixed moments, give an alternative way to express *reciprocal relationships* resembling the Maxwell relations of thermodynamics and Onsager's reciprocal relations for dynamical processes near equilibrium. In essence, this means that one trajectory observation counts for two: small perturbations on a trajectory are equivalent to observing covariances; thus,

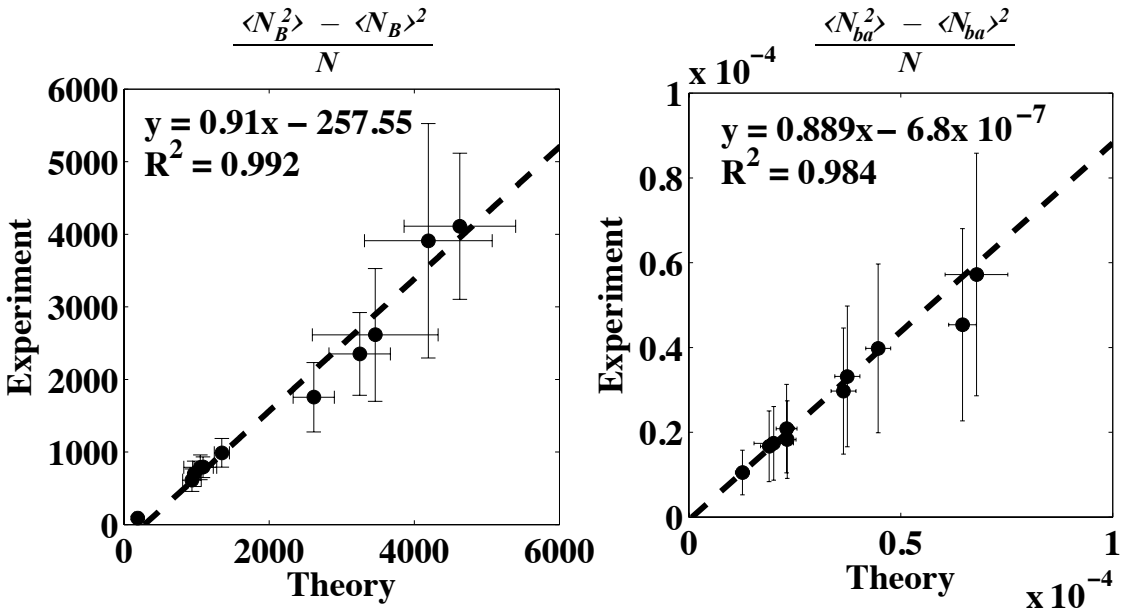

Figure 2.4: **Second moment of the trajectory observables.** The x-axes are the predicted second moments from the MaxCal approach, based on the known first moments. The y-axes are the experimental values of the second moments. **Left**: variance of $\langle N_B \rangle$, **right**: variance of $\langle N_{ba} \rangle$. The dashed lines are the best linear fits; fitting parameters are inset. Each point represents one experimentally observed trajectory. Trajectories were 30,000 Δt units long, and errors were calculated for around 600 trajectories (standard deviation). Vertical error bars are determined by the uncertainty in ω_r and ω_f for a given trajectory; this also sets a bound on the horizontal error bars, since experimental variation is propagated into theoretical predictions through Equations 2.12 and 2.13. ω_r and ω_f values ranged from 1×10^{-5} to 1×10^{-3}.

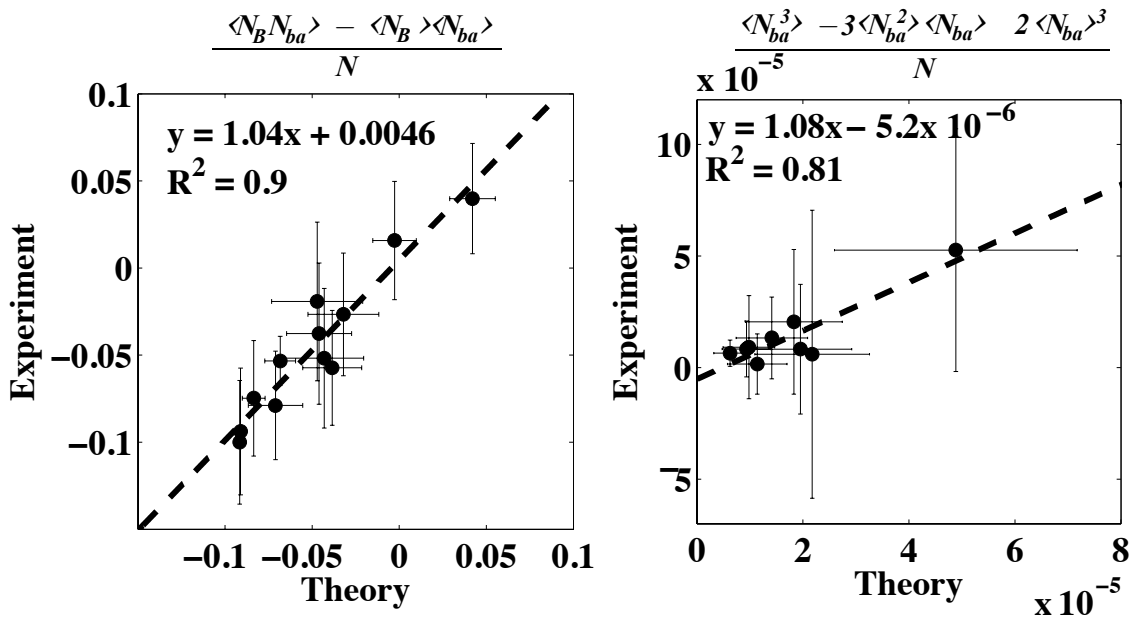

Figure 2.5: **Experiments vs. theory for the covariance and third moment. Left**: one covariance quantity. **Right**: The third moment of N_{ba}. The dashed lines are the best linear fits; fitting parameters are inset. Errors were determined as described in Figure 2.4.

without performing additional experiments or recalculating Q_d, we know how the system will behave for different potential wells - just looking at the fluctuations is enough.

We compute the ratio $N_A/N_B = K$. As $t \to \infty$, this ratio simply becomes the equilibrium constant, K_{eq}, for the relative populations of the two states A and B. In the small-time limit, for this single particle, this ratio is not a single number, as it would be in a bulk equilibrium experiment; rather in single-particle cases, this has a distribution of values. Figure 2.6 shows these distributions for a situation in which the average is $\langle N_A/N_B\rangle \sim 1$. The distribution approaches a δ-function as $t \to \infty$ and thus $K \to K_{eq}$. In diffusion-related problems, small-numbers situations in which particles flow up concentration gradients, rather than down, have been referred to as "bad actors" [20]; the number of bad actors diminishes as trajectories get longer. We also see that simulation of the partition function matches the experimentally measured distributions of N_A/N_B. This indicates that the chosen first moment constraints are sufficient to describe the entire trajectory space.

In summary, we have studied a single colloidal particle undergoing a two-state process, $A \leftrightharpoons B$, with stationary rates. By measuring short trajectories, we obtain first moment observables $\langle N_{bb}\rangle$, $\langle N_{aa}\rangle$, $\langle N_{ba}\rangle$, and $\langle N_{ab}\rangle$. The variational principle of Maximum Caliber

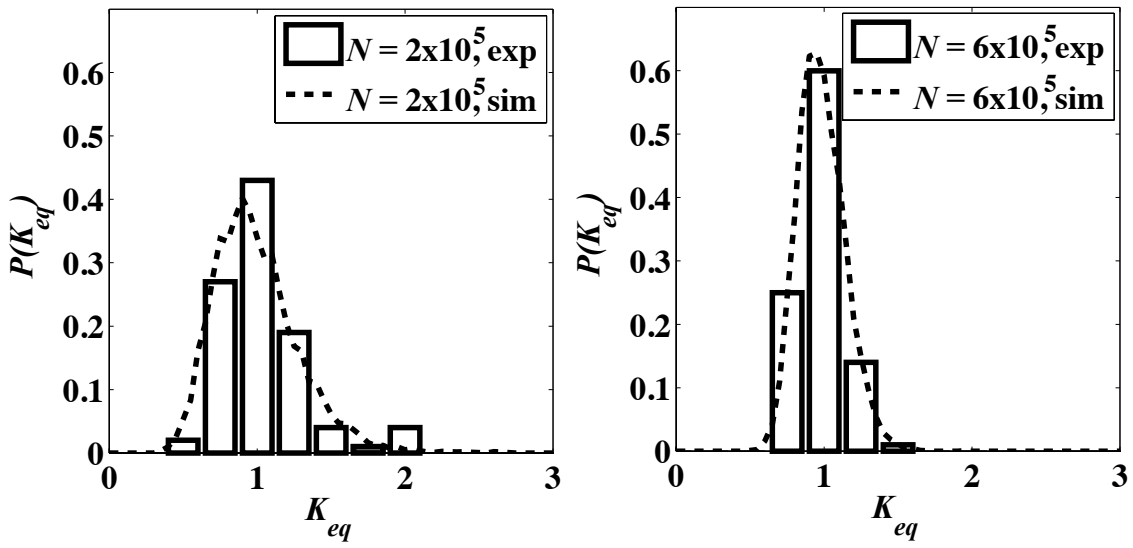

Figure 2.6: **The probability distribution of $N_A/N_B = K_{eq}$ as a function of time.** We obtain the dashed line from Monte Carlo simulation of Q_d and corresponding columns from experimental data. The distribution of time spent in A versus B is broad for short times (**left**) but becomes narrower for increasing trajectory length (**right**). N denotes the length of each trajectory, each repeated around 100 times. As the length of trajectories increases, the equilibrium constant assumes a delta-function distribution, commensurate with equilibrium assumptions regarding chemical reactions.

is then used to predict the higher moments of the observables as well as the full probability distribution of the trajectories. Maximum Caliber also gives other dynamical reciprocal quantities, resembling Maxwell-like relations. I hope that trajectory-based dynamical modeling such as this will be useful in single-molecule and few-molecule science.

2.4 Maximum Caliber's relation to the Master equation

The trajectory observables or random variables chosen are admittedly "odd", in the sense that a two-state trajectory is conventionally defined by the probability distribution for transitioning between states. Thus a rigorous test of the "correctness" of the Maximum Caliber formalism is its ability to reproduce exponential-type waiting time statistics.

Here, we demonstrate that Maximum Caliber predicts the same dynamics as the Master equation formalism for the two state system. In the language of Master equations, we deal directly with transition probabilities, not entire trajectories, and the goal is to find the probability of being in a certain state after a certain time. Now, consider again the two state system. We start with the following assumptions: the probability of being in state b

after a period of time, having been in state a some *short* time dt ago is

$$P\left(b, dt \mid a, 0\right) = k_{ab} dt \tag{2.29}$$

and the converse process is

$$P\left(a, dt \mid b, 0\right) = k_{ba} dt. \tag{2.30}$$

Since the total probability must sum to 1; i.e., $P\left(a, dt \mid b, 0\right) + P\left(b, dt \mid b, 0\right) = P\left(a, dt \mid a, 0\right) + P\left(b, dt \mid a, 0\right) = 1$, then

$$\begin{aligned} P\left(a, dt \mid a, 0\right) &= 1 - k_{ab} dt \\ P\left(b, dt \mid b, 0\right) &= 1 - k_{ba} dt. \end{aligned} \tag{2.31}$$

Thus we can write the more general time evolution formula for any time t, that in the next instant dt,

$$\begin{aligned} P\left(a, t + dt \mid a, 0\right) &= P\left(a, dt \mid a, t\right) P\left(a, t \mid a, 0\right) + P\left(a, dt \mid b, t\right) \times \\ &\quad P\left(b, t \mid a, 0\right) \\ &= P\left(a, t \mid a, 0\right) \left(1 - k_{ab} dt\right) + P\left(b, t \mid a, 0\right) k_{ba} dt \\ &= P\left(a, t \mid a, 0\right) \left(1 - k_{ab} dt\right) + \left(1 - P\left(a, t \mid a, 0\right)\right) k_{ba} dt \end{aligned} \tag{2.32}$$

by substituting Eqns. 2.29, 2.30, and 2.32 above. The master equation is then:

$$\frac{P\left(a, t + dt \mid a, 0\right) - P\left(a, t \mid a, 0\right)}{dt} = -\left(k_{ab} + k_{ba}\right) P\left(a, t \mid a, 0\right) + k_{ba} \tag{2.33}$$

and becomes

$$\frac{dP\left(a, t \mid a, 0\right)}{dt} = -\left(k_{ab} + k_{ba}\right) P\left(a, t \mid a, 0\right) + k_{ba} \tag{2.34}$$

for $dt \to 0$. The solution to this ODE is

$$P\left(a, t \mid a, 0\right) = \frac{k_{ba}}{k_{ba} + k_{ab}} + \frac{k_{ab}}{k_{ba} + k_{ab}} e^{-\left(k_{ab} + k_{ba}\right) t}. \tag{2.35}$$

It follows that

$$\begin{aligned} P\left(b,t\mid a,0\right) &= \frac{k_{ab}}{k_{ab}+k_{ba}}\left(1-e^{-(k_{ab}+k_{ba})t}\right) \\ P\left(a,t\mid b,0\right) &= \frac{k_{ba}}{k_{ab}+k_{ba}}\left(1-e^{-(k_{ab}+k_{ba})t}\right) \\ P\left(b,t\mid b,0\right) &= \frac{k_{ab}}{k_{ba}+k_{ab}}+\frac{k_{ba}}{k_{ba}+k_{ab}}e^{-(k_{ab}+k_{ba})t}.s \end{aligned} \tag{2.36}$$

Note that the probability of being in state a or b as $t\rightarrow\infty$ is independent of starting condition, as expected: $P\left(a,t\rightarrow\infty\right)=\frac{k_{ba}}{k_{ba}+k_{ab}}$ and $P\left(b,t\rightarrow\infty\right)=\frac{k_{ab}}{k_{ba}+k_{ab}}$.

The equations above (2.37) are the solutions to the random telegraph problem. Given an initial state, one can find the probability of being in that state or another one after some arbitrary time. This question is different than the one Maximum Caliber asks, which is the probability of a trajectory. However, as hinted above in Equation 2.19, it is possible to compute the state probability as a function of time as well. However, we need to formulate the question in a different manner in order to use our trajectory-based tools: namely, what is the probability of a trajectory which starts in state a and ends in state b, for example. To that end, we need the probability of a given trajectory (Eqn. 2.11), and the transfer matrix form of the partition function (Eqn. 2.22) and to furthermore rewrite the trajectory probability specifically enumerating the initial and final states; this is easily written in matrix form as:

$$p_i = P\left(b,t\mid a,0\right)=\frac{1}{Q_d}\begin{pmatrix} 0 & 1\end{pmatrix}\begin{pmatrix} 1-\omega_f & \omega_r \\ \omega_f & 1-\omega_r\end{pmatrix}^{N-1}\begin{pmatrix} 1 \\ 0\end{pmatrix} \tag{2.37}$$

where we have applied the conservation of probability constraint, Equation 2.21.

To evaluate Equation 2.37, we first compute the partition function. We apply the probability constraint to Equation 2.25, resulting in

$$\begin{aligned} Q_d &= \frac{\omega_r}{\omega_r+\omega_f}\left[a_0+b_0+\left(\frac{\omega_f a_0}{\omega_r}-b_0\right)\lambda^N\right]+\frac{\omega_f}{\omega_f+\omega_r}\left(a_0+b_0\right)- \\ &\quad \frac{\omega_r}{\omega_f+\omega_r}\left(\frac{\omega_f a_0}{\omega_r}-b_0\right)\lambda^N \end{aligned} \tag{2.38}$$

where $\lambda=1-\omega_f-\omega_r$, the smaller non unity eigenvalue of $\mathbf{G}$. Consider large N: $\lambda^N\rightarrow 0$, and so $Q_d=a_0+b_0=1$. Note that ω_f and ω_r are both positive and greater than zero.

Furthermore, since a_0 and b_0 are initial state probabilities for a and b, respectively, they must sum to 1. Then

$$P\left(b, t \to \infty\right) = \frac{\omega_f}{\omega_r + \omega_f}, \tag{2.39}$$

and similarly,

$$P\left(a, t \to \infty\right) = \frac{\omega_r}{\omega_r + \omega_f}, \tag{2.40}$$

as expected from Equations 2.37 and 2.20 above; also note that we choose to assign the initial state probabilities $a_0 = P\left(a, t \to \infty\right)$ and $b_0 = P\left(b, t \to \infty\right)$.

As we noted before, N designates the number of time points of span Δt that the experiment takes place in, and so $N = t/\Delta t$, where t is the total time of the experiment. Then we can rewrite λ^N as

$$\lambda^N = \left(1 - \left(\omega_r + \omega_f\right)\right)^{\frac{t}{\Delta t}} = \left(1 - \frac{\left(k_{ba} + k_{ab}\right)}{1/\Delta t}\right)^{\frac{t}{\Delta t}} \tag{2.41}$$

since $\omega_f \to k_{ab}\Delta t$ and $\omega_r \to k_{ba}\Delta t$. But Equation 2.41 is nothing more than the definition of an exponential as $1/\Delta t \to \infty$, and so

$$\lambda^N = e^{-\left(k_{ab} + k_{ba}\right)t}. \tag{2.42}$$

We have satisfied the condition that $\Delta t \to dt$ since our experimental sampling rate is much faster than either k_{ab} or k_{ba}. Finally, we can fully compute Equation 2.37, the trajectory probability:

$$P\left(b, t \mid a, 0\right) = \frac{\omega_f}{\omega_f + \omega_r}\left(1 - \left(1 - \omega_f - \omega_r\right)^N\right) = \frac{k_{ab}}{k_{ab} + k_{ba}}\left(1 - e^{-\left(k_{ab} + k_{ba}\right)t}\right). \tag{2.43}$$

This is the same as in Equation 2.36; thus, Maximum Caliber predicts the same dynamics as the Master equation - a basic test has been passed.

However this suggests a deeper connection between Maximum Caliber and Markov processes, which can be written as the probability of going to vector of states j from i in n time steps as

$$p_{ij}^{(n)} = P\left(X_n = j \mid X_o = i\right). \tag{2.44}$$

for a vector of random variables X_i. If we invoke the Markov property that

$$P\left(X_{n+1}=x \mid X_1=x_1, X_2=x_2 \cdots, X_n=x_n\right)=P\left(X_{n+1}=x \mid X_n=x_n\right), \tag{2.45}$$

or in other words, that the current state only depends on one previous state, then

$$p_{ij}^{(n)}=P\left(X_n=j \mid X_{n-1}\right) \cdots P\left(X_2 \mid X_1\right) P\left(X_1 \mid X_o=i\right). \tag{2.46}$$

But since $P\left(X_n \mid X_m\right)$ is nothing more than a transition probability in dt, we can express $e^{\lambda_{m,n}}=P\left(X_n \mid X_m\right)$ as the probability of transitioning between state m and state n (again, the Lagrange multipliers are log transition probabilities). Thus, summing over Equation 2.46 (that is, accounting for all possible combinations of states, Γ), and accounting for all the possible transitions between different combination of states (m,n), we recover the partition function:

$$\sum_{\Gamma} \prod_{(m,n)} e^{\lambda_{m,n} N_{m,n,\Gamma}} \tag{2.47}$$

where $N_{m,n,\Gamma}$ accounts for the degeneracy of transitions $P\left(X_n \mid X_m\right)$ in trajectory Γ. This partition function reduces to Equation 2.10 for two-state trajectories.

2.5 Performance of Maxmium Caliber

In order to obtain better statistics regarding higher moments of the Maximum Caliber observables, we decided to perform Brownian dynamics simulations of trajectories. That is, we modeled a particle diffusing on a potential landscape as if the landscape had been created by optical traps.

The simulations were carried out using an algorithm by Gillespie [22]. Briefly, we simulated the Langevin equation:

$$m\dot{(v)}\left(t\right)=-\gamma v\left(t\right)+\sqrt{2\gamma k_B T}R\left(t\right)+U\left(x\right) \tag{2.48}$$

where γ is the Stokes drag for a 1 μm particle in water, k_B is Boltzmann's constant, and T the temperature, 298 K. $U\left(x\right)$ is a double-well potential modeled from 2 Gaussian shaped optical traps consisting of laser light at 532 nm. Each potential had spring constants

approximately $\kappa = 2.0 \times 10^{-5}$ N/m, as deduced by considering the wavelength of light, numerical aperture of the microscope (NA = 1.4), and typical laser powers. The resulting width of the potentials was then simply $\langle x^2 \rangle = k_B T/\kappa = 200$ nm^2. $R(t)$ is a fluctuating force that obeys Gaussian white noise statistics. $v(t)$ is the velocity of the particle, and m is the mass. The Brownian dynamics simulations were computed with a time step sufficiently short such that the particle never errantly left the trap.

After recording the simulated trajectories (200,000 seconds each), we set the transition between two states as the prescribed maximum in the simulations (where the two optical traps meet). Similarly, in the experimental data, the negative logarithm of positions was computed and a double-Gaussian potential fit to this histogram (see Figure 2.2). The transition point, in this case, was determined as the inter-well maximum for each potential landscape. The criterion for a transition is a dwell time in either of the wells for greater or equal than .002 sec; that is, the sampling rate of the experiment was set at 1 KHz; thus, in order to get rid of uncorrelated noise we simply made sure a particle dwelled for two time points at a minimum. This choice of a transition produced a waiting time distribution for transitioning between states that fits an exponential type distribution (see Figure 2.7), which serves as an alternate way to confirm the predictions of Maximum Caliber; that is, the propagator (Eq. 2.18) will generate exponential-type dynamics. We then computed the statistics of the simulations and compared them to the predicted statistics from Maximum Caliber. The results are shown in Figures 2.8, 2.9, and 2.10 for observables shown in Figures 2.4 and 2.5. The measured moments / theoretical predictions were compared for all moments (up to 3rd - though not all data is shown), and the correlation was always near 1. Note that the absolute scale is not the same as in the experiments described since the potentials used in the simulations were simple models of an optical trap, not the actual wells themselves, and the intra-well barrier heights were not the same in the experiments; i.e., the transition rates between experiments and simulations were not comparable.

A note on error analysis: to compute the experimental error, we divided a thousand second trajectory into 10 second increments. Thus the error on the mean (for example, N_{ab}) is the standard deviation of the distribution of N_{ab}. In order to compute the confidence intervals on higher moments, we repeated the experiment 10 times and measured the distribution of the higher moments on these 10 trajectories. This was done for each set of potential landscapes. In order to compute the error on the theory, we simply propagated

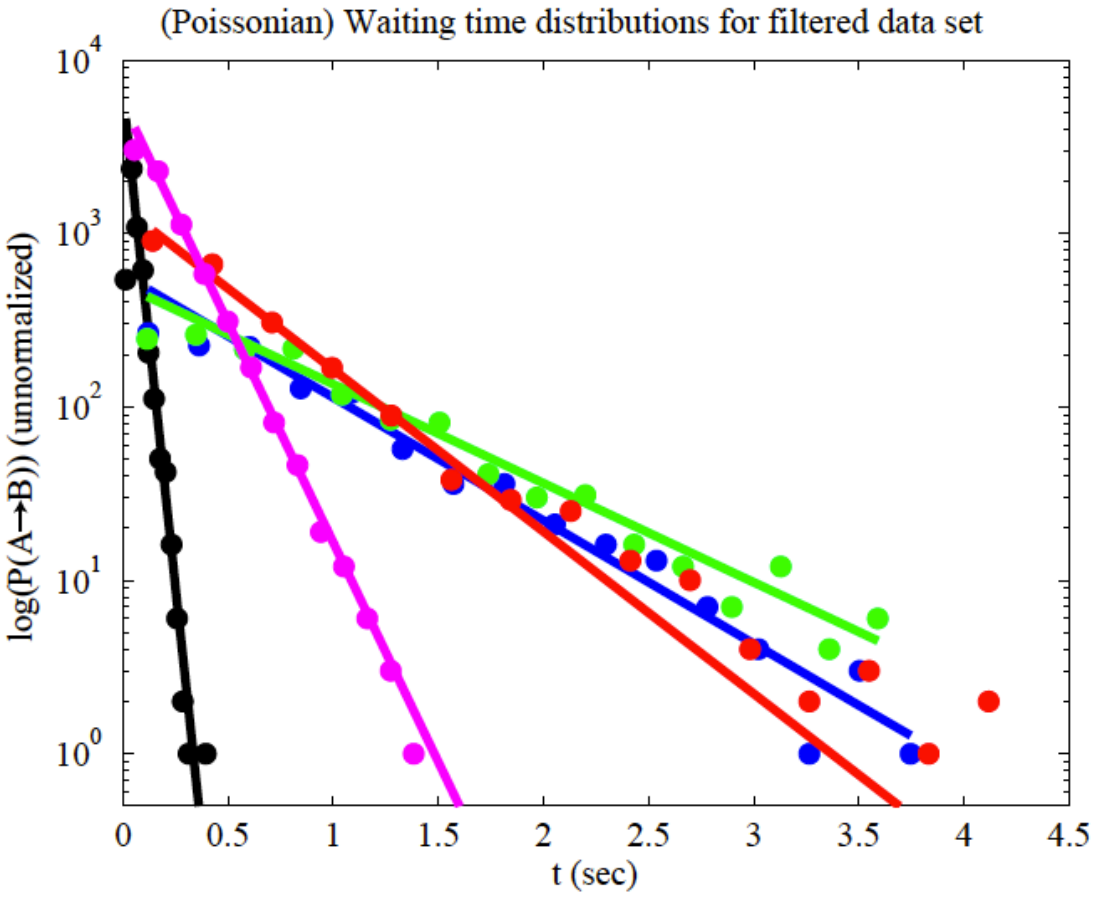

Figure 2.7: **Waiting times are exponentially distributed.** The waiting time distributions for transitioning from state A to state B are linear on a log plot, suggesting that the waiting times are exponentially distributed.

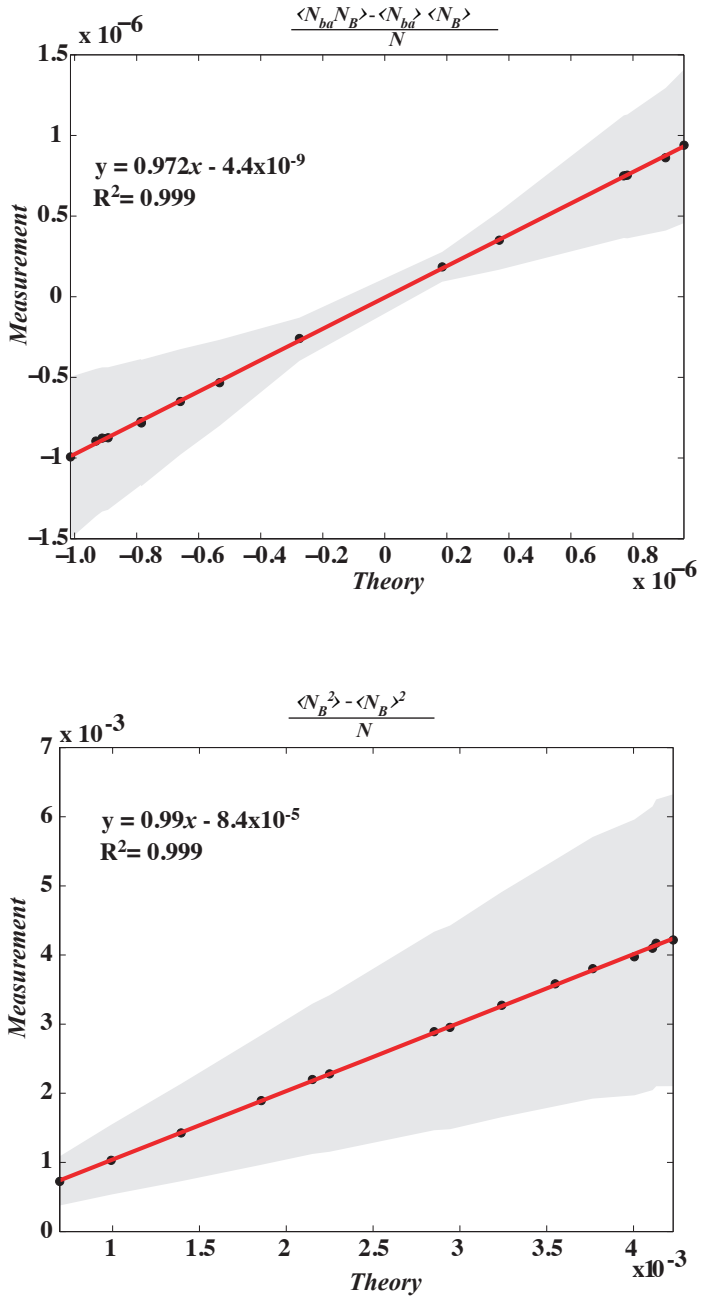

Figure 2.8: **Simulated second moments of N_{ba} and N_B.** The simulations as described were processed identically to optical trapping data. The moments were calculated from the data (y-axes) and plotted against the theoretical predictions (x-axes). The correlation (red line, linear fit) is better than Figure 2.4. Fit statistics are inset. Simulations, naturally, are performed under idealized conditions. The gray shaded region represents the estimated error in both the measurement of the moments, and the theoretical predictions, as described in the text.

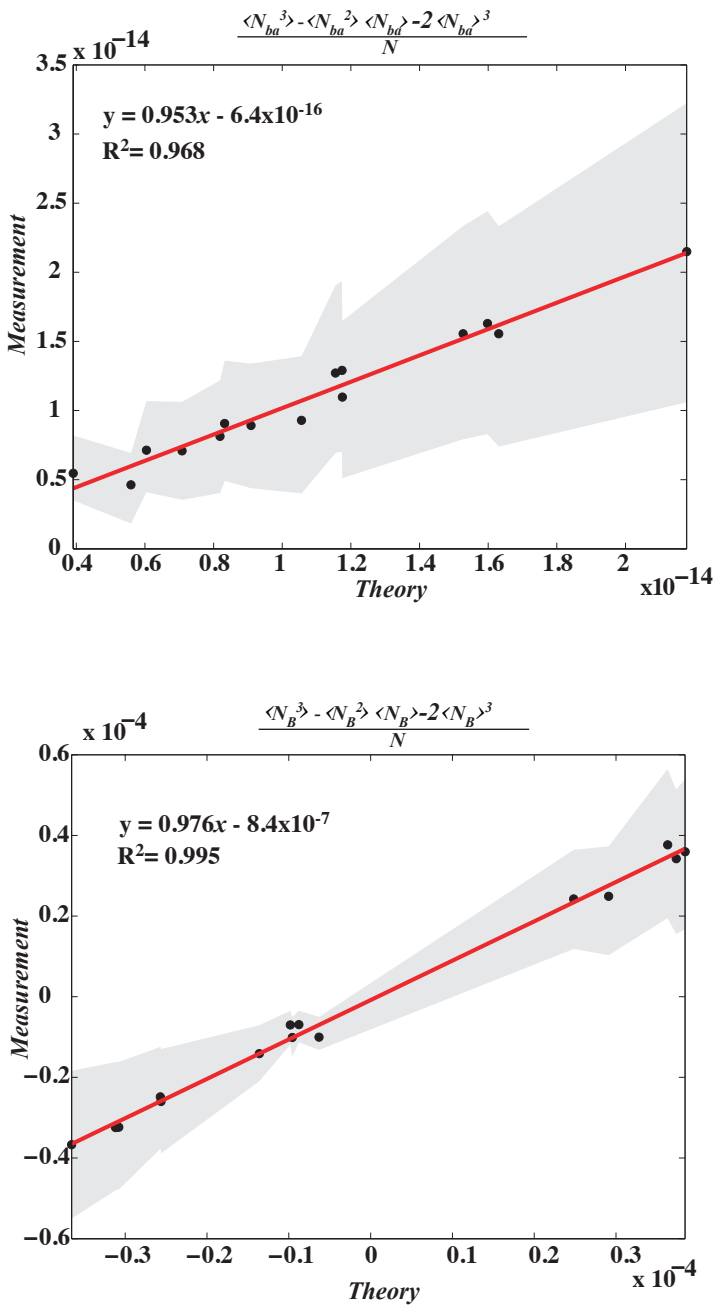

Figure 2.9: **Simulated third moments of N_{ba} and N_B.** Simulated data was processed as described. The gray shaded region is the estimated error for both the measured data (y-axes) and theoretical predictions (x-axes). Compared to Figure 2.5, the correlation (red line, linear fit) is markedly improved. Fit statistics are inset. Errors (gray regions) were determined as described in the text.

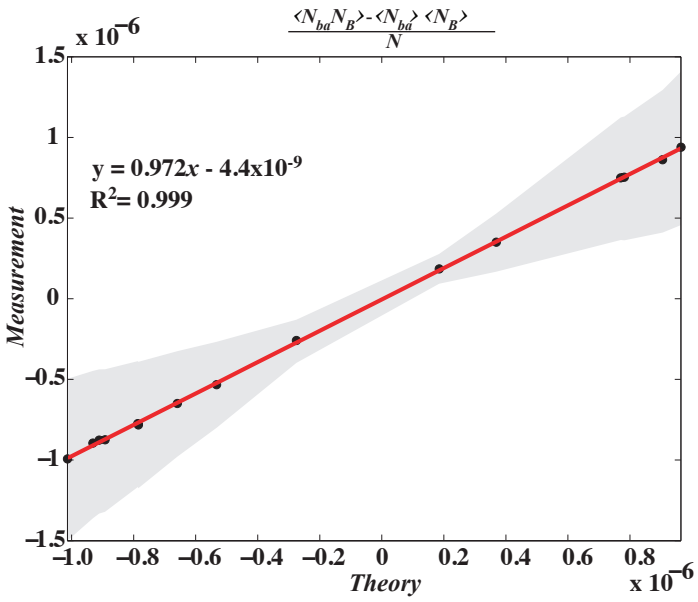

Figure 2.10: **Simulated covariant moments of N_{ba} and N_B** The covariance between two observables of the simulated data was compared to theoretical predictions by Maximum Caliber. The gray shaded region is the estimated error for both the measured data (y-axis) and theoretical predictions (x-axis). Compared to Figure 2.5, the correlation (red line, linear fit) is markedly improved. Fit statistics are inset. Errors (gray regions) were determined as described in the text.

the standard deviation of the distribution of rate constants obtained by fitting the first moment data to equations 2.12 and 2.13.

We also make the claim that all the higher cumulants, which would require much longer trajectory data, can be predicted from short-trajectory information. We show this below: In Figures 2.11, 2.12, 2.13, and 2.14, we plot the moments for two of the elementary observables (N_{aa}, N_{ab}) as a function of length of trajectory. In each graph, we plot both the simulation derived moments ("sim" or "simulation"), and the moments obtained from the partition function (marked "thr" or "theory"). What is immediately apparent is that in all cases, the "thr" moments approach the "true" values as least as fast as if not faster than the "sim" moments. The "true" value of the moments is assumed to be the moment obtained from the longest trajectory. The reason for the enhanced accuracy of the theory is that rates k_{ab} and k_{ba} are obtained from the expected values of N_{aa} and N_{ab} only. Thus, whereas the computation of higher moments from simulated data ("sim") is subject to fluctuations within the higher moments themselves, higher moments computed from the rate constants ("thr") are subject only to first moment fluctuations. Thus it can be said that we can predict higher moments from short-trajectory information. This is especially apparent for third moments (Fig. 2.13) and the first cross-moment (covariance) (Fig. 2.14).

2.6 Summary

Maximum Caliber is a method for evaluating the probability of a trajectory given constraints on how the trajectory can (or did) behave, utilizing the algorithm of the Principle of Maximum Entropy, and hence information theory, as a foundation. Prior to our characterization of two-state trajectories [9], Maximum Caliber had been used to derive Fick's Law of particle transport, Fourier's Law of heat transport, and Newton's Viscosity Law of momentum transport [20], all of which were heretofore phenomenological in origin. We found that using Maximum Caliber, we could predict higher moments of certain trajectory observables, and that the dynamics generated by the Maximum Caliber (or Maximum Entropy) algorithm were the same as expected from Master equations. One crucial aspect in the transition from information theory to physics was the identification of Lagrange multipliers as log transition probabilities, given the similarity between the Maximum Caliber propagator, $\mathbf{G}$, and a Markov process propagator for the random telegraph model. We

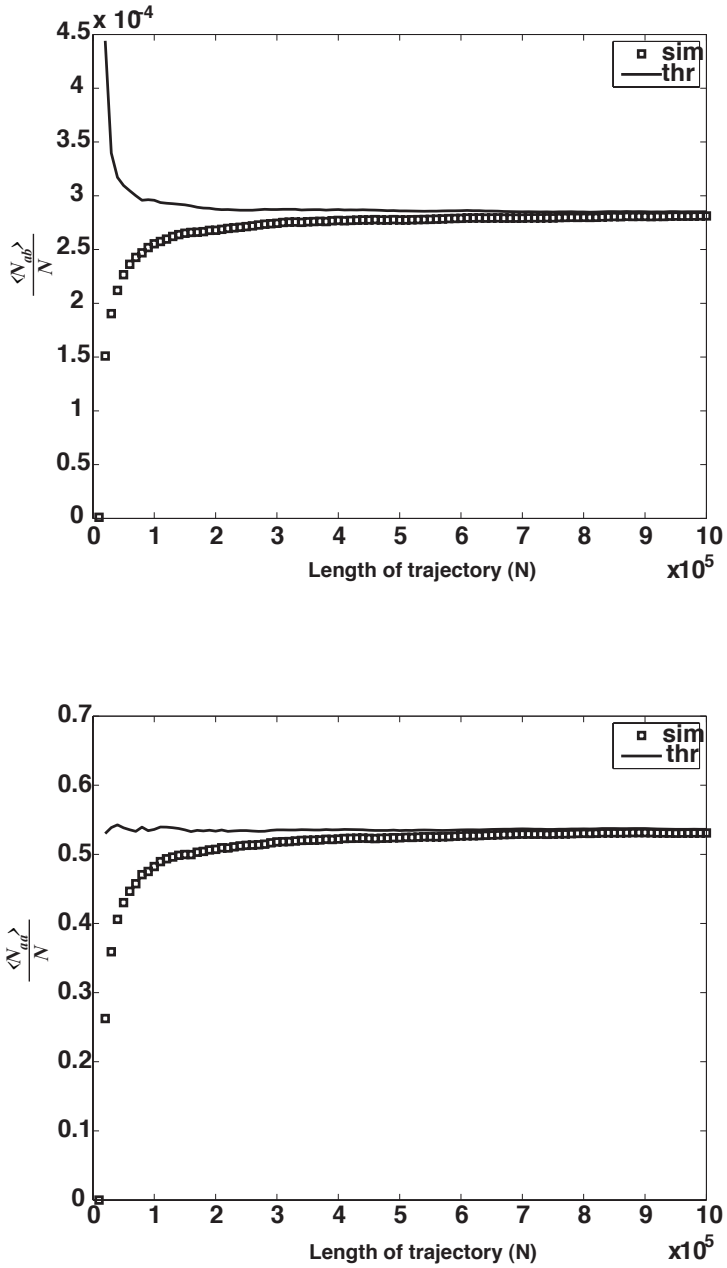

Figure 2.11: **First moment of N_{ab} and N_{aa} as a function of trajectory length**. First moment of N_{ab} and N_{aa} as a function of trajectory length, for Brownian dynamics (solid line), and from the dynamical partition function (squares). It is especially apparent from the N_{aa} observable, that the Maximum Caliber predictions are accurate, even for short trajectories.

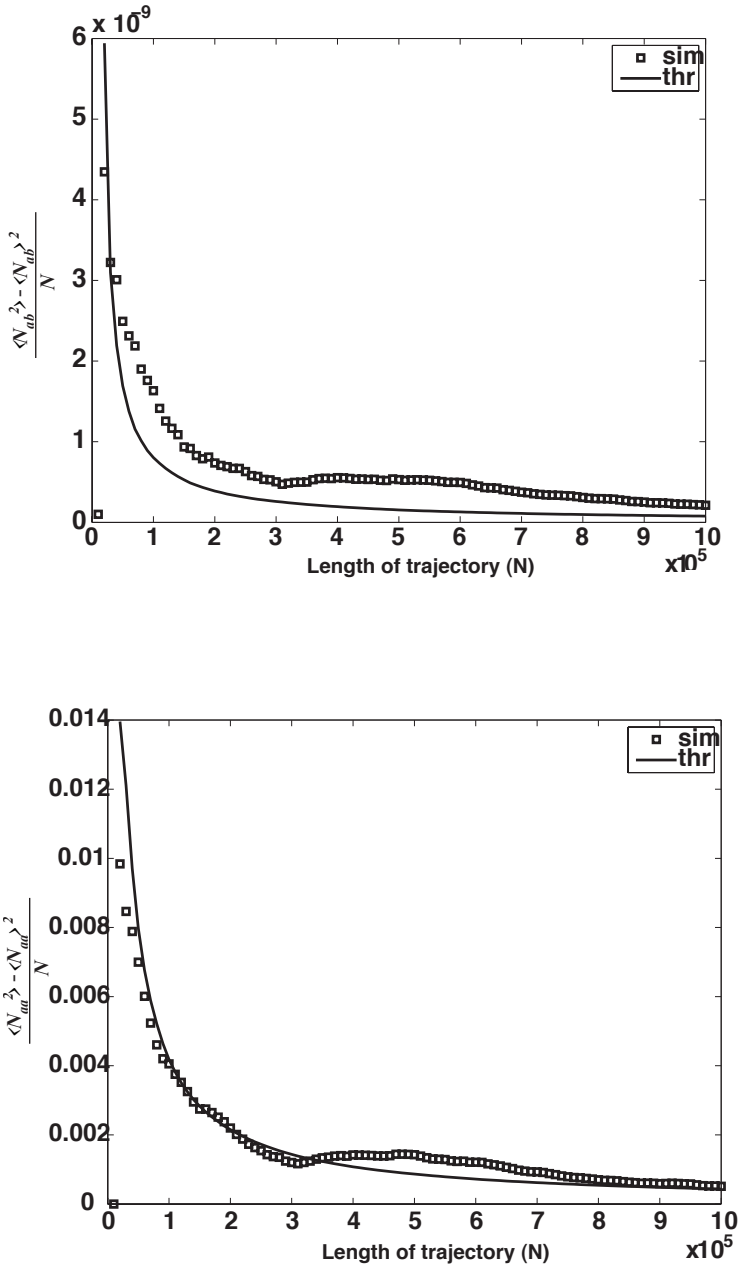

Figure 2.12: **Second moment of N_{ab} and N_{aa} as a function of trajectory length**. Second moment of N_{ab} and N_{aa} as a function of trajectory length, for Brownian dynamics (solid line), and from the dynamical partition function (squares). Note the amount of time it takes for the simulation to converge to the "true" value of the second moment of N_{ab}, whereas the Maximum Caliber prediction arrives much faster.

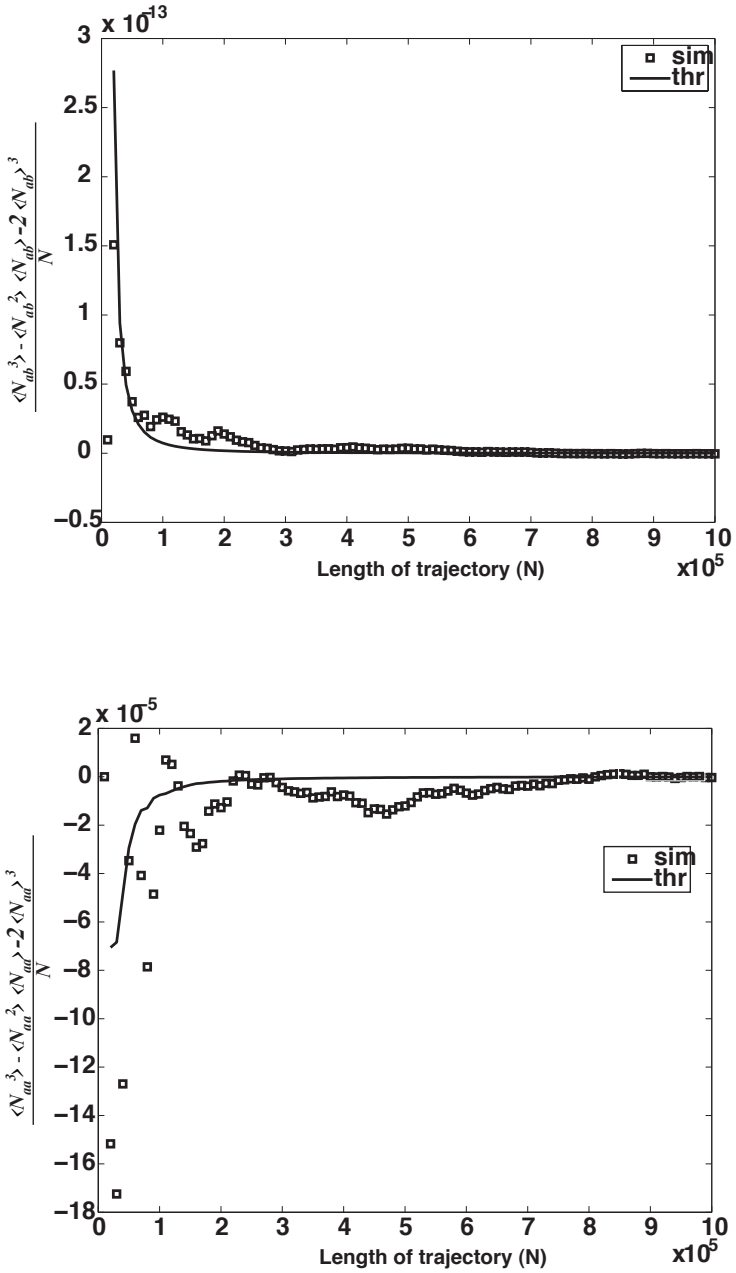

Figure 2.13: **Third moment of N_{ab} and N_{aa} as a function of trajectory length**. Third moment of N_{ab} and N_{aa} as a function of trajectory length, for Brownian dynamics (solid line), and from the dynamical partition function (squares). Both simulations and theory are fairly accurate; this is likely due to the nature of 3rd moment fluctuations themselves - i.e., in this system, there are few.

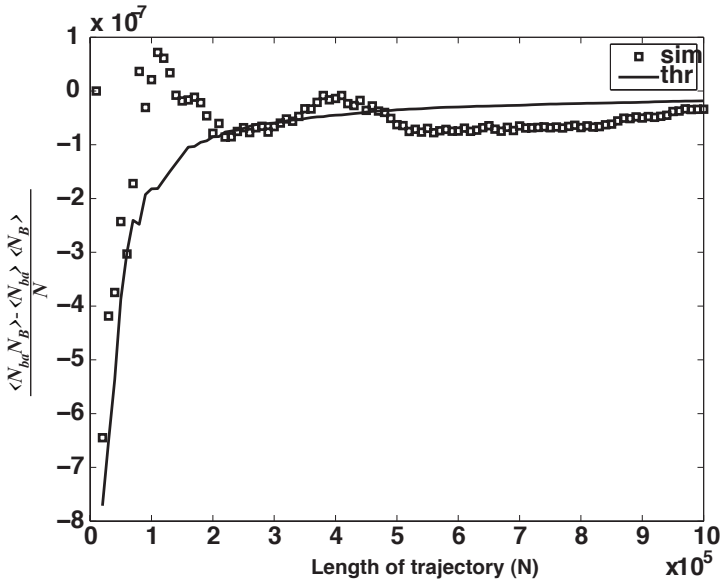

Figure 2.14: **Cross moment of N_{ab} and N_{aa} as a function of trajectory length**. Cross moment of N_{ab} and N_{aa} as a function of trajectory length, for Brownian dynamics (solid line), and from the dynamical partition function (squares). Like the second moment (Figure 2.12), this quantity converges to the "true" value much quicker when predicted by Maximum Caliber.

also discussed the possible equivalence of Maximum Caliber trajectory distributions and Markov Process distributions. In the two-state trajectories considered here, the dynamics were stationary in time, although stochastic.

This could lead us in a fruitful direction for the use of Maximum Caliber in time-dependent dynamics. That is, Jaynes' formulation for time and space dependent constraints ($\sum_t \int d^3x dt \lambda_j (x,t) A_j (x,t)$) could perhaps be formulated as a Markov chain of order $m > 1$; that is, a chain with memory which decays in m time steps. This could result in correlation functions as constraints in the Caliber, not simply first moments. This also leads to another corollary, that it is possible to interpret Lagrange multipliers as log transition probabilities when an equivalence to Markov Processes can be established, though I do not claim that this is true in general. In fact, it has been shown by S. Marzen that the random telegraph process is equivalent to an Ising model - and so the Lagrange multipliers are interpreted as coupling energies and magnetic fields. In either case, a model is necessary to complete the transition from information theory to physics, thereby imbuing the Lagrange multipliers with a different meaning. In the Principle of Maximum Entropy, there is thermodynamics to complete this transition - no such luck here.

Chapter 3

DNA Ejections of Bacteriophage Lambda

3.1 Introduction

Bacteriophages have played a key role in the emergence of both molecular and physical biology. They were an essential component of the Hershey-Chase experiment [23], which established that DNA was the molecule of inheritance, and have since proved an important technology for cloning and protein expression [24]. Phages have also been important model organisms for the study of macromolecular self-assembly; recent work has demonstrated assembly of viruses from their constituent components *in vitro* [25]. Bacteriophages have also been instrumental in the field of systems biology, as evidenced by the dissection of the transcriptional program responsible for the decision between lysis and lysogeny [26, 27, 28, 29, 30]. Finally, bacteriophages have played an important role in the field of single-molecule biophysics, as evidenced by the single-phage packaging experiments which revealed the large (many pico-Newton) forces generated by motors that package phage DNA into protein capsids [31]. The study of the bacteriophage life cycle has yielded much insight in the physical biology setting and we anticipate that it will continue to serve as a useful model system.

As a reminder, bacteriophages are bacterial parasites - they are viruses that hijack the host machinery and utilize it for the viruses' own reproductive purposes. We are concerned with the tailed class of bacteriophages; these have capsids that are around 100 nm in diameter and a tail that extends approximately 150 nm, so they are small compared to typical bacterial dimensions ($\sim$ 3 x 1 microns). They have no known mechanism of motility

besides diffusion in the surrounding fluid - in fact, the presence of water (and certain ions) is an absolute requirement for maintaining stability of the capsids - dehydration causes capsid collapse, as measured by atomic force microscopy [32]. Upon binding to the cell surface, usually through a specific receptor, they inject their genetic material (and some protein) into the cell. Then a choice is made between lysis (the immediate production of more phages) or lysogeny (integration into the host genome) [33]. See Figure 3.1 for a brief introduction to the phage lifecycle.

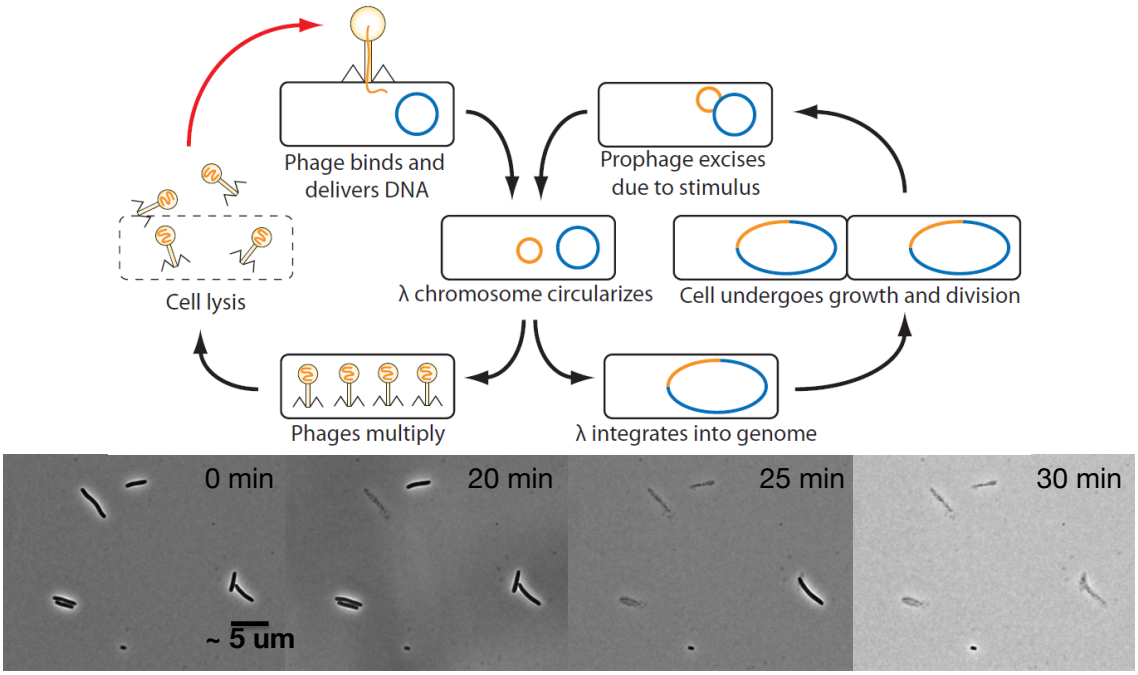

Figure 3.1: **Phage life cycle. Top**. A lambda phage, diffusing in the medium, lands on the specific receptor LamB, on the outer membrane of the bacterium. The phage inserts its genome - at this point a linear strand of DNA - into the cell, and the DNA molecule circularizes within 0.5 minutes [34, 35, 36]. Later, a choice is made whether to undergo lysis or lysogeny. *Lysogeny* means the genome integrates with the *E. coli* host and is propagated along during normal cell division. *Lysis* means phages are immediately reproduced and the hosts are lysed. A lysogenic cell can convert to a state of lysis upon appropriate stimulus. **Bottom**. Montage of infected *E. coli*. At time 0, bacteria are infected. After 20 minutes, the first cell has lysed. After half an hour, all the cells have lysed.

This chapter of the thesis is concerned with the initial part of the bacteriophage lifecycle: that of DNA entry into the cell. In the first section is described our efforts to determine the control parameters for the velocity of ejection of DNA and the measurement of the amount of force phage lambda can exert during ejection under a variety of ionic conditions. In the second section is described our attempts at measuring the rate of DNA injection into cells.

DNA, at physiological pH, is highly negatively charged due the presence of the sugar-phosphate backbone. For lambda phage, the genome is 16 microns in length when completely stretched. At 1 nm in radius, the total volume it occupies is ∼50% of the volume inside the capsid. The maximal spacing between strands inside the capsid is therefore around 2.5 nm, and looks hexagonally packed under electron microscopy [37], although the issue of DNA structure inside the capsid is still a debated issue [38]. Regardless, the DNA inside is tightly packed (bends at distances much shorter than the commonly quoted persistence length of ∼50 nm for dsDNA in physiological buffers [39]), and the motor (terminase) that moves DNA inside the capsid can (and must) exert forces much larger than those found inside eukaryotic cells [40] - upwards of 60 pN. It is accepted within the scientific community [41] that the phage uses this tightly packed DNA - a concomitant build up of both electrostatic and bending energy - to generate large forces to force its DNA into the bacterium; indeed, phages with artificially shortened genomes are usually not infectious [42].

3.2 Control parameters for phage lambda ejections *in vitro*

We study the control parameters that govern the dynamics of *in vitro* DNA ejection in bacteriophage lambda. Past work has demonstrated that bacteriophage DNA is highly pressurized; this pressure has been hypothesized to help drive DNA ejection. Counter-ions influence this process by screening charges on DNA; however, a systematic variation of salt concentrations to explore these effects has not been undertaken. To study the nature of the forces driving DNA ejection, we performed *in vitro* measurements of DNA ejection in bulk and at the single-phage level. We present measurements on the dynamics of ejection and on the self-repulsion force driving ejection. We examine the role of ion concentration and identity in both measurements, and show that the charge of counter-ions is an important control parameter. These measurements show that the frictional force (or its inverse, mobility) acting on the ejecting DNA is subtly dependent on ionic concentrations for a given amount of DNA in the capsid. We also present evidence that phage DNA forms loops during ejection; we confirm that this effect occurs using optical tweezers. We speculate this facilitates circularization of the genome in the cytoplasm.

Here, we highlight four recent experimental techniques that examine how phage DNA

is packaged into and released from protein capsids. These four techniques include single-molecule packaging of DNA, single phage ejection measurements, osmotic suppression of DNA ejection, and cryo-electron tomography of partially packed phages. Single-molecule DNA packaging experiments have sought to elucidate the mechanics of how DNA gets packaged into the capsid; optical tweezers have been used to make systematic measurements of the packaging force for phage lambda and phi29 in a variety of different salt conditions [40]. What these experiments demonstrated was that by increasing the charge of the salts, the genome is packaged at a higher velocity. Additionally, the internal force of the capsid DNA that resists packaging increases monotonically with a reduction in the charge of the salts.

These packaging experiments are complemented by single-phage ejection experiments, wherein phages are coerced into ejecting their DNA by addition of a trigger protein and then observed under a microscope with the aid of flow and DNA staining dyes [43, 44, 45]. These experiments illustrated the dynamics of the ejection process and have provided some insight into the frictional forces experienced by the DNA as it exits the capsid [44, 45, 46]. The principal quantity measured in these experiments is the velocity of ejection as a function of the quantity of DNA inside the capsid. The observations garnered from these ejection experiments reveal (broadly speaking) a picture in which the forces responsible for the ejection process decay as a function of packaged length in the same way as the forces that build up during the packaging process depend upon the packaged length: a reduction in charge increases the speed of ejections. However, the available ejection data only reflect measurements on a few ionic conditions.

It is also possible to measure the force exerted by the DNA inside phage capsids during ejections by inducing phages to eject their DNA into a series of increasingly osmotically-resistive solutions [47]. By varying the concentration of an osmolyte like polyethylene glycol (PEG), the resistive pressure is also varied. One can therefore measure the amount of DNA inside the phage capsid as a function of external pressure, and therefore how much force is generated by the DNA inside the capsid as a function of genome length [48, 49, 50]. It has been proposed that the DNA self-repulsion force (again, a combination of electrostatic and elastic forces) can help push the DNA into the bacterial cytoplasm [51], but a consensus has yet to be reached. Alternative models propose that highly osmotic environments serve as a condensing agent for DNA exiting phage and actually promote ejection [50, 52]. Others

posit that the osmotic difference [53] between the intra- and extracellular environment is sufficient to "flush" DNA from the phage into the host [54]. However, when certain experimental conditions are met, by increasing the external pressure of the solution, phage ejections are inhibited [52]. To our knowledge, a systematic study of how different salt conditions influence ejections at different resistive pressures has yet to be undertaken.

Another way to study ejection and packaging is by looking at the structure of the DNA itself inside the capsid. Cryo-electron tomography experiments in which the packaging process of phage phi29 was paused by freezing have provided information on the structure of viral DNA as a function of length of DNA inside the capsid [55]. Others have investigated T5 [56], lambda [57, 58], T3 [59], and P22 (see [60] and references therein). Recently, the interaxial spacing of condensed DNA was measured as a function of salts in order to corroborate viral DNA packaging theory [61].

The four experimental techniques described above have shed light on the forces, dynamics, and structure of DNA entering and leaving the viral capsid, and have been complemented by a vigorous modeling effort. These include simple structural models taking into account bending energies and *in vitro* measurements of electrostatic repulsion [62, 51, 63, 64, 65], density functional theory with few structural constraints that takes into account electrostatic repulsion/correlations and van der Waals forces [66], and molecular mechanics [55, 38, 67]. This body of work deepens our physical understanding of the packaging and ejection process.

In this work, we focus on the measurement of velocity and force of DNA ejection in bacteriophage lambda as a function of charge at fixed ionic strength. In previous experiments, it was shown that ejections are slower in the presence of magnesium as opposed to sodium [45]; however, these experiments were not performed at fixed ionic strength, making it difficult to discern the role of other ion specific factors, such as charge, or hydrodynamic radius, although we neglect the latter issue in this study. Our results demonstrate that the ionic composition controls the observed velocity and force, rather than ionic strength. We thus propose that the charge of the counter-ion species is an important control parameter for this system.

We also examined "looped" ejections, a type of ejection that was not analyzed in previous experiments and was assumed to be an artifact [45]. In these ejections, the first portion of the DNA exiting the capsid is stuck at the site of origin, leading to a very bright piece

of DNA. This attachment is eventually broken by the flow, fully unfolding the DNA. We demonstrate that looped ejections exhibit the same dynamics as unlooped ejections and that they are another ejection class, and not an artifact. We confirm this using optical traps. Finally, we provide technical improvements on the single-phage ejection assay, in particular showing that low dye concentrations are necessary to avoid spurious (non-LamB induced) ejections, as well as a reliable protocol for using field inversion gel electrophoresis to measure the amount of DNA ejected in bulk osmotic suppression assays, instead of spectrophotometric characterizations.

3.2.1 Ejections into solution

Our first set of experiments focused on optimizing the single phage ejection assay with regards to SYBR gold concentration, since we noticed that phages spontaneously eject their DNA in high concentrations of SYBR gold. SYBR gold is thought to affect the mechanical properties of DNA since other DNA stains have been shown to affect DNA's persistence length [68]. To investigate the origin of these ejections and to test the hypothesis that they are triggered by SYBR gold, we incubated phages in different salts and different amounts of SYBR gold and subsequently measured the number of active phages by titering. The results are given in Table 3.1; errors in the titer values follow $\sqrt{N}$ (counting) statistics. For high concentrations of SYBR gold (1:10000 dilution from stock), we see a steep drop in the number of active phages, between 2- and 10-fold for the buffers containing magnesium. The drop is particularly drastic in pure sodium (1000-fold), a condition thought to increase the DNA pressure inside the capsid. One explanation is that sodium in concert with SYBR gold increases the DNA pressure enough to destabilize the phage. Alternatively, magnesium and SYBR gold could compete with each other for binding sites on the DNA, providing a protective effect. This hypothesis is partially borne out by the fact that phage ejections, under the microscope, appear dimmer in magnesium-containing buffers, as compared to buffers with equivalent concentrations of sodium. Another possibility is that SYBR gold acts by a mechanism similar to LamB. Regardless, the drop in titer is consistent with the hypothesis that SYBR gold induces ejections. When the SYBR gold concentration is reduced even more (1:1000000), we recover almost the entirety of the original titer value. We concluded that it was preferable to perform the experiment at this lower concentration to minimize the effect of SYBR gold. The concomitant reduction in signal did not affect

our DNA segmentation algorithms for measuring ejections as a function of time.

When performing the single phage ejection assay (Fig. 3.2), we always noticed two types of ejections - some that look similar to those previously reported and those that revealed a different type of dynamics that have the appearance of a "partial ejection" and were previously viewed as artifactual [45] (Fig. 3.3 and 3.5, B). Furthermore, we always saw spurious ejections of both types. In our investigations into the origins of the spurious ejections, we found that, under certain salt conditions (Table 3.1), we saw more "artifact" ejections after addition of LamB (up to 3 fold increase) in the single phage ejection assay. This led us to question their designation as "artifact."

However, it is well known that DNA will stick to glass beads [69], and the previous experiment does not rule out DNA sticking to the microscope coverslip, although this seems unlikely since the addition of LamB (in excess, at $\sim 20 \mu$g/ml) would tend to block sites on the glass for the ejecting DNA to bind to. The stickiness of glass was confirmed by incubating lambda phage DNA on freshly cleaned coverslips (see Appendix, Section A.2.4); upon observation, the glass was covered in DNA (data not shown). Thus as another test, we performed the ejection assay in the presence of the surface blocking agents BSA, casein, and heparin. These blocking agents significantly reduced DNA's affinity to the surface [70] - when bare lambda DNA was again incubated in a flow chamber with these blocking agents, only a single strand was found after futile searching efforts (data not shown). However, even with these blocking agents, "artifactual" ejections were seen in the phage ejection assay (data not shown). Fortunately, the content of the "artifact" ejections could be deduced from serendipitous ejections: occasionally, it could be seen that the DNA was in fact in a looped state. This was quantified by an intensity histogram and is shown in Figure 3.3, A. We therefore term this class "loop" ejections in contrast to the ejections previously characterized, which we call "continuous" ejections. The addition of LamB tends to increase the amount of looping ejections (Table 3.1) which suggests that looping ejections are physiological.

We further demonstrated that the looping ejections were not surface mediated by ejecting biotinylated phages off of optically trapped streptavidin coated polystyrene spheres (Fig. 3.3, B). A dual-syringe pump pushes fluid into the chamber (Fig. 3.2, B). Using an optical trap, we grabbed hold of a microsphere, and moved it across the laminar flow boundary layer into the ejection buffer. The continuous flow system limits diffusive mixing at the

Ionic composition	Titer (x 10^{11})	Titer in high SYBR (x 10^{11})	Titer in low SYBR (x 1011)	% looped in low SYBR with LamB	% looped in low SYBR with no LamB
50 mM Tris 10 mM Mg 0 mM Na	1	0.41	0.55	88	35
10 mM Tris 2.5 mM Mg 0 mM Na	0.76	0.07	0.59	58.8	13.2
10 mM Tris 1.875 mM Mg 2.5 mM Na	0.90	0.10	0.86	57.6	25
0 mM Tris 1.25 mM Mg 5 mM Na	0.79	0.03	0.97	50	48
10 mM Tris 0.625 mM Mg 7.5 mM Na	0.93	0.08	1.10	44.9	20
10 mM Tris 0 mM Mg 10 mM Na	0.69	0.001	0.55	55.3	6.9

Table 3.1: **Phage titer in SYBR gold.** SYBR gold triggers DNA ejection independent of LamB; the presence of LamB influences the character of ejection. **Column 1**. The components of the buffers used. **Columns 2-4**. Titers of phage lambda solutions as a function of buffer composition and SYBR gold concentration. CsCl purified lambda phage were dialyzed in the appropriate buffer by washing and spin filtering. SYBR gold was added to bring the solution to the right concentration (none, high (1:10,000) and low (1:1,000,000)). The number of viable phage remaining was measured by titering. High concentrations of SYBR gold reduce the titer by more than an order of magnitude, especially in the absence of magnesium. This reduction in titer is because SYBR gold induces the bacteriophage to eject their DNA. Lowering the concentration of dye recovers the original titer levels. **Columns 5-6**. Character of ejection in the presence and absence of LamB. A single phage ejection assay was run for each condition with and without LamB. The number of ejections, both continuous and looped, was counted manually and is reported above. The fraction of ejections that are looped is higher in the presence of LamB.

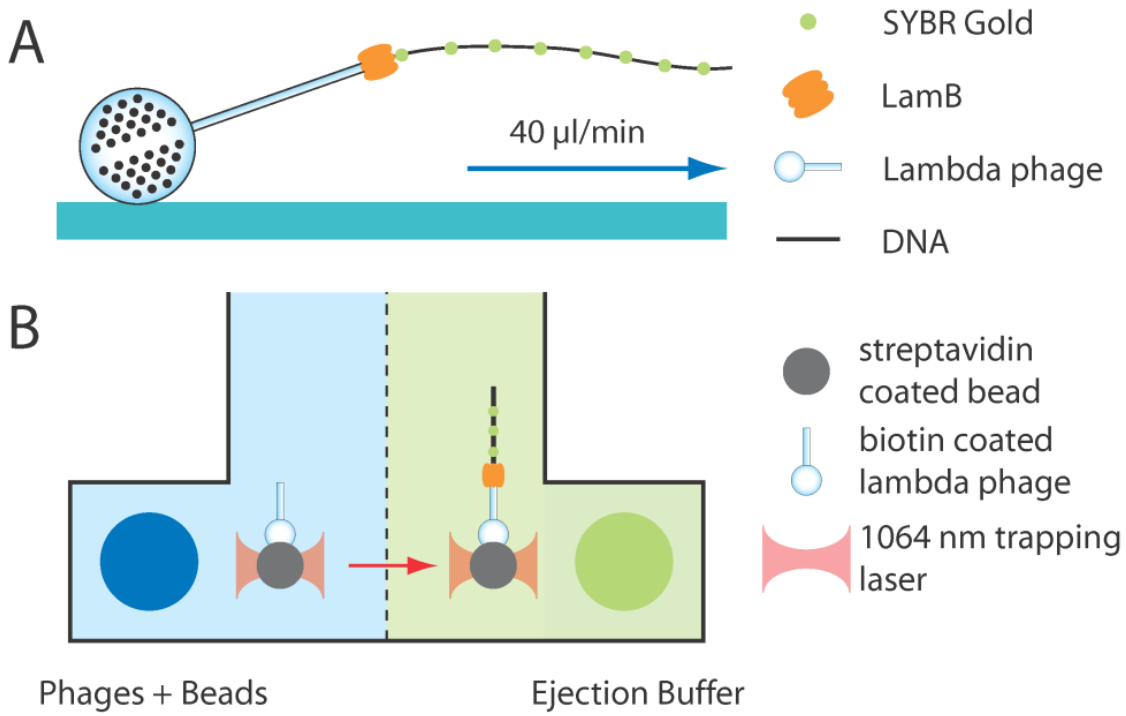

Figure 3.2: **Methodology of ejections.** **A**. Ejection at a surface. A flow chamber was incubated with lambda phage and the viruses were allowed to non-specifically adhere on to the surface. DNA ejection was triggered by flowing in LamB; the ejected DNA was visualized using SYBR gold. The flow field extends the ejected DNA, allowing quantification of the amount of DNA ejected by either measuring the length in pixels or measuring the total intensity. **B**. Ejection off a bead. A parallel ejection assay using an optical trap was developed. Biotinylated phages were bound to 2 μm streptavidin coated polystyrene beads. A dual-input flow chamber was used; beads coated with lambda phage entered the chamber through one input and an ejection buffer consisting of LamB and SYBR gold entered through the other. In the presence of flow, the two fluids are well separated. An optical trap was used to move a phage-coated bead into the ejection buffer to initiate DNA ejection.

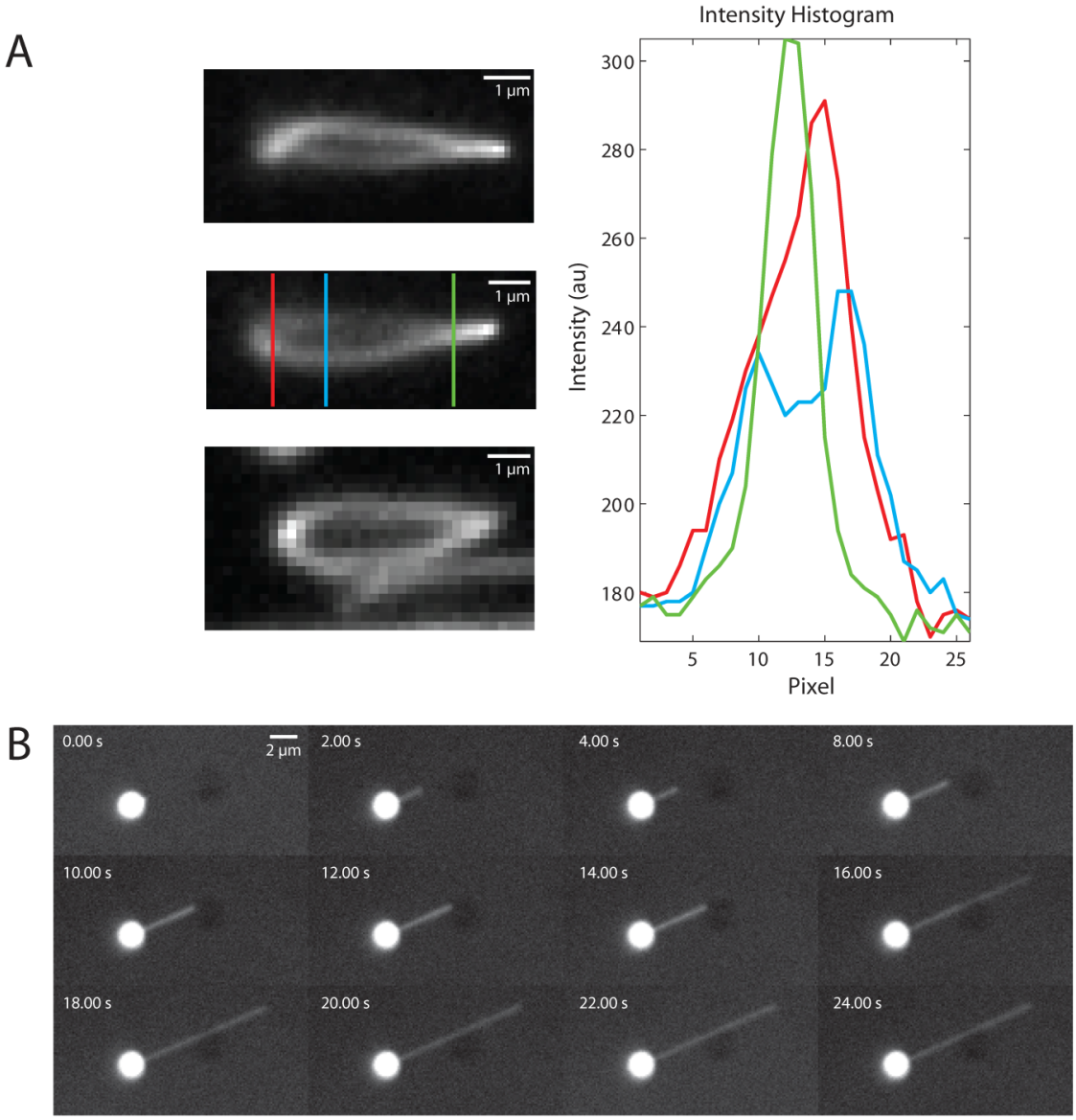

Figure 3.3: **Looping ejections. A**. Three examples of loops observed during the single phage ejection assay. An intensity histogram constructed from one of the examples demonstrates the presence of loops during in vitro ejections. **B**. Montage observation of a looped ejection during an optical trapping experiment. Phages were ejected off of optically trapped polystyrene beads to suppress effects caused by the glass surface of a regular microscopy coverslip. Looped ejections are still observed, suggesting that they are not the byproduct of surface effects. The bead is 2 microns in diameter. Looping ejections were also observed in the context of high concentrations of surface blocking agents (data not shown).

meeting juncture. After a LamB trimer finds its target, a phage ejects and we can monitor the ejection (Fig. 3.3, B). We found that the looped ejections were as common as continuous ejections. These experiments support the hypothesis that loops occur when the exiting DNA sticks to the LamB or the phage capsid.

We next characterized the dynamics of both the looped and continuous ejections under different ionic compositions, again using low concentrations of SYBR gold as described above (Table 3.1). We first flowed in the dye front to visualize any spontaneous or SYBR gold-induced ejections. Even at a 10 fold lower concentration of SYBR than previously reported [45], there were still some spurious ejections, although much less than that would occur with SYBR gold concentrations used previously [45]. Any lower concentration of dye would have precluded accurate segmentation of the ejecting DNA. After a period of time upon which the rate of spurious ejections was observed to be steady, we added LamB to the solution. A sudden large increase in the rate of visualized ejections indicated that LamB was inducing a large fraction of subsequent ejections. However, it should be noted that the dynamics of ejections induced by SYBR gold and those induced by LamB are indistinguishable. The experiment was repeated for 5 different salt conditions, in which we systematically varied the amount of sodium and magnesium ions while keeping the ionic strength constant.

We analyzed as many ejections within a field of view as possible - reasons for excluding an ejection from analysis included overlapping with another ejecting phage, photo-damage during an ejection, or a looped ejection that did not completely unfold. Ejections extracted from the field of view were partitioned into two categories - “continuous” and “looped”. These are highlighted in Fig. 3.5, A and B, respectively. To quantify the dynamics, we designed a custom segmentation algorithm for the DNA strands. The relation between length of DNA in basepairs and in pixels was determined by measuring, under flow, different known lengths of lambda DNA cut with restriction enzymes, and fitting the result to a quadratic function (Fig. 3.4.) This calibration disentangles polymer stretch and shear flow from actual DNA length [71]. The DNA’s long axis length for each time point in a trajectory was then interpolated according to a quadratic function and normalized by 48.5 kbp, the full length of lambda phage DNA. This calibration is only accurate for continuous ejections; for looped ejections it is necessary to use intensity to discern the amount of DNA ejected. To do so, we take the total intensity of the DNA above background and normalize by the

maximum intensity observed in a trajectory. This was done for both continuous and looped ejections, as shown in Fig. 3.5, C and D, (see Fig. 3.6, A-E, for all trajectories used).

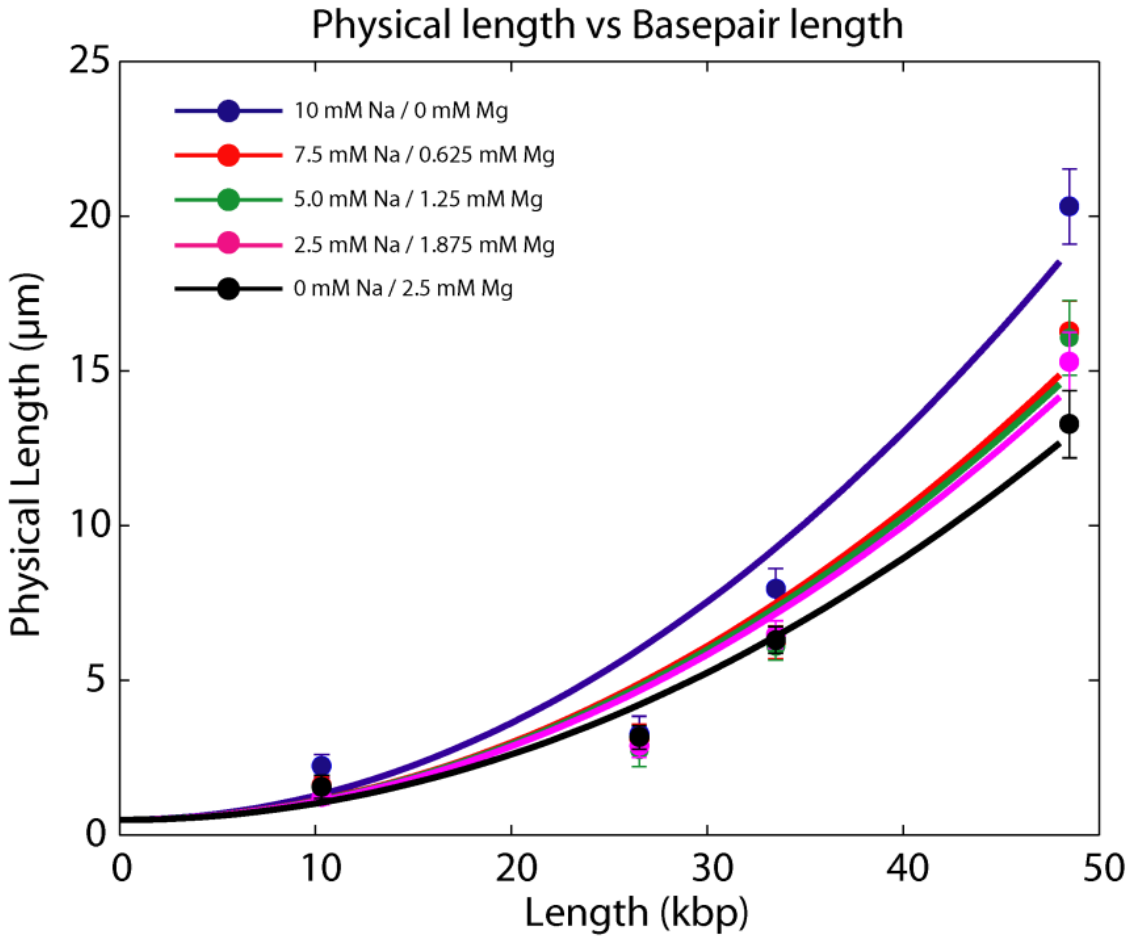

Figure 3.4: **Calibrating flow-sheared DNA.** To convert the physical length of DNA observed optically to the length in kilobasepairs (kbp), we performed a calibration as pioneered by [45]. Biotinylated lambda genomes were either treated with restriction enzymes (XhoI, NsiI, and PmlI) or kept untreated, in order to produce different defined lengths of DNA (as verified by agarose gel electrophoresis). The biotinylated DNA was attached to a glass coverslip coated with streptavidin, nonspecifically. The DNA was extended with a 40 μl/min flow of the different buffers used in the experiments, and the lengths of different pieces of DNA were measured manually using ImageJ. The mean length was fit to a quadratic function; error bars represent the standard deviation of the measured length.

A representative example of the trajectories is shown in Fig. 3.5, C and D; trajectories for each ionic condition are in Fig. 3.6, A-E. The fraction of DNA ejected is plotted versus time - the green curve uses fluorescence intensity to quantify total DNA ejected while the blue curve uses the calibrated length. It is clear in "looped trajectories" that the DNA is

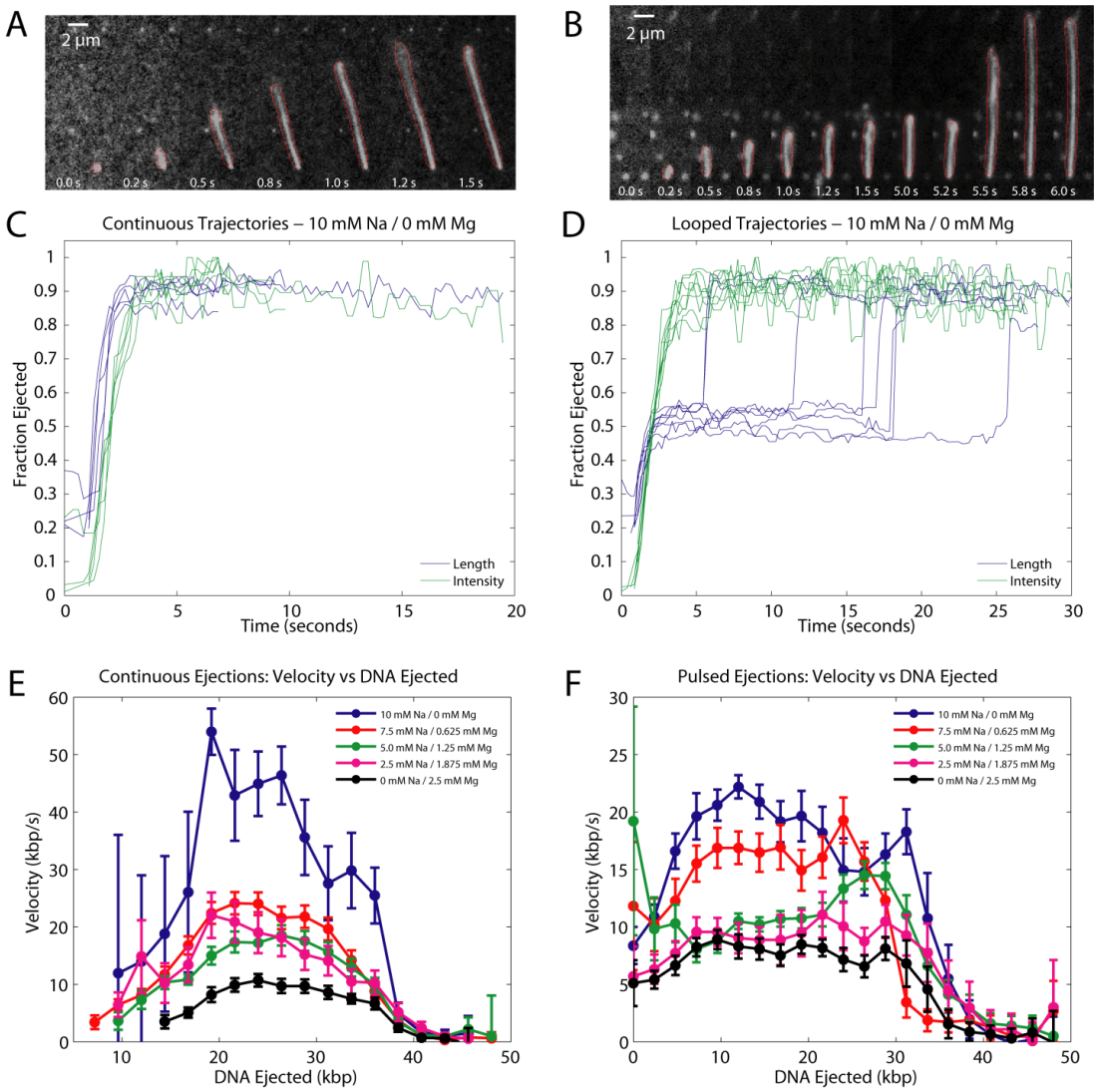

Figure 3.5: **Ejection characteristics for continuous and looped or pulsed ejections.** **A**. Montage of continuous and (**B**) looped ejections. The identified pieces of DNA are outlined in red. **C**, **D**. Sample trajectories for continuous and looped ejections. The amount of DNA ejected was quantified by measuring either the long axis length or the total intensity of fluorescence of the segmented region, outlined in red in (**A**). Lengths were determined by calibrating against restriction enzyme digested lambda DNA, as described in Figure 3.4. Individual trajectories are normalized by the maximum length/intensity observed during an individual trajectory to obtain the fraction ejected. Two qualitatively different ejections are observed - continuous ejections and looped ejections. The looped ejections reach half-maximal length before unfolding. **E**. Velocity of ejection as a function of buffer composition for continuous and (**F**) looped trajectories. For each trajectory, the velocity of the DNA (measured using total intensity) at different lengths was recorded. The mean velocity and the standard error of the DNA at each length are plotted for each buffer condition. There is a clear trend in the data - buffers with more magnesium ions have a longer timescale for DNA ejection. Continuous and looped ejections have similar ejection dynamics in all buffer conditions.

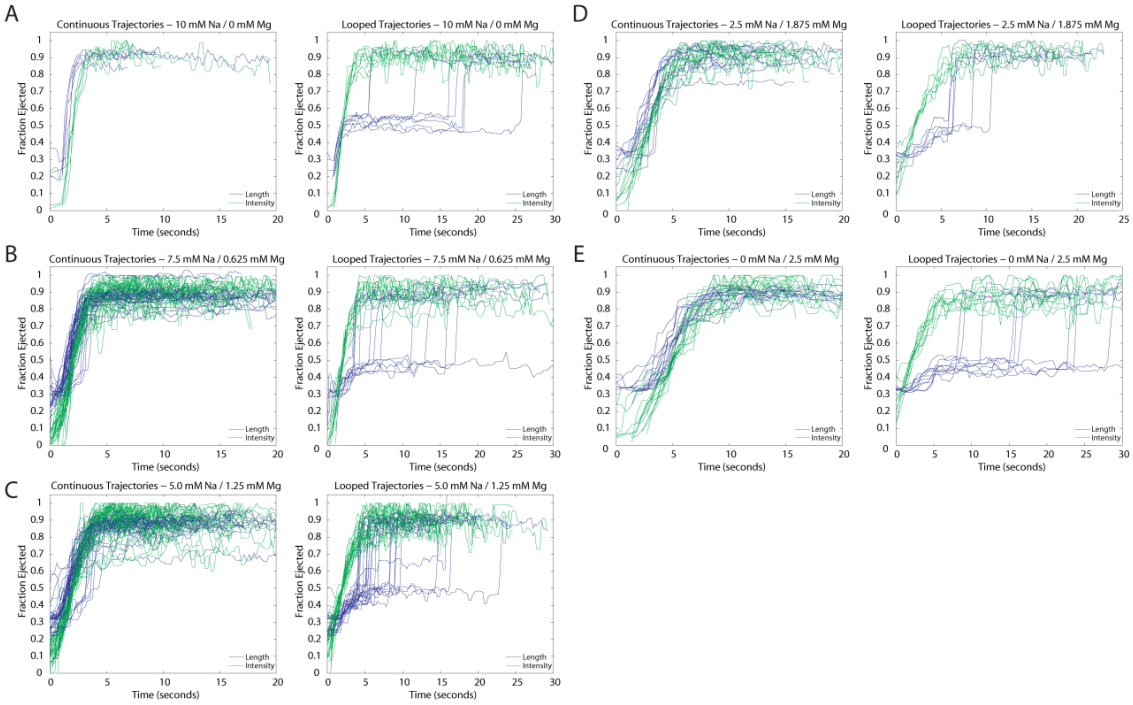

Figure 3.6: **Ejection trajectories.** Trajectories used to calculate the ejection velocity as a function of length. Green: intensity, blue: length. Intensity is the summed intensity of the DNA labeled by SYBR gold. The length is calibrated by measuring defined-length lambda DNA, via restriction digests, under the same flow conditions. Length is then calculated by interpolation. Looping trajectories uniformly unfold at half the maximum length, suggesting that the first bit of DNA that exits the phage tail is tethered to the phage. **A**. Salt condition: 10 mM Tris, pH 7.4, 10 mM NaCl, 0 mM $MgSO_4$. Number of trajectories: 5 continuous and 8 looped. **B**. Salt condition: 10 mM Tris, pH 7.4, 7.5 mM NaCl, 0.625 mM $MgSO_4$. Number of trajectories: 36 continuous and 13 looped. **C**. Salt condition: 10 mM Tris, pH 7.4, 5.0 mM NaCl, 1.25 mM $MgSO_4$. Number of trajectories: 43 continuous and 25 looped. **D**. Salt condition: 10 mM Tris, pH 7.4, 2.5 mM NaCl, 1.875 mM $MgSO_4$. Number of trajectories: 14 continuous and 6 looped. **E**. Salt condition: 10 mM Tris, pH 7.4, 0 mM NaCl, 2.5 mM $MgSO_4$. Number of trajectories: 15 continuous and 10 looped.

fact pinned at one end, as the trajectories exhibit a discontinuity in length at half-maximal ejection. A comparison between using calibrated DNA lengths and intensity as a measure of total ejected DNA is shown in Fig. 3.7, A-E. Intensity measures give a larger estimate for the velocity of DNA ejected at early times because our segmentation algorithm misses the first bits of DNA ejection, and so changes in DNA length appear relatively large at small lengths; whereas at late stages in the ejection, length and intensity measures are equivalent metrics for amount of DNA ejected. Looped trajectories clearly show a discontinuous change in length as a function of time, while the intensity measurements suggest a continuous exit of DNA from the capsid as a function of time and that all of the DNA has exited the capsid even though the length is much shorter than the fully stretched DNA. This suggests that for the "looped" trajectories the DNA is pinned to the capsid (Fig. 3.3, A) and ultimately unfolds in the presence of the flow, resulting in a discontinuous change in length as shown in the figure.

For each condition, we binned the trajectories to compute the average velocity as a function of DNA remaining in the capsid. This is plotted in Fig. 3.5, E and F; Fig. 3.5, E, was computed using calibrated length while Fig. 3.5, F, was computed using intensities. Velocity plots for individual salt conditions are in Fig. 3.8, A-E. From our analysis of the dynamics, we observed that individual trajectories were very similar to each other. As with previous work [45], this leads us to conclude that we are observing the same intrinsic dynamical process and that differences between trajectories are likely the result of measurement error. Secondly, our systematic perturbation of the sodium and magnesium concentrations - at fixed ionic strength - showed a consistent trend. As the amount of magnesium was lowered and the amount of sodium was increased, the speed of the ejections increased (Fig. 3.5, E and F). From this, we conclude that it is the type of ion, not simply how much is present, that is an important control parameter that governs DNA ejection dynamics. We posit that the role of the positive ions is to screen the negative charge of the DNA backbone, which suggests that the charge of the counter-ions is the property of interest.

Additionally, we observe that the continuous and looped ejections have velocity curves that are within error of each other (Fig. 3.5, E and F). This suggests that the ejection mechanism for these two classes of ejections are very similar, if not identical, and that what happens to the first segment of DNA that exits the capsid determines whether an ejection

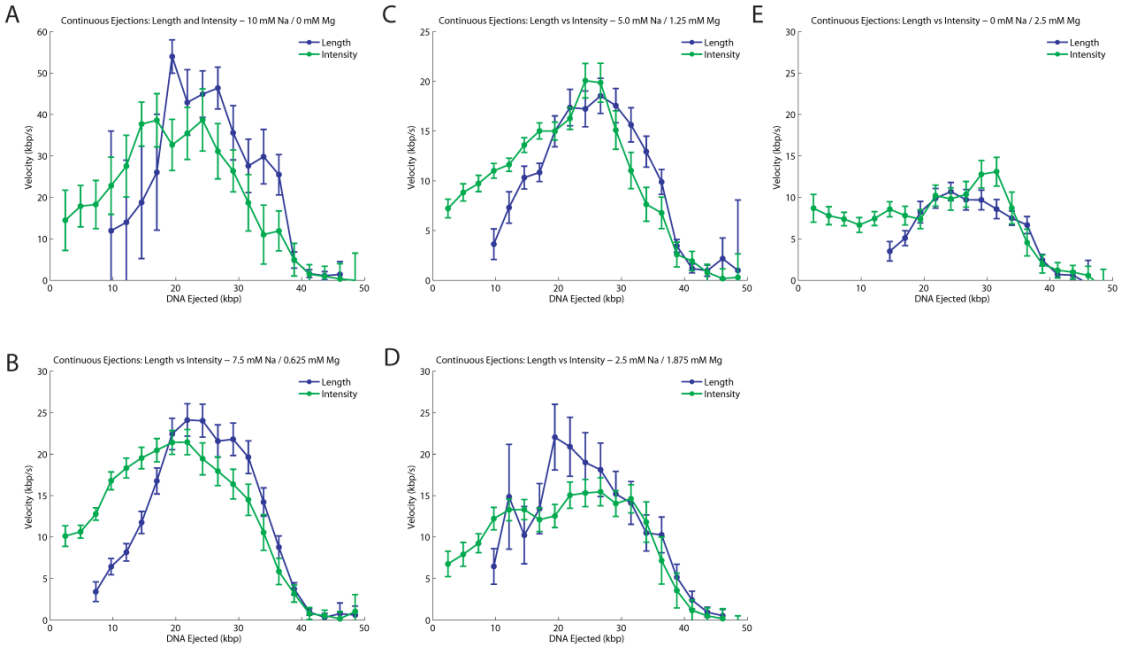

Figure 3.7: **Ejection velocities for continuous ejections.** Velocities from the single-phage ejection experiment. Each panel has two classes - green lines denote velocities measured by intensity; blue lines denote velocities measured by length. Intensity measures give a larger estimate for the velocity of DNA ejected at early times because our segmentation algorithm misses the first bits of DNA ejection, and so changes in DNA length appear relatively large at small lengths. Since DNA lengths are hard to directly measure via restriction digest calibration at early times in ejections, we don't measure lengths less than ∼5 kbp. The number of trajectories used in each velocity plot is listed in the caption of Fig. 3.6. The errors were determined by standard error. **A**. Salt condition: 10 mM Tris, pH 7.4, 10 mM NaCl, 0 mM $MgSO_4$. **B** Salt condition: 10 mM Tris, pH 7.4, 7.5 mM NaCl, 0.625 mM $MgSO_4$. **C**. Salt condition: 10 mM Tris, pH 7.4, 5.0 mM NaCl, 1.25 mM $MgSO_4$. **D**. Salt condition: 10 mM Tris, pH 7.4, 2.5 mM NaCl, 1.875 mM $MgSO_4$. **E**. Salt condition: 10 mM Tris, pH 7.4, 0 mM NaCl, 2.5 mM $MgSO_4$.

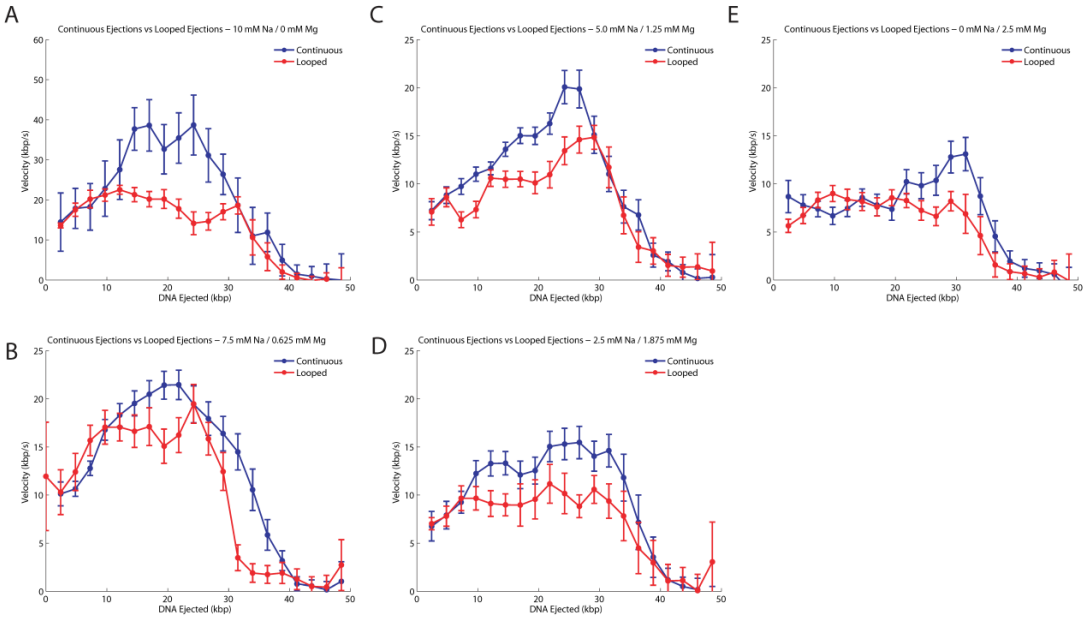

Figure 3.8: **Velocities for continuous and looping ejections.** Red: velocity based on looped trajectories. Blue: velocities based on continuous trajectories. All velocities were determined using intensities; both classes of ejections show similar dynamics. The number of trajectories used in each velocity plot is listed in the caption of Fig. 3.6. The errors were determined by standard error. **A**. Salt condition: 10 mM Tris, pH 7.4, 10 mM NaCl, 0 mM $MgSO_4$. **B**. Salt condition: 10 mM Tris, pH 7.4, 7.5 mM NaCl, 0.625 mM $MgSO_4$. **C**. Salt condition: 10 mM Tris, pH 7.4, 5.0 mM NaCl, 1.25 mM $MgSO_4$. **D**. Salt condition: 10 mM Tris, pH 7.4, 2.5 mM NaCl, 1.875 mM $MgSO_4$. **E**. Salt condition: 10 mM Tris, pH 7.4, 0 mM NaCl, 2.5 mM $MgSO_4$.

will be continuous or looped.

To continue the physical characterization of the ejection process, we performed osmotic suppression experiments to determine the forces driving ejection in each of the different salt conditions. Osmotic pressure varies with PEG 8000 concentration as given by Michel, [72]. Previous experiments have measured the amount of DNA ejected by pelleting phage capsids and measuring the absorbance at 260 nm. This measures the amount of DNA that has been chopped up by the DNAse, which is assumed to be entirely ejected DNA. While the mass of DNA is thus accurately measured, it is not clear if the mass of ejected DNA can be quantitatively related to the length of DNA remaining in the phage capsids. In fact, Sao-Jose et al., [73], found that adding PEG to phage SPP1 preparations changed the relative number of inactive phages. Moreover, in Evilevitch et al., [47], where the PEG-based force suppression experiments were originally carried out, they note a 30% variability in their A_{260} measurement of DNA.

We used an alternative approach - purifying the DNA inside the capsids by standard extraction techniques and measuring its length directly by using field inversion gel electrophoresis (Fig. 3.9) [47]. Above each lane in Fig. 3.9 is indicated the amount of external pressure induced by the presence of the PEG as measured in atmospheres. Lanes labeled "L" correspond to the DNA ladder, with the marker lengths noted in Fig. 3.9, A. Increasing amounts of external pressure results in increasing amounts of DNA left inside the capsid after ejection. Migration distance in each lane was measured by looking for the maximum fluorescence peak relative to the 48.5 kbp peak, and comparing that to the corresponding ladder. Since electrophoresis was performed in many different batches, we present the results in such a way that the relevant pressure experiment in the appropriate salt condition is to the right of its corresponding ladder. Electrophoresis parameters: 100 V forward, 0.8 sec; 60 V backwards, 0.8 sec; 7-10 hours.

This method is advantageous because we no longer need to assume that a constant fraction of phages eject for each PEG concentration. Care was taken to avoid centrifugation, as it tends to fragment DNA (data not shown). Also, excess DNAse tends to produce streaking in the lanes [73]. The pressure driving ejection is shown in Fig. 3.10, A. The general trend is that decreasing magnesium and increasing sodium increases the driving force, although the 5, 7.5, and 10 mM Na samples appear to be within error of each other. We observed that 40 atmospheres (14 pN) of pressure was not enough to stall ejections in

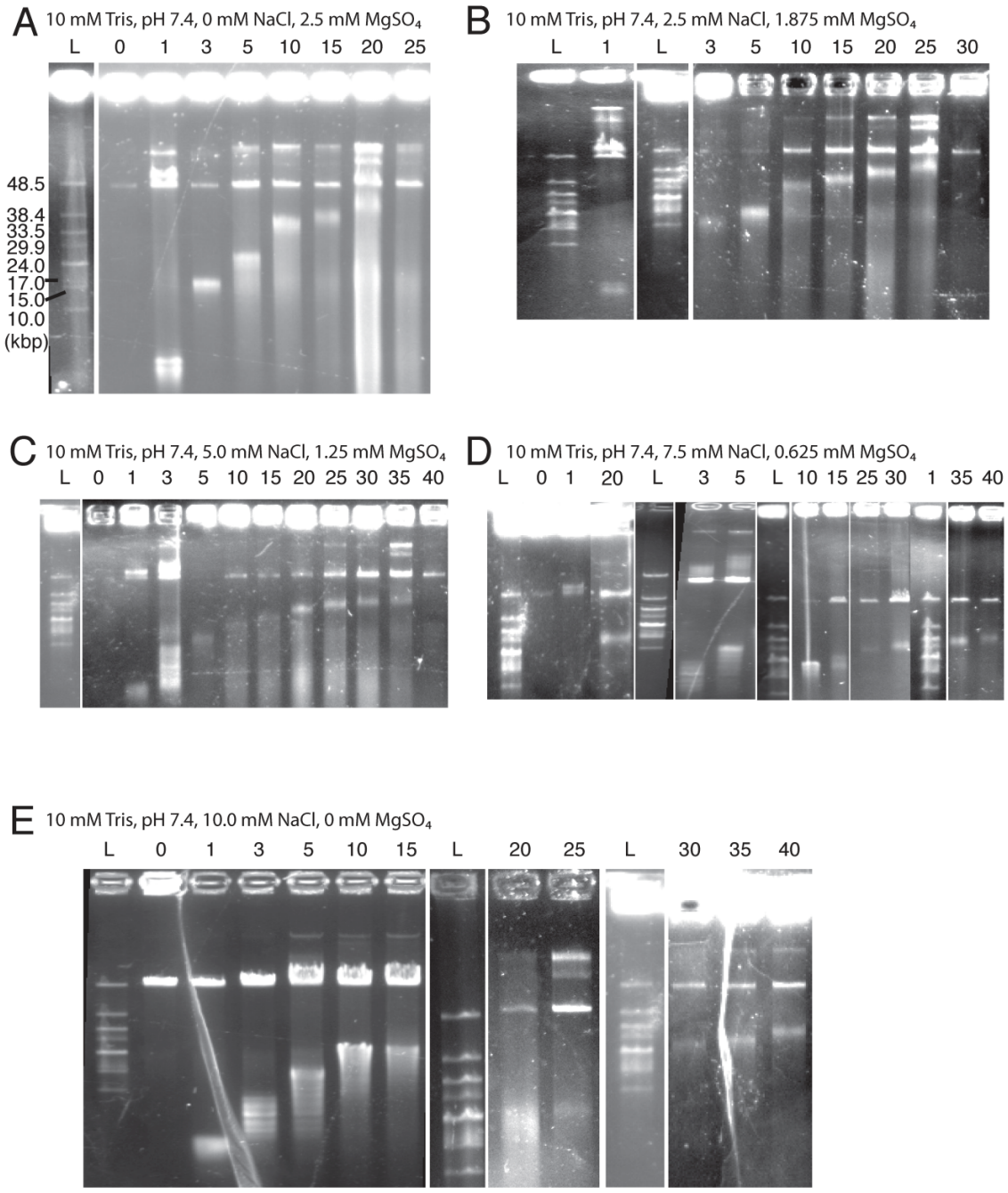

Figure 3.9: **Field inversion gel electrophoresis of retained DNA.** A trend of DNA retention in the capsid with increasing external osmotic pressure is clearly visible. **A**. Salt condition: 10 mM Tris, pH 7.4, 0 mM NaCl, 2.5 mM $MgSO_4$. **B**. Salt condition: 10 mM Tris, pH 7.4, 2.5mM NaCl, 1.875 mM $MgSO_4$. **C**. Salt condition: 10 mM Tris, pH 7.4, 5.0 mM NaCl, 1.25 mM $MgSO_4$. **D**. Salt condition: 10 mM Tris, pH 7.4, 7.5 mM NaCl, 0.625 mM $MgSO_4$. **E**. Salt condition: 10 mM Tris, pH 7.4, 10 mM NaCl, 0 mM $MgSO_4$.

some salt conditions, which is consistent with theoretical expectations [45]. Atmospheres can be converted to force by multiplying the pressure by the end-on area of DNA, assuming a radius of 1.2 nm (the use of 1.2 nm versus 1.0 nm as the radius of DNA takes into account the size of PEG [49]). The lines are fit to Equation 19 in Purohit et al., [63].

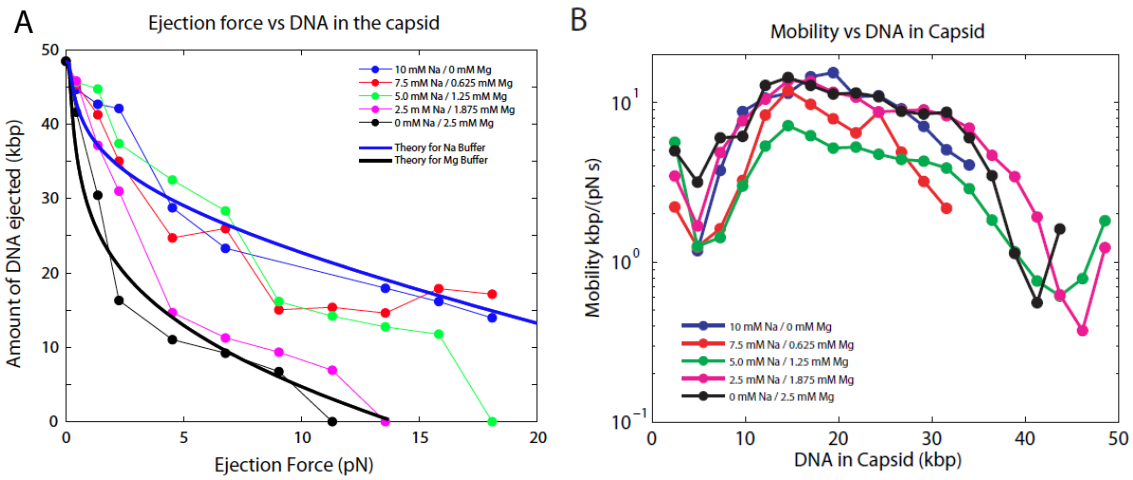

Figure 3.10: **Ejection stall forces.** Osmotic suppression experiments were performed in different buffer conditions (listed inset) to measure the force driving ejection. The fraction of DNA ejected was determined by measuring the amount of capsid DNA remaining using field inversion gel electrophoresis, as shown in Figure 3.9. **A**. Increasing monovalent ion concentration raises the stall force of ejection at each length of DNA. The theory lines are fits to Equation 19 in Purohit et al., [63]. **B**. The mobility is measured as $v\left(l\right)/F\left(l\right)$. The trend is less clear regarding mobility and ion composition, though it appears that higher amounts of divalent cations increase mobility.

We can determine how the mobility, denoted by $\mu\left(l\right)$, of DNA inside the capsid depends on the salts (as shown in Fig. 3.10 B) by assuming a linear relation between force and velocity, $F(l) = v\left(l\right)/\mu\left(l\right)$, where l is the DNA length in the capsid, F is the force as measured in Fig. 3.10, A (multiplied by the area of end-on DNA), and v is the velocity as measured in Fig. 3.5, E and F. As previously observed [45], the mobility depends strongly on the amount of DNA remaining in the capsid. We are unable to conclude that mobility is dependent on salt condition, although there is a slight trend that the measured mobility is higher for solutions with more multivalent salts.

3.3 Injections into cytoplasm

3.3.1 The Pressure Conundrum

The PEG ejection suppression experiments above (pioneered and performed by others on lambda phage [47, 48, 57, 49, 52] and SPP1 [73]) suggest a conundrum. From Fig. 3.10, we see that as the phage releases its DNA into the environment, there is less and less force available for it to complete ejection; DNA becomes less and less compacted as more comes out: intrastrand repulsion forces reduce monotonically. Even at 1 atm of pressure there is significant retention of DNA inside the phage capsid, as shown in Fig. 3.9. Given that the turgor pressure in a gram-negative bacterium such as *Escherichia coli* is between 1 atm and 30 atm (depending on the cell's division cycle) [53], how does phage lambda complete its injection into the host?

In fact, Sao-Jose et al. [73] have suggested that the ejection suppression experiments are an accurate way of determining intra-strand repulsion forces. The expected lattice constant of DNA crystals decreases exponentially with the amount of external PEG,

$$p\left(d_s\right) = F_o \exp\left(-d_s/c\right), \tag{3.1}$$

with the osmotic pressure p and strand spacing d_s [74, 75]. Since the osmotic pressure in PEG solutions is well-calibrated [72] and the amount of retained DNA accurately measured by agarose gel electrophoresis, one can calculate the expected lattice constant for DNA inside the capsid as a function of external osmotic pressure. It turns out that the expected lattice constant obeys the phenomenological exponential relation determined *in vitro* (Eq. 3.1) [74, 75] quite well for equivalent osmotic pressures [73], suggesting that ejection suppression experiments faithfully use force as a knob to control intra-strand repulsion.

Thus, it can be said that the *in vitro* experiments are in conflict with the biological reality - the entire genome must enter for the cycle to start. However, the pressure conundrum is just one worry. Another related issue is the structure of the bacteria cell wall - the genome must pass through this structure before accessing the cytoplasm. Gram-positive species (such as *Bacillus subtilis*) carry a multi-layer peptidoglycan wall that is ∼25 nm on the outside of the plasma membrane; gram-negative species have a ∼2.5-7.5 nm thick single layer in the periplasmic space (recall that gram-negative bacteria have both an outer

and inner membrane with a space in between called the periplasm) [76]. The effective mesh size of the cell wall acts as a molecular sieve, the spacing of which must be taken into account when considering DNA passage. For gram-negative bacteria, the passage of proteins greater than 50 kDa in size is hindered, which means that the mesh size is approximately 2.06 nm and surprisingly, 2.16 nm for *B. subtilis* despite its significantly thicker cell wall [77]. Furthermore, the intra-strand spacing in the peptidoglycan layer will increase 12% for every 1 atm increase in turgor pressure, as measured by atomic force microscopy; the same group (Yao et al., [78]) reported a natural spacing of 1.6 to 2.0 nm for gram negative bacteria. Thus bacteria carry with them a wide array of cell-wall degrading enzymes used during growth or for export of extracellular materials, such as during flagella production as a specific example [79] - as do bacteriophage. The tail of phage T4 (host: *E. coli*) has a lysozyme-like enzyme which is thought to degrade the cell wall during infection so that DNA can be directly injected into the cytoplasm [80], as does phi29 (whose host is *Bacillus subtilis*) [81]. Phage T7 is thought to inject endopeptidase proteins that also form a tube through which DNA can travel through the cell wall [82]. A literature search could not confirm that lambda phage itself has active lysozyme or endopeptidase activity on its tail, and it was not found through biochemical assays despite a thorough effort [83]. However, cell-wall penetrating enzymes are thought to be a universal, necessary feature of bacteriophages [41, 76]; otherwise, alternative mechanisms are necessary for lambda entry.

If the phage is able to defeat the cell wall - and perhaps it does not need to, as the radius of a DNA molecule is $\sim$1 nm - the pressure conundrum still exists. The available data is surprisingly sparse on this issue. Phage T7 requires RNA polymerase to complete its entry (presumably to pull DNA in - *in vitro* studies have shown that it can exert 20 pN of force, sufficient to overcome the pressure barrier [84]) [85]; it is thought that phi29 requires a motor as well [86], as does phage N4 [87]. One can imagine other types of mechanisms, including Brownian ratchets, Langmuir adsorption forces, or force-producing osmotic gradients, as illustrated in Fig. 3.11. In all cases, however, pressure provides the initial impetus, delivering a majority of the genome into the cell, whereupon the last retained bit is pulled in. In fact, when lambda phage is packaged with a shorter genome ($<$ 36 kbp), the particles are not infectious [49], which demonstrates that DNA intrastrand repulsion forces are necessary for infections. The latter two mechanisms are especially intriguing as Jeembaeva et al., [52], have shown that DNA condensation after ejection provides a pulling

force *in vitro*; however, this only occurs at significant pressures (> 5 atm, and may be the specific result of using PEG as the condensing agent) [50], and the amount of extra DNA pulled out is not enough to completely empty the capsid [52]. The other possibility is that of an osmotic gradient or "toilet flush." Essentially, binding of phage to the cell membrane creates a conduit between extracellular and intracellular space, and the osmotic difference between the two creates water flux that could potentially hydrodynamically drag remaining phage DNA into the cell [87], although at this point this is merely a proposition.

3.3.2 The process of λ entry into cells

There are other factors that lambda specifically needs to contend with. As described in the *in vitro* part (Section 3.2), lambda phage binds to LamB on the outer membrane of *E. coli*; LamB is a trimer of a maltose importer [89], each subunit of which contains a pore between 0.5 and 0.6 nm in diameter [90]. It is unlikely that DNA is ejected through this pore due to steric considerations; furthermore, it was experimentally determined that phage docking does not distort the structure of the maltoporin (as verified by electrophysiology), although access to the maltose binding sites is blocked when lambda binds LamB [91, 92]. The next steps after binding are unclear in lambda phage but have been revealed in phage SPP1, which has roughly the same dimensions (60 nm diameter head with 191 nm long non-contractile tail) and genome length (45.1 kbp) as lambda [73], although its host is a gram-positive cell. Briefly, a signal is transmitted from the tail tip to the head-tail connector via a cascade of tail protein structural rearrangements (like falling dominoes) [93] whereupon a β-sheet stopper complex unzips and lets DNA out [94]. The tail tip of lambda phage, like SPP1, is a 20 nm blind-end tube [95, 93] that once lambda has bound to its receptor, must disappear if DNA ejection is to occur [95]. The purpose of the tail tip is not known (besides the requirement for binding LamB), especially in the absence of any convincing evidence of lysozyme or peptidase activity [83]. However, in *in vitro* preparations, binding of phage to liposomes containing LamB causes leakage of ATP, a phenomenon that does not occur when using purified tails or phage ghosts, suggesting that DNA or a protein carried by lambda is required to puncture membrane [96], if not the cell wall. Incidentally, this leakage supports the hypothesis that lambda opens a communication portal between intra- and extracellular space, as required in the "toilet flush" model [87]. Regardless, phages that deposit their DNA into liposomes reconstituted with LamB are always devoid of the tail

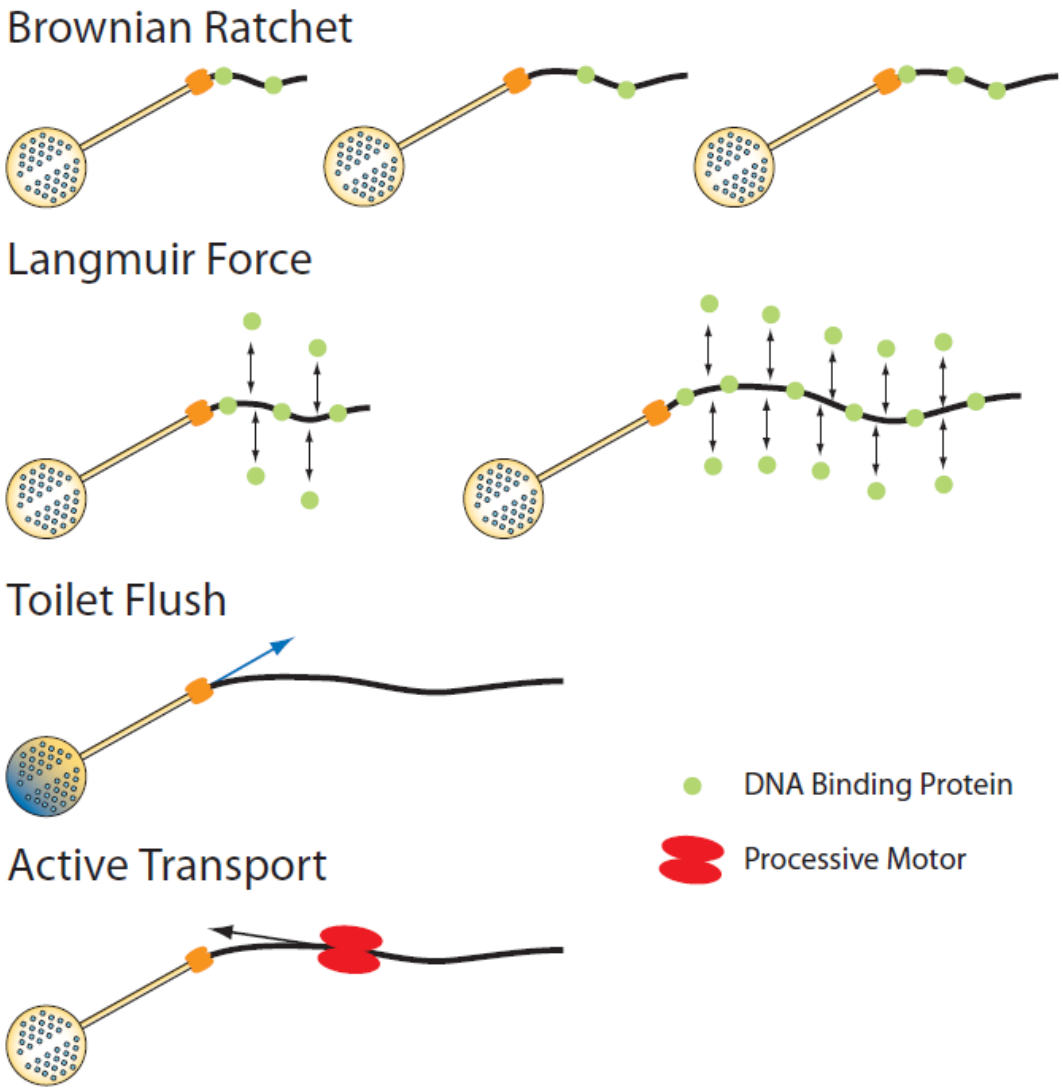

Figure 3.11: **Possible mechanisms for phage entry. Brownian ratchet** relies on fluctuations of DNA out of the tail of the phage, upon which a DNA protein binds and disallows backwards fluctuations. See Howard, J., [88] for an extensive explanation. **Langmuir force**. The time scale for binding is much faster than in the **Brownian ratchet** case; each time a protein binds DNA, there is energetic benefit, which favors entry of DNA into the cell. **Toilet flush**. An osmotic gradient produced when phage opens a hole into the cell creates water flux which hydrodynamically pulls in DNA. **Active transport**. An energy-consuming processive motor that binds DNA can possibly ratchet in DNA. Examples include the DNA and RNA polymerases, as well as gyrases.

tip [95]. The next few steps - precisely how lambda DNA crosses the cell wall, periplasmic space, and inner membrane - are unknown. One final requirement is the *ptsM* mannose transport pathway, which is present on the inner membrane - so-called *pel* ("penetration of lambda") mutants deficient in *manXYZ* (the genes are in locus *ptsM*) are immune to lambda - especially if their genomes are less than 36 kbp [42]. This suggests that some combination of pressure and a specific receptor are required in the last step. It is unclear if DNA ever sees the periplasmic space, as there is conflicting evidence as to whether λ is sensitive to DNAses exogenously expressed in the periplasmic space [97, 98].

There are many biochemical issues that need to be resolved, but we study a much simpler issue: as phage DNA is transferred into bacteria, the amount of force available to the phage will at some point fall below the turgor pressure of the bacterium. However, at this point there will still be DNA left inside the capsid, as demonstrated in Figure 3.9. As a baseline experiment, then, what we therefore wish to do is to perform experiments which might allow us to watch the early stages of the infection process *in vivo*.

One crucial aspect of our method is the ability to look at the continuous entry of DNA into cells, much like we were able to measure the length of a continuous strand of DNA as it left the capsid in *in vitro* ejection experiments. Thus, we decided to use DNA staining fluorescent dyes that have enhanced fluorescence as they intercalate into DNA [99]. However, the problem with infecting a cell *in vivo* is that the chromosomal background is large, at 4.6 x 10^6 basepairs, whereas the lambda phage genome is 4.5 x 10^4 bp, so the phage signal on top of the DNA would be one part in one hundred. Fortunately, there are ways of generating DNA free cells including inducing mismatch repair enzymes to degrade the genome in *dam* deficient cells [100] or by expressing inducible nucleases [101]. In the next section, I will discuss our efforts to use a third method, that of minicells, first discovered in the late 1960's by Adler and coworkers [102].

3.3.3 Minicells are miniature cells

Minicells are generally derived from mutants of the *min* system [103]. The genetic basis was narrowed down to two loci, *minA* and *minB* [103]. However, it was later discovered there was an error in the identification of *minA* and it is now thought that *minA* does not exist [104]; *minB* is the locus or operon of genes *minCDE*. The variant discussed in the ensuing text is a deletion of the *minC* gene from the Keio collection, a collection of *E. coli*

gene deletion mutants [105]. In short, gene products MinC, MinD, and MinE together set the positioning of FtsZ ring which recruits other factors to divide the cell (see Fig. 3.12). MinD (an ATPase) assembles on the membrane until it reaches the midcell (Fig. 3.12, a), at which point MinE molecules are added onto the leading edge and forms the E-ring upon which FtsZ will polymerize (Fig. 3.12, d). Here, MinE activates the ATPase activity of MinD-ATP (Fig. 3.12, e). MinC is initially associated with FtsZ which inhibits ring formation; however, when MinD polymerizes and assembles onto the membrane, it recruits MinC which releases its association with FtsZ, allowing ring formation to occur. However, upon hydrolysis of MinD-ATP into MinD-ADP, MinD dissociates from the membrane (Fig. 3.12, f and g) and MinC can once again cage FtsZ. As MinD diffuses into the cytoplasm, it is converted back into MinD-ATP and the cycle is started anew; see Rothfield et al. [106] for a review.

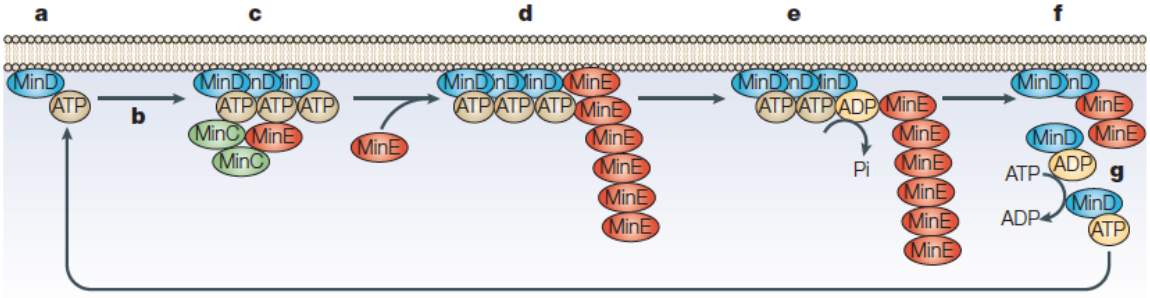

Figure 3.12: **The MinCDE cycle.** **a**. MinD-ATP associeates with the inner surface of the cytoplasmic membrane. **b**. MinD-ATP polymerizes by lateral diffusion and interaction with other membrane-associated MinD-ATP molecules; this happens in the polar zone of the bacterium. **c**. MinC and MinE associate with MinD-ATP. **d**. MinE molecules attach to the leading edge of the polar zone, forming a scaffold for FtsZ and associated division machinery. **e**. MinE activates the MinD ATPase, leading to conversion of ATP to ADP. **f**. MinD-ATP is released into the cytoplasm (due to lowered affinity for membrane while in the diphosphate state) and is converted back to MinD-ATP in the cytoplasm (**g**), restarting the cycle. [Figure and caption adapted from Rothfield et al., [106].]

The advantage of using minicells is that they do not contain the bacterial chromosome, and therefore have lower background in the presence of dsDNA stains. It was shown by Adler et al., [102], via electron micrographs that the minicells are instead filled with cytoplasm. However, it was later found that plasmids and RNAs do segregate during minicell formation into the minicell [107] and that synthetic activity (RNA, protein synthesis) is maintained for up to 3 hours [108] under normal conditions (proof being: the synthesis of complete T4

virions upon infection of minicells), and that lyophilized or frozen minicells preserve their metabolic activity indefinitely [109]. The 3-hour time limit may be due to the half-life of RNA - as incubation of minicells for 4 hours at 37^{o}C will destroy all RNA inside minicells [110]. It was discovered that sex factor is transferred to minicells [111] in the course of figuring out how plasmids are maintained in cells - and was found that the chromosome is linked to the cell membrane [112]. Later, it was shown that RNA polymerase segregates with plasmids into minicells [108] although the ability to quantitatively detect active RNA polymerase in lysates is believed to be the result of bad technique [113], and there is ample evidence of RNA synthesis as well as protein synthesis [114] inside at least ∼20% of minicells in a given preparation [113]. In fact, lambda phage (which doesn't carry along its own polymerases, unlike T4) has been shown to not only be infective, but also to produce some of its gene products inside minicells [114]. The conclusion of all these studies is that 1) minicells are capable of being infected by phage and 2) minicells have enough of the native bacterial cytoplasmic components to initiate transcription and translation.

The mechanism for plasmid segregation into minicells was finally confirmed by using temperature senstive plasmid replication mutants: at both permissive and nonpermissive temperatures, the plasmid always remains within the minicells. This suggests that plasmid segregation is independent of plasmid replication. Instead, they found that plasmids are associated with the membrane [115], and the distribution of plasmids stochastic, similarly to what we observe, as indicated by the random staining of RNA in plasmid-free minicells (see Fig. 3.13) - it should be noted that the minicell signal in Fig. 3.13 is basically zero compared to chromosome-containing cells, as shown in Fig. 3.14. We also demonstrate in Fig. 3.14 that the chromosome stain is much, much brighter than any nucleotides in minicells.

Additionally, it is possible to visualize the infection process of minicells; Reeve [114] was able to monitor the production of phage proteins (phi29, phi105, SP02, TF, and lambda) inside minicells. However, other studies suggest that there are very few active RNA polymerase molecules in minicells [113]. They report that only 20% of minicells possessed sufficient RNA polymerase to produce T7 progeny, a phage that requires RNA polymerase to finish infection [85]. There is additional evidence that lambda, specifically, can infect minicells, as Witkiewicz and co-workers, [36], showed circular variants of lambda DNA sticking to the inner membranes of minicells 0.5 minutes after infection. Recently it was shown

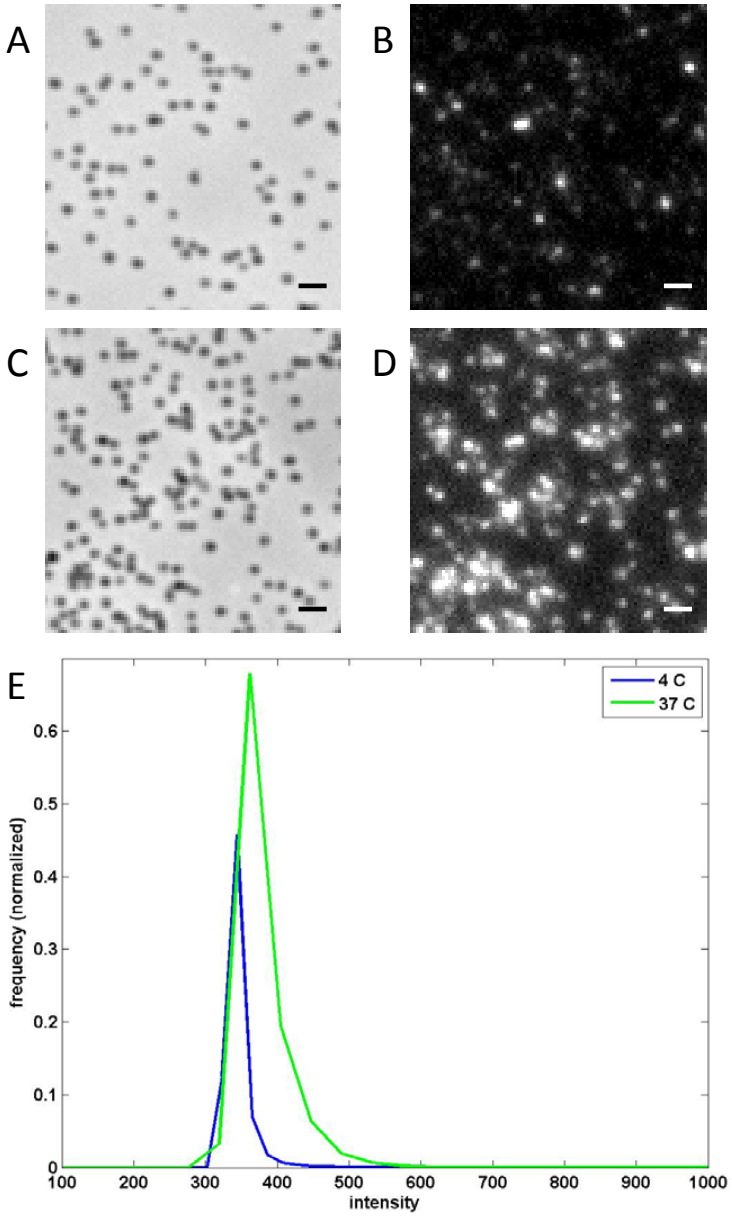

Figure 3.13: **Phage temperature jump.** Background staining of phages can be a problem unless we find a way to distinguish phages that inject versus phages that do not inject - one solution to this is temperature jumping [116]. As described in the main text, phages are incubated at 4^oC with minicells for 30 min on ice (**A**), and the other half the sample is incubated at 23^oC for the same amount of time (**C**). After incubating, we then add to both an overwhelming amount of dye which will prevent further ejections, as described in Table 3.1. Samples are loaded onto a microscope chamber and excess minicells and phages which do not bind after 10 minutes are washed off; the samples are imaged with the exact same parameters. **B**. 4^oC sample shows dim fluorescence, compared to (**D**), the 23^oC sample. Images (**B**) and (**D**) are set so that the range of displayed values is the same. **E**. Histogram of fluorescent intensities inside minicells in the 4^oC sample (**B**) and the 23^oC sample (**D**). The number of minicells is around 200. The multiplicity of infection (MOI - the ratio of phages to minicells) is $\sim$10. Scalebar: 2.5 μm

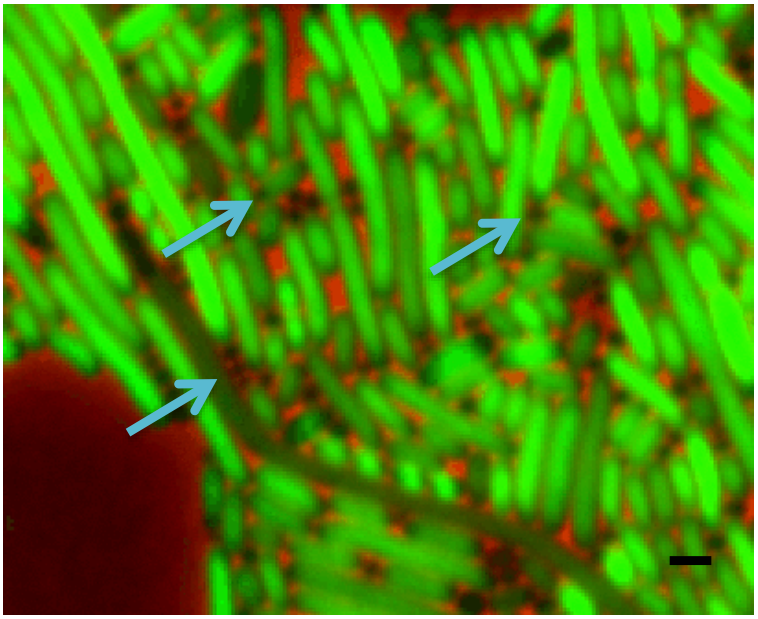

Figure 3.14: **Minicells have reduced nucleotide content.** A sample of $\Delta minC$ cells were stained with Vybrant Green, a dsDNA specific dye. Arrows point to minicells, which appear as empty (black) circles, indicating the dearth of nucleotides. In contrast, the filamentous cells have an intense green color, signaling the presence of large amounts of DNA and RNA. Scalebar: 2μm.

that one can visualize DNA transfer into *H. pylori* by direct, covalent fluorescent labeling of DNA [117]. Much precedence exists for the visualization of DNA transfer, such as the use of binding site arrays to localize genes [118], and the use of SeqA-YFP to localize along hemimethylated DNA, which is passed between bacteria during horizontal gene transfer [119].

However, the use of fluorescent protein localization to DNA has a drawback in that the diffusion of the reporter is always convolved with the dynamics of DNA transfer - indeed, it may be that diffusion is much slower than DNA injection - this would certainly be the case *in vitro*, as GFP has a diffusion coefficient of 1 μm^2/sec inside bacteria [120]; DNA ejects within a few seconds *in vitro*, as shown in Figure 3.6. Below we discuss the use of DNA intercalating dyes in the visualization of DNA translocation, which does not rely on specific binding sites on DNA and is therefore much faster to find binding sites, as well as being much smaller molecules than fluorescent proteins, and therefore has a much larger diffusion coefficient.

3.3.4 *In vivo* minicell infection - endpoint experiments

In order to visualize the process of minicell infection in real-time, it is necessary to first determine if it is possible to fluorescently distinguish different lengths of DNA in tightly confined environments. With *in vitro* DNA ejections, the DNA is stretched near its contour length, and so it is reasonable to assume that one can determine the amount of DNA by just summing up the fluorescence intensity (this must be the case such that we can see the DNA ejecting from phage as a function of time, as shown in Figure 3.6). However, it is not so clear that this is possible with tightly packed DNA, for instance, inside the phage capsid. Below (Fig. 3.15) we demonstrate that 37.7 kbp phages have different DAPI fluorescence levels than 48.5 kbp phages.

Next, we demonstrate using endpoint experiments that excess DNA can be visualized in minicells - suggesting that watching the dynamic injection process is possible. In Figure 3.13 below what one can see is that the brightness of minicells in the population is much higher in samples where there were minicells incubated with phages at 23^oC versus 4^oC. Briefly, phages and minicells in the same proportion (10:1) were incubated at 4^oC or 23^oC for 30 minutes. SYBR gold dsDNA stain was then added to the samples at either 4^oC or 23^oC for 30 minutes. The samples were then mounted onto microscope coverslips for 10 minutes before washing with more dye, at the appropriate temperature. The samples were immediately visualized at room temperature thereafter. We used the convenient fact that lambda only injects at temperatures $> 4^oC$, as shown by Roessner et al., [116]. Since the signal is much brighter in samples that were incubated at room temperature, as compared to at 4^oC (Fig. 3.13), this allows us to conclude that our phages are capable of infecting minicells, and that our minicells are capable of being infected by phages.

We next demonstrate that minicells with YFP phages (in which a capsid protein has been fused with YFP [29]) attached have a larger fluorescence signal than minicells without YFP phages attached; the YFP phages allow us to visualize the attachment location of the phage and DNA stain allows us to visualize the DNA inside the minicells. As seen in Figure 3.16, minicells (black) often contain blue signal (DAPI) as long as there is a YFP-phage (green) attached.

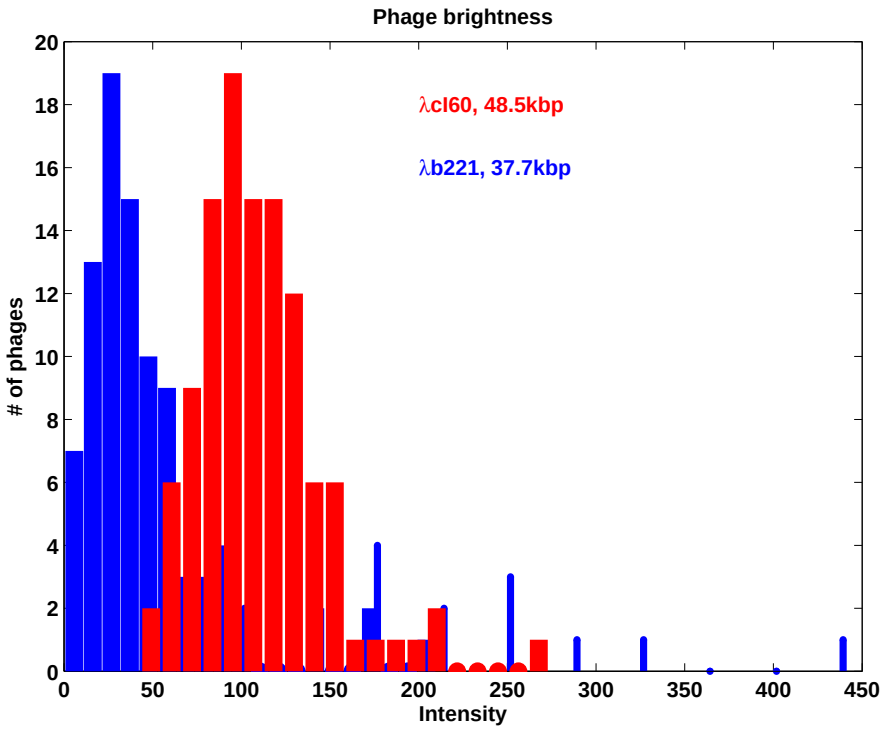

Figure 3.15: **DNA content of phages can be determined from a simple stain.** It is possible to differentiate the amount of DNA inside very tight spaces, such as phage capsids. Phages (either 37.7 kbp or 48.5 kbp) were diluted such that individual diffraction limited spots were able to be visualized using DAPI DNA stain. The intensity of individual spots were summed and plotted in a frequency histogram. In blue (37.7 kbp λ), the distribution is shifted to the left of the red (48.5 kbp λ), which is expected for a genome that is shorter. Though the distributions are shifted with respect to each other, they are also overlapping which means that a given phage with the smaller genome could be brighter than a given phage with the larger genome. It is disappointing that not every single phage has the same brightness.

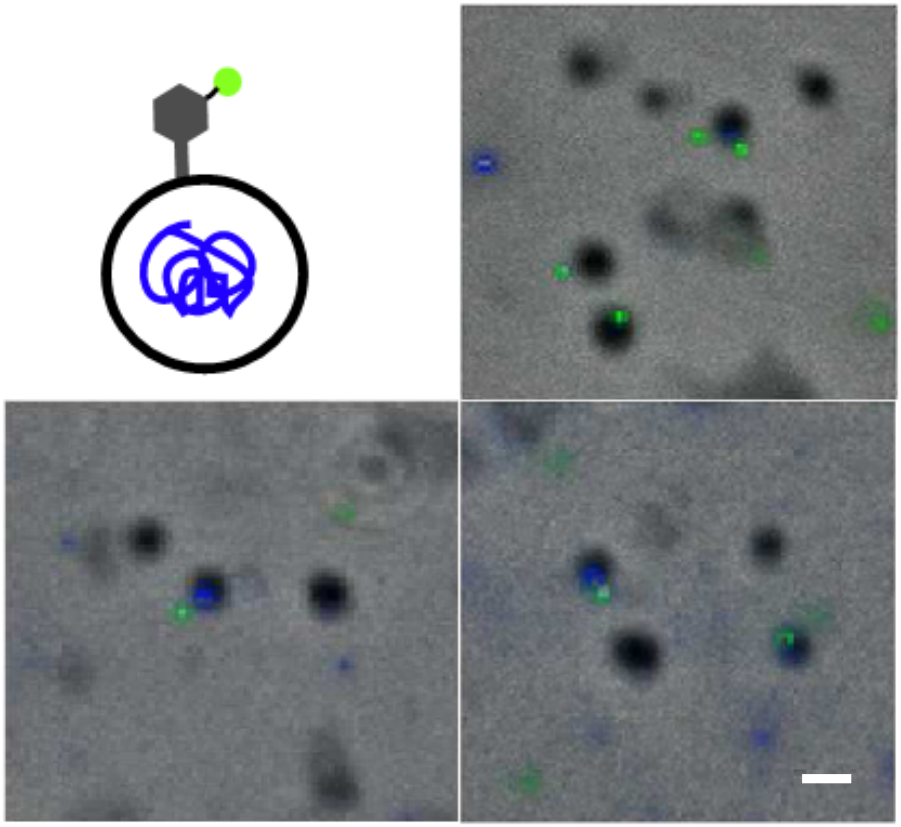

Figure 3.16: **YFP phages infecting minicells with DAPI stain. Top Left.** YFP-lambda phages were incubated with minicells for 30 minutes at room temperature before adding DAPI dsDNA stain. The mixture was then mounted on a microscope coverslip and washed with additional DAPI stain before visualization (**Top Right, Bottom Left, Bottom Right**). The preponderance of DAPI signal occurs in minicells that have YFP phage attached. YFP phages were generously donated by Ido Golding. Scalebar: 1μm.

3.3.5 *In vivo* minicell infection - dynamic experiments

The ability to distinguish different DNA lengths in confined spaces, coupled with the ability to distinguish infected and uninfected minicells buoyed our hopes for watching the infection process in real-time. We first tried mixing regular phages (no YFP label) with minicells and quickly (within 30 seconds) flowing the mixture onto a coverslip: in Figure 3.17, one can see phages bind to the minicells, and possibly even see their DNA transfer into the minicell over time (snap shots are 10 minutes apart). Note that we subsequently verified that DAPI stained phages are able to eject their DNA (discussed below, we show that DAPI stained phages are still able to eject their genomes *in vitro*), in contrast to SYBR gold which reduces the amount of viable phage, as discussed in Table 3.1.

Subsequently, we tried this same assay with YFP-phages covalently attached to the microscope coverslip via an antibody to GFP (Fig. 3.18). A separate experiment determined that anti-GFP was sufficient to bind YFP. The raw data is in Fig. 3.19. We couple the YFP phages to the slide in the following manner: anti-GFP is reduced such that the disulfide bonds in the Fc region of the antibody are separated. At the same time, the slides are amino-silanized (which creates an amino instead of a hydroxyl termination on the coverslip) and are activated to bind sulfhydryl groups using sulfo-SMCC, a heterobifunctional cross-linker that links amine groups with sulfhydryl groups (see Appendix, Section A.2.10). Presumably, the antigen binding region of anti-GFP now sticks into the solution and can bind YFP-phages. Since the YFP-phages have YFP only on the capsid, and not the tail, the orientation of the phages is no longer random, and the tail of the phage should always be pointing into the solution. The coverslips are then incubated with YFP-phages before being washed with buffer. At this point, the surface of the coverslip is covered in a sparse monolayer of YFP-phages. Minicells which have heretofore been purified, are incubated with DAPI and flowed onto the phage-coated coverslips, as shown in Figure 3.18, A. It is evident in Fig. 3.18, B, that a minicell drops to the surface and undergoes Brownian motion before it finds a binding site on the phage tail - at which point its motion reduces; the minicells get brighter over a period of time. In Fig. 3.18, C, we plot a typical fluorescence curve (taken from Fig. 3.19) and note the averaged time constants ($0.035 \pm .012\ s^{-1}$ and $0.006 \pm .001\ s^{-1}$) for the two phases of fluorescence increase.

The assay described in the previous paragraph is as near to the ideal DNA-dye based

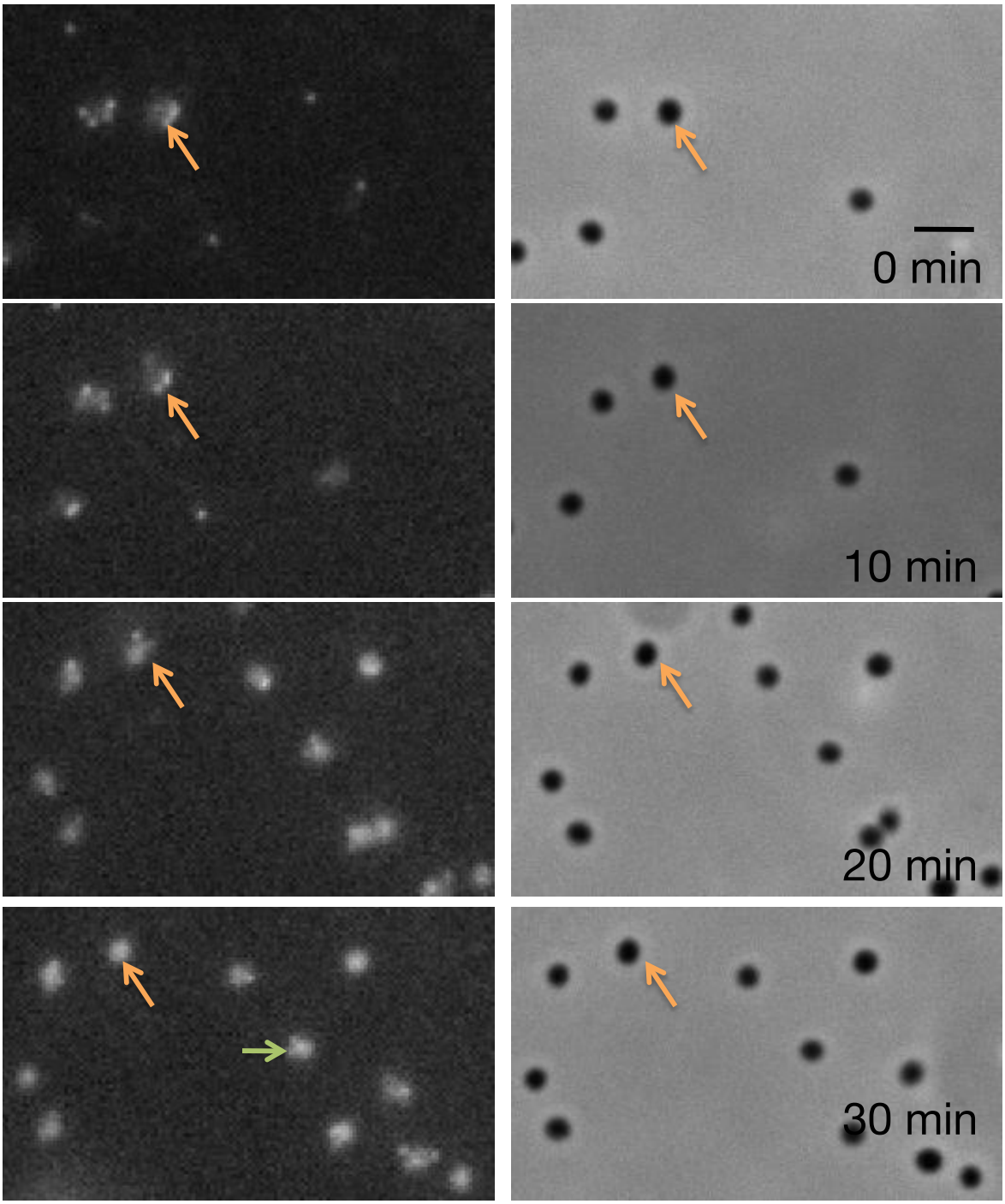

Figure 3.17: **Phages infecting minicells in the presence of DAPI stain. Left**. Fluorescence counterpart images to (**right**), the brightfield (phase) images. The arrows on the **right** point to minicells; the same minicell in fluorescence is pointed to on the **left**. Over time, the minicells on the **left** can be seen to get brighter, suggesting that their DNA content is increasing, perhaps as a result of phages (puncta on the surface of the minicells) injecting their DNA; simultaneously, the puncta get dimmer, suggesting that the phage DNA content is decreasing. The green arrow in the bottommost fluorescence frame points to another example of increasing fluorescence within a minicell. Frames are 10 minutes apart, and the scalebar is 2 μm.

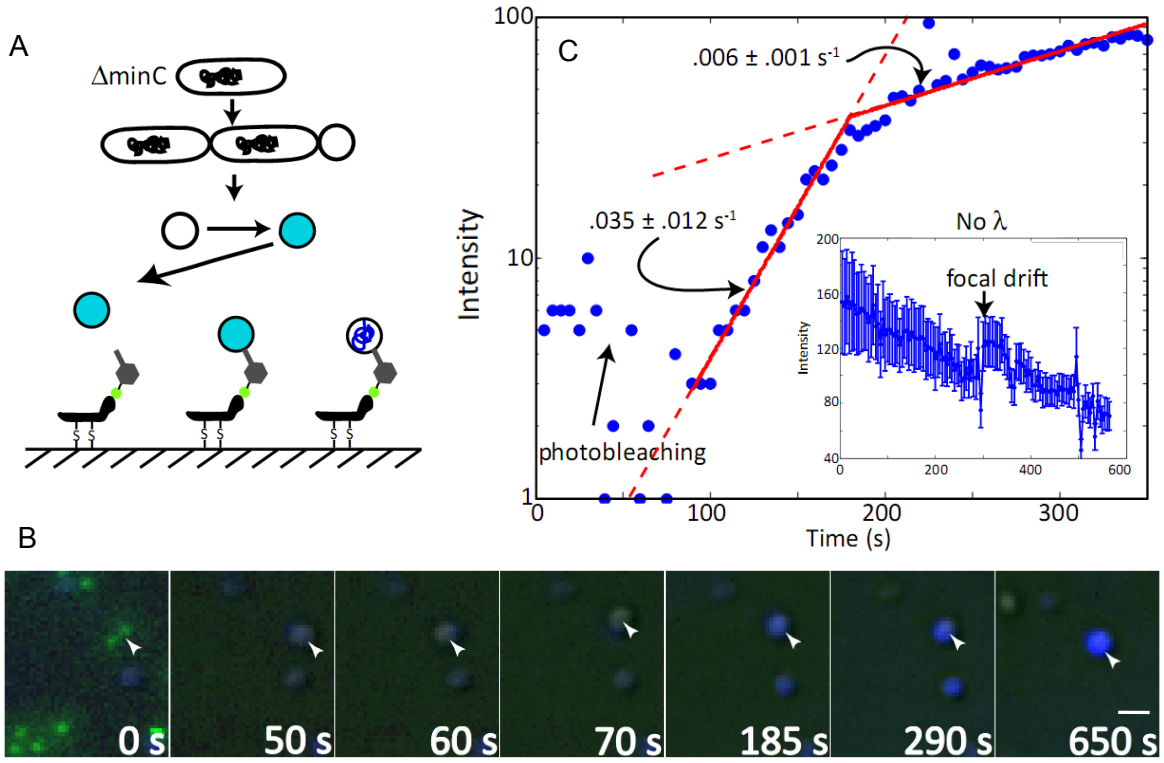

Figure 3.18: **Real time phage injection.** **A**. Antibodies to GFP were reduced and linked with sulfo-SMCC to an aminosilylated microscope coverslip. YFP phages were then incubated on the surface before being washed off. Minicells were purified and incubated in DAPI before application to the YFP-phage covered coverslip. The green dots are the phages which are apparent in (**B**). **B**. A timelapse of the fluorescence increase of a minicell during this process. After a few seconds, a minicells finds the phage. After a while (∼185 sec), the signal finally starts to increase. **C**. Quantification of the increase in fluorescence. There seem to be two time scales; the fluorescence increase takes place over ∼100 sec. Inset: when there are no phages lying around, a typical minicell will photobleach (there is always excess dye around which is visible under fluorescence, even in the absence of DNA). Scale bar is 1 μm.

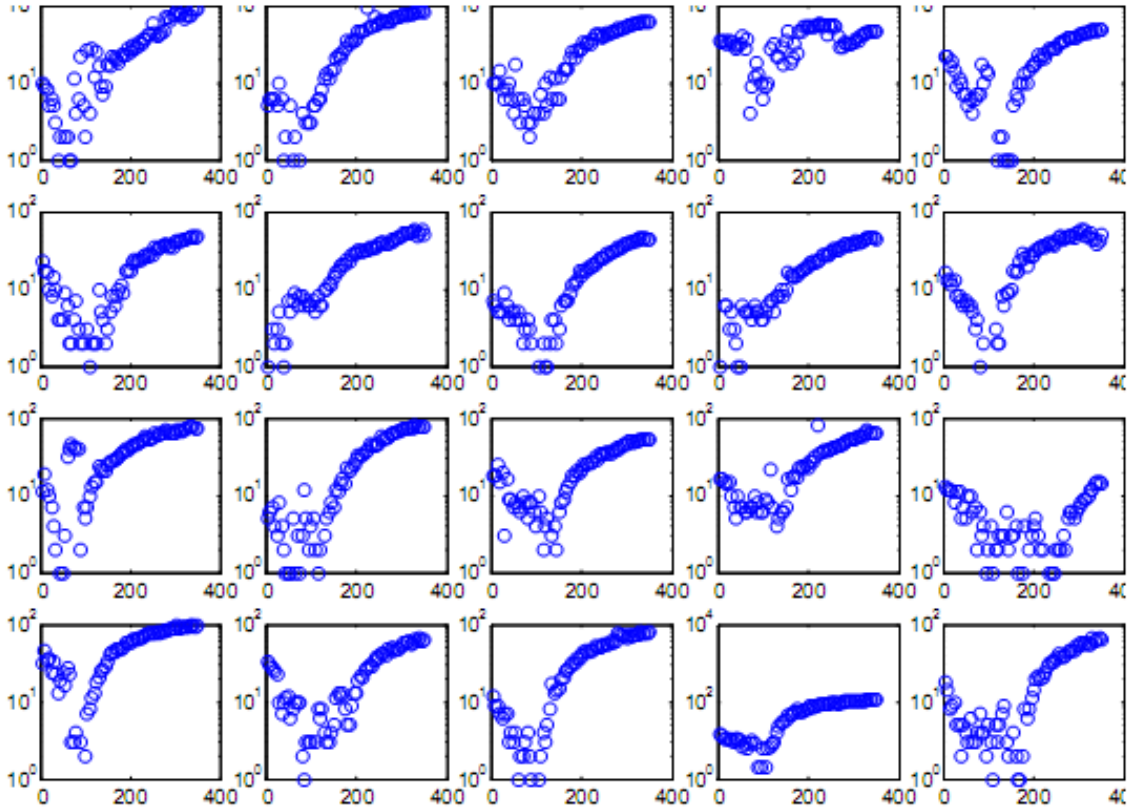

Figure 3.19: **Real time phage injection, raw data.** Minicells as shown in Fig. 3.18, B were segmented and their DAPI signal processed. x-axis is time in seconds; y-axis is arbitrary units, although it is the same scale in all plots. The plots display an eerie uniformity, which is discussed below. The data were fit to two exponentially increasing functions, resulting in the time constants inset in Figure 3.18, C.

experiments that I will have performed by the time that I graduate. Although it was later found by Zeng et al., [29], that these particular YFP phages are somewhat atypical, the concept retains its power. The phages are attached to the surface in a specific manner, such that their tails are pointed up. We have also tried to randomly deposit phages on the surface, but this never revealed as many "clean" ejections as the current assay (see Figures 3.18 and 3.19) due to (presumably) this precise issue. Moreover, the ability to see the phages and minicells simultaneously gives us a handle on how many phages are infecting each minicell. Finally, microscopy allows us to view multiple infections simultaneously, which gives us the power of statistics. I am optimistic that this type of assay is the right one to perform for the reasons listed above. However, there are a few caveats to the interpretation of this data, which are located in Section 3.3.7 below.

3.3.6 *In vivo* minicell infection - miscellaneous dynamic experiments - real-time RNA monitoring and optical traps

We also attempted to monitor the increase of RNA at the same time as DNA, using the permissive nucleotide stain acridine orange, as shown in Fig. 3.20. The special property of acridine orange is that its fluorescence is different depending on whether it is bound to DNA (fluorescence at 530 nm) or RNA (fluoresence at 630 nm). In this case, minicells were first bound to the coverslip surface via poly-L-lysine and phages subsequently flowed on, followed by an acridine orange wash (Fig. 3.20, A). There is a palpable delay between the DNA (blue dots) and RNA signal (green dots) in the two examples shown (Fig. 3.20, B and C). The data are exciting, but begs a few questions: does this reflect RNA production after DNA injection? Why is it that the RNA channel follows the DNA? If it is the case that light-induced permeation changes of the cells (see below, Sec. 3.3.7) causes minicells to get brighter by becoming dye sinks, don't we expect both channels to arise simultaneously? Or is it possible that at early times, the fluorescence in the 630 nm channel is below the detection threshold? After we see RNA signal start to rise, it clearly follows that of the DNA. This sort of behavior is expected; according to Reeve, citeReeve2, expression of lambda peptides occurs within 10 minutes of infecting minicells with lambda phage (via autoradiography), so RNA production clearly occurs, but only after DNA has entered the minicells.

Similar to the *in vitro* studies, we eventually need to directly deliver phage to minicells

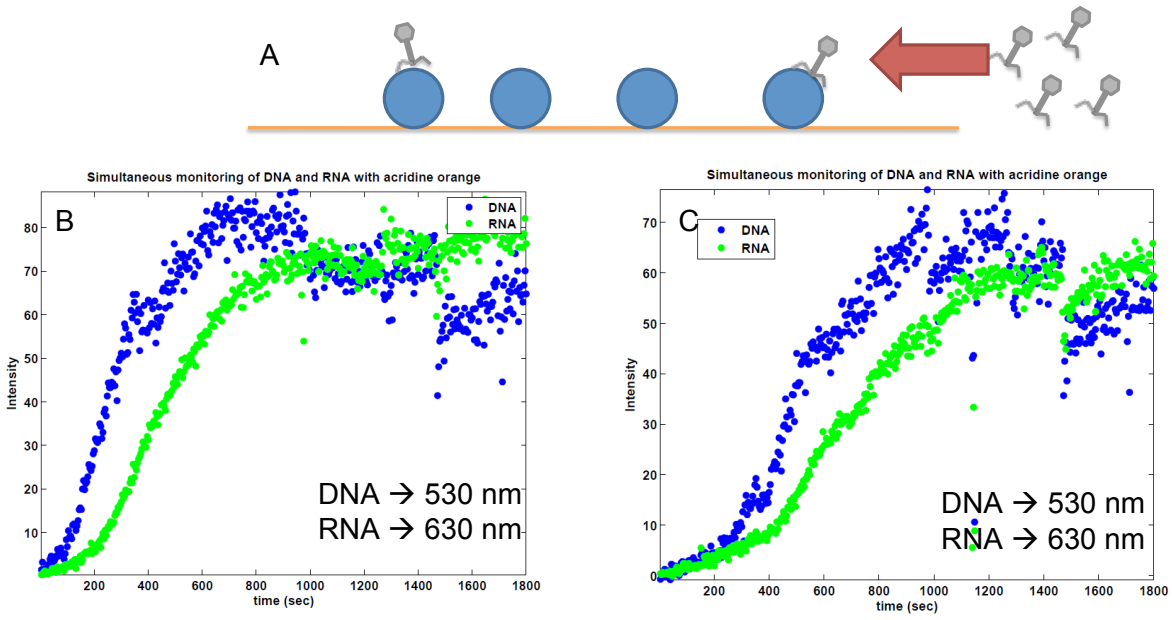

Figure 3.20: **Monitoring RNA and DNA simultaneously. A**. Minicells, incubated in acridine orange, are stuck to a surface using poly-L-lysine. After minicells have settled and bound to the surface (10 minute incubation at room temperature), phages are flowed on and imaging commences. **B**, **C**. Two examples of an increase in fluorescence in both DNA (blue dots) and RNA (green dots) after adding phage. There is a delay in the RNA channel (it follows after the DNA channel), suggesting that it is possible to monitor both RNA and DNA simultaneously.

(or other anucleate cells) so that we know there is a phage attached to an anucleate cell and that the reason the anucleate cell is getting brighter is because of the phage. In order to achieve this, we biotinylated phages and purified the result on CsCl gradients (see Appendix, Section A.2.1) before attaching them to 2 micron diameter beads conjugated with streptavidin. However, since centrifugation can destroy phages, we needed a way to get rid of excess free phages, and the solution we employed was through a flow-exchange system, as schematized in Fig. 3.21. Using an optical trap, we can take a bead coated with phages and move it into a solution that is free of phages, but filled with minicells. For a review of useful fluidics systems in single-molecule biophysics, see Brewer et al., [121]. We first verified that the beads have phages attached to them, and that they are capable of ejecting, by performing *in vitro* ejection experiments off the beads, as shown in Fig. 3.22.

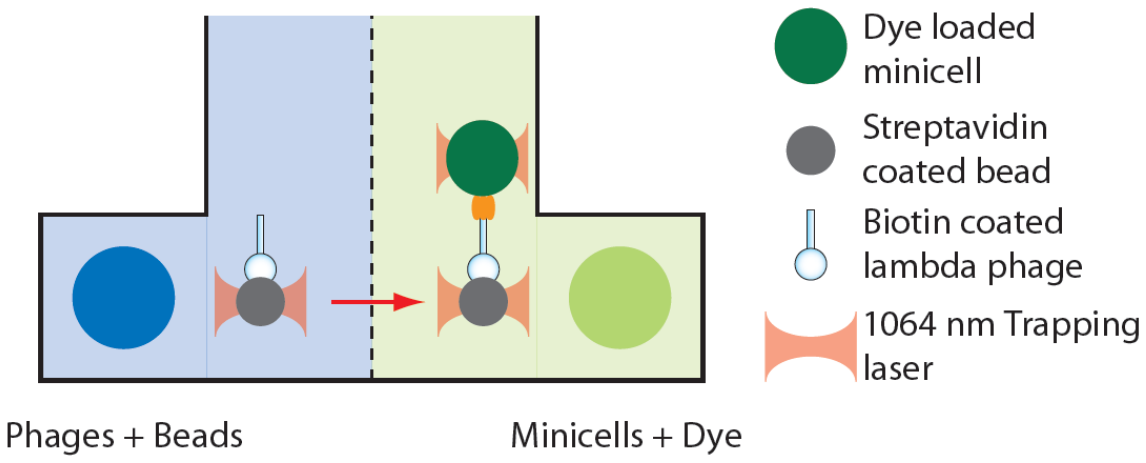

Figure 3.21: **Bi-flow buffer exchange system.** This two-flow system allowed us to "purify" beads conjugated with phages away from phages free in solution. This is accomplished by grabbing beads with optical tweezers and moving them into a solution free of phages, but filled with minicells. Mixing of the two solutions is minimized through the use of constant flow, at 10 μl per minute, resulting in the formation of a boundary between the two solution: any diffusion orthogonal to the flow direction is carried away.

Using beads coated with phages is similar in spirit to the packaging experiments pioneered in the Bustamante lab [31], and our own protocol performed during the *in vitro* part (Fig. 3.3). As schematized in Fig. 3.21, in one stream we flow beads coated with phages and in the other stream we flow minicells at a constant rate of 10 μl/min. There is SYBR gold dye present everywhere. We use a dual trap similar to the one in the Maximum Caliber section (Sec. 2.3), except this time with an infrared laser ($\lambda = 1064$ nm) and do not time-share the laser (for the setup, see Fig. 3.23), but instead perform beam steering with

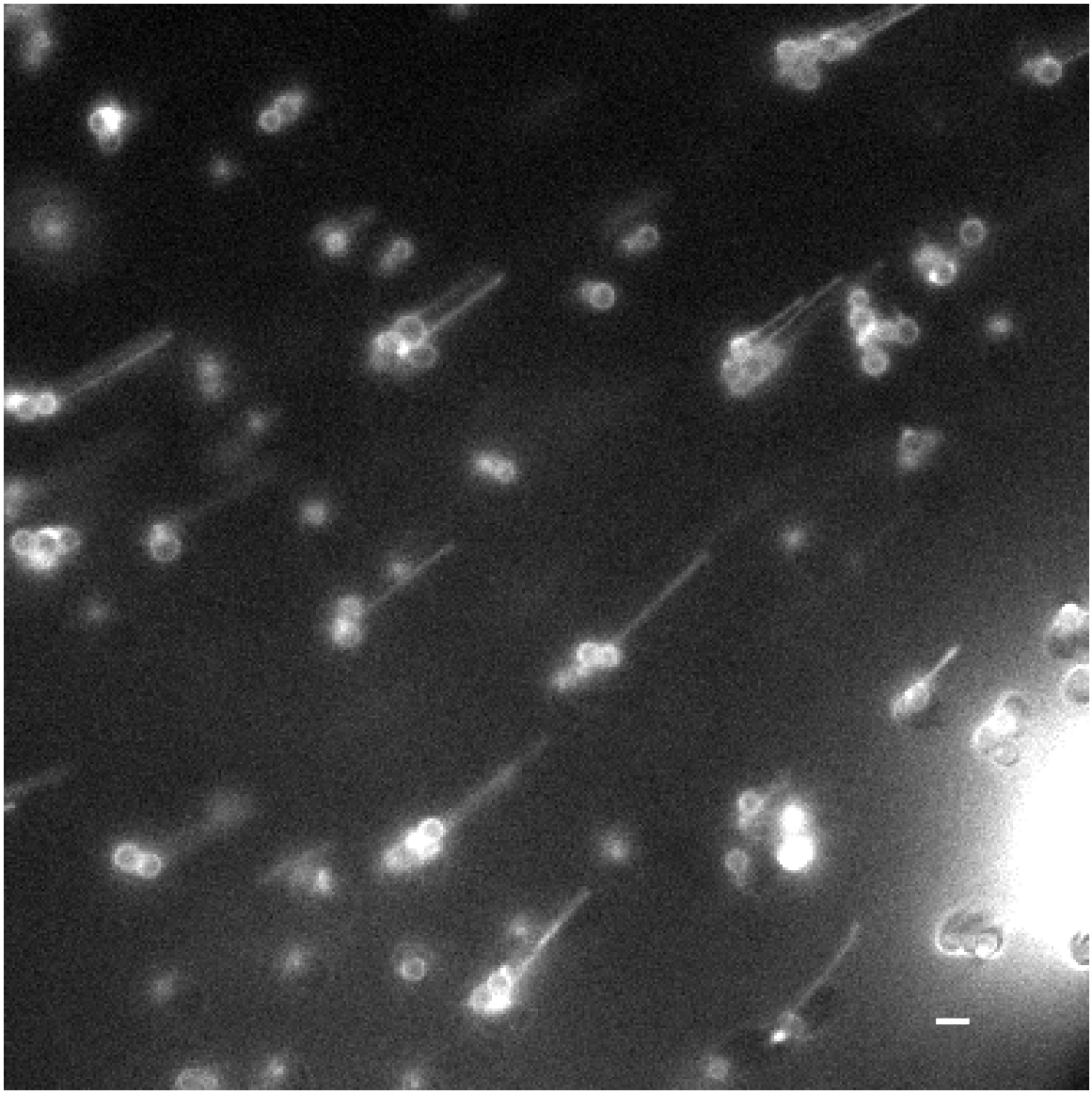

Figure 3.22: **Ejections off beads.** It is clear that we have phages conjugated to beads by performing *in vitro* ejections on biotinylated phages off of streptavidin beads that have been stuck down to biotinylated glass (see Appendix, Section A.2.12). The DNA is stained with SYBR gold, enabling visualization. The circular objects are the streptavidin-coated polystyrene spheres. Scalebar: 2 μm.

mirrors. The total laser power used was ∼50 mW per trap at the back focal plane with additional losses through the 1.2 NA water objective. With two laser traps running, we first block one beam and grabbed a bead coated with phages using the other beam. Then we translate the sample so now we are in the minicell flow and trap the minicell with the now unblocked second trap. Next we use mirror "C" positioned at the plane conjugate to the sample such that an angular deflection becomes a translation in the sample. By doing this, we are able to make the beads with phage and the minicell "kiss" and monitor the concomitant increase in fluorescence (Fig. 3.24). The graph shown displays an increase in fluorescence with a time scale of about 100 seconds, same as in Figure 3.18, but much shorter than Figure 3.20, suggesting active infection. However, with this data there are few unknowns: how many phages are doing the infection? Whey are there plateaus in the data?

3.3.7 *In vivo* minicell infections - caveats

The protocols described in this section have been developed over the last several years and are the result of many attempts to view the real-time ejection of phage DNA into cells. Even early on, we thought we had evidence of putative ejections since we observed minicells increase their fluorescence when incubated with phages. However, our ultimate conclusion was that these initial experiments were not successful. In the past, we kept on seeing fluorescence increases of minicells mixed with phages - so what made those infections not true? For one, we saw DNA leaking out of those cells, so that led us to conclude that the dye (and light) were somehow changing the permeability of the minicells. Moreover, when we imaged minicells in the absence of phage at non-permissive temperatures ($< 4^o$C), we saw some get brighter - which meant that we don't have a good way to differentiate increasing signal in minicells due to true phage injection and increasing signal due to permeability changes. However, a conclusion we can draw is that the combination of SYBR gold and light is somehow bad for the minicells. In fact, we should have known this to begin with.

Another caveat: one might ask the question whether stained phages can even eject, given Table 3.1, since there is dye everywhere in all the assays described above. The answer is yes - as long as the dye is DAPI. SYBR gold, on the other hand, causes phages to eject spontaneously, as demonstrated in Table 3.1. Furthermore, we know that constant illumination of stained DNA somehow damages phage. We discovered this when we incubated phages in DAPI and flowed on a solution of ejection buffer containing LamB: what was in

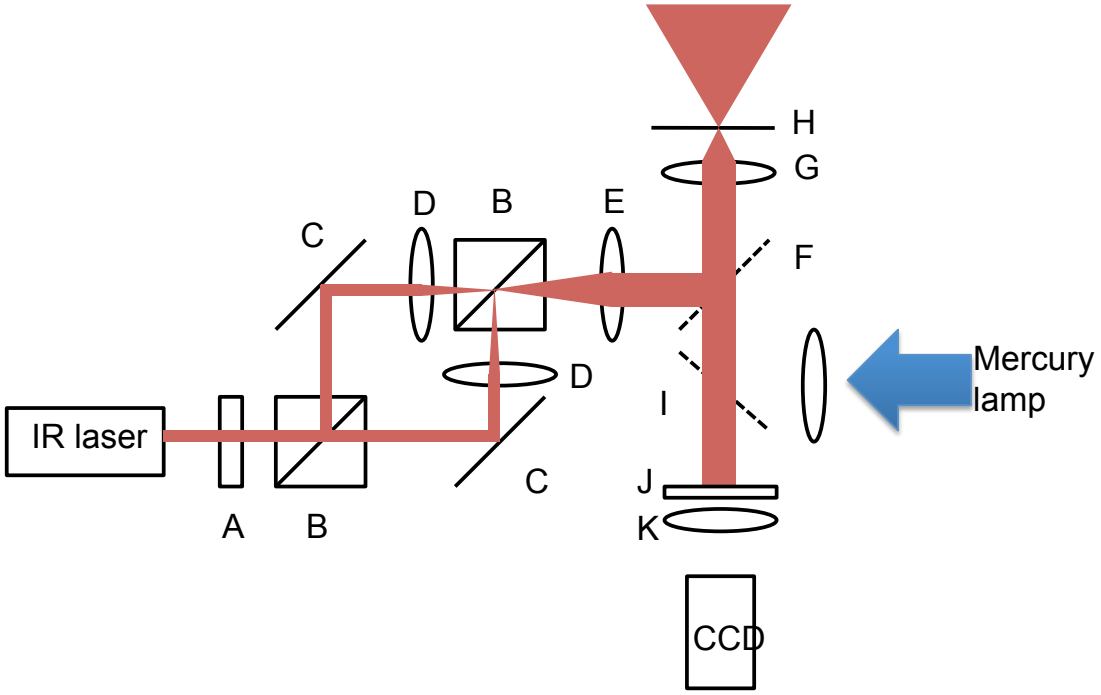

Figure 3.23: **Optical trap/fluorescence system.** A dual-laser tweezer microscope was constructed by polarization-splitting a 1064 nm diode laser. A half-wave plate (**A**) selects the amount of **s** and **p** polarization before passing through (**B**), a polarizing beam splitting cube, which generates two traps. The relative amount of polarization determines the strength of each trap. Steering mirrors (**C**), placed at the image of the back focal plane of the objective (**G**) determine the location of the traps in the sample plane (**H**). The lasers are recombined by an additional polarizing beam splitting cube (**B**). **D**, **E**. Beam expanding telescope for overfilling back aperture of objective. **F**. A short pass dichroic reflects the long wavelength laser into the objective (**G**), but passes shorter wavelength visible light. The objective (**G**) is a 1.2 NA water immersion from Olympus. **I**. A dichroic is placed in the imaging path to allow for fluorescence imaging of samples. **J**. A Raman filter and fluorescence emmission filters are placed in the Fourier plane to block 1064 nm light from reaching the camera. **K**. Tube lens.

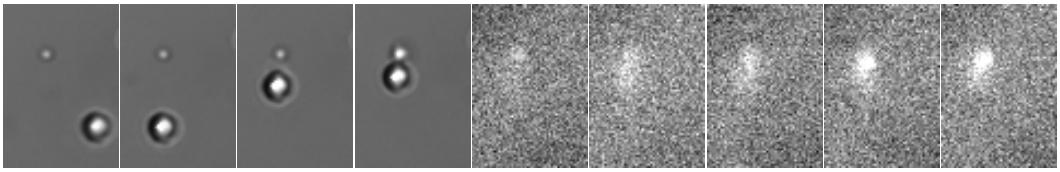

Brightfield alignment → switch to fluorescence

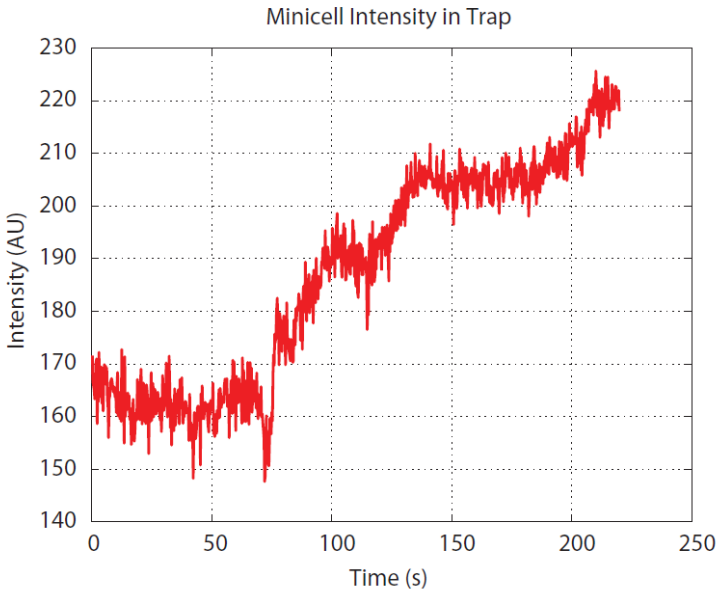

Figure 3.24: **Optically trapped minicell fluorescence increases. Top**: montage sequence of a trapped bead with phages approaching a trapped minicell. After they are made to kiss, the fluorescence source is turned on (top right). **Bottom**: After a while, an increase in signal can be seen, with an increase taking place over ∼100 seconds.

the field of view did not eject, but what was outside the field of view did eject. Hence, the interaction of DAPI and light and DNA will inactivate the phages. The mechanism should be similar to the induced permeability changes observed in bacteria as described above. A corollary to this experiment is that DAPI stained phages can eject, as mentioned above (Fig. 3.17) - as long as the DAPI-stained phages don't see so much light.

In general, many of our earlier experiments looked at minicells continuously, which causes changes in permeability of the cells and more dye to leak in, which can look like an ejection due to the resultant increase in fluorescence (this is discussed in more detail in the following section (Sec. 3.3.8). The following classes of experiments were performed with minicells: 1. Phages are attached to the surface and minicells are flowed on. 2. Minicells are attached to the surface and phages flowed on. 3. Minicells are incubated with phages and the end-point looked at. 4. Minicells are incubated with phages and we look at it over time. In my opinion, sequence 1 is the best experiment, since one can look at labeled phages directly (with either DAPI or YFP-capsid) and flow on minicells at high density, resulting in large statistics. One can also choose to follow minicells' fluorescence increase and correlate the result with whether or not it colocalizes with a phage.

3.3.8 *In vivo* infections

In this section, we discuss our efforts to look at infections of bacteria-proper with phages, instead of minicells. The problem remains: how to look at a tiny signal above a huge background? One idea is to generate chromosome-less cells[1] [100] or to spatially restrict the extent of the chromosome and use the fact that phages tend to infect the poles of the cell [118] (note that this is disputed by others that have looked at the spatial distribution of LamB [122]; they claim a spiral-like distribution of receptors, which is at odds with polar localization of phages [118]). The impetus for spatial restriction of the chromosome comes from DnaA mutants that lack the ability to replicate their chromosomes. This causes the cell to filament but allows the visualization of episomes and plasmids upon DAPI staining - since they can now "diffuse" away from the nucleoid [123].

It turns out that chloramphenicol (a ribosome inhibitor) can turn chromosomes into compact toroids in appropriate doses [124] (see Appendix, Section A.2.8 for method). Use of nalidixic acid (blocks gyrase activity) is also possible, but often results in chromosomal

[1] this was unsuccessful on my part, but I didn't try so hard

fragmentation [125]. Use of these drugs results in chromosomal compaction in the middle of the cell (see Fig. 3.25). The subsequent application of lambda phage - and ejection - should be able to be visualized due to the slight preference for polar localization (see Fig. 3.25).

We infected chromosomally-restricted bacteria with different doses of phages and imaged the result to see if we can see infections along the poles of the cells. In Fig. 3.26, A, are example cells treated with chloramphenicol and subsequently stained with DAPI (but no phages). In Fig. 3.26, B, phages were also incubated with the chromosomally-restricted cells, resulting in puncta around the edges of the cells. Fig. 3.26, C, is the same assay with nalidixic acid. Also apparent are green masses at the poles of the cells, absent in Fig. 3.26, A. After application of phages to chromosome-compacted bacteria, samples were removed at different time points and their poles assayed for fluorescence. As a function of time, the amount of DNA at the poles increase, but with large variability, as shown in Fig. 3.26, D. The increase of fluorescence at the poles is suggestive of the process of infection or lambda gene duplication. We also performed the same chromosome compaction experiment with both wild-type (48.5 kbp DNA) and a shortened phage genome (37.7 kbp DNA) and quantified the level of fluorescence at the poles of the cells. Using the same MOI, it was discovered that bacteria infected with the shorter phage variant had less DAPI signal than bacteria infected with the wild-type length genome, as shown in Fig. 3.26 - again, suggestive of our ability to quantify the amount of DNA inside a cell, critical when trying to assay infection in real-time.

3.3.9 The Path to the Future - *in vivo*

Regarding *in vivo* infection experiments, I believe that we are a short time away from obtaining good, clean data free of experimental artifacts, such as the light-induced permeability changes. This problem can obviously be alleviated by taking pictures spaced farther apart in time. We have shown that it is possible to see differences in DNA length in tightly confined spaces, and have shown that minicells infected with phages exhibit a globally brighter fluorescence, and that chromosomally constricted cells develop puncta near their poles. What is left to be done, therefore, is to fill in the time in between. We also know how to set a $t = 0$ for the process, either by flowing on minicells onto a bed of phages, using optical traps, or raising the temperature.

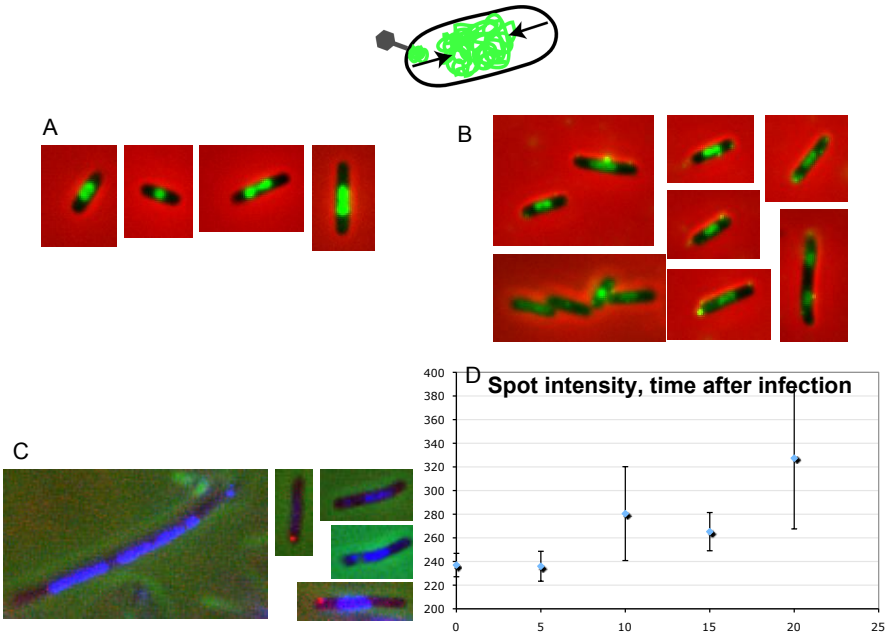

Figure 3.25: **Infection of cells with phage. Top**. Schematic of the experiment. The genomes of cells are first compacted with a drug, either chloramphenicol (**B**), a ribosomal inhibitor, or nalidixic acid (**C**), a gyrase inhibitor, then stained with DAPI. **A**. With no phages added, one can see that the genome is only occupying the center. **B**. Phages are added to the bacteria with their chromosomes compacted by chloramphenicol, resulting in puncta at the edge of the cells, and green masses near the poles of the cells. **C**. The experiment in **B** was repeated with nalidixic acid, resulting in more variable results. The red color is due to the use of quantum dot-labeled phage (see Appendix, Section A.2.13 and Edgar et al., [118]). **D**. After application of phages to chromosome-compacted bacteria, samples were removed at different time points and their poles assayed for color (all cells in this figure were stained with DAPI; the images are false color). As a function of time (x-axis is in minutes, y-axis is arbitrary fluorescence units), the amount of DNA at the poles increase, but with large variability.

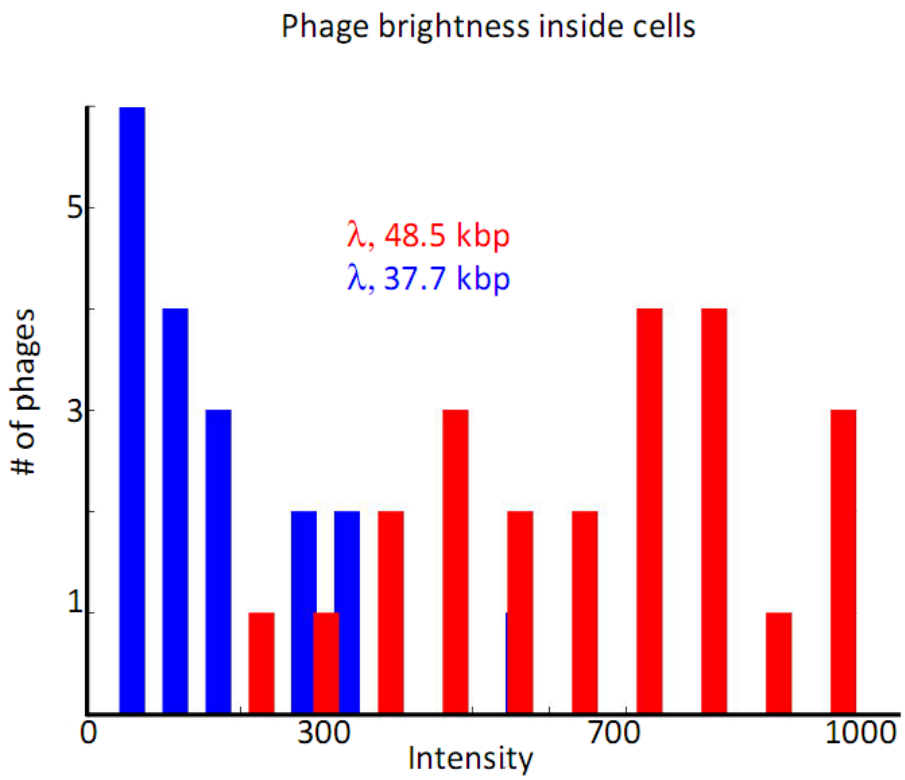

Figure 3.26: **Puncta brightness inside cells.** This is the sister graph to Figure 3.15 in the sense that the brightness differences of two different lambda genomes is again compared (λcI60, 48.5 kbp, versus λb221, 37.7 kbp), but this time inside cells with their chromosomes compacted with chloramphenicol, as in Figure 3.25. It is shown that λcI60 has the larger signal, as expected. Data were taken 20 minutes after infection.

The next step in this set of experiments is to obtain fluorescently labeled phages (xFP-λ) that are healthy. Antibodies to xFP-λ should be covalently bound to a microscope coverslip coated with a monolayer of PEG to prevent non-specific xFP-λ binding to glass. Minimal amounts of DAPI dye or SYBR gold should be used, since we know that long UV exposure, in the presence of DAPI (Sec. 3.3.7), inactivates phage, and that too much SYBR would do the same (Sec. 3.2). Snapshots should be spaced apart; minicells should be purified the same day or come from frozen stock [108]. With these set of conditions met, I believe that this experimental protocol, that of using DNA staining dye to watch increases in fluorescence upon infection, should be possible. Of course, one can think of numerous other experiments, but I won't discuss those here.

3.4 Summary

We investigated the dynamics of DNA ejection in a variety of different salts, and also performed measurements on the self-repulsive force driving this process. We demonstrated that the counter-ion charge is an important control parameter for this class of experiments. These measurements should be of use to theorists working in physical virology. Of particular interest would be models that predict the force driving ejection in different salts, in addition to a better understanding of the time scale of the ejection process. We also investigated the origin of looped ejections. From our data, we can develop several possible models for these processes. It is possible that the end of the DNA gets stuck on the tail of the phage or LamB as it comes out, and that the rest of the genome subsequently comes out of the tail, accounting for the DNA loops occasionally seen (Fig. 3.3). This may make it possible for phage to circularize even faster as the genome rushes to get inside its host, *E. coli*, as it is theorized that lambda delivers its genome directly into the cytoplasm without going through the periplasmic space [98]. Although the observation of looped ejections was first made in 2007 by Grayson et al., [45], this is the first attempt to explain them and propose that they might represent an important part of phage lambda's life cycle.

Of particular note, is the relation of the *in vitro* work to Fuller et al., [40], which is an investigation of the packaging process as a function of salts; they note that by increasing the amount of multivalent cations in their packaging assay, the virus packages faster, and requires less force at an equivalent fraction of DNA packaged. This suggests that increasing magnesium reduces the amount of intrastrand DNA repulsion. In this current study, we see a similar effect; namely, an increased force is required to stall ejecting DNA at the same length, with increased concentration of monocharged ions. However, the mobility during DNA ejection appears to be independent of salt composition at our detection resolution. Notably, the speed of ejection is faster during ejection in the presence of larger fractions of monovalent cations, which is consistent with the packaging data. Altogether, this work is a step forward in understanding the forces at play when bacteriophage lambda infects bacteria.

We also made attempts at looking at phages infecting minicells and bacteria in real time. Based on our endpoint experiments, it is possible to fluorescently distinguish infected and uninfected cells, especially with the use of YFP or biotinylated phages, and the measured

time scale is around 100 seconds. However, there is the big issue of light-induced permeability changes in the presence of DNA binding dyes that needs to be addressed before any of this data can be taken seriously. However, we have made progress in the direction of finding an appropriate assay to continue work on this class of experiments, of which I gave a broad overview.

Chapter 4

Otolith Formation in Zebrafish

4.1 Symmetry breaking is an agenetic event

As I see it, in biology, scientists try to divine the general from specific examples, and this method of reasoning works because biology is a historical process. If evolution is the mechanism by which diversity is generated (and invoke the assumption that there was a single "mother" cell), then any two species on this earth have a common ancestor. Therefore, there is an unbroken chain of connected species from the present back to the dawn of organismal time. Technical advancements are thusly built over eons, and extinction a true threat to life, as only life can beget more life.

Another layer of complexity exists. Let's posit for the moment that we have the ability to synthesize entire genomes - as has been done for *Mycoplasm genitalium*, which however "only" has a ∼600 kbp genome [126]. I wager that throwing such a genome into an lipid bilayer sac would not spontaneously produce "life" and its attendant features: namely, the inherent desire to reproduce. What is missing, no matter what the life-form, are the ancillary milieu of chemicals, whether bacteriophages or bacteria or stem cells; i.e., its hard to create life *de novo*. But life, since it does exist after all, makes this process easier. And in fact we, as scientists or engineers, harness the synthetic capabilities of bacteria to produce nucleic acid polymers and protein either because we do not know how to, or because synthesis would be too expensive.

DNA, the molecule of inheritance, is like a set of functions - useless without users that perform the actual programming (string functions together in a logical manner to perform a task). And hence this last layer of complexity, the ancillary stuff that activates transcription, must be considered. Perhaps the only "organisms" that don't have the stuff are viruses, but

even viruses are obligated to seek appropriate hosts in order to activate transcription. DNA, by itself is a blobby shapeless polymer that has minimal spatial organization in relation to its host carrier, although it does persist in a consistent manner, in both prokaryotes and eukaryotes [127, 128]. DNA certainly does not specify that attached to our arms are 5 appendages - all it does is make RNA. It seems that, on the other hand, direct spatial localization by DNA is limited to the cytoplasm: localization sequences in protein [129] and RNA [130]. Instead, programs are differentially activated based on their location in, or age of, a multicellular organism.

Differentiation requires activation of different sets of programs and so requires external factors to dictate just what combinations of genes are expressed. In developing embryos of the animal kingdom, we can classify development and differentiation into three categories. In *Caenorhabditis elegans*, cell-fate is specified by a clock-like internal division program - cells are mostly autonomous and are ignorant of the surrounding milieu [131]. In flies, axial patterning is generated all-at-once through morphogen gradients in the embryo syncitium prior to cellular membranization [132]. In chordates, tissue patterns in the presence of cell membranes through asymmetric cell division and morphogen concentration gradients, but also through mechanical factors, such as local forces via cell-cell or cell-extracellular matrix contacts [133]. Naturally, all three categories can exist in the same organism: lung branch formation in mice is thought to occur via in a cell autonomous manner [134]. There are additional issues of penetrance stochasticity, even in such the cell lineage-based *C. elegans* [135].

Animals have clear anisotropies and asymmetries. The three axes are known as anterior-posterior, left-right, and dorsal-ventral. Anterior-posterior is traditionally the first axis established, followed by dorsal-ventral, and finally left-right. The scientific consensus states that these axes are never spontaneously formed, but always due to an external influence. In *C. elegans*, sperm entry location determines anterior-posterior axis by causing local cytoskeletal reorganization [136]. This is also found in *drosophila* although the A-P axis is determined during oogenesis before the zygote is formed [137] by asymmetric maternal deposition of mRNA into the oocyte [138]. In *Xenopus laevis*, maternally derived mRNAs are transported to specific locations in the single cell stage, resulting in axis specification [139]. In mice, it is not known what the earliest signals of the A-P axis are, but they occur before implantation into the uterus [140]. In order to generate left-right asymmetry

in mice, fluid flow is needed to push signaling molecules across space [141, 142]. Similarly, cytoskeletal dynamics, specifically organization of the microtubule-centrosome complex, determines left-right asymmetry in *Physa acuta*, a sinistral-only (left-handed) gastropod [143]. In all cases encountered in the literature, an external factor determines the new axis - the DNA doesn't do it by itself.

With the exception of certain gravity-sensing neurons [144], it is not clear if cells "know" their orientation or location within an organism. A signal from the outside is transduced into the cell which fixes spatial relations and enacts genetic programs to produce identity and hence spatial diversity within an organism. A similar role is played by hydrodynamics in the placement and shape of the otolith - the accelerometer and hearing organ - in the zebrafish, the content of this chapter of the thesis. During the process of otolith formation, the cell cannot possibly know where and how much and what shape the otolith has to be in the adult - a few days *after* otolith formation, stereocilia must grow into the otolith and form a functioning organ - there must be external forces or events that dictate the formation of the structure ahead of time in a consistent fashion. Here, we show how fluid flow can help organize otolith formation and robustly determine the otolith's shape. We use a flow probe approach with optical tweezers and a physical model based on Stokes flow to explain the observed hydrodynamical processes as the otolith assembles: flow in the core of the cilia-mediated-vortex has an inhibiting influence on spherule agglomeration and that the vortex lines outline a negative shape of the otolith. Note that there are studies on high Reynolds number flow induced changes in gene expression [145, 146], but instances of low Reynolds flow influencing morphology are few, the one example in the literature being neurons in the adult mouse brain that follow the flow of cerebrospinal fluid generated by motile cilia [147].

4.2 Cilia are force sensors and motility generators

The cilium (or flagella) in eukaryotic cells is a radial structure resembling a tube composed of 9 outer microtubule doublets and occasionally an inner pair of microtubules (the "$9+2$" rule). It is typically a few microns in length and $\sim$120 nm in width. The cilium is commonly found on cells that need to either generate or sense flows (classically, as sperm tails or in the lungs), although cilia are also used as chemical antennae for sensing the chemical

environment (for a review of cilia-related receptors, see Berbari et al., [148]) - and sometimes cilia both generate flow and sense chemicals [149]. Violations of the $9 + 2$ rule abound in nature, of course, but principally by insect sperm [150]. The cilium is attached to the cell via a centriole/basal body, although it is more accurate to say that cilia grow out of the centriole. For the purposes of our following discussion, dynein (molecular motors) are anchored between the outer microtubule doublets, and their power stroke causes the doublets to slide with respect to each other, generating a characteristic beat pattern, as in Figure 4.1. The outer doublets connect to the inner pair via radial spokes, and the outer doublets are connected to each other through nexin (Gas11) [151]. Its rather complex organization is thought to predate the endosymbiotic event (and draws its ATP source from glycolysis, not oxidative phosphorylation) that gave rise to mitochondria [152] and some have even proposed that its origins are viral [153]. However, the complexity may be a red herring, as simple rules can often generate complex patterns (snowflakes, fractal structures), and only nine genes are necessary to reconstitute centriole type structures [154, 155].

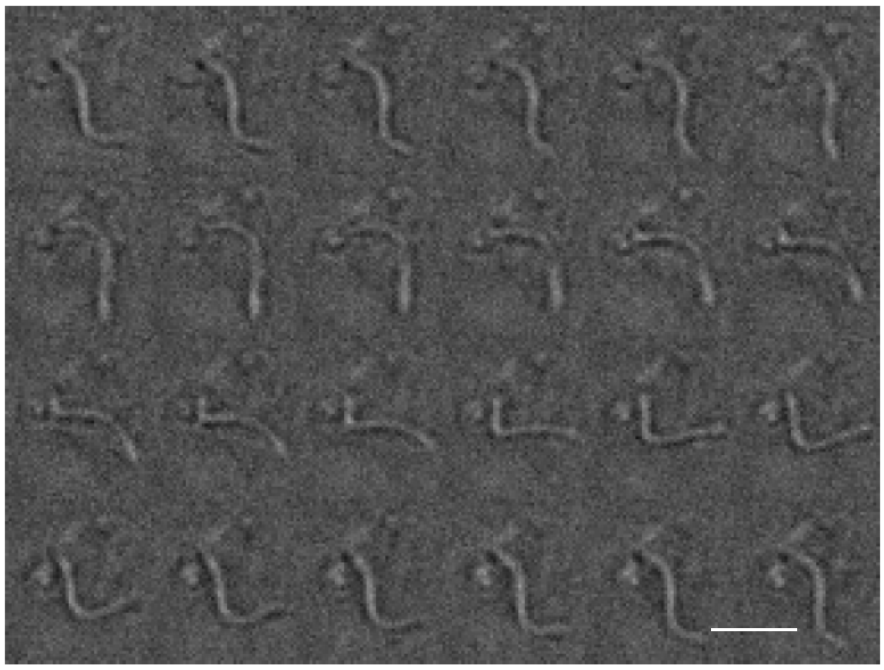

Figure 4.1: **Typical flagellar motion in Kupffer's vesicle.** A montage of cilium motion in the Kupffer's vesicle of zebrafish. Images are 0.004 seconds apart; the cilium beats at a frequency of 10 Hz. Scalebar: 5 μm.

The origin of the cilia beat is proposed to be one of the following non-mutually exclusive mechanisms: 1) enzymatic regulatory cascade through the dynein regulator complex

in which the central pair regulates the outer pairs [156], 2) spontaneous tuned oscillations of entrained molecular motors [157], and 3) geometric clutch whereby motors are able to detach and reattach to microtubules to modulate shear forces [158]. Waveform modulation is accomplished through second messengers such as cAMP, cGMP, calcium, and pH [159]. Non-motile, primary cilia (with a "$9 + 0$" configuration of microtubule doublets - no central pair), on the other hand, are cellular sensors that respond to ubiquitous external cues such as strain, shear, chemical gradients, and even gravity (see [144] and references therein). Presumably, as an appendage, they sense chemicals by sticking out of the large hydrodynamic friction layer at the surface of the cells that slows the diffusion of chemicals.

4.2.1 Cilia are necessary for proper formation of the inner ear otolith

In protists, cilia are controlled by the dynein regulatory complex (DRC) which regulates axonemal dynein activity in response to signals from the radial spokes and central pair apparatus [160] (the enzymatic regulatory cascade hypothesis). In zebrafish, Gas8 is the dynein regulatory protein [161]. At 12 somites, RNA transcripts of *gas8* are localized to the inner ears, brain neural tube, indicating that *gas8* is expressed in ciliated tissues during organogenesis, as seen in Fig. 4.2. Antisense morpholinos (MOs), which inhibit transcript translation, to *gas8* produces hydrocephaly, neural tube cell death, and left-right axis defects. MOs also affect ear development, as expected, as shown in Fig. 4.3, g. Moreover, we showed with live imaging that injection of MOs resulted in immobile cilia, as demonstrated in Fig. 4.4, b-n, and that particles near the cilia featured purely diffusive behavior in the knockdowns, in contrast to unmanipulated embryos, as in Fig. 4.5, c and f. This suggests a cilium-dependent hydrodynamic mechanism for otolith biogenesis. In the following sections, we try to establish this mechanism definitely.

4.3 Otolith development and cilia in the inner ear of the zebrafish

The function of the inner ear in zebrafish is to sense motion and hear sound - both use fluid coupling to drive an inertial mass against neurons. For instance, in order to sense motion (acceleration) the ear uses a mass balanced, called an otolith (or ear-stone), atop stereocilia such that when the organism moves, causes a transient displacement of the otolith which

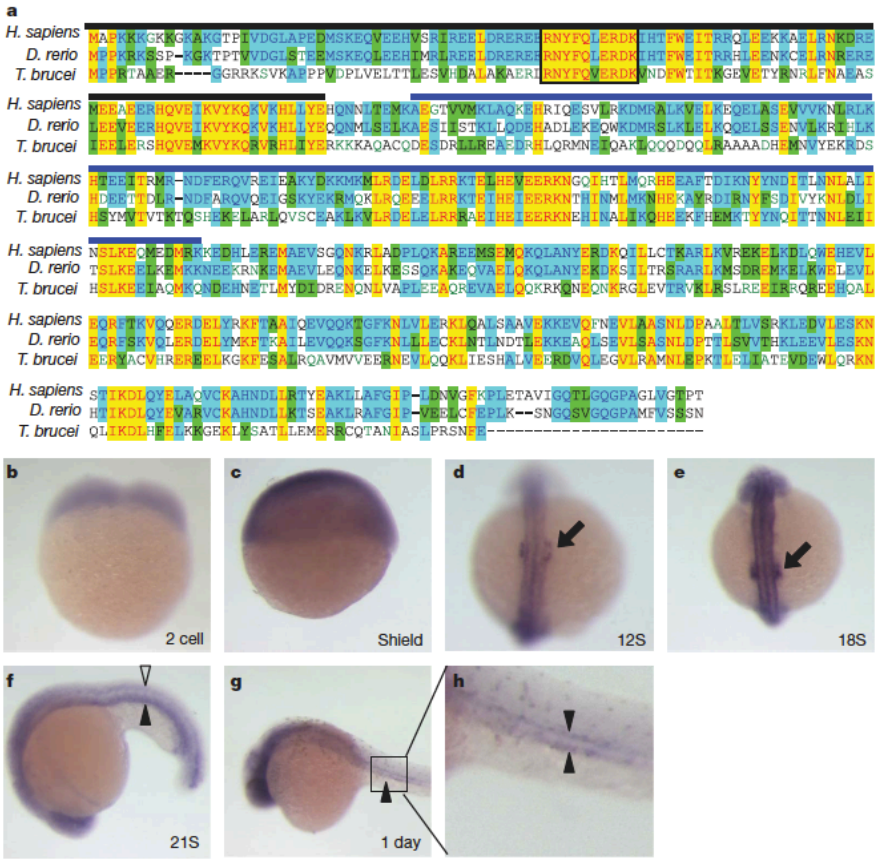

Figure 4.2: ***gas8* is expressed in ciliated tissues. a**. Protein sequence alignment of trypanin/Gas8 from *Homo sapiens*, *Danio rero*, and *Trypanosoma brucei*. Yellow highlighting indicates residues conserved in two homologues and green indicates residues that are conservative substitutions. The boxed region indicates a conserved RNYFQERDK stretch that is found in every known trypanin/Gas8 homologue [162]. The conserved microtubule binding domain "GMAD" and the regulatory domain "IMAD" [163] are indicated with blue and black overlines, respectively. **b**-**h**. *In situ* hybridizations show the *gas8* expression pattern during the first 24 hours of embryonic development. Developing ears (black arrows), neural tube (open arrowhead) and pronephric ducts (filled arrowheads) are shown. Developmental stages are indicated in each panel; S, somite. **h**. An enlargement of the boxed region in **g**.

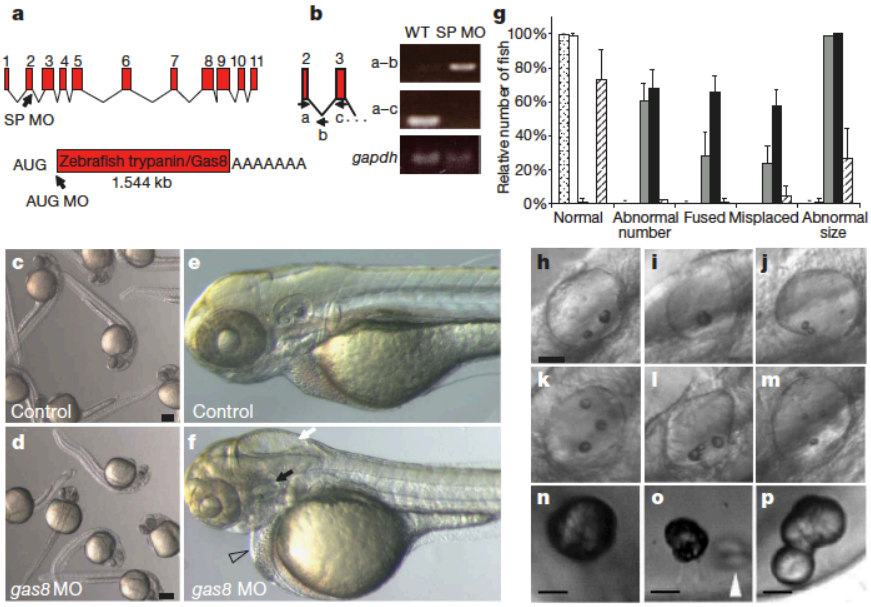

Figure 4.3: ***gas8* morphants exhibit developmental defects. a**. Intron/exon structure of the *gas8* locus, which encodes a predicted 1.54 kb transcript. The positions of splice blocking (SP MO) and translation blocking (AUG MO) morpholino oligonucleotides are shown. **b**. RNA from wild-type (WT) and *gas8* splice morphant embyos was analyzed by PCR with reverse transcription (RT-PCR) using a forward primer (a) in the second exon and a reverse primer in either the second intron (b) or the third exon (c). In the morphant, blocking of the exon-2 splice donor site leads to a 315-bp RT-PCR product with the first primer set and no product with the second primer set. Controls for RT-PCR were provided by amplification of a 95-bp fragment of *gadph*. **c-f**. *gas8* morphants have a variety of defects: overall morphology of controls (**c**) and *gas8* morphants (**d**) at 24 hpf; detail of control (**e**) and morphant (**f**) embryos at 3 days post-fertilization (dpf) showing hydrocephaly (white arrow), pericardial edema (open arrowhead), disorganized somites and otolith abnormalities (black arrow). **g**. Quantitative analysis of otolith defects at 3 dpf. The relative number of fish having the indicated defect is shown for uninjected embryos (stippled bars; $n = 324$, five experiments), embryos injected with control MO (white bars; $n = 167$, two experiments), SP MO (grey bars; $n = 89$, two experiments), AUG MO (black bars; $n = 96$, two experiments) or co-injected with AUG MO and 250 pg *in vitro* transcribed *gas8* mRNA (hatched bars; $n = 225$, two experiments). Error bars are standard deviation. **h-p**. Panels show the spectrum of otolith defects observed in *gas8* morphants at 3 dpf (**h-m**) and earlier times (**n-p**): normal otoliths (**n**); a single otolith (**i**); ectopic, fised and small otoliths (**j-m**); and nasent otoliths in control (**n**, 27 hpf) and *gas8* morphant (**o**, 24 hpf; **p** 27 hpf) ambryos. Scale bars, 30 μm (**h-m**); 20 μm (**n-p**). White arrowhead indicates ectopic and fused otoliths in the *gas8* morphant. Embryos were injected with 6 ng (AUG MO), 4 or 5 ng (SP MO), 6 ng (standard control MO) or 6 ng (mismatch AUG MO) morpholinos.

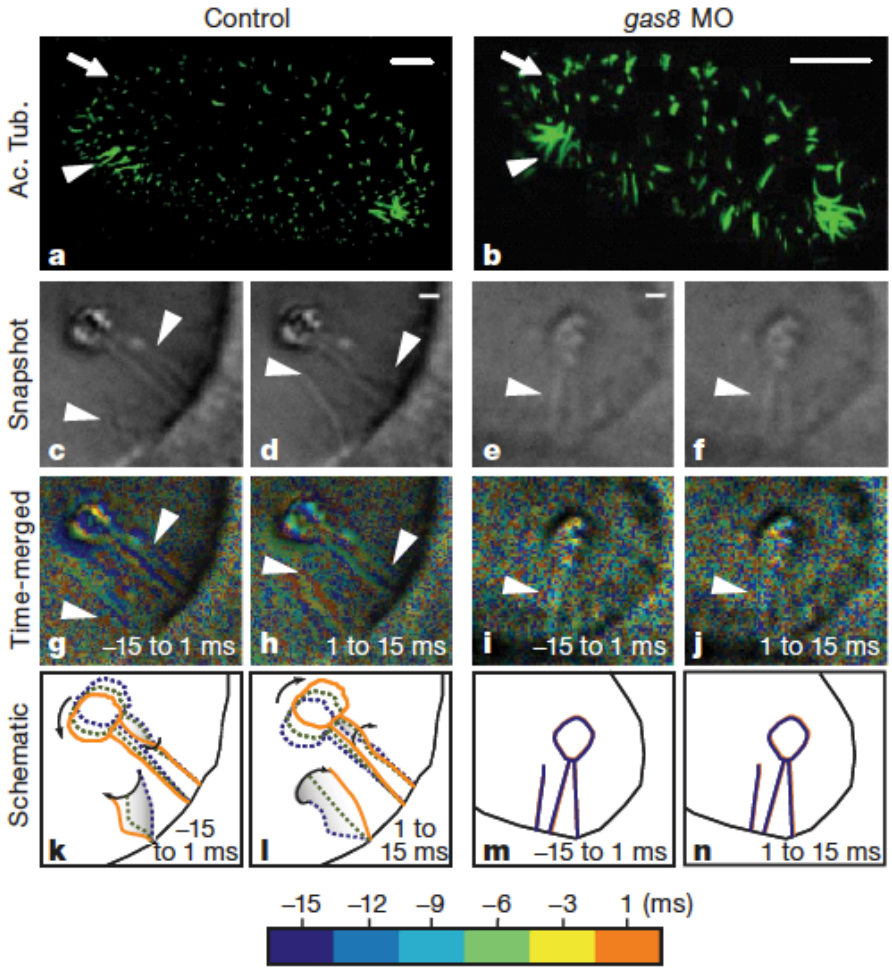

Figure 4.4: **Gas8 is required for tether cilia motility. a**,**b**. Cilia in control (**a**) and *gas8* morphant (**b**) embryos at 24 hpf, visualized by immunofluorescence labeling with anti-acetylated tubulin antibodies (Ac. Tub.). Arrowheads indicate the location of the tether cilia and arrows indicated short cilia. Scale bars, 10 μm. **c**-**n**. Tether cilia are motile in control embryos, but not in *gas8* morphants. Bright-field snapshot images from high-speed videos of cilia in controls (**c**, **d**) and *gas8* morphants (**e**, **f**), showing two steps of the cilia beat cucle with a 15-ms interval (half the period of a beat). **g**-**j**. Time-to-color merge of six frames encompassing 15 ms of the cilia motion immediately preceding the still images shown in **c**-**f**, respectively. Cilia position in time is marked by different colors following the color bar. When merged, moving objects are visible in the corresponding colors, whereas immotile objects only show background noise. **k**-**n**. Diagrams showing cilia and otolith motion in control (**k**, **l**) and immotility in *gas8* morphant (**m**, **n**) embryos with three time points along the half period (15 ms) of the cilia beat cycle (see color bar). Still images from control (**c**, **d**) and *gas8* morphant (**e**, **f**) embryos are taken from movies available upon request. Scale bars, 1 μm (**c**-**f**). Arrowheads point to tether cilia.

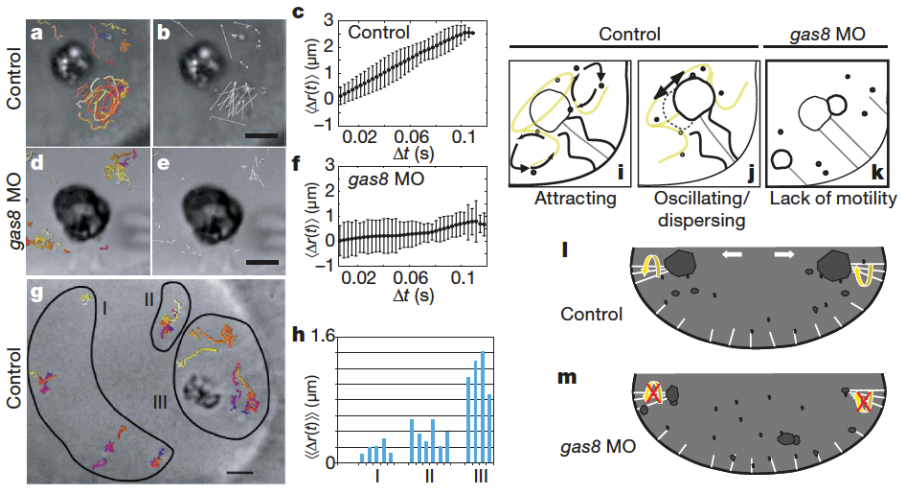

Figure 4.5: **Tether cilia motility drives otolith biogenesis. a-h**. Particle tracking analysis demonstrates that cilium-dependent dluid dynamics drive precursor particle movement near the otolith. In control embryos, particle tracks (**a**) and displacements (**b**) show that particles near the otolith move by non-Brownian motion. Each track has a different color. **d**, **e**. In *gas8* morphants, particle tracks (**d**) and displacements (**e**) show decreased particle displacements in comparison with control. **c**, **f**. Mean particle displacement, $\langle \Delta r\,(t) \rangle$, plotted as a fucntion of time. In control embyros, mean particle displacement is large and non-random, indicating diffusive transport. In *gas8* morphants, mean particle displacement is small and random, indicating Brownian motion only. Error bars indicate the variance in the calculation of $\langle \Delta r\,(t) \rangle$. **g**, **h**. Particle tracking in control embryos shows that particle displacement is directly correlated with position relative to the otolith. **g**. Particle tracks. **h**. Displacements of particles in regions I, II, and III of **g** were calculated as a function of time and the average of the mean displacement, $\langle \langle \Delta r\,(t) \rangle \rangle$, for each particle is shown. Net particle displacement decreases with increasing distance from tether cilia, indicated the reduction of the influence of ciliary beating. **i-k**. Diagrams depicting cilium-dependent otolith biogenesis. **i**. Tether cilia motility creates vortices that attract precursor particles. **j**. Cilia motility further serves to disperse particles locally and causes oscillation of the otolith, together facilitating uniform otolith growth. **k**. In *gas8* morphants, absence of ciliary motility limits particles to Brownian motion. **l**. In wild-type embryos, the net consequence of tether cilia motility is that precursor particles are concentrated near the tethers, preferentially seeding otoliths at two poles of the otic vesicle. **m**. In *gas8* morphants, loss of normal ciliary motility leads to formation of ectopic aggregates, non-uniform otolith growth, and small particles that fail to coalesce into full-sized otoliths. Scale bars, 5 μm.

is measured by the stereocilia underneath, as shown in Figure 4.6. This in turn results in the opening of ion channels and electrical propagation of the signal to the central nervous system. Thus the otolith is in a precarious situation - it is always on the verge of movement by balancing on top of a bed of cilium - the structure of the otolith-cilia complex is crucial to its function. There are two otoliths, one located at the anterior and another at the posterior pole of the inner ear. The otoliths sit on hair cell patches oriented orthogonally to each other, so that the fish may sense in plane and out of plane motion.

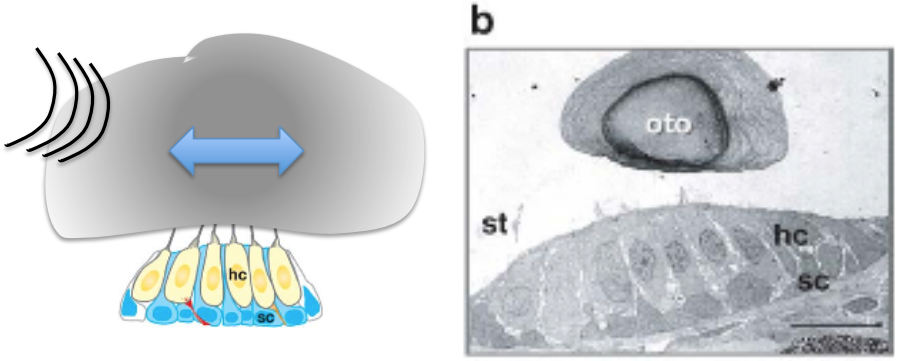

Figure 4.6: **The otolith sits on a bed of stereocilia.** A schematic of the zebrafish otolith (**oto**) as it sits on top of a bed of sterocilia (**st**) (**right**) is shown on the **left**. The stereocilia are projections from hair cells (**hc**). Support cells (**sc**) provide nourishment to the hair cells. The otolith is coupled to the movement of the fish through the fluid in the inner ear cavity. Movement causes deflections in stereocilia which results in the opening of ion channels and second messenger signaling to a cranial nerve. The panel on the **left** was adapted from Nicolson, [164], and **right** is directly from Nicolson, [164]. Scalebar: 7 μm.

The inner ear becomes visible next to rhombomeres 4-6 in the hindbrain about 14 somites, or $\sim$16 hours post fertilization. An initial oval group of cells in the ectoderm forms a ball, after which the cells in the ball become polarized, and their respective nuclei begin to migrate towards the surface of the ball. Shortly thereafter, a lumen starts to form at the center of the ball [165]. The lumen as it starts is slit-like, and enlarges by expanding perpendicular to the major axis of the slit. From our experience, otoliths can first be distinguished as an attachment to tether cilia around 18 hpf. By this time, there is also an appreciable lumen of around 100 μm in the long axis; two-thirds of that value in the short axis. For a review of genetics in inner ear development, see Whitfield et al., [166]. According to Riley et al., [167], the majority of otolith growth takes place between 18 and 24 hpf; after this, growth is slowed substantially as the fish reaches its adult size. We therefore focus on this short 6 hour period in our study.

At 18 hpf, Pisam et al., [168], observed that glycogen particles accumulate in the apical side of the cells lining the lumen; these particles are also found in the cavity, suggesting that glycogen molecules are excreted into the cavity as the so-called "spherules" that one can visualize by light microscopy. At 23 hpf, the nascent otolith appears to be comprised of 3 micron glycogen globules, as indicated by electron microscopy. It is this evidence that suggests that otolith is grown by an accretion of secreted spherules [168]. Presumably, the otolith mineralizes after 24 hpf, but evidence of mineralization in the form of electron microscopy data is not especially apparent until ∼50 hpf. The mineralization process uses calcium and proteins, one major component of which is Starmaker, which shares sequence homology with human dentin sialophosphorprotein (DSPP), involved in the biomineralization of teeth in humans (however, the major anion is carbonate in fish whereas it is phosphate in humans) [169]. Curiously, loss of DSPP results in hearing loss in humans [170]. Knockdowns of *starmaker* result in the inability of the otolith to biomineralize, but instead results in the formation of salt crystals. The *starmaker* knockdown study [169] did not look at otoliths earlier than 24 hpf, but otolith seeding occurs before 24 hpf [167], and mineralization occurs after 24 hpf [168]. In support of this interpretation, morpholino knockdown of *starmaker* preserves formation of an otolith nucleus - just that the otolith does not develop correctly afterwards. Otopetrin1 (Otop1) is a protein that is present during the early stages of otolith nucleus formation, although its role is unknown [171]; knockdown of Otop1 results in the absence of otolith growth between 18-24 hpf, but a crystalline structure forms afterwards. Thus we hypothesize that an organic matrix (first, Otop1, then later, Starmaker) holds together a calcium-based matrix that is secreted after 24 hpf. After 24 hpf, otoliths seem to grow like rings on a tree [171], which supports Riley's data [167] on exponential otolith growth from 18 to 24 hpf, only. The chemical process of otolith formation is far from settled: only a few proteins have been discovered in zebrafish otoliths: Otoconin 90, Otolith matrix protein-1, Otolin-1, Starmaker, Osteopontin, SPARC [172], in addition to Otop1 and Cadherin-11 [173], which interestingly is known to provide cell-cell contacts with strength.

On the one hand, cells are the fundamental unit of multicellular organisms, but on the other hand they also exist in a matrix of protein and minerals, which are crucial to provide structural support in the absence of cell walls. We live in an environment of appreciable gravity, and have to physically defend ourselves from the terrors of nature. Thus, turtles have shells, insects have armor, and we have bones. Without teeth, the succor of a nice

meal would instead be a sour mash of pastes: a lifetime of baby food. The basis of bony objects is the biomineralization process [174], and in fact their material properties and design have probably played an important role in the evolutionary success of vertebrates ([175]). However, the mechanisms that control biomineralization are poorly understood.

4.3.1 Inner ear morphology and cilia motion

The inner ear provides a special example where we may investigate this further - biomineralization occurs concomitant with motile cilia. The otolith-forming region comprises a cluster of beating cilia located next to the tether cilia at each pole of the inner ear [167, 176], as in Figure 4.4, a. Previous experiments showed that motile cilia are essential for normal otolith positioning, proper spherules seeding and agglomeration [167]. Flow differences at the poles of the inner ear have been proposed to concentrate spherules around the tether cilia such that their aggregation is spatio-temporally controlled to inhibit random clustering of the spherules [161, 167]. Here, we use a flow probe approach with optical tweezers and a physical model based on Stokes flow to explain the observed hydrodynamical processes as the otolith assembles. We show that flow in the core of the cilia-mediated-vortex has an inhibiting influence on spherule agglomeration and that the vortex lines outline a negative shape of the otolith. A surprising consequence of such hydrodynamics is that otolith self-assembly is the result of the balance between Brownian motion and cilia driven flow, leading to the conclusion that this balance is responsible for the shape of the otolith. Alternatively, cilia motion might set a mixing flow necessary for increasing spherules-spherules contacts and, as a consequence, act as a catalyst for agglomeration. A physical theory uniting otolith defect based on flow dynamics and cilia strength is lacking, and whether cilia affect growth and otolith shape is also unknown.

First, some quantification of the morphology of the inner ear and beating pattern of the motile cilia at $\sim$22 hpf is in order. At this stage in development, the inner ear is ovoid in shape with a major axis of $\sim$100 μm, and minor axes around two-thirds that size, as shown in Figure 4.7, A. Along with the cells that line the cavity are protrusions of immotile cilia; near the anterior and posterior poles are a few (usually 2) long tether cilia around 10 microns in length, which are also immotile but nucleate the nascent otolith. We found that the beating cilia density next to the tether cilia can vary from one to three, each being contained in an area very close from the growing otolith (10 microns $\pm$ 4). Beating cilia

can be embedded within the growing otolith or in contact with the otolith (56%). Thus the otolith organizes at a position slightly displaced from the beating cilia, as in Figure 4.7, B and F. In this condition, the circular path of a beating cilium has a radius of $R = 9 \pm 3\mu$m and the time for one revolution was $\sim$ 33 ms corresponding to a frequency of 44 $\pm$ 4 Hz. The inner ear cilia frequency is higher and their amplitude decreased, as compared to free beating cilia (24 $\pm$ 4 Hz and 13 $\pm$ 2 μm amplitude) at the same stage. We also noticed that a majority of beating cilia are circling counterclockwise (top view), yet, clockwise rotation is occasionally seen (23%, n=15). No major difference was seen between anterior and posterior clusters of beating cilia in the inner ear. We then analyzed the three dimensional motion of the free beating cilia by making multiple z sections, as shown in Figure 4.7, F and G. Overall, cilia motion depends on its length, orientation and frequency, values that varied little from animal to animal. Accordingly, we found that the three dimensional motion was consistently based on a three phase beat, describing a stroke and recovery stroke at each cycle, as seen and schematized in Figure 4.7, C-G. These observations show that the self-organizing properties of growing otoliths rely on a system where the beating cilia number, orientation and rotation may vary from embryo to embryo. Nevertheless, the location of the beating cilia and the rotation frequency seem constrained, suggesting that these features have been strongly selected and constitute the most important parameters for otolith self-assembly.

4.3.2 Hydrodynamic models of the inner ear

We developed a physical model that captures the essential features of flow inside the inner ear by simulating cilium-induced flow inside a spherical cavity. The relative strength of this deterministic flow relative to stochastic motion of the spherules is parameterized by the Peclet number, $Pe = v_{\max} l/D$, ($v_{\max}$ is the maximum velocity in the system, l- the diameter of the observed particle, and $D_{\max}$- the maximum of the diffusion tensor). A system with $Pe \ll 1$ is primarily diffusive whereas a system with $Pe \gg 1$ is advective, dominated by deterministic flow. Diffusive transport of the spherules is included using Brownian dynamics and we adjust Pe most easily through changing the frequency of the cilium, which is directly related to $v_{\max}$.

Since the Reynolds number is $\sim$0.001, and the cilia are much smaller than the overall scale of the cavity, we approximate the advected fluid motion in the inner ear with Stokes

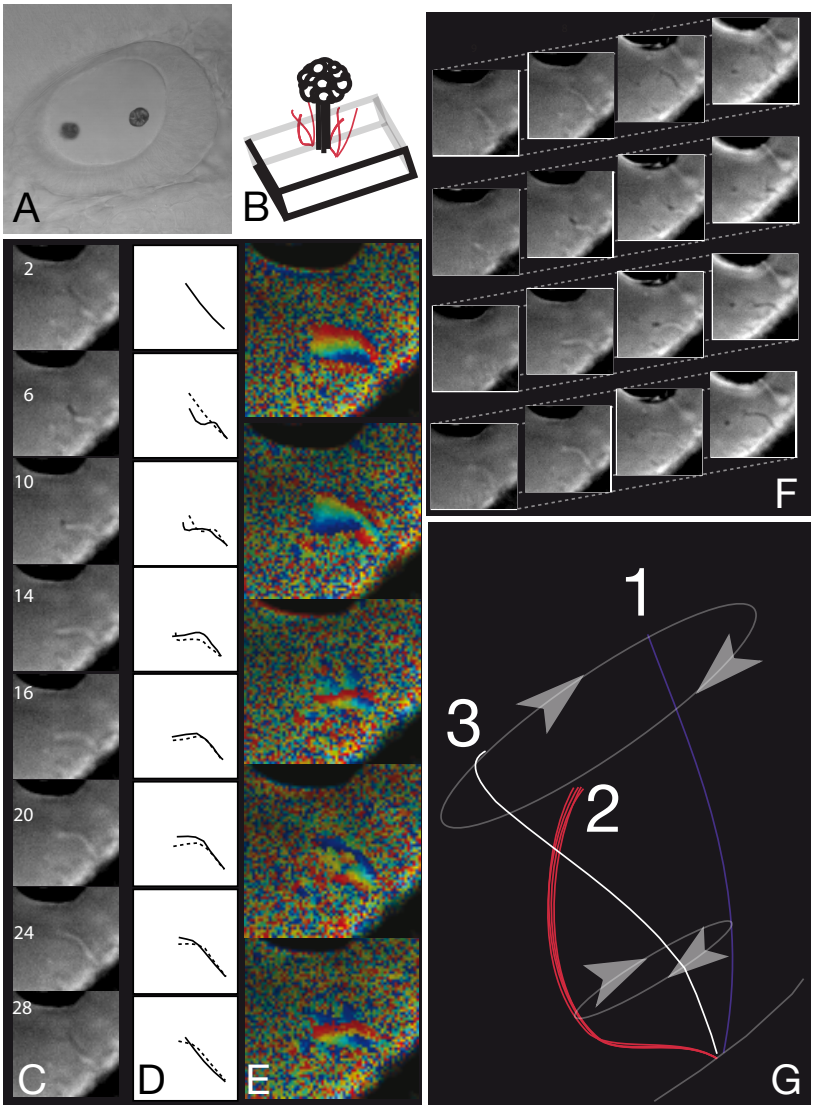

Figure 4.7: **Topology of the inner ear of the zebrafish.** **A**. Side view of the inner ear at 24 hpf. **B**. Schematic 3-D view of the otolith nucleus. Red line represent beating cilia next to the otolith. **C-E**. Camera lucida of the motion of one cilium next to the otolith. Image of a beating cilium over one cycle of rotation (**C**). Representation of the cilium position in space during one revolution manually extracted from **C** (**D**). Dotted lines represent cilium position in the previous step of motion. Diagrams showing cilia motion along a third of the period of the cilium beat cycle (**E**) showing cilium flexibility during the process. (**F**, **G**) 3-D reconstruction of the motion. Visualization of the motion at different depths showing the amplitude of the cilium during a full beat (**F**). Manual reconstitution of the three dimensional motion from **F** (**G**).

flow, $-\nabla p+\mu\nabla^2\mathbf{v}=\mathbf{F}_i\delta\left(\mathbf{x}-\mathbf{x}_i\right)$ together with the constraint of incompressibility, $\nabla\cdot\mathbf{v}=0$. p is the pressure, μ is the viscosity, $\mathbf{v}$ the velocity field, and $\mathbf{F}_i$ the magnitude of the ith cilium's effective force located at $\mathbf{x}_i$. For the purposes of our model, $i=1$. The equation admits analytical solutions inside a sphere [177], which we choose to represent as the inner ear cavity. The Greens function solution to Stokes flow is composed of a singular term and a regular term; i.e., the Oseen tensor, which describes fluid response to a Stokeslet in an unbounded fluid, and image terms that account for the no-slip/no-penetration boundary conditions in the system. The velocity field is thus

$$\mathbf{v}\left(\mathbf{x}\right)=\frac{\mathbf{F}_i}{8\pi\mu}\cdot\left(\mathbf{G}^s\left(\mathbf{x}-\mathbf{x}_i\right)+\tilde{\tau}\right) \tag{4.1}$$

where $\mathbf{G}^s$ is the Oseen tensor (superscript s denotes Stokeslet),

$$\mathbf{G}^s\left(\mathbf{x}-\mathbf{y}\right)=\frac{\delta}{\left|\mathbf{x}-\mathbf{y}\right|}+\frac{\left(\mathbf{x}-\mathbf{y}\right)\left(\mathbf{x}-\mathbf{y}\right)}{\left|\mathbf{x}-\mathbf{y}\right|^3}, \tag{4.2}$$

μ is the viscosity (here, 0.001 Pa·s) and

$$\begin{aligned}\tilde{\tau} \;=\;& e_m e_k\left[\frac{R\left(R^2-3x_i^2\right)}{2x_i^3}\mathbf{G}^s_{jk}\left(\mathbf{x}-\bar{\mathbf{x}}_i\right)-\frac{R^3\left(R^2-x_i^2\right)}{x_i^4}e_l\nabla_l\mathbf{G}^s_{jk,l}\left(\mathbf{x}-\bar{\mathbf{x}}_i\right)-\right.\\ &\left.\frac{R^3\left(R^2-x_i^2\right)^2}{4x_i^5}\nabla^2\mathbf{G}^s_{jk}\left(\mathbf{x}-\bar{\mathbf{x}}_i\right)\right]+\left(\delta_{km}-e_k e_m\right)\left[\frac{R\left(3x_i^2-5R^2\right)}{2x_i^3}\mathbf{G}^s_{jk}\left(\mathbf{x}-\bar{\mathbf{x}}_i\right)+\right.\\ &\left.\frac{R^3\left(R^2-x_i^2\right)^2}{4x_i^5}\nabla^2\mathbf{G}^s_{jk}\left(\mathbf{x}-\bar{\mathbf{x}}_i\right)\right]+\frac{R^3\left(R^2-x_i^2\right)}{x_i^4}e_k\left(\delta_{lm}-e_l e_m\right)\nabla_l\mathbf{G}^s_{jk,l}\left(\mathbf{x}-\bar{\mathbf{x}}_i\right)-\\ &\frac{3R\left(x_i^2-R^2\right)}{x_i^2}\frac{\left(\delta_{jm}-e_j e_m\right)}{\left|\mathbf{x}-\bar{\mathbf{x}}_i\right|}+\left[\left(\frac{x}{R}\right)^2-1\right]\left(\delta_{km}-e_k e_m\right)\frac{\partial\varphi_k}{\partial x_j}\end{aligned} \tag{4.3}$$

where

$$\varphi_k \;=\; -\frac{3R\left(x_i^2-R^2\right)}{2x_i^2}\frac{\mathbf{x}_k}{\left|\mathbf{x}-\bar{\mathbf{x}}_i\right|}\frac{\frac{x}{R}-R^2\bar{x}_i\cos\nu+\left|\mathbf{x}-\bar{\mathbf{x}}_i\right|\cos\nu}{Rx\bar{x}_i\sin^2\nu}; \tag{4.4}$$

ν is the angle between $\mathbf{e}$ and $\mathbf{x}_i$. x (or x_i) denotes the magnitude of $\mathbf{x}$ (or $\mathbf{x}_i$). $\mathbf{x}_i$ is the location of the Stokeslet; $\bar{\mathbf{x}}_i$ is the position of the image Stokeslet, defined by $\bar{\mathbf{x}}_i=\frac{R^2}{\left|\mathbf{x}_i\right|}\hat{\mathbf{x}}_i$. δ is the Kroenecker delta. The radius of the inner ear is R ($R=50$ μm) (see Figure 4.8, B). $\mathbf{F}_i\delta\left(\mathbf{x}-\mathbf{x}_i\right)$ is a force (called Stokeslet) due to the ith cilium motion, discussed below. Of note is that the leading order behavior is dominated by an inverse distance relationship, as

can be seen in $\mathbf{G}^s$, Equation 4.2. This Green's function for Stokes flow inside a unit sphere is given in [177]; we present it here (Equation 4.3) for arbitrary sphere size.

However, Equation 4.1 above is purely advective; we are also interested in modeling movement of the spherules caused by thermal motion. Brownian motion imparted by temperature also must obey boundary conditions of the system, as the size of the noise is proportional to the product between drag and temperature; i.e. $\gamma k_B T$, and the drag must go to infinity at the surface of the inner ear sphere to satisfy the no-slip/no-penetrate boundary condition. The precise form of the drag tensor is unknown inside a sphere, however, so we instead approximate inside the sphere with an infinite wall as a first order correction to the free space drag:

$$\tilde{\gamma} = \frac{\delta}{6\pi\mu a} + \mathbf{b} \tag{4.5}$$

where $\mathbf{b}$ is the Green's function that decreases the sphere's mobility through hydrodynamic coupling to a wall [178]. Here, a is the radius of the particle executing Brownian motion, either spherules (0.5 μm), or the cilium radius (0.05 μm). The hydrodynamic friction is given by

$$\tilde{\gamma}_i = \frac{1}{6\pi\mu a_i}\left[\delta + \frac{9a_i}{16\left(R - x_i\right)}\begin{pmatrix} 1 & & \\ & 1 & \\ & & 2 \end{pmatrix}\right]. \tag{4.6}$$

In this manner, the drag is underestimated which leads to an overestimate of the local diffusion coefficient used when computing Brownian motion. Our model for the cilium

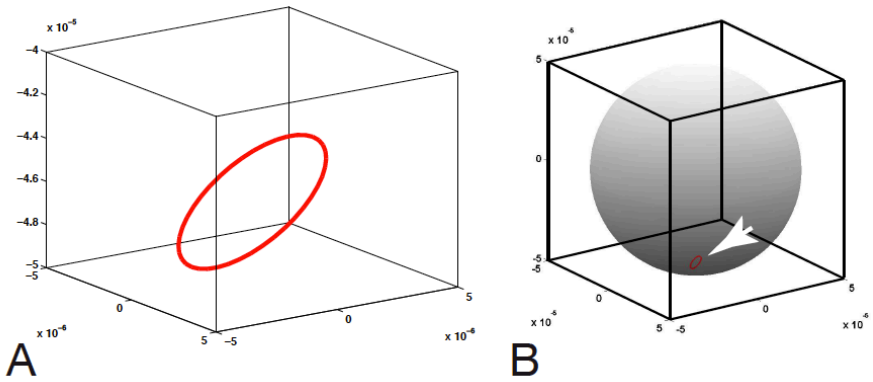

Figure 4.8: **Cilium and inner ear model. A**. The model uses a simplified representation of the cilium by a small sphere moving on a tilted elliptical trajectory. **B**. The cilium is positioned in a sphere, representing the inner ear, in order to analytically calculate the resulting flow field.

consists of a small sphere, which traverses an elliptical track, as seen in Figure 4.8, A. The velocity field is computed through Equation 4.1; $\mathbf{F}_i$ is the force generated by a cilium undergoing oscillations according to the following trajectory:

$$\mathbf{x}_i = \begin{pmatrix} x_i + A\cos\phi_i \\ y_i + B\sin\phi_i \\ z_i + C\cos\phi_i \end{pmatrix}, \tag{4.7}$$

where the center of the oscillation is at (x_i, y_i, z_i) and the coefficients in 4.7 cause the cilium to trace out an ellipse [176]. A, B, and C were 2.5 μm; (x_i, y_i, z_i) was at (0, 0, -45 μm). The radius of the ellipse traced out by $\mathbf{x}_i$ was assumed to be 1.25 μm. The cilium traveling on this ellipse experiences increased drag as it nears the surface of the inner ear-sphere, so its equation of motion is

$$\mathbf{F}_i = \tilde{\gamma}_i \mathbf{v}_i \tag{4.8}$$

where

$$\mathbf{v}_i = \frac{\mathbf{t}_i f_o}{k\hat{\mathbf{t}}_i + \hat{\mathbf{t}}_i \tilde{\gamma}_i \mathbf{t}_i} \tag{4.9}$$

and $\mathbf{t}_i = d\mathbf{x}_i/d\phi_i$. $\tilde{\gamma}$ is given in Equation 4.6. The radius of the cilium was 125 nm [179]. Normal forces arise to keep the cilium on track $\mathbf{x}_i$, so in a simplified model the force obeys

$$\hat{\mathbf{t}}_i \cdot \mathbf{F}_i = f_o - k v_i, \tag{4.10}$$

where constant k denotes that the cilium, which generates a tangential force $\mathbf{f}_i = f_i \hat{\mathbf{t}}_i$, is linear in velocity; $f_i = f_o - k v_i$. This cilium model was proposed by Vilfan et al., [176]; our contribution is the implementation of this cilium inside the inner ear-sphere. We chose values of f_o and k (k-, constant at 1×10^{-13} kg/sec; f_o- from 1×10^{-14} to 1×10^{-11} N) such that the oscillation frequency spanned from 0 to 540 Hz. Reported values of f_o, the maximum amount of force a cilium can generate at the tip, are 62 $\pm$ 18 pN, so our chosen parameters are close to physiological [180]. We obtained the local average velocity by integrating the velocity over one period of cilium oscillation. Since the field velocity, Equation 4.1, is proportional to $\mathbf{F}_i$, and $\mathbf{F}_i$ is in turn proportional to the cilium velocity, Equation 4.8, we simply change f_o by a multiplicative factor in order to adjust Pe.

We found that the details of the cilium (tilt, major/minor axis ratio) were unimportant

for producing a flow pattern that advects towards the cilium - as long as the cilium contained motion along the z-axis. For the cilium parameters given above, Equation 4.7, the deterministic flow field is shown in Figure 4.9. Moreover, we confirmed that $Pe \ll 1$ led to purely diffusive behavior, and when diffusion was turned off, that particles simply followed the flow lines.

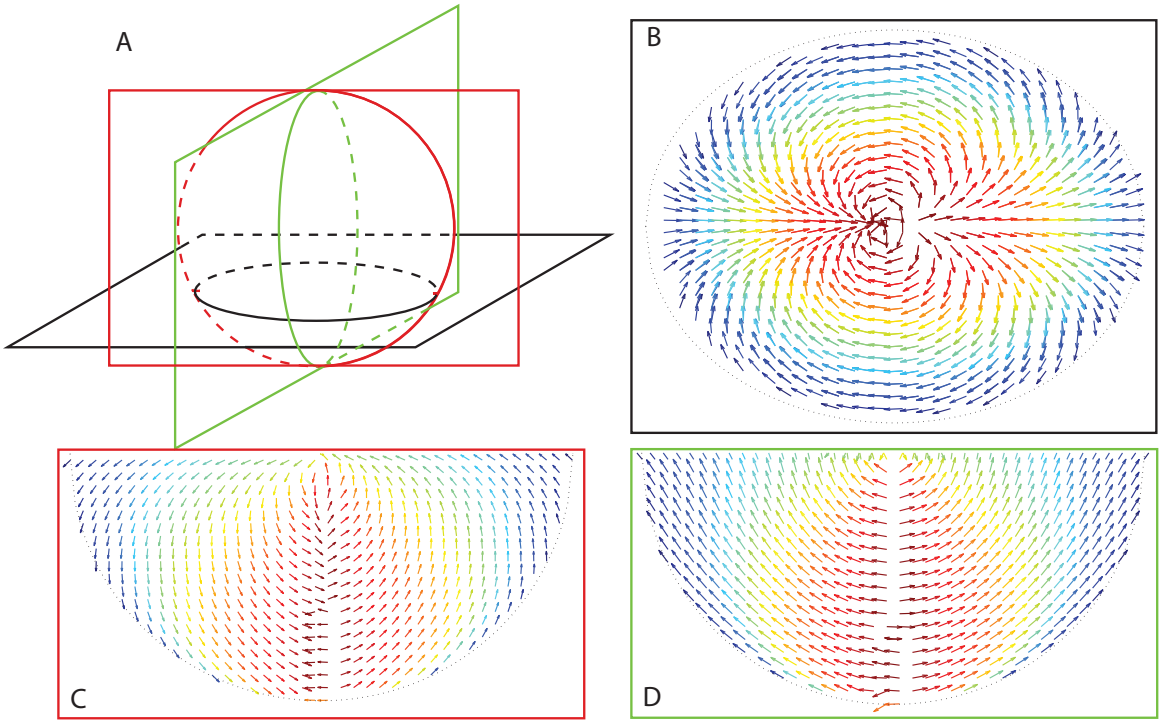

Figure 4.9: **Time-average flow field inside the inner ear-sphere.** The flow field was determined by computing Equation 4.1 on a grid inside the inner ear-sphere. The plotted vectors were time-averaged velocities over one period of cilium motion. Cilium parameters are described in the text. The cilium is located at the bottom of the sphere in (**A**). **A**. The planes shown in (**B**), (**C**), and (**D**). **B**. x-y plane, outlined in black in (**A**). The flow field is reminiscent of the electric field lines of an oscillating dipole. **C**. x-z plane, outlined in red in (**A**). **D**. y-z plane, outlined in green in (**A**). Only the bottom half ($z < 0$) of the flow fields are shown in (**C**) and (**D**); the upper half ($z > 0$) are mirror images, but at slower speeds. Red colored arrows represent the fastest speeds; blue colored arrows are the slowest speeds. The maximum speed is determined as $v_{\max} = r\omega$, where r is the length of the cilium (here, 1.25 μm), and ω is the frequency (see Appendix, Section A.3.2.4 for more details). As expected from Equation 4.1, the velocity is zero at the boundaries, satisfying the boundary conditions to Stokes flow.

For the simulation, we isotropically seeded 1 μm spherules near the wall of the cavity as a starting condition, mimicking glycogen particle secretion. Their position in the next

instant of time is given by

$$\Delta \mathbf{x}_j = \int_0^{\Delta t} \int_0^{2\pi} \mathbf{v} d\phi dt + N(0,1) \sqrt{2 \frac{k_b T}{\tilde{\gamma}(\mathbf{x}_j, a_j)} \Delta t} \tag{4.11}$$

where $N(0,1)$ is a normal random variable with mean 0 and standard deviation 1 [22]. Subscript j denotes the seeded particles. Simulations were run until a statistical steady state was reached (typically, hundreds of seconds). The particle flux near the cilium is enhanced non-linearly in accordance with the Peclet number, which is directly proportional to the frequency of the cilium, as shown in Figure 4.10. For low Pe, the only way for particles to reach the position of the tether cilia, which are physically adjacent to the beating cilium, is via Brownian motion. However, as the frequency of the cilium is "turned on", the time to capture for all particles in increased. Typical Pe in zebrafish inner ears is ∼50-100.

The model predicts that the spherule population can be hydrodynamically focused by cilium-mediated advection according to the Pe in a non-linear manner. The mechanism for this is deduced from Figure 4.9, B. Particles in the x-y plane shown experience a "dipole"-type of flow field, which results in an effective increase in the residence time particles spend near the cilium, since the closed streamlines have a smaller radius and are faster near the cilium. At $Pe \sim 0$, there is only Brownian motion, and no focusing occurs. At high Pe ($Pe \to \infty$), particles simply follow their streamlines, and so no focusing occurs. At intermediate Pe, particles still advect but also undergo Brownian motion; thus, particles are advected but are able to transition between streamlines. Then in the intermediate Pe case, particles near the cilium undergo relatively pure advection ($Pe \sim 100$) but rapidly transition to Brownian motion microns away, since the Green's function decays as $1/r$. This means that particles are drawn in from the far field into the advection zone, but that diffusion supplies new particles into this area of increased residence time, resulting in a focusing of particles. Since the probability of leaving the advection zone is the same as the probability entering (Brownian motion is roughly isotropic), the increased residence time in the advection zone is itself transient. To put it another way, particles are able to diffuse into areas of high Pe, and are then maintained on the streamlines for a while before randomly walking out. Particles moving a streamline at velocity v will, on average, move a distance $\langle \Delta x \rangle = v \langle \tau \rangle$ where $\langle \tau \rangle = 1/k$, the mean waiting time before leaving a streamline, assuming that the probability of leaving the streamline in some small unit of

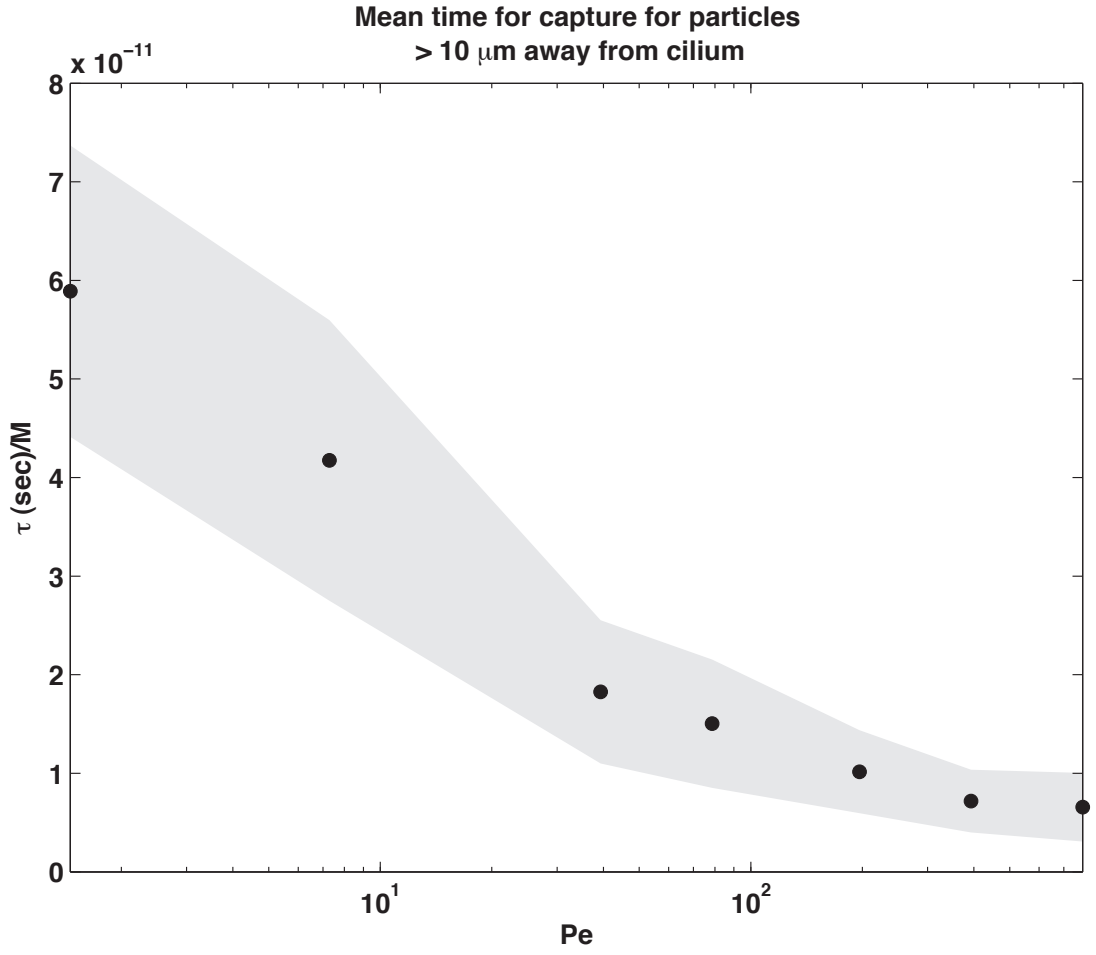

Figure 4.10: **Mean time to capture for particles as a function of** Pe**.** The time to capture per molar volume of particles more than 10 μm away from the beating cilium, was determined as a function of Peclet number. For $Pe \sim 0$, the only method of capture is through a random walk. For advected particles, the chance of capture is greatly enhanced. The gray shaded area is the standard deviation for time to capture.

time is $k\Delta t$. $k \sim D/A$, D is the diffusion constant, and A is some area. Thus the number of times a particle will circulate on a closed streamline of radius r is $\langle N_{circ} \rangle = \frac{\langle \Delta x \rangle}{2\pi r} = \frac{v}{2\pi r k}$. Intuitively, this makes sense: particles that are traveling on streamlines of smaller radius and faster velocity will circulate more times before they randomly walk away than particles that move on slow streamlines of large radius. Thus we can write $\langle N_{circ} \rangle \sim \frac{PeA}{2\pi r l}$. This is shown in a simulation, snapshots of which are shown in Figure 4.11. Because of the special geometry of the cavity, spherules in the far field are preferentially localized above beating cilia, suggesting that vortical flow can act as a spherule attractant and break the intrinsic symmetry of a diffusion-only system. Thus, cilia can mediate hydrodynamic focusing at far field.

All dimensions in Figure 4.11 are real, as given in this section. The Peclet number for the montage shown is 750; frequency of the cilium was 540 Hz. Similar effects exist for lower cilium frequencies - at *in vivo* frequencies (∼30 Hz), a lower steady state accumulation of particles is reached, since the Pe is 40. We verified that $Pe = 0$ resulted in no focusing of particles, and $Pe \to \infty$ only had particles traveling on their streamlines. The use of this 540 Hz example was to show the more extreme effects of cilium-mediated advection. Simulation movies at different Pe accompany this document.

4.3.3 Experimental Results

4.3.3.1 Probing the local mean squared displacement using blinking optical traps

Collectively, these theoretical data anticipate that the localization and diffusion behavior of the spherules is non-linearly balanced by cilium frequency. More generally, the simulations suggest that the agglomeration predicted by Pe for any reduced cilia frequency, which could be due to exogenous knock-down or a dynein mutation *in vivo*, could dramatically change spherule behavior [161]. Yet, it is unclear what flow regimes are dictated by beating cilia *in vivo* in constrained, non-ideal geometries. To address this point, we measured the flow hydrodynamics next to the beating cilia. To locally access the flow field, we optically trapped spherules and assessed their mean-squared displacement behavior, as shown in Figure 4.12, A-E, using the blinking optical traps technique (BOTs) [181], schematically presented in Fig. 4.12, D-H.

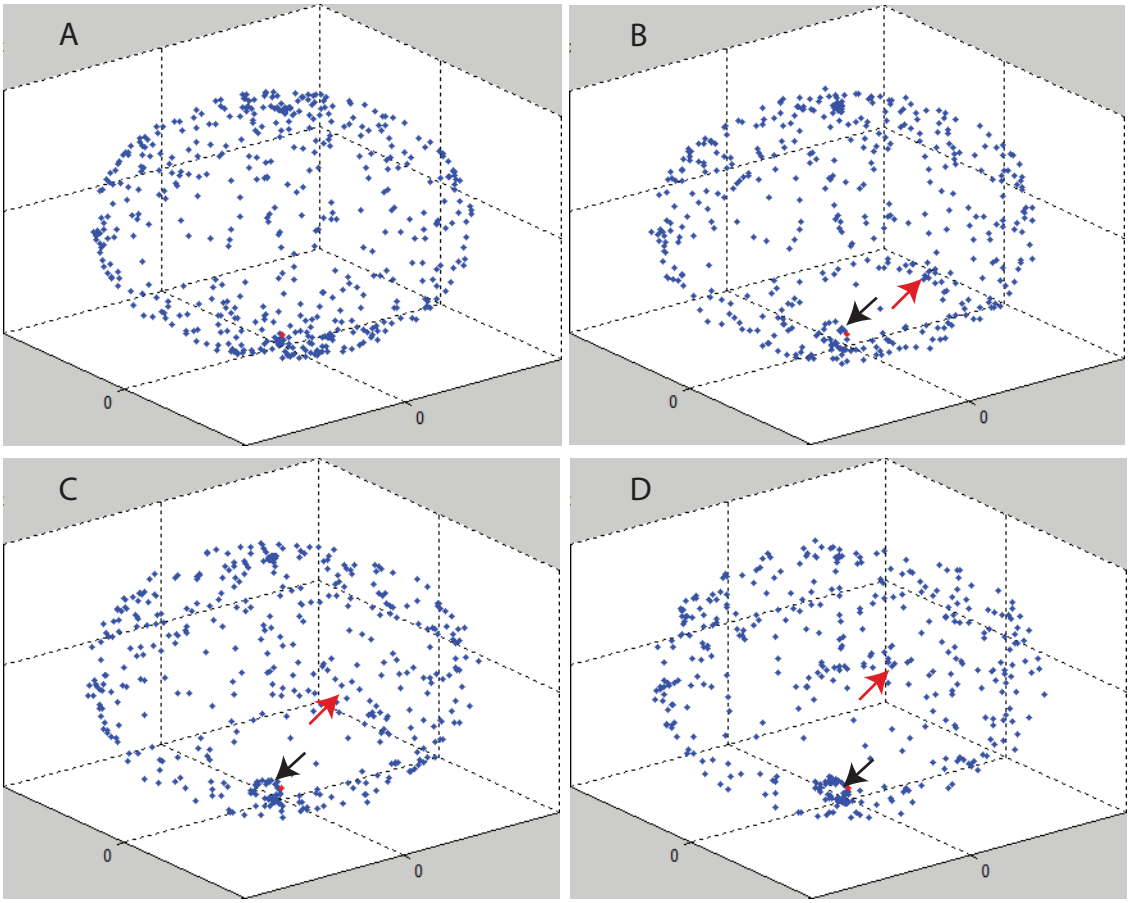

Figure 4.11: **Evolution of particle distribution in the inner ear-sphere.** 500 particles are initially randomly seeded along the border of the inner ear sphere, as a simulacrum of border cells releasing glycogen particles [168], as shown in (**A**). **B**. After 10 seconds, a slight focusing of particles (black arrow) can be seen near the location of the beating cilium (red dot). The red arrow shows particles streaming away, demonstrating advection away from the cilium concomitant with the focusing of particles. **C**. 20 seconds after (**A**) and 50 seconds later (**D**).

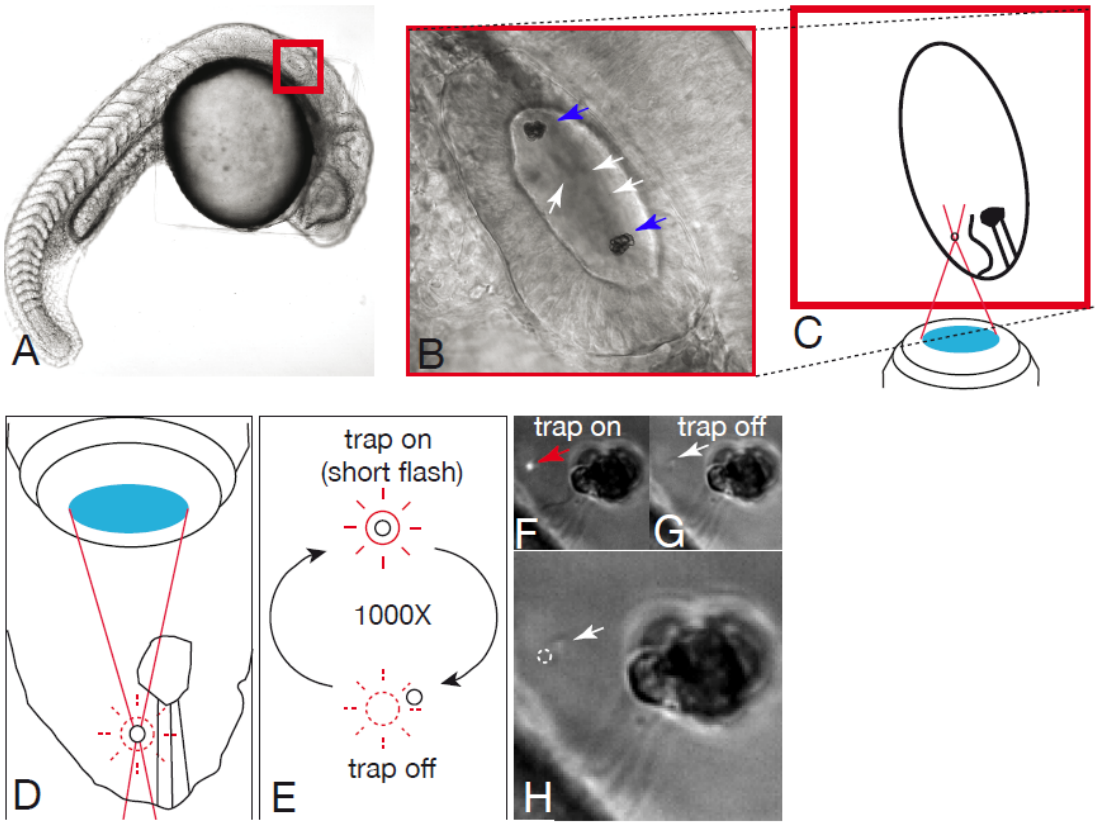

Figure 4.12: **Probing inner ear hydrodynamics at work during otolith biogenesis using blinking optical traps.** **A** Side view of a zebrafish embryo at the stage of optical tweezing. The red box outlines the inner ear. **B** Magnified version of the inner ear corresponding to the box in (**A**). White arrows point to spherules, which are numerous at that stage, and blue arrows point on the otoliths at the nucleus stage. **C**, **D**. Schematic view of the tweezing approach depicting the role of focused light in positioning spherules in the inner ear (**C**) and next to the otolith (**D**). **E**-**H**. Trap and release approach for probing the cilia mediated flow. Schematic view of the optical tweezing depicting the sequence of trap and release used to generate multiple recordings of the flow at a single point inside the inner ear (**E**). *In vivo*, spherules are trapped (**F**) and released (**G**) so that the overall motion of the particle indicates if a directed flow is generated in this point (**H**). The white circle indicates the location of trapping and the white arrow point to the spherules position .002 seconds after release.

A 1064 nm laser was used in conjunction with an acousto-optic deflector (AOD) and 60x 1.2 NA water immersion objective. A custom Labview program controlled the frequency modulation. The switching frequency was 10 Hz at a 50% duty cycle. The laser output power (at the back focal plane of the objective) was 100 mW. Imaging frame rate was 492 fps. Since the camera was not synchronized to the laser pulses, we used a moving threshold algorithm to ascertain which frame contained laser pulses, and which frames were pulse-free - the laser was slightly visible on the camera. After discarding frames with the laser on, we tracked the center of mass of the trapped particles (there were in all likelihood more than one particle trapped at a time) by using a least-squares fit to a 2D Gaussian function and recording the displacement as a function of Δt, the frame rate of the camera. We assumed that the width of the 2D Gaussian fit represented the diameter of the particles trapped. Note that the maximum range of time that can be explored by this technique is limited by the blinking frequency; here, 10 Hz, or 100 ms. The maximum range is also limited by the distance a released particle moves in the time when the trap is off: if the particle moves too far away, it cannot be trapped again. Thus the BOTs technique inherently measures short-time dynamics, in contrast with the 'trap and delivery' technique, discussed in Section 4.3.3.2, which measures time-averaged dynamics.

We now attempt to model the mean-squared displacement of a particle undergoing Brownian motion whilst fluidically-coupled to the motion of a cilium some distance away. A Brownian particle undergoing external perturbation obeys the following Langevin equation:

$$m\dot{v}_d = -\gamma\left(v_e + v_d\right) + 2\gamma k_B T\Gamma\left(t\right) \tag{4.12}$$

where we only consider one dimensional motion for simplicity and only consider free space Stokes drag $\gamma = 6\pi\mu a$, a being the radius of a typical spherule. v_e is any drift velocity induced by the cilium and v_d is the velocity of the particle itself. We avoided performing BOTs next to the cells lining the inner ear due to boundary effects that would modulate drag. The local disturbance generated by the velocity of a cilium can be approximated by a sinusoidal function:

$$v_e = \sigma_l \sin\left(\omega t + \phi\right) + b, \tag{4.13}$$

where ω is the frequency of the cilium, ϕ is the phase of the cilium, and b is a possible global flow. σ_l is the local oscillation amplitude transduced through the fluid by the cilium

(subscript l means "local"); i.e., σ_l determines the degree of fluidic coupling. A sinusoidal model of cilium velocity is an accurate model, as a typical trace of the cilium tip executes approximately sinusoidal motion, as shown in Figure 4.13.

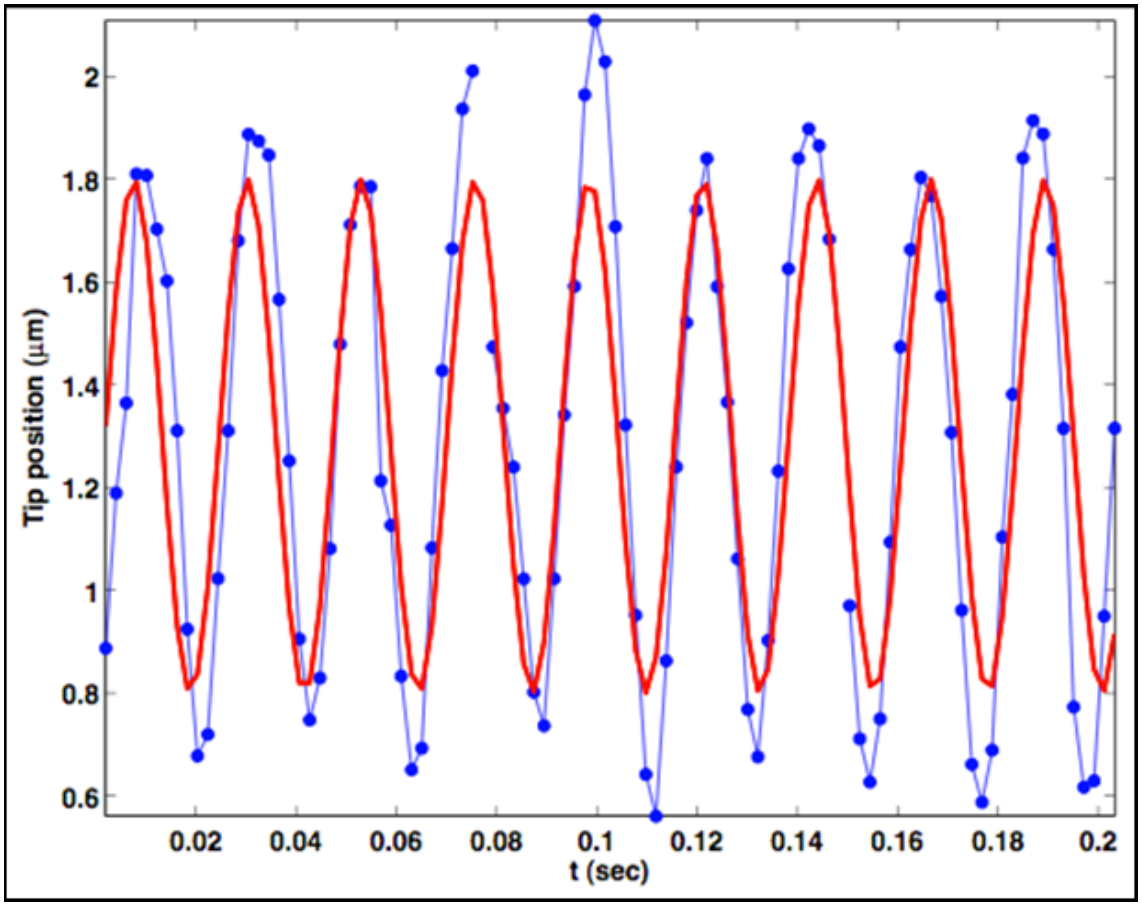

Figure 4.13: **Cilium motion is approximately sinusoidal.** Blue dots mark the position of a typical motile cilium tip in the inner ear, imaged perpendicular to its axis of rotation. The red line is a plot of a sinusoidal function overlayed on top (no fitting). This graph displays the motion of the cilium in one axis only; the perpendicular axis behaves in a similar fashion; see Figure 4.7.

The mean squared displacement is usually calculated as

$$\langle x^2\left(t,\phi\right)\rangle = \int_0^t \int_0^t \langle v\left(t_1\right) v\left(t_2\right)\rangle dt_1 dt_2. \tag{4.14}$$

However, since we do not know when the BOT measurement started relative to the phase

of the cilia, we must integrate the phase:

$$\langle x^2(t)\rangle = \int_0^{2\pi} \langle x^2(t,\phi)\rangle d\phi. \tag{4.15}$$

The result is

$$\langle x^2\rangle = 2Dt + \frac{a_0^2}{\omega^2}(1-\cos\omega t)\left[1+\left(\frac{\rho\omega}{6\pi\mu}\right)^2\right]^{-2} + b^2t^2. \tag{4.16}$$

To measure the flow forces generated in this area, we extracted physical parameters from the mean squared displacement (Fig. 4.16, A and B) according to 4.16, where D is the diffusion coefficient, a_0 is the local amplitude of the oscillating velocity (related to σ_l), ω is the frequency of the oscillation, ρ is the density of the trapped material, and b is an external constant velocity representing drifts or global flows in the system. We assumed that the viscosity μ was constant.

We first verified this equation by performing Brownian dynamics simulations (according to [22]) in an oscillating field of force, the statistics of which are shown in Figure 4.14. The Langevin equation (Eqn. 4.12) was simulated for seven different velocity amplitudes of oscillatory motion (σ_l), and the mean-squared displacement was plotted (black dots, in Figure 4.15). The theoretical mean-squared displacement equation (Eq. 4.16) computed using the parameters for simulation was plotted in red lines, Fig. 4.15. The match requires no free parameters. Since the theory matches the simulation well, we applied equation 4.16 to our BOTs data to extract local parameters (a_0, ω, D, ρ, b) assuming the size of the particle could be measured optically. The term that interests us the most is a_0 which describes the strength of the fluidic coupling to cilia at the measurement location.

Equation 4.16 allows us to quantify the degree of influence the cilium exerts on the surrounding fluid, the results of which are plotted in Figure 4.16, C. The fitted parameters (see Fig. 4.17, A, for an example) were strikingly similar to expected measured parameters *in vivo* and reported values in the literature (amplitude a_0, frequency ω, weight ρ, and diffusion coefficient D; see Fig. 4.17) thereby allowing us to use the a_0 parameter (Fig. 4.17, B) with confidence. The values reported in Figure 4.17, C, are similar to values reported in Section 4.3.1. Note that these are distributions taken over many embryos at many different field points. Diffusion coefficients (Fig. 4.17, E) of $0.1\mu\text{m}^2/\text{s}$ are reasonable for 1 micron sized particles in water. Our fitted linear densities of the trapped particles

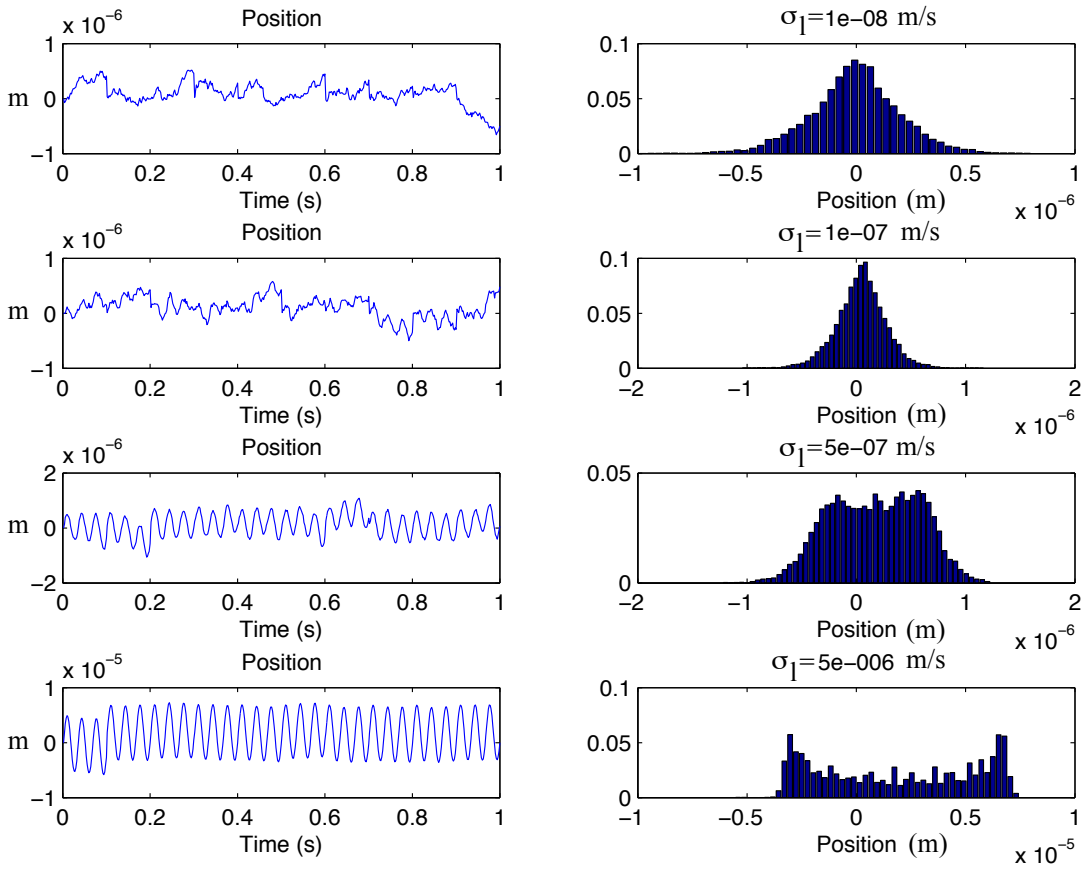

Figure 4.14: **Brownian motion with an oscillating point force.** Brownian motion simulations of BOTs of 1 micron diameter particles were performed. The particles were released at time 0 and allowed to undergo Brownian. A time-dependent point force γv_e (v_e is given in Equation 4.13 above) is applied with increasing amplitude σ_l. **Left**. Typical traces of the position of the released particles as a function of time. When the velocity reaches tens of nanometers per second, the motion already looks pseudo-deterministic. **Right**. Position distribution of the released particle. Under low velocity, the distribution looks Gaussian, as expected. With increasing applied force, the distribution becomes deterministic.

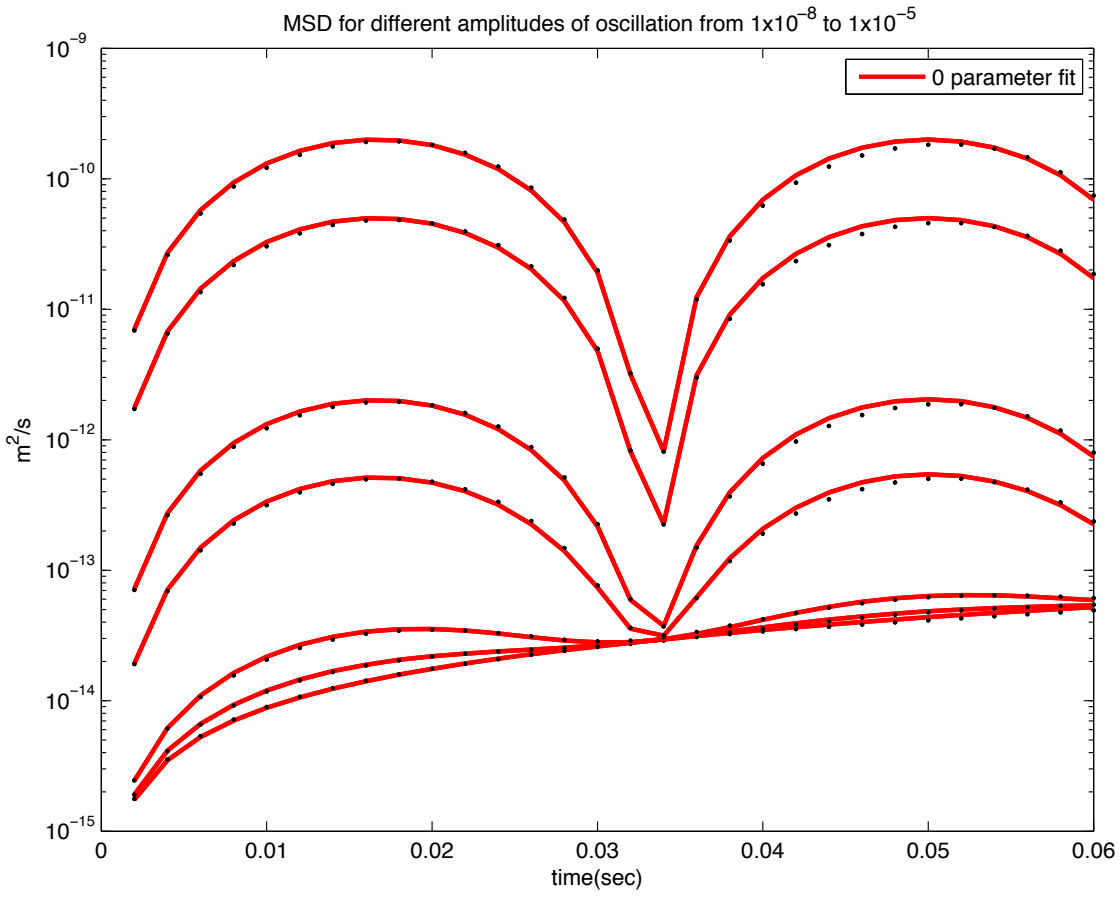

Figure 4.15: **Mean squared displacement with an oscillating point force.** The MSD as a function of time for different σ_l conditions (parameters given in Fig. 4.14) in the Brownian dynamics simulation (Eq. 4.12), black dots, was plotted against the predicted MSD (Eq. 4.16), red line, with no free parameters.

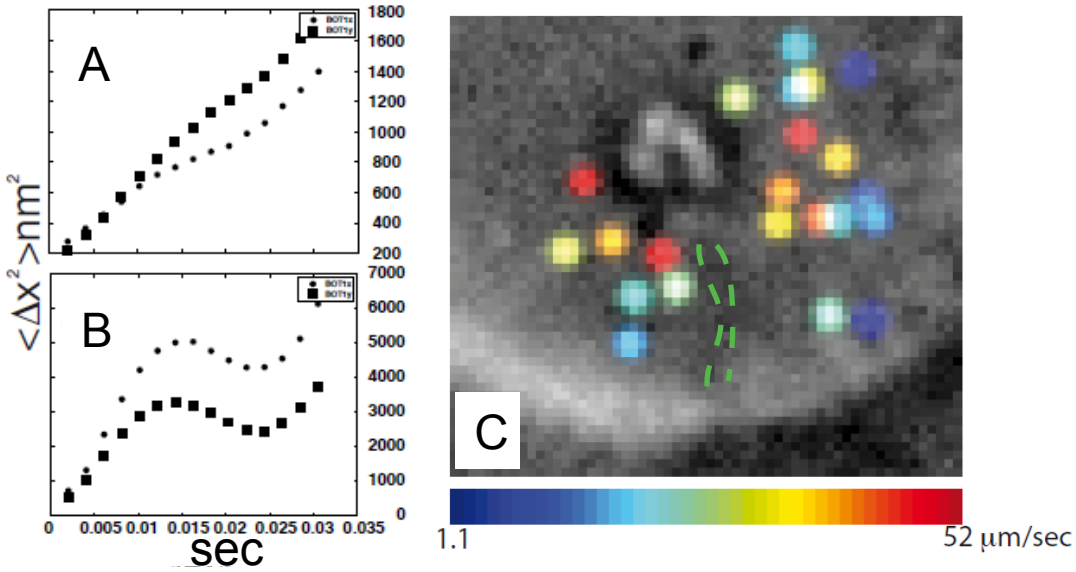

Figure 4.16: **Mean squared displacement in the inner ear.** **A**-**B**. Examples of mean squared spherule displacement plotted as a function of time illustrating a typical diffusive spherule motion (**A**) and driven motion (**B**). **C**. Flow map reconstituted using the BOTs model shows an expected velocity field that decays with increasing distance from the cilium, outlined in the green dotted-line. Cilia are often hard to see on still images without extensive image processing. The otolith is the central mass in the image, located above the cilium. The colors represent fit parameter a_0. In this particular embryo, fluid moves at a maximum speed of 52 μm/sec, averaged over many periods of cilia motion, and decays in a regular fashion.

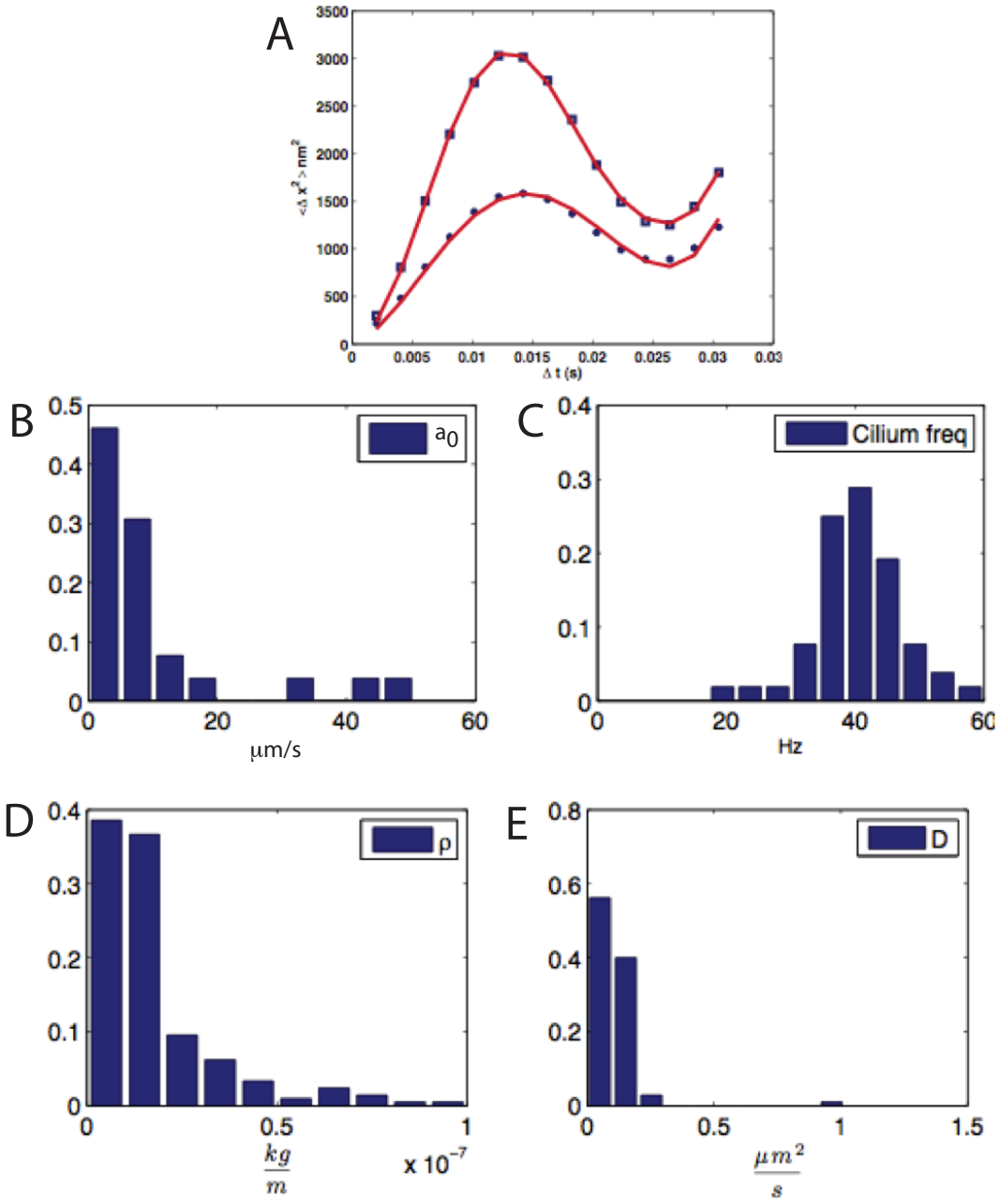

Figure 4.17: **Extracted BOTs parameters.** **A**. A typical mean displacement curve fit using Equation 4.16. **B**. Fitted values of a_0, the local fluid coupling strength. **C**. Fitted values of ω, the frequency of the cilia. The values obtained from fitting are 43 $\pm$ 8 Hz, compared to the values obtained from imaging, which were 44 $\pm$ 4 Hz. **D**. Fitted values of ρ, the linear density of the otolith precursor particles. We obtained 0.038 $\pm$ 0.078 μm/kg. There are no known measurements of zebrafish otolith densities. **E**. Fitted values of D, the diffusion coefficient. The values obtained from fitting are 0.1 $\pm$ 0.1 μm^2/sec, which is in the range of expected diffusion constants in water for 1-3 μm particles, the expected size of spherules [168].

(Fig. 4.17, D), which are otolith precursor particles, are predictions of zebrafish otolith densities at 18-24 hpf, since there are no known measurements of said otoliths; however, there are density measurements of otoliths for much larger fish of the Northwest Atlantic [182]. Note that Equation 4.16 was fit without b, since drift velocities will only dominate at long time scales, due to the t^2 term; we only fit the first 30 ms of a given MSD curve, and the maximum range of the BOTs procedure was 100 ms (10 Hz blinking). We found that flows (a_0) induced by the motile cilia dropped to within 10% of their initial value in less than 4 μm (Fig. 4.16, C). The correlation between a fast flow decay length observed *in vivo* and the spherical inner ear model which also predicts a quick fall off in velocity ($G \sim 1/r$), suggests that the model faithfully represents the key features of hydrodynamics at work in the inner ear and that hydrodynamic focusing could happen *in vivo*. Illustrated in Figure 4.18 is the 90% area velocity in three separate embryos.

4.3.3.2 Trap and delivery of otolith precursors particles

To address the hydrodynamics of spherule focusing *in vivo*, we again used optical trapping and quantified the main features of the inner ear flow. By trapping and releasing multiple spherules, we can seed and image hundreds of particle taken in the flow (Fig. 4.19, A-D), and thereby visualize the average flow field. Trapping did not affect embryonic development, as among all embryos manipulated through this approach, none of them displayed developmental malformations ($n = 6$) or otolith defects when compared to non-manipulated littermates ($n = 11$). This allowed us to confirm the model predictions by showing that spherules are propelled through fluid along helical paths inside the cavity, and that the motile cilia generate circular flow that entrains spherules, effectively localizing them to the location of the nascent otolith (Fig. 4.19, E), similar to Figure 4.11. We also found that multiple beating cilia could work in concert to generate flow rotation around the growing otolith (Fig. 4.19, D - this is more clear in the supplemental movie). The time for one revolution was $T = 4.6 \pm .9$ sec. The deterministic portion of the induced flow encompasses the near field of the cilia next to the otolith (3.1 ± 0.5 microns) and drops off quickly into purely diffusive behavior (Fig. 4.19, D and E) in $\sim$4 microns, similar to the spherule behavior predicted in the simulation at equivalent Pe and verified by BOTs as described above. The particle image velocimetry maps in Fig. 4.19, D and E were generated by averaging velocity vectors over tens of seconds.

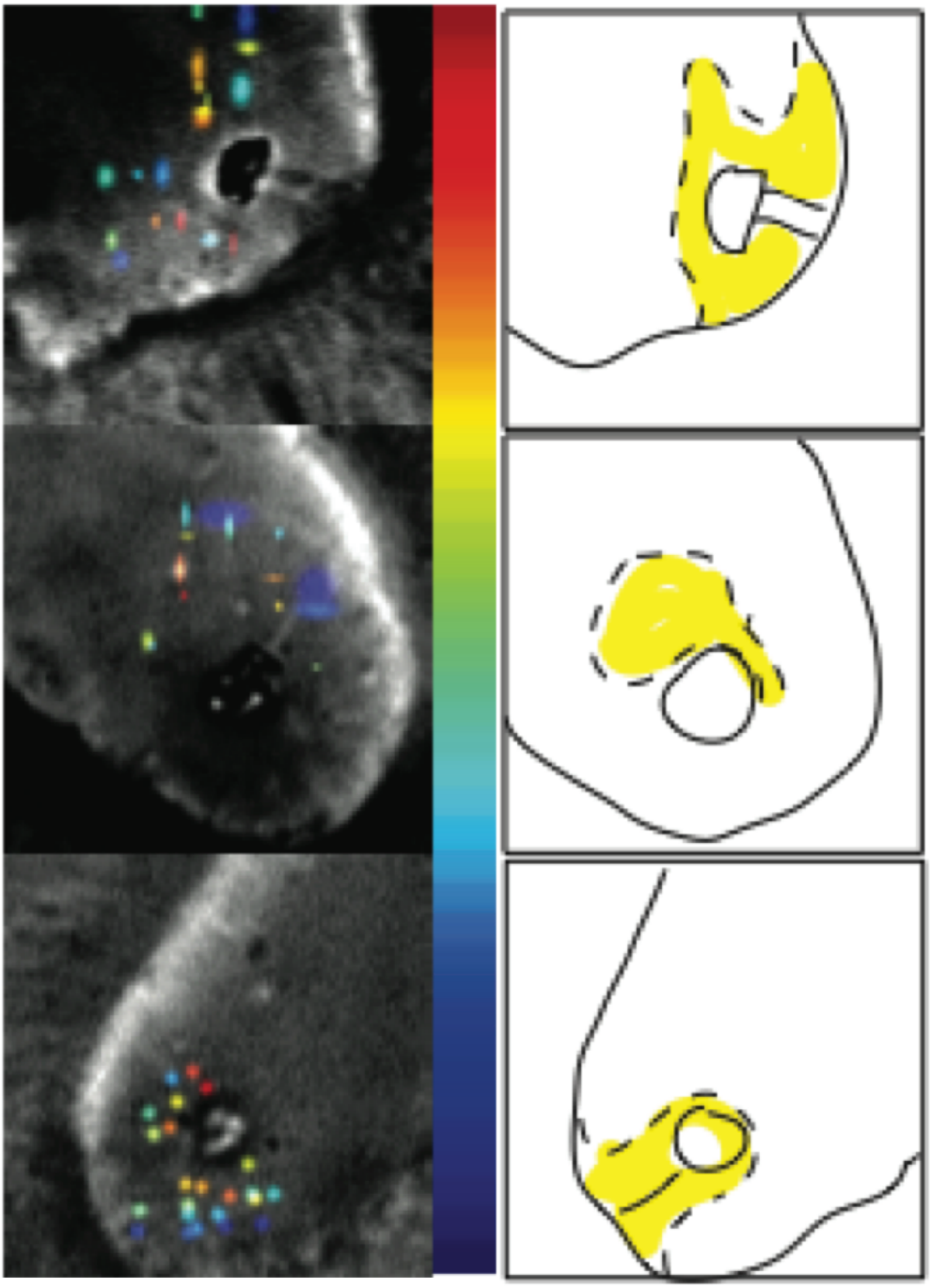

Figure 4.18: **Velocity drop off for 3 separate embryos. Left**. 3 separate embryos, color coded for magnitude of velocity (red is high velocity, 30-50 μm/sec, blue is low velocity, $\sim$1 μm/sec). **Right**. Schematic of where the $Pe \gg 1$ is in yellow. The field of view is 30 x 30 μm.

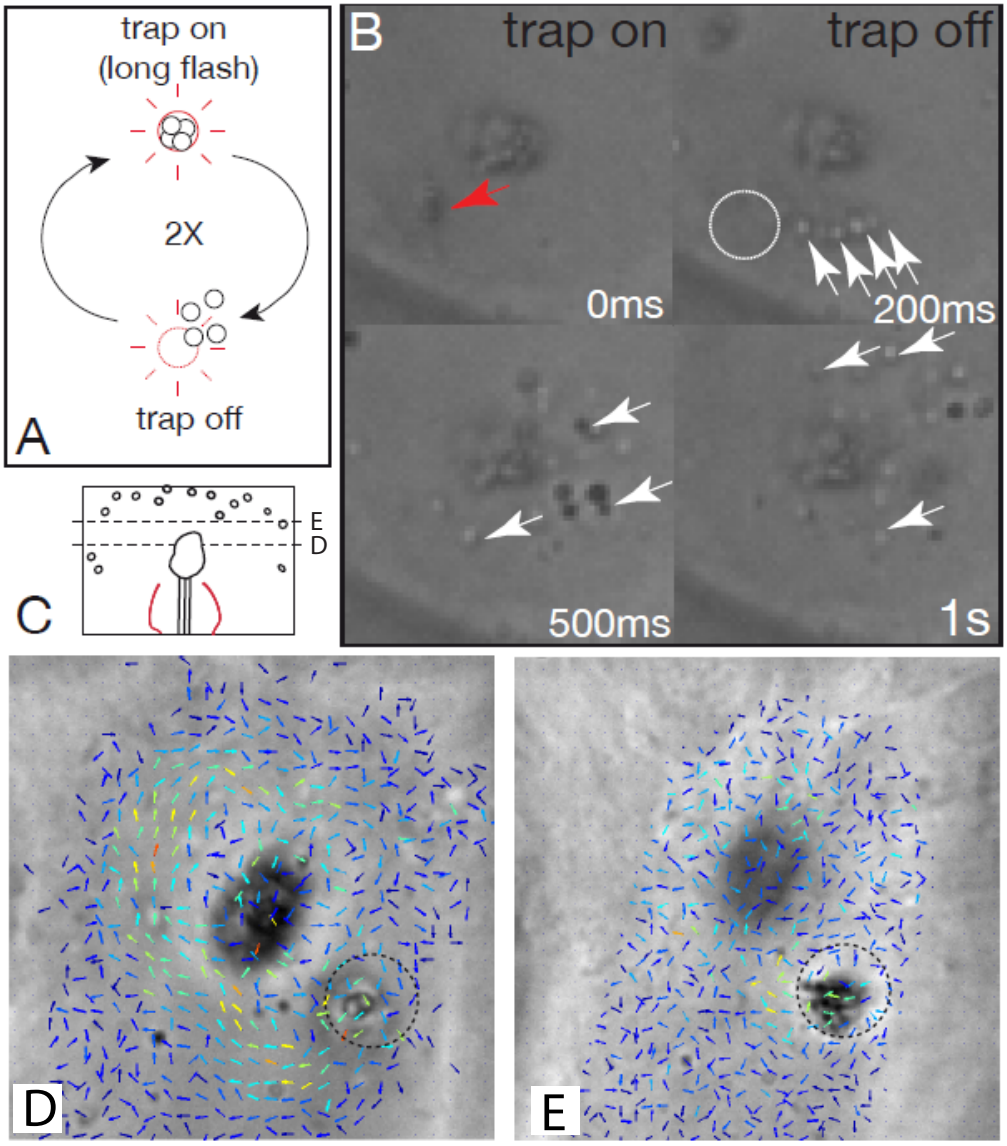

Figure 4.19: **Mapping the flow field using optical trapping. A-B**. The "package and delivery" flow mapping approach. Schematic view of the tweezing approach depicting the package and delivery method (**A**) and next to the otolith (**B**, side view of inner ear). Parcels of spherules are aggregated using the optical trap and positioned at a desired location in the inner ear (**B**, red arrow). The trap is then turned off and the particles are "delivered" following the flow field generated by beating cilia (**B**, white arrows). **C-E**. Particle image velocimetry (PIV) comparisons of the near field versus far field flow after release (top view of inner ear). **C**. Relative position of the focal plan where the measurements were performed in (**D**) and (**E**). Flow near the otolith is vortical (green-yellow arrows); the far field is diffusive (blue arrows). the difference in positioning between (**D**) and (**E**) is < 5 microns. In both cases, particles are "sucked" in near to the otolith, where they have a long residence time (seconds). Movies of (**D**) and (**E**) are included with this document.

Since the balance between flow and diffusion is highly dependent on Pe, we measured the velocities obtained at different planes of the inner ear and mapped the border between diffusion and vortical flow (Fig. 4.19, D and E). A clear separation between a disordered and an ordered regime was seen, reflecting the increasingly pronounced vortical flow towards the forming otolith. Particles moving through these two regimes are whipped around due to their entrainment by the cilia, only to be executing Brownian motion a few microns away, demonstrating that the cilia influence drops quickly (Fig. 4.19, D and E). In this area is an effective stagnation point which enhances particle aggregation [183]; we were unable to account for this in our hydrodynamic model (Section 4.3.2 above). Overall, the *in vivo* Pe, as measured by PIV, is 50-100, which is similar to the values obtained from the BOTs measurements (Fig. 4.17 and 4.18). According to the model, such a Pe has two implications for otolith biogenesis: first, the high velocity in an enclosed structure results in spherule localization near the tether cilia in vivo. Second, the rapid reduction in flow propagation results in a transition to diffusion in the otolith-forming area, within 2 microns. The otolith thus emerges at the juxtaposition between near and far field. Importantly, such a Pe explains why ectopic beating cilia can alter otolith biogenesis by changing the localization zone, a situation which is observed in the *gas8* morphants [161].

4.3.3.3 Laser ablation of motile cilia

To support the interpretation that otoliths are juxtaposed at the near and far field, and to gain insight into the physiological role of beating cilia during this process, we quantified the effects of motile cilia ablation during the period of rapid otolith growth (18-24 hpf). We used focal laser ablation to inactivate cilia motion (Fig. 4.20, A-D) and addressed the effect of decreased flow forces on otolith shape. To analyze the shape of the otolith, we segmented the otolith shape before and after laser ablation by measuring the mean of the sum of squared residuals (SSR) relative to a circle (Fig. 4.20, E-J, L-M; 4.21, A-D). For this analysis, a SSR closer to 0 implies that the shape is more spherical. The mean SSR in ablated embryos was 0.31 (n=24), and the wild-type 0.53 (n=33). The significance of the difference, at p-value < 0.03, was validated by a bootstrap analysis.

In order to compare otoliths from wild-type embryos with those with their inner ear motile cilia ablated, either due to laser ablation or morpholinos, we compared the otolith shape to a perfect circle. Embryos were aged-matched and mounted on the microscope

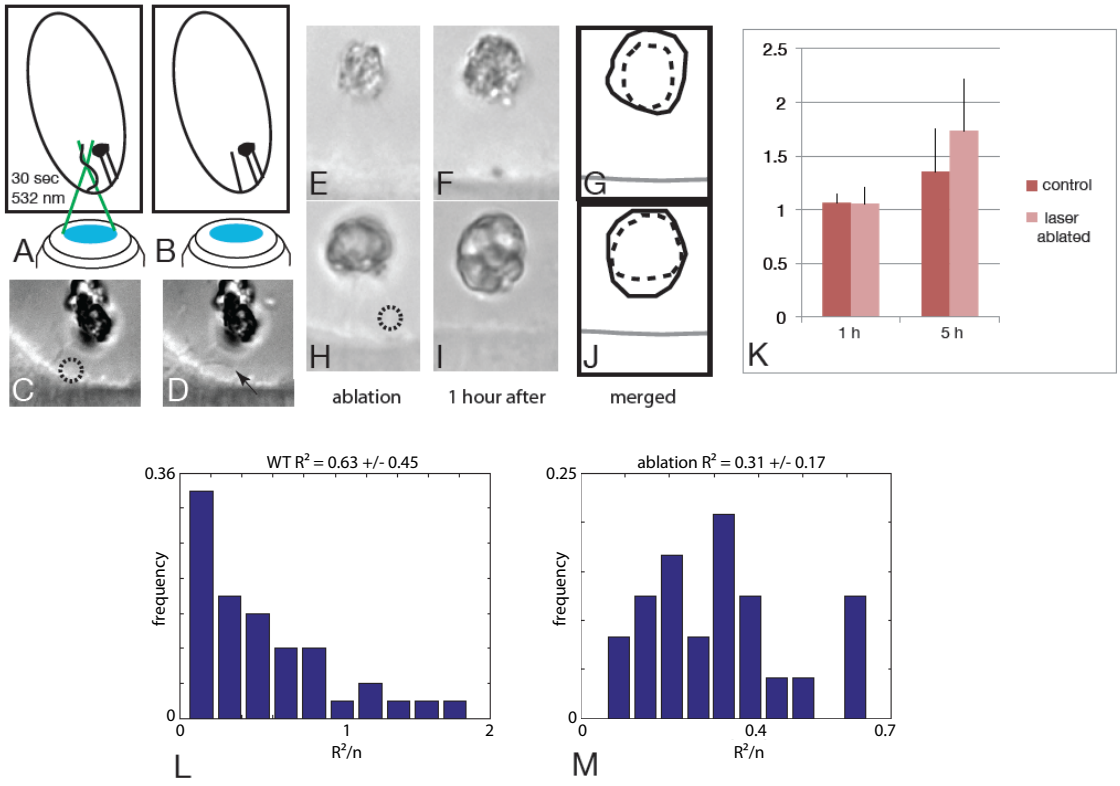

Figure 4.20: **Laser ablation of motile cilia.** **A**-**D**. Schematic of the laser ablation experiment. A 532 nm laser was aimed squarely at the motile cilium in increments of 30 seconds at 1 W of power at laser output (**A**, **C**) until the cilia paused their movement (**B**, **D**). The dotted line indicates the ablation spot. **E**-**F**. Control otolith before and after sham ablation. Otolith before and (**H**) and 1 hour after local cilium ablation (**I**). The otolith clearly grows as seen in the schematic representing the overlay of the otoliths before and after 1 hour after ablation (**G**, **J**). **K**. Segmentation of the otoliths shows that ablation does not affects otolith growth area 5 hours after ablation. **L**, **M**. Distribution of the otolith shape in controls (**L**) and cilia ablated embryos (**M**) less than 5 hours after ablation shows a clear difference in the SSR ($\mu = 0.63$ in unmanipulated embryos; $\mu = 0.31$ in ablated embryos; p-value < 0.03), confirming the necessity of cilia beat for maintaining ovoid otolith shape.

such that the tether cilia could be seen. Using this as a reference point, we focused through the otoliths until we found their widest extent. The otoliths were then traced by hand using MATLAB, and the outline was rotated such that the tether cilia was pointed due south. The widest extent of the rotated shape was then used to generate a circle of equal diameter, and the difference between the circle and the outline of the otolith was computed. These differences were squared, and the result summed; we call this the "sum of squared residuals" (SSR). However, since the values of a given SSR only admits positive values, and the frequency of SSRs values does not follow a normal distribution, we decided to compare the SSR between experiments via bootstrapping. The SSRs of many embryos (both wild-type and ablated) were pooled together, and random SSR distributions were generated from this pool; a mean SSR was determined. In doing so, we found that the probability of randomly generating two distributions with a mean SSR of greater than 0.3, the difference between wild-type and ablated, was less than 3%, for both the laser ablated samples and the morpholino samples versus the control groups.

Thus, the secondary process of ovoid shape creation depends on flow generated in a highly local manner - specifically to create otoliths of ovoid (higher SSR) versus circular shape (lower SSR). However, the primary process of otolith growth is less dependent on cilia induced flow since we found that growth was not significantly affected by cilia ablation (Fig. 4.20, K). To confirm these observations, we used genetic ablation of *gas8*, an essential gene for cilia beating and otolith biogenesis [161, 147]. After knock down, the mean SSR is 0.30 (n=36) showing that ovoid otolith shape necessitates the presence of beating cilia (Fig. 4.21, D). This result implies that pure diffusion would prefer to form a spherical otolith. Thus, in addition to localizing spherules to the poles of the inner ear, cilia motion induces a high-speed flow field around the tether cilia beneath the nascent otolith, which creates stagnation areas immediately superior, at the sides and top of the nascent otolith, because of the quick decay of induced fluid flow. This biases spherule deposition away from the bottom of the otolith, resulting in an ovoid shape (SSR > 0) (Fig. 4.22).

4.3.4 Summary of results

Cilia have dual effect - they serve as a stir bar to globally pull in spherules to stimulate otolith growth and locally deplete spherule concentration such that the otoliths have a mushroom top shape, as seen in the electron micrograph in Figure 4.6. Altogether, the

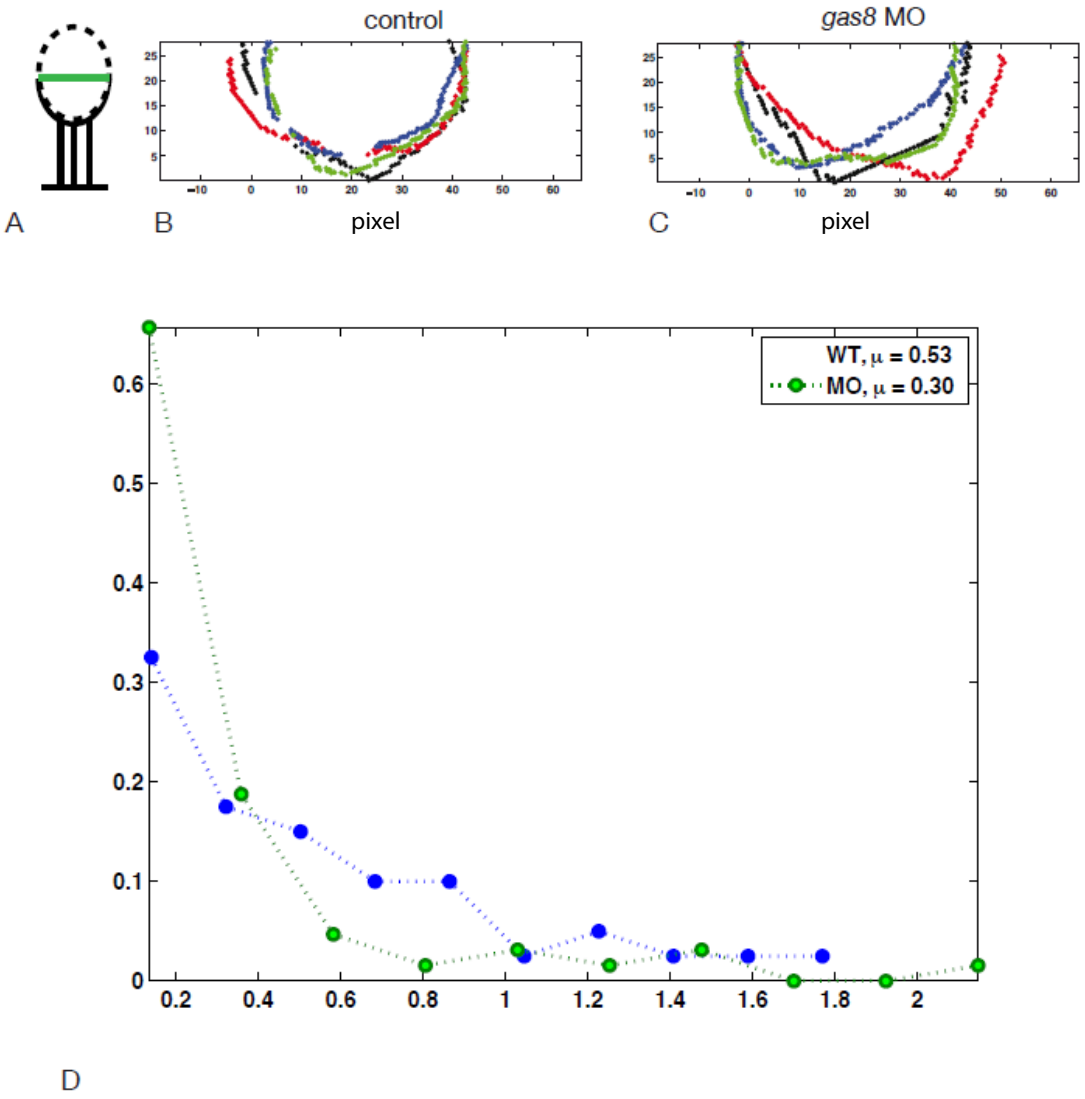

Figure 4.21: **Abnormal otolith shape in *gas8* morphants. A**. A circle (dotted red lines) is fit to the segmentation (solid black line encircling the otolith) and the midline (green line) is found after aligning the otolith relative to the tether cilium (solid black line). A few representative traces are plotted in controls (**B**) and *gas8* morphants (**C**). **D**. SSR distribution for controls ($\mu = 0.53$) and *gas8* morphants ($\mu = 0.30$). The p-value was also < 0.3 by bootstrap (same as in laser ablated samples).

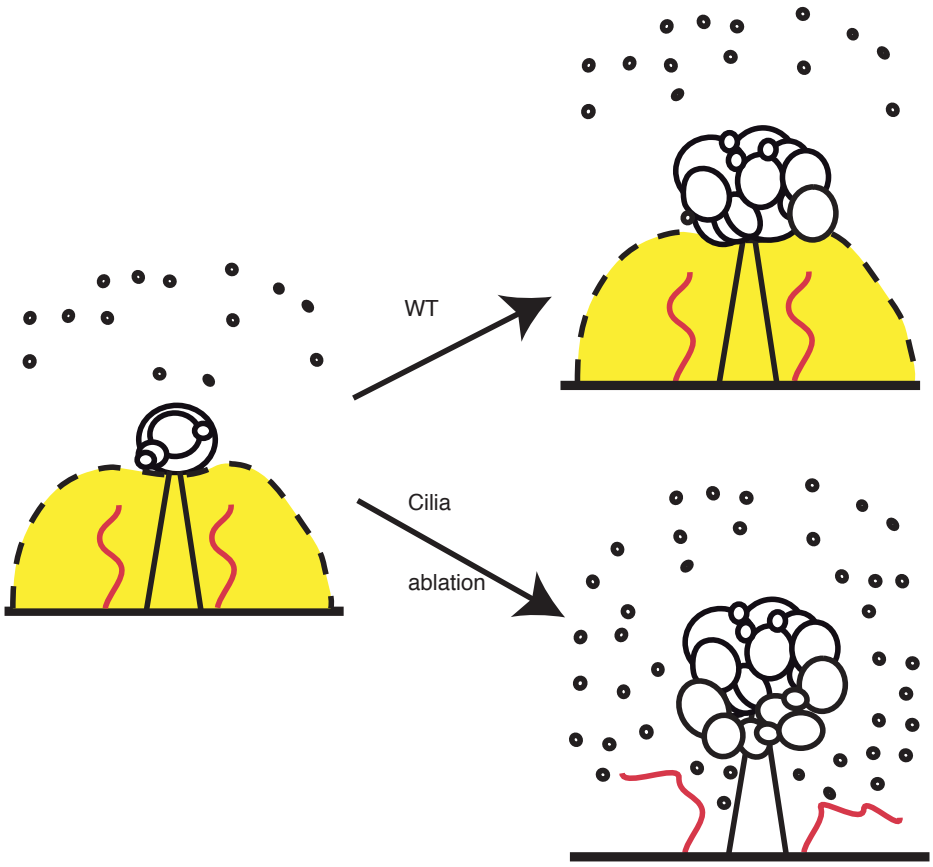

Figure 4.22: **Model for otolith self assembly.** The vortical flow at the base of the otolith inhibits agglomeration while diffusion starting at the level of the diffusion front permits agglomeration. When the cilia are ablated, particles are able to uniformly diffuse around the otolith nucleus, resulting in spherical growth.

hydrodynamics uncovered through the optical methods employed suggest a refined model for otolith biogenesis. While a normal flow field can shape the otolith, it also participates in attracting spherules next to the otolith, perhaps setting the 6 hour time scale for otolith growth as reported by Riley et al., [167]. Yet, the main influence controlling otolith biogenesis is Brownian motion, as the otoliths clearly only form where the Pe is low; complete knockdown of inner ear cilia doesn't prevent otolith formation, they are just misshapen and hence non-functional (Fig. 4.3, h-p). Importantly this model explains why ectopic beating cilia can modulate otolith biogenesis by altering the flow field and changing the localization concentrating zone. Such a situation is observed in the *gas8* morphants [161].

Systems where simple mechanical principles participate in self-assembly [184] or in feedback mechanisms coordinating size and shape [185] are now emerging as being essential elements of the developmental programs. For example, we show here that the self-organizing properties of otolith formation could solely depend on the hydrodynamics mediated by cilia and the self-aggregation properties of the spherules 4.22. This study also illustrates the complexity of cilia driven advection as well as the multiplicity of biological outcomes they can effect in vertebrates. Surprisingly, the hydrodynamics mediated by inner ear cilia is similar in action to what has been described in bi-flagellate algae *Chlamydomonas reinhardtii* and *Chlamydomonas* colony *Volvox carteri*, which uses the same type of advection-diffusion system to drive metabolite uptake and waste exchange [186, 187]. Nevertheless, the nonlinearity of the particle time-to-capture and particle focusing depends on the particular physical boundaries of the inner ear and the ability of the tether cilia to immobilize spherules. Otolith biogenesis is thus the result of fairly simple biochemical and geometrical constraints of the system, in addition to mechanics - an example of cells creating elaborate spatial structures through physical, rather than genetic, principles. The hydrodynamics uncovered here may correspond to properties of other cilia mediated flow in vertebrate cavities, such as during stem cell migration in the brain [147] and morphogen gradient formation in the left-right organizer [141, 188], could share.

Chapter 5

Conclusions

I've been here 6 years, plus 3 summers worth of rotations (in Pat Collier, Scott Fraser, and Rob Phillips' labs). I spent the first year and a half taking classes for my department, and the second and third years after that studying the hydrodynamics of the Kupffer's vesicle in zebrafish, as well as the part on Maximum Caliber. The next year, my 4th, I spent investigating the *in vitro* reconstitution of cilia, purified from *Chalmydomonas reinhardtii*. My 5th and 6th years were spent investigating phage lambda and the inner ear otolith formation, which has many similarities to the Kupffer's vesicle. In the interest of brevity, I omitted my work on the Kupffer's vesicle and the reconstituted cilia, as those stories are the least developed, even after this time. For those interested, please consult my lab notebooks.

In the part concerning Maximum Caliber, we discovered that it is possible to use information theory to find the distribution of trajectories in an analogous way to finding the probability distribution of states in the Principle of Maximum Entropy. We verified that the predicted moments matched those attained from experiments on sculpted energy landscapes, and from Brownian dynamics simulations. We were, moreover, able to use the partition function to derive and generate the expected dynamics of the system, which suggests a connection between Maximum Caliber models and Markov processes, as evidenced by the appearance of a matrix propagator in each.

In the part concerning bacteriophage lambda, we learnt that changing the counterion composition of the buffers significantly changes the ejection velocity and the stall force during ejection - specifically, a reduction in divalent ions spurs increased ejection velocities and a concomitant increase in the osmotic pressure necessary to stall an ejection. We also saw a possible new mode of ejection that involves looping during the ejection process - perhaps to facilitate the formation of circularized DNA and evade attack by host exonucleases. Finally,

it is now becoming possible to visualize the ejection of DNA directly into cells or minicells, though the experimental results are preliminary.

In the part concerning zebrafish, we discovered that a crucial organ in the life of the zebrafish, the inner ear otolith, was constructed according to hydrodynamic principles, as opposed to genetic principles. Motile cilia are able to focus otolith precursor particles into the vicinity of tether cilia through a dipole-type flow field. They also shape how the otolith is built, eventually resulting in a mushroom-top structure as opposed to a symmetric otolith which would be the expected result from isotropic Brownian motion.

The common theme in the three stories in this thesis is one of information - how it is analyzed and transferred, beyond the typical *gene* $\rightarrow$ *gene product* algorithm, for this type of model can hardly account for the spatial diversity of biology, the origins of which must lie in a physical process. I hope that *Biomechanical Information Transfer* has uncovered new territory, and perhaps new ways of thinking about biology, beyond the staid paradigms.

Bibliography

[1] E T Jaynes. The minimum entropy production principle. In R. D. Rosenkrantz, editor, *E. T. Jaynes: Papers on probability, statistics and statistical physics*, chapter 14. Kluver academic publishers, 1980.

[2] E T Jaynes. Where do we stand on maximum entropy? In R. D. Rosenkrantz, editor, *E. T. Jaynes: Papers on probability, statistics and statistical physics*, chapter 10. Kluver academic publishers, 1978.

[3] Arieh Ben-Naim. *A Farewell to Entropy: Statistical Thermodynamics Based on Information*. World Scientific, 2008.

[4] C E Shannon. A mathematical theory of communication. *Bell Systems Technical Journal*, 27(379):623–56, 1948.

[5] K Dill and S Bromberg. *Molecular driving forces: statistical thermodynamics in chemistry and biology*. Garland Science, New York, 2003.

[6] E T Jaynes. Information theory and statistical mechanics. In R. D. Rosenkrantz, editor, *E. T. Jaynes: Papers on probability, statistics and statistical physics*, chapter 1. Kluver academic publishers, 1957.

[7] H B Callen. *Thermodynamics and an Introduction to Thermostatistics*. John Wiley and Sons, 1985.

[8] K Ghosh, K Dill, M M Inamdar, E Seitaridou, and R Phillips. Teaching the principles of statistical dynamics. *American Journal of Physics*, 74(2):123–33, 2006.

[9] D Wu, K Ghosh, M M Inamdar, H J Lee, S Fraser, K Dill, and R Phillips. Trajectory approach to two-state kinetics of single particles on sculpted energy landscapes. *Physical Review Letters*, 103:050603, 2009.

[10] L Finzi and J Gelles. Measurement of lactose repressor-mediated loop formation and breakdown in single DNA-molecules. *Science*, 267(5196):378–380, 1995.

[11] J Liphardt, B Onoa, S B Smith, I Tinoco, and C Bustamante. Reversible unfolding of single RNA molecules by mechanical forces. *Science*, 292(5517):733–7, 2001.

[12] G Baldini, F Cannone, and G Chirico. Pre-unfolding resonant oscillations of single green fluorescent protein molecules. *Science*, 309(5737):1096–100, 2005.

[13] D Collin, F Ritort, C Jarzynski, S B Smith, I Tinoco Jr., and C Bustamante. Verification of Crooks fluctuation theorem and recovery of rna folding free energies. *Nature*, 437:231–4, 2005.

[14] G Popescu, A Robert, J R Howe, and A Auerbach. Reaction mechanism determines nmda response to repetitive stimulation. *Nature*, 430:790–793, 2004.

[15] C W Gardiner. *Handbook of Stochastic Methods, 3rd ed.* Springer-Verlag, Heidelberg, Germany, 2004.

[16] H A Kramers. Brownian motion in a field of force and the diffusion model of chemical reactions. *Physica*, 7(4):284–304, 1940.

[17] K Svoboda and S M Block. Biological applications of optical forces. *Annual Review of Biophysical and Biomolecular Structure*, 23:247, 1994.

[18] M J Lang, C L Asbury, J W Shaevitz, and S M Block. An automated two-dimensional optical force clamp for single molecule studies. *Biophysical Journal*, 83:491–501, 2002.

[19] E T Jaynes. Macroscopic prediction. In H. Haken, editor, *Complex systems: Operational approaches in neurobiology, physics and computers*, page 254. Springer-Verlag, 1985.

[20] E Seitaridou, M M Inamdar, K Ghosh, K A Dill, and Rob Phillips. Measuring flux distributions for diffusion in the small-numbers limit. *Journal of Physical Chemistry B*, 111(51):2288–92, 2006.

[21] G Stock, K Ghosh, and K Dill. Maximum caliber: A variational approach applied to two-state dynamics. *Journal of Chemical Physics*, 128:194102, 2008.

[22] D T Gillespie. Fluctuation and dissipation in Brownian motion. *American Journal of Physics*, 61:1077–83, 1993.

[23] A D Hershey and M M Chase. Independent functions of viral protein and nucleic acid in growth of bacteriophages. *Journal of General Physiology*, 36:39–56, 1952.

[24] G P Smith. Surface presentation of protein epitopes using bacteriophage expression systems. *Current Opinion in Biotechnology*, 2(5):668–73, 1991.

[25] C E Catalano, D Cue, and M Feiss. Virus DNA packaging: the strategy used by phage lambda. *Molecular Microbiology*, 16(6):1075–86, 1995.

[26] A M Oppenheim, O Koniler, J Stavans, D L Court, and S Adhya. Switches in bacteriophage lambda development. *Annual Review of Genetics*, 39:409–29, 2005.

[27] A Arkin, J Ross, and H H McAdama. Stochastic kinetic analysis of developmental pathway bifurcation in phage lambda-infected *Escherichia coli* cells. *Genetics*, 149:1633–48, 1998.

[28] F St-Pierre and D Endy. Determination of cell fate selection during phage lambda infection. *Proceedings of the National Academy of Sciences*, 105:20705–10, 2008.

[29] L Zeng, S O Skinner, C Zong, J Sippy, M Feiss, and I Golding. Decision making at a subcellular level fetermines the outcome of bacteriophage infection. *Cell*, 141:682–91, 2010.

[30] I B Dodd, K E Shearwin, and J B Egan. Revisited gene regulation in bacteriophage lambda. *Current Opinion in Genetics and Development*, 15:145–52, 2005.

[31] D E Smith, S J Tans, S B Smith, S Grimes, D L Anderson, and C Bustamante. The bacteriophage straight phi29 portal motor can pack dna against a large internal force. *Nature*, 413(6857):748–52, 2001.

[32] C Carrasco, M Douas, R Miranda, M Castellanos, P A Serena, J L Carrascosa, M G Mateu, M I Marques, and P J de Paclo. The capillarity of nanometric water menisci confined inside closed-geometry viral cages. *Proceedings of the National Academy of Sciences*, 106:5475–80, 2009.

[33] Mark Ptashne. *A Genetic Switch, Phage Lambda Revisited, Third Edition.* Cold Spring Harbor Laboratory Press, 2004.

[34] E T Young and R L Sinsheimer. Novel intra-cellular forms of lambda DNA. *Journal of Molecular Biology*, 10:562–4, 1964.

[35] V C Bode and A D Kaiser. Changes in the structure and activity of lambda DNA in a superinfected immune bacterium. *Journal of Molecular Biology*, 14:399–417, 1965.

[36] H Witkeiwicz and K Taylor. The fate of phage lambda DNA in lambda-infected minicells. *Biochimica et Biophysica Acta*, 564:31–6, 1979.

[37] M E Cerritelli, N Cheng, A H Rosenberg, C E McPherson, F P Booy, and A Stevenson. Encapsidated conformation of bacteriophage T7 dna. *Cell*, 91:271–80, 1997.

[38] A S Petrov and S C Harvey. Structural and thermodynamic principles of viral packaging. *Structure*, 15:21–7, 2007.

[39] C Bustamante, Z Bryant, and S B Smith. Ten years of tension: single-molecule DNA mechanics. *Nature*, 421:423–7, 2003.

[40] D N Fuller, J P Rickgauer, P J Jardine, S Grimes, D L Anderson, and D E Smith. Ionic effects on viral dna packaging and portal motor function in bacteriophage phi29. *Proceedings of the National Academy of Sciences*, 104:11245–50, 2007.

[41] M M Poranen, R Daugelavicius, and D H Bamfod. Common principles in viral entry. *Annual Reviews in Microbiology*, 56:521–38, 2002.

[42] S W Emmons, V MacCosham, and R L Baldwin. Tandem genetic duplications in phage lambda. III. The frequency of duplication mutants in two derivatives of phage lambda is independent of known recombination systems. *Journal of Molecular Biology*, 91:133–146, 1975.

[43] S L Novick and J D Baldeschwieler. Fluorescence measurements of the kinetics of DNA injection by bacteriophage lambda into liposomes. *Biochemistry*, 27:7919–24, 1988.

[44] S Mangenot, M Hochrein, J Radler, and L Letellier. Real-time imaging of DNA ejection from single phage particles. *Current Biology*, 15:430–5, 2005.

[45] P Grayson, L Han, T Winther, and R Phillips. Real-time observations of single bacteriophage λ DNA ejections in vitro. *Proceedings of the National Academy of Sciences*, 104(37):13652–7, 2007.

[46] N Chiaruttini, M de Frutos, E Augarde, P Boulanger, and L Letellier. Is the in vitro ejection of bacteriophage DNA quasi-static? a bulk to single virus study. *In Press*, 2010.

[47] A Evilevitch, L Lavelle, C M Knobler, E Raspaud, and W M Gelbart. Osmotic inhibition of DNA ejection from phage. *Proceedings of the National Academy of Sciences*, 100(16):9292–5, 2003.

[48] A Evilevitch, J W Gober, M Phillips, C M Knobler, and W M Gelbart. Measurements of DNA lengths remaining in a viral capsid after osmotically suppressed partial ejections. *Biophysical Journal*, 88:851–66, 2005.

[49] P Grayson, A Evilevitch, M M Inamdar, P K Purohit, W M Gelbart, C M Knobler, and R Phillips. The effect of genome length on ejection forces in bacteriophage lambda. *Virology*, 348(2):430–6, 2006.

[50] A Leforestier, S Brasiles, M de Frutos, E Raspaud, L Letellier, P Tavares, and F Livolant. Bacteriophage T5 DNA ejection under pressures. *Journal of Molecular Biology*, 384:730–9, 2008.

[51] J Kindt, S Tzlil, A Ben-Schaul, and W M Gelbart. DNA packaging and ejection forces in bacteriophages. *Proceedings of the National Academy of Sciences*, 98(24):13671–4, 2001.

[52] M Jeembaeva, M Castelnovo, F Larsson, and A Evilevitch. Osmotic pressure: resisting or promoting DNA ejection from phage? *Journal of Molecular Biology*, 381:310–23, 2008.

[53] J B Stock, B Rauch, and S Roseman. Periplasmic space in *Salmonella typhimurium* and *Escherichia Coli*. *Journal of Biological Chemistry*, 252(21):7850–60, 1977.

[54] I J Molineux. Fifty-three years since Hershey and Chase: much ado about pressure but which pressure is it? *Virology*, 344:221–9, 2006.

[55] L R Comolli, A J Spakowitz, C E Siegerist, P J Jardine, S Grimes, D L Anderson, C Bustamante, and K H Downing. Three-dimensional architecture of the bacteriophage phi29 packaged genome and elucidation of packaging process. *Virology*, 371:267–77, 2008.

[56] A Leforestier and F Livolant. Structure of toroidal DNA collapsed inside the phage capsids. *Proceedings of the National Academy of Sciences*, 106:9157–62, 2009.

[57] A Evilevitch. Effects of condensing agent and nuclease on the extent of ejection from phage lambda. *Journal of Physical Chemistry B*, 110:22261–5, 2006.

[58] N V Hud and K H Downing. Cryoelectron microscopy of lambda phage DNA condensates in vitreous ice: The fine structure of DNA toroids. *Proceedings of the National Academy of Sciences*, 98:14925–30, 2001.

[59] P A Fang, E T Wright, S T Weintrab, K Hakala, W Wu, P Serwer, and W Jiang. Visualization of bacteriophage T3 capsids with dna incompletely packaged in vivo. *Journal of Molecular Biology*, 384:1384–99, 2008.

[60] J E Johnson and W E Chiu. DNA packaging and delivery machines in tailed bacteriophages. *Current Opinion in Structural Biology*, 17:237–43, 2007.

[61] A Evilevitch, L T Fang, A M Yoffe, M Castelnovo, D C Rau, A Parsegian, W M Gelbart, and C M Knobler. Effects of salt concentrations and bending energy of the extent of ejection of phage genomes. *Biophysical Journal*, 94:1110–20, 2008.

[62] T Odijk. Hexagonally packed DNA within bacteriophage T7 stabilized by curvature stress. *Biophysical Journal*, 75:1223–7, 1998.

[63] P K Purohit, J Kondev, and R Phillips. Mechanics of DNA packaging in viruses. *Proceedings of the National Academy of Sciences*, 100:3173–8, 2003.

[64] S Tzlil, J T Kindt, W M Gelbart, and A Ben-Schaul. Forces and pressures in DNA packaging and release from viral capsids. *Biophysical Journal*, 84:1616–27, 2004.

[65] P K Purohit, M M Inamdar, P D Grayson, T M Squires, J Kondev, and R Phillips. Forces during bacteriophage DNA packaging and ejections. *Biophysical Journal*, 88:851–66, 2005.

[66] Z Li, J Wu, and Z G Wang. Osmotic pressure and packaging structure of caged DNA. *Biophysical Journal*, 94:737–46, 2008.

[67] A S Petrov and S C Harvey. Packaging double-helical DNA into viral capsids: structures, forces, and energetics. *Biophysical Journal*, 95:497–502, 2008.

[68] D E Smith, T Perkins, and S Chu. Dynamical scaling of dna diffusion coefficients. *Macromolecules*, 29:1372–3, 1996.

[69] E. Joly. *Purification of DNA fragments from agarose gels using glass beads in Methods in Molecular Biology: Basic DNA and RNA protocols.* Humana Press, 1996.

[70] L Han, H G Garcia, S Blumberg, K B Towles, J F Beausang, and R Phillips. Concentration and length dependence of DNA looping in transcriptional regulation. *PLoS One*, 4:e5621, 2009.

[71] J F Marko and E D Siggia. Stretching DNA. *Macromolecules*, 28:8759–70, 1995.

[72] B E Michel. Evaluation of the water potentials of solutions of polyethylene glycol 8000 both in the absense and presence of other solutes. *Plant Physiology*, 72:66–70, 1983.

[73] C Sao-Jose, M de Frutos, E Raspaud, M A Santos, and P Tavares. Pressure built by DNA packaging inside virios: enough to drive DNA ejection *in vitro*, largely insufficient for delivery into the bacterial cytoplasm. *Journal of Molecular Biology*, 374:346–355, 2007.

[74] D C Rau, B Lee, and V A Parsegian. Measurement of the repulsive force between polyelectroplyte molecules in ionic solution: hydration forces between parallel DNA double helices. *Proceedings of the National Academy of Sciences*, 81:2621–5, 1984.

[75] D C Rau and V A Parsegian. Direct measurement of temperature-dependent solvation forces between DNA double helices. *Biophysical Journal*, 61:260–71, 1992.

[76] G Koraimann. Lytic transglycosylases in macromolecular transport systems of Gram-negative bacteria. *Cellular and Molecular Life Sciences*, 60:2371–88, 2003.

[77] P Demchick and A L Koch. The permeability of the wall fabric of *Escherichia coli* and *Bacillus subtilis*. *Journal of Bacteriology*, 178:768–73, 1996.

[78] X Yao, M Jericho, D Pink, and T Beveridge. Thickness and elasticity of Gram-negative murein sacculi measured by atomic force microscopy. *Journal of Bacteriology*, 181:6865–75, 1999.

[79] T Nambu, T Minamino, R M Macnab, and K Kutsukake. Peptidoglycan-hydrolyzing activity of the FlgJ protein, essential for flagellar rod formation in *Salmonella typhimurium*. *Journal of Bacteriology*, 181:1555–61, 199.

[80] M G Rossmann, V V Mesyanzhinov, F Arisaka, and P G Leiman. The bacteriophage T4 DNA injection machines. *Current Opinion in Structural Biology*, 14:171–80, 2004.

[81] Y Xiang, M C Morais, D N Cohen, V D Bowman, D L Andrerson, and M G Rossmann. Crystal and cryoEM structural studies of a cell wall degrading enzyme in the bacteriophage ϕ29 tail. *Proceedings of the National Academy of Sciences*, 105:9552–7, 2008.

[82] I J Molineux. No syringes please, ejection of phage T7 DNA from the virion is enzyme driven. *Molecular Microbiology*, 40:1–8, 2001.

[83] M Moak and I J Molineux. Peptidoglycan hydrolytic activities associated with bacteriophage virions. *Molecular Microbiology*, 51:1169–83, 2004.

[84] M D Wang, M J Schnitzer, H Yin, R Landick, J Gelles, and S M Block. Force and velocity measured for single molecules of RNA polymerase. *Science*, 282:902–7, 1998.

[85] P Kemp, M Gupta, and I J Molineux. Bacteriophage T7 DNA ejection into cells is initiated by an enzyme-like mechanism. *Molecular Microbiology*, 53:1251–65, 2004.

[86] V Gonzalez-Huici, M Salas, and J M Hermoso. The push-pull mechanism of bacteriophage phi29 DNA injection. *Molecular Microbiology*, 52:529–40, 2004.

[87] P Grayson and I J Molineux. Is phage DNA "injected" into cells - biologists and physicists can agree. *Current Opinion in Microbiology*, 10:401–9, 2007.

[88] J Howard. *Mechanics of Motor Proteins and the Cytoskeleton*. Sinauer Associates, Inc., 2001.

[89] T A Keller, T Ference, A Prilipov, and J P Rosenbusch. Crystallization of monodisperse maltoporin from wild-type and mutant strains of various enterobacteriaceae. *Biochemical and Biophysical Research Communications*, 199(2):767–71, 1994.

[90] T Schirmer, T A Keller, Y-F Wang, and J P Rosenbusch. Structural basis for sugar translocation through maltoporin channels at 3.1 *å* resolution. *Science*, 267:512–4, 1995.

[91] P A Gurnev, A B Oppenheim, M Winterhalter, and S M Bezrukov. Docking of a single phage lambda to its membrane receptor maltoporin as a time-resolved event. *Journal of Molecular Biology*, 359:1447–55, 2006.

[92] J Wang, M Hofnung, and A Charbit. The c-terminal portion of the tail fiber protein of bacteriophage lambda is responsible for binding to LamB, its receptor at the surface of *Escherichia coli* K-12. *Journal of Bacteriology*, 182:508–12, 2000.

[93] C Plisson, H E White, I Auzat, A Zafarani, C Sao-Jose, S Lhuillier, P Tavares, and E V Orlova. Structure of bacteriophage SPP1 tail reveals trigger for DNA ejection. *The EMBO Journal*, 26:2730–8, 2007.

[94] S Lhuillier, M Gallopin, B Gilquin, S Brasiles, N Lancelot, G Letellier, M Gilles, G Dethan, E V Orlova, J Couprie, P Tavares, and S Zinn-Justin. Structure of bacteriophage SPP1 head-to-tail connection reveals mechanism for viral DNA gating. *Proceedings of the National Academy of Sciences*, 106:8508–12, 2009.

[95] C A Roessner, D K Struck, and G M Ihler. Morphology of complexes formed between bacteriophage lambda and structures containing the lambda receptor. *Journal of Bacteriology*, 153:1528–34, 1983.

[96] C A Roessner and G M Ihler. Formation of transmembrane channels in liposomes during injection of λ DNA. *Journal of Biological Chemistry*, 261:386–90, 1985.

[97] V Zgaga, M Medic, E Salaj-Smic, D Novak, and M Wrischer. Infection of *Escherichia coli* envelope-membrane complex with lambda phage: adsorption and penetration. *Journal of Molecular Biology*, 79:697–708, 1973.

[98] M Esquinas-Rychen and B Erni. Facilitation of bacteriophage lambda DNA injection by inner membrane proteins of the bacterial phosphoenol-pyruvate:carbohydrate phosphotransferase system (PTS). *Journal of Molecular Microbiology and Biotechnology*, 3:361–70, 2001.

[99] R S Tuma, M P Beaudet, X Jin, L J Jones, C-Y Cheung, S Yue, and V L Singer. Characterization of SYBR gold nucleic acid gel stain: a dye optimized for use with 300-nm ultraviolet transilluminators. *Analytical Biochemistry*, 268:278–88, 1999.

[100] I Matic, D Ekiert, M Radman, and M Kohiyama. Generation of DNA-free *Escherichia coli* cells by 2-aminopurine requires mismatch repair and nonmethylated DNA. *Journal of Bacteriology*, 188:339–42, 2006.

[101] W Haidinger, U B Mayr, M P Szostak, S Resch, and W Lubitz. *Escherichia coli* production by expression of lysis gene E and *Staphylococcal* nuclease. *Applied and Environmental Microbiology*, 69:6106–13, 2003.

[102] H I Adler, W D Fisher, A Cohen, and Alice A Hardigree. Miniature *Escherichia coli* cells deficient in DNA. *Proceedings of the National Academy of Sciences*, 57:321–6, 1967.

[103] A C Frazer and R Curtiss 3rd. Production, properties and utility of bacterial minicells. *Current Topics in Microbiology and Immunology*, 69:1–84, 1975.

[104] E Davie, K Sydnor, and L I Rothfield. Genetic basis for minicell formation in *Escherichia coli* K-12. *Journal of Bacteriology*, 158:1202–3, 1984.

[105] T Baba, T Ara, M Hasegawa, Y Taka, Y Okumura, M Baba, K A Datsenko, M Tomita, B L Wanner, and H Mori. Construction of *Escherichia coli* K-12 in-frame, single-gene knock-out mutants – the keio collection. *Molecular Systems Biology*, 2:1–11, 2006.

[106] L Rothfield, A Taghbalout, and Y-L Shih. Spatial control of bacterial division-site placement. *Nature Reviews Microbiology*, 3:959–68, 2005.

[107] S B Levy. Physical and functional characteristics of R-factor deoxyribonucleic acid segregated into *Escherichia coli* minicells. *Journal of Bacteriology*, 108:300–8, 1971.

[108] J H Crooks, M Ullman, M Zoller, and S B Levy. Transcription of plasmid DNA in *Escherichia Coli* minicells. *Plasmid*, 10:66–72, 1983.

[109] K J Roozen, R G Fenwich Jr, and R Curtiss III. Synthesis of ribonucleic acid and protein in plasmid-containing minicells of *Escherichia coli* K-12. *Journal of Bacteriology*, 107:21–33, 1971.

[110] J N Reeve. Use of minicells for bacteriophage-directed polypeptide synthesis. *Methods in Enzymology*, 68:493–503, 1979.

[111] A Cohen, W D Fisher, R Curtiss III, and H I Adler. DNA isolated from *Escherichia coli* minicells mated with F+ cells. *Proceedings of the National Academy of Sciences*, 61:61–8, 1968.

[112] L R Kass and M B Yarmolinsky. Segregation of functional sex factor into minicells. *Proceedings of the National Academy of Sciences*, 66:815–22, 1970.

[113] N Shepherd, P Dennis, and H Bremer. Cytoplasmic RNA polymerase in *Escherichia coli*. *Journal of Bacteriology*, 183:2527–34, 2001.

[114] J N Reeve. Bacteriophage infection of minicells. *Molecular and General Genetics*, 158:73–9, 1977.

[115] A Rashtchian, S W Brown, J Reichler, and S B Levy. Plasmid segregation into minicells is associated with membrane attachment and independent of plasmid replication. *Journal of Bacteriology*, 165:82–7, 1986.

[116] C A Roessner, D K Struck, and G M Ihler. Injection of DNA into liposomes by bacteriophage lambda. *Journal of Biological Chemistry*, 258:643–8, 1982.

[117] K Stingl, S Muller, G Scheidgen-Kleyboldt, M Clausen, and B Maier. Composite system mediates two-step DNA uptake into *Helicobacter pylori*. *Proceedings of the National Academy of Sciences*, 107:1184–9, 2010.

[118] R Edgar, A Rokney, M Feeney, S Semsey, M Kessel, M B Goldberg, S Adhya, and A B Oppenheim. Bacteriophage infection is targeted to cellular poles. *Molecular Microbiology*, 68:1107–16, 2008.

[119] A Babic, A B Lindner, M Vulic, E J Stewart, and M Radman. Direct visualization of horizontal gene transfer. *Science*, 319:1533–6, 2008.

[120] M B Elowitz, M G Surette, P E Wolf, J B Stock, and S Leibler. Protein mobility in the cytoplasm of *Escherichia coli*. *Journal of Bacteriology*, 181:197–203, 1999.

[121] L R Brewer and P R Bianco. Laminar flow cells for single-molecule studies of DNA-protein interactions. *Nature Methods*, 5(6):517–25, 2008.

[122] K A Gibbs, D D Isaac, J Xu, R W Hendrix, T J Silhave, and J A Theriot. Complex spatial distribution and dynamcs of an abundant *Escherichia coli* outer membrane protein, LamB. *Molecular Microbiology*, 53:1771–83, 2004.

[123] A Eliasson, R Bernander, S Dasgupta, and K Nordstrom. Direct visualization of plasmid DNA in bacterial cells. *Molecular Microbiology*, 6:165–70, 1992.

[124] S B Zimmerman. Toroidal nucleoids in *Escherichia coli* exposed to chloramphenicol. *Journal of Structural Biology*, 138:199–206, 2002.

[125] E P Johnson, S Yao, and D R Helinski. Gyrase inhibitors and thymine starvation disrupt the normal pattern of plasmid RK2 localization in *Escherichia coli*. *Journal of Bacteriology*, 187:3538–47, 2005.

[126] D G Gibson, G A Benders, C Andrews-Pfannkoch, E A Denisova, H Baden-Tillson, J Zaveri, T B Stockwell, A Brownley, D W Thomas, M A Algire, C Merryman, L Young, V N Noskov, J I Glass, J C Venter, C A Hutchinson 3rd, and H O Smith. Complete chemical synthesis, assembly, and cloning of a *Mycoplasma* genitalium genomes. *Science*, 319:1215–20, 2008.

[127] M Thanbichler, P H Viollier, and L Shapiro. The structure and function of the bacterial chromosome. *Current Opinion in Genetics and Development*, 15:153–62, 2005.

[128] E Lieberman-Aiden, N L van Berkum, L Williams, M Imakaev, T Ragoczy, A Telling, I Amit, B R Lajoie, P J Sabo, M O Dorschner, R Sandstrom, B Bernstein, M A Bender, M Groudine, A Gnirke, J Stamatoyannopoulos, L A Mirny, E S Lander, and J Dekker. Comprehensive mapping of long-range interactions reveals folding principles of the human genome. *Science*, 326:289–93, 2009.

[129] Bruce Alberts, Alexander Johnson, Julian Lewis, Martin Raff, Keith Roberts, and Peter Walters. *Molecular Biology of the Cell*. Garland Science, 2008.

[130] K C Martin and A Ephrussi. mrna localization: gene expression in the spatial dimension. *Cell*, 136:719–30, 2009.

[131] J E Sulston, E Schierenberg, J G White, and J N Thomson. The embryonic cell lineage of the nematode *Caenorhabditis elegans*. *Developmental Biology*, 100:64–119, 1983.

[132] T Gregor, W Bialek, R R de Ruyter van Steveninck, D W Tank, and E F Wieschaus. Diffusion and scaling during early embryonic pattern formation. *Proceedings of the National Academy of Sciences*, 102:18403–7, 2005.

[133] E Paluch and C-P Heisenberg. Biology and physics of cell shape changes in development. *Current Biology*, 19:R790–9, 2009.

[134] R J Metzger, O D Klein, G R Martin, and M A Krasnow. The branching programme of mouse lung development. *Nature*, 453:745–50, 2008.

[135] A Raj, S A Rifkin, E Andersen, and A van Oudenaarden. Variablity in gene expression underlies incomplete penetrance. *Nature*, 463:913–8, 2010.

[136] S Q Schneider and B Bowerman. Cell polarity and the cytoskeleton in the *Caenorhabditis elegans* zygote. *Annual Review of Genetics*, 37:221–49, 2003.

[137] H Doerflinger, R Benton, I L Torres, M F Zwart, and D St Johnston. *Drosophila* anterior-posteror polarity requires actin-dependent PAR-1 recruitment to the oocyte posterior. *Current Biology*, 16:1090–5, 2006.

[138] A Gonzalez-Reyes and D St Johnston. Role of oocyte position in establishment of anterior-posteror polarity in *Drosophila*. *Science*, 266:639–42, 1994.

[139] J K Yisraeli, S Sokol, and D A Melton. A two-step model for the localization of maternal mRNA in Xenopus oocytes: Involvement of microtubules and microfilaments in the translocation and anchoring of Vg1 mRNA. *Development*, 108:289–298, 1990.

[140] K Takaoka, M Yamamoto, H Shiratori, C Meno, J Rossant, Y Saijoh, and H Hamada. The mouse embryo autonomously acquires anterior-posteror polarity at implantation. *Developmental Cell*, 10:451–459, 2006.

[141] Y Okada, S Takeda, Y Tanaka, J-C Izpisua Belmonte, and N Hirokawa. Mechanism of nodal flow: A conserved symmetry breaking event in left-right axis determination. *Cell*, 121:633–644, 2005.

[142] Y Tanaka, Y Okada, and N Hirokawa. Fgf-induced vesicular release of sonic hedgehog and retinoic acid in leftward nodal flow is critical for left-right determination. *Nature*, 435:172–177, 2005.

[143] Y Shibazaki, M Shimizu, and R Kuroda. Body handedness is directed by genetically determined cytoskeletal dynamics in the early embryo. *Current Biology*, 14:1462–7, 2004.

[144] S J Moorman and A Z Shorr. The primary cilium as a gravitational force transducer and a regulator of transcriptional noise. *Developmental Dynamics*, 237:1955–9, 2008.

[145] J R Hove, R W Koster, A S Forouhar, G Acevedo-Bolton, S E Fraser, and M Gharib. Intracardiac fluid forces are an essential epigenetic factor for embryonic cardiogenesis. *Nature*, 421:172–7, 2003.

[146] J Vermot, A S Forouhar, M Liebling, D Wu, D Plummer, M Gharib, and S E Fraser. Reversing blood flows act through *klf2a* to ensure normal valvulogenesis in the developing heart. *PLoS Biology*, 7:e1000246, 2009.

[147] K Sawamoto, H Wichterle, O Gonzalez-Perez, J A Cholfin, M Yamada, N Spassky, N S Murcia, J M Garcia-Verdugo, O Marin, J L R Rubenstein, M Tessier-Lavigne, H Okano, and A Alvarez-Buylla. New neurons follow the flow of cerebrospinal fluid in the adult brain. *Science*, 311:629–32, 2006.

[148] N F Berbari, A K O'Conner, C J Haycraft, and B K Yoder. The primary cilium as a complex signaling center. *Current Biology*, 19:R526–35, 2009.

[149] A S Shah, Y Ben-Shahar, T O Moninger, J N Kline, and M J Welsh. Motile cilia of human airway epithelia are chemosensory. *Science*, 325:1131–4, 2009.

[150] David M Phillips. *Cilia and Flagella*. Academic Press, Inc., 1974.

[151] T Heuser, M Raytchev, J Krell, M E Porter, and D Nicastro. The dynein regulatory complex is the nexin link and a major regulatory node in cilia and flagella. *Journal of Cell Biology*, 186(6):921–3, 2009.

[152] H Hartman and T F Smith. The evolution of the cilium and the eukaryotic cell. *Cell Motility and the Cytoskeleton*, 66:215–9, 2009.

[153] P Satir, C Guerra, and A J Bell. Evolution and persistence of the cilium. *Cell Motility and the Cytoskeleton*, 64:906–13, 2007.

[154] J Dobbelaere, F Josue, S Suijkerbuijk, B Baum, N Tapon, and J Raff. A genome-wide rnai screen to dissect centriole duplication and centrosome maturation in *Drosophila*. *PLoS Biology*, 6:e224, 2008.

[155] W Marshall. Centriole evolution. *Current Opinion in Cell Biology*, 21:14–9, 2009.

[156] E F Smith. Regulation of flagellar dynein by the axonemal central apparatus. *Cell Motility and Cytoskeleton*, 52:33–42, 2002.

[157] I H Riedel-Kruse, A Hilfinger, and F Julicher. How molecular motors shape the flagellar beat. *HFSP Journal*, 1:192–208, 2007.

[158] C B Lindemann and K S Kanous. A model for flagellar motility. *International Review of Cytology*, 173:1–72, 1997.

[159] M Salathe. Regulation of mammalian ciliary beating. *Annual Reviews of Physiology*, 69:401–22, 2007.

[160] B Huang, Z Ramanis, and D J Luck. Suppresor mutations in *Chlamydomonas* reveal a regulatory mechanism for flagellar function. *Cell*, 28:115–24, 1982.

[161] J R Colantonio, J Vermot, D Wu, A D Langenbacher, S E Fraser, J-N Chen, and K L Hill. The dynein regulatory complex is required for ciliary motility and otolith biogenesis in the inner ear. *Nature*, 457:205–9, 2009.

[162] K L Hill, N R Hutchings, P M Grandgenett, and J E T Donelson. T lymphocyte triggering factor of african trypanosomes is associated with the flagellar fraction of

the cytoskeleton and represents a new family of proteins that are present in several divergent eukaryotes. *Journal of Biological Chemistry*, 275:39369–78, 2000.

[163] J M Bekker, J R Colantonio, A D Stephens, W T Clarke, S J King, K L Hill, and R H Crosbie. Direct interaction of Gas11 with microtubules: Implications for the dynein regulatory complex. *Cell Motility and the Cytoskeleton*, 64:461–73, 2007.

[164] T Nicolson. The genetics of hearing and balance in zebrafish. *Annual Review of Genetics*, 39:9–22, 2005.

[165] C Haddon and J Lewis. Eary ear development in the embryo of the zebrafish, *Danio rerio*. *The Journal of Comparative Neurology*, 365:113–28, 1996.

[166] T Whitfield, B B Riley, M-Y Chung, and B Phillips. Developmenf of the zebrafish inner ear. *Develpmental Dynamics*, 223:427–58, 2002.

[167] B B Riley, C Zhu, C Janetopoulos, and K J Aufderheide. A critical period of ear development controlled by distinct populations of ciliated cells in the zebrafish. *Developmental Biology*, 191:191–201, 1997.

[168] M Pisam, C Jammet, and D Laurent. First steps of otolith formation of the zebrafish: role of glycogen? *Cell and Tissue Research*, 310:163–8, 2002.

[169] C Sollner, M Burghammer, E Busch-Nentwich, J Berger, H Schwarz, C Riekel, and T Nicolson. Control of crystal size and lattice formation by Starmaker in otolith biomineralization. *Science*, 302:282–6, 2003.

[170] S Xiao, C Yu, X Chou, W Yuan, Y Wang, L Bu, G Fu, M Qian, J Yang, Y Shi, L Hu, B Han, Z Wang, W Huang, J Liu, Z Chen, G Zhao, and X Kong. *Dentinogenesis imperfecta* 1 with or without progressive hearing loss is associated wth distinct mutations in DSPP. *Nature Genetics*, 27:201–4, 2001.

[171] Inna Hughes, Brian Blasiole, David Huss, Mark E. Warchol, Nigam P. Rath, Belen Hurle, Elena Ignatova, J. David Dickman, Ruediger Thalmann, Robert Levenson, and David M. Ornitz. Opterin 1 is required for otolith formation in the zebrafish *Danio rerio*. *Developmental Biology*, 276:391–42, 2004.

[172] Y-J Kang, A K Stevenson, P M Yau, and R Kollmar. Sparc protein is required for normal growth of zebrafish embryos. *Journal of the Association for Research in Otolaryngology*, 9:436–51, 2008.

[173] S G Clendenon, B Shah, C A Miller, G Schmeisser, A Walter, V H Gattone II, K F Barald, Q Liu, and J A Marrs. Cadherin-11 controls otolith assembly: evidence for extracellular cadherin activity. *Developmental Dynamics*, 238:1909–22, 2009.

[174] Y Bouligand. The renewal of ideas about biomineralisations. *Genearl Palaeontology*, 3:617–28, 2004.

[175] F H Wilt. Developmental biology meets materials science: Morphogenesis of biomineralized structures. *Developmental Biology*, 280:15–25, 2005.

[176] A Vilfan and F Julicher. Hydrodynamic flow patterns and synchronization of beating cilia. *Physical Review Letters*, 96:058102, 2006.

[177] C Maul and S Kim. Image systems for a Stokeslet inside a rigid spherical container. *Physics of Fluids*, 6:2221–3, 1994.

[178] E R Dufresne and D G Grier. Optical tweezer array and optical substrates created with diffractive optics. *Review of Scientific Instruments*, 69(5):1974–7, 1998.

[179] E E Davis, M Brueckner, and N Katsanis. The emerging complexity of the vertebrate cilium: new functional roles for an ancient organelle. *Developmental Cell*, 11:9–19, 2006.

[180] D B Hill, V Swaminathan, A Estes, J Cribb, E T O'Brien, C W Davis, and R Superfine. Force generation and dynamics of individual cilia under external loading. *Biophysical Journal*, 98:57–66, 2010.

[181] B Lin, J Yu, and S A Rice. Direct measurements of constrained Brownian motion of an isolated sphere between two walls. *Physical Review E*, 62:3909–19, 2000.

[182] J J Hunt. Morphological characteristics of otoliths for selected fish in the Northwest Atlantic. *Journal of Northwest Atlantic Fish Science*, 13:63–75, 1992.

[183] J Choi, D Margetis, T M Squires, and M Z Bazant. Steady advection-diffusion around finite absorbers in two-dimensional potential flows. *Journal of Fluid Mechanics*, 536:155–84, 2005.

[184] G M Whitesides and B Grzybowski. Dynamic aggregation of chiral spinners. *Science*, 296:718–21, 2002.

[185] T Lecuit and L Le Goff. Orchestrating size and shape during morphogenesis. *Nature*, 450:189–92, 2007.

[186] M B Short, C A Solari, S Ganguly, T R Powers, J O Kessler, and R E Goldstein. Flows driven by flagella of multicellular organisms enhance long-range molecular transport. *Proceedings of the National Academy of Sciences*, 103:8315–9, 2006.

[187] C A Solari, S Ganguly, J O Kessler, R E Michod, and R E Goldstein. Multicellularity and the functional interdepedence of motility and molecular transport. *Proceedings of the National Academy of Sciences*, 103:1353–8, 2006.

[188] P Vick, A Schweickert, T Weber, M Eberhardt, S Mencl, D Shcherbakov, T Beyer, and M Blum. Flow on the right side of the gastrocoel roof plate is dispensable for symmetry breakage in the frog *Xenopus laevis*. *Developmental Biology*, 331:281–91, 2009.

[189] J Sambrook and D W Russell. *Molecular cloning: a laboratory manual*. Cold Spring Harbor Laboratory Press, 2001.

[190] S B Levy. Resistance of minicells to penicillin lysis: a method of obtaining large quantities of purified minicells. *Journal of Bacteriology*, 103:836–9, 1970.

[191] P R Selvin and T Ha. *Single-Molecule Techniques: A Laboratory Manual*. Cold Spring Harbor Laboratory Press, 2007.

[192] H Risken. *The Fokker-Planck Equation*. Springer-Verlag, New York, NY, 1989.

Appendix A

Supplemental Methods

A.1 Maximum Caliber

The microscope was home built around an Olympus 1.4 NA oil immersion objective, and is highly schematized as shown in Figure 2.1. The laser, a 2 Watt (maximum) Verdi laser at 532 nm from Coherent, at its exit has a radius of ∼3 mm and was expanded once by a factor of 2 prior to entry into the acousto-optic deflector (AOD). Beam expansion, in order to fill the back aperture of the objective, is crucial to achieve adequate trapping forces. The AOD was placed at the same plane as the back focal plane of the objective, and a 1:1 telescope was placed in between the AOD and the objective. In this manner, a deflection at the AOD produces a beam rotation at the back focal plane of the objective which translates into optical trap translation in the sample plane. The power of the laser at the back focal plane was ∼ 100 mW. The potential was shaped by rapidly scanning the green laser at a rate of 10 KHz using a digitial frequency synthesizer coupled to a broadband amplifier that outputs 1 W of power into the AOD. We scanned around the center deflection frequency of the AODs (80 MHz). The deflection equation is:

$$\theta = \frac{\lambda f}{v} \tag{A.1}$$

where the deflection angle, θ, is modulated by the applied frequency, f, at the wavelength of the laser, λ, and the speed of sound in the crystal, v. In our system, $v = 660$ m/s (tellurium dioxide), and the amplifier bandwidth is 40 MHz, so the total deflection is 1.85^o. Since the focal length of the objective is 1.8 mm, the full deflection in the sample plane is 58 μm, which is more than enough for our purposes. In practice, deflection is less than 500 nm to

generate the bi-minima potentials.

An optically trapped particle can be modeled by the following Langevin equation:

$$m\ddot{x} = -\gamma\dot{x} - \kappa x + 2\gamma k_B T\Gamma(t) \tag{A.2}$$

where γ is the Stokes drag for a spherical particle, κ is the force constant from the optical trap, and $\Gamma(t)$ is the random force imparted by temperature. Since the mass of the particle is very small (overdamped limit), we can drop the acceleration term. Now since $\langle\Gamma(t)\rangle = 0$,

$$\gamma\langle\dot{x}\rangle = -\kappa\langle x\rangle \tag{A.3}$$

and so

$$\langle x\rangle \approx e^{-\frac{\kappa}{\gamma}t}. \tag{A.4}$$

For experimentally relevant parameters, we find that $\gamma/\kappa \sim 9.4\times10^{-9}$ kg·s^{-1} / 10×10^{-3} N·m^{-1} = 1×10^{-6} sec for a 1 micron particle. Thus scanning at 10 KHz, a laser residence time of 50 μs is sufficient for the particle to "feel" as though it is on a stationary potential. Another way to say this is that the corner frequency of the trap is higher than the bead relaxation frequency.

Another laser, at 658 nm (the detection beam), 1 mW, was placed in a different optical path and focused into the sample plane, much like an optical trap would be. However, the beam was configured such that the width of the focus was around 1 micron, instead of diffraction limited, as the trapping laser was. The detection beam is deflected by the bead trapped by the green laser, and resultant deflections are imaged through the microscope condenser onto a lateral effect detector (position sensitive detector, PSD), which is essentially a gradient photoresist. The photoresist outputs a current that is converted to voltage via a series resistor; the voltages are amplified via differential operational amplifiers before being recorded by a National Instruments acquisition board (PCI-6052E) running at 10 KHz per channel. The output was recorded by MATLAB, using custom written software (by the author). Since the total amount of power impinged upon the PSD influences the recorded voltage, the position was calculated as $x = V_x/(V_x + V_y)$; $y = V_y/(V_x + V_y)$, where V_x is the voltage in the x-direction and V_y is the voltage in the y-direction.

Deflections are calibrated by scanning a trapped bead through the focus of the detec-

tion laser; the trapping laser is then positioned such that trapped beads are in the linear range of the detection laser, which is, again, not more than a few microns in extent. An interference filter ultimately separates the trapping laser from the detection laser prior to the detector. The 1 micron detection beam size represents a trade off between the size of the linear detection area versus the amount of power required at the PSD to detect a signal. Additionally, the detection laser will weaken the trapping forces, so the power needs to be kept low.

We used silica beads at sufficient dilution such that there was around 3 beads per 10 microliters of water to prevent beads from randomly diffusing into the traps, since recording sessions lasted approximately half an hour at a time. It was determined that drifts in the system were from temperature gradients, so all electronics were turned on for 6 hours and the environment thermally sealed (as much as possible), before the experiment was commenced. The experiment was then performed for 16 hours straight.

A.1.1 Laser alignment tips

It is crucial for a rotation at the back focal plane to translate into a translation at the sample plane, such that the optical trap loses as little power as possible. This is principally accomplished by fixing the position of the microscope objective such that it does not translate, but instead having the sample stage move in x, y, and z (here, z is defined as the optical axis), which is contrary to commercial microscopes, which translate the sample stage in x and y but fix the stage in z. Of course, if one fixes the stage in z and assumes that the sample used will always be mounted at the same plane, then these two different strategies are the same in practice, as an optical trapping objective has at most a depth of focus of 100 μm (for expensive high numerical aperture water immersion objectives with IR wavelength correction), which translates to a beam deviation off axis for the largest deflections (1.85^o as stated above) of 3.23 μm, which is around the expected precision of translation stages that are used to position lenses, and hence the accuracy of determination of the precise location of the back focal plane of the objective. However, in my case, the setup was also used for imaging embryos that require mounting at different sample planes, at millimeter distances in z, which results in beam deviations of $> 30\mu$m. Thus, I fixed the objective in z.

The laser beam is then propagated by mirrors alone (no lenses) from the output of the

laser through the objective, making sure that there is enough path length to incorporate all optics later. Two mirrors (or dichroics, as the case may be) are used to align the beam along a straight path (which is defined by two irises), just as two points are required to define a line. Naturally, if the beam is to be expanded first, then those set of lenses are put into place. A mirror is placed on the mount which carries the objective, and reflects the laser back to its origin. In this manner, we can test that the laser is normal to the objective mount. On the objective mount is placed an iris, so we can make sure that the incoming laser is also centered, in addition to being normal. At this point, the imaging camera is placed at its appropriate location; if the laser mirror which reflects the laser into the objective is at 45^o with respect to the objective, then the camera position is well defined. Since there is at least one dichroic in the optical path, we can also see the laser reflecting into the camera. Once the laser is properly normal and centered, we adjust the camera such that the laser appears in the center of the detector element. The tube lens is placed in front of the camera at the proper distance such that the beam is still in the center of the detector.

All that is left to do is to place any telescopes in the beam path. There will be at least one telescope if one chooses to use an AOD or set of mirrors to deflect the optical trap from its centered position. A telescope is therefore required to image the deflection onto the back focal plane of the objective. The lens closest to the objective must be at a distance of one focal length away from the back focal plane. This is achieved by placing the lens in the path with the objective in place. Since the beam is collimated going into the lens, and is focused into the back focal plane, the beam will appear collimated coming out of the objective. One should look at a spot far away from the objective to make sure that the laser is indeed collimated, and parallel to the optical axis. The second lens in the telescope is now placed at its proper location after the collimation and parallel requirements are met. The location is determined by removing the objective and once again putting a mirror on top of the objective mount. The light should be reflected back along the correct path, and when removing the mirror, the beam should be collimated at infinity. In this or similar manner, the lenses are put into place. When adding telescopes to the optical system (in general), I use a set of irises to define the optical path, and check to make sure that the beam stays a constant width (i.e., its collimated) after a long distance, after the beam has been expanded to its desired size. This is accomplished either through translation stages

(expensive) which have micron-level precision or through the use of clamps (cheap), which allow the optical elements to be placed arbitrarily on the grid defined by the optical table.

Additionally, it is crucial that lenses are normal to the optical axis. Thus it is wise to define the height of the optical path with respect to the optical table as an initial condition. The normal condition is achieved by looking at the back reflection of the laser off the surfaces of the lens. There are usually two to three visible reflections: a reflection off the incident surface of the lens, and a reflection off the exit surface of the lens, and other higher order reflections, also depending on the whether the lens is a singlet, doublet, or triplet. When all the back reflections are aligned with the incident beam, then one can be sure that the lens is properly normal and centered about the laser.

There are a host of other mostly mechanical issues with how to mount the various components, what is the best sample stage, how to make filter wheels on the cheap, etc. But these issues are best learnt by trial and error (in addition to being too numerous to discuss), as each part has varying advantages and disadvantages depending on its contextual use, and more importantly, the manufacturer. I hope the above discussion is sufficient for the ingenue to begin trapping experiments. Small changes to the laser alignment produces total-internal reflection fluorescence (TIRF) microscopes, dark-field illumination, stroboscopic illumination, etc. Small changes to the detection side results in fluorescence correlation spectroscopy, and even confocal microscopy. These are all variations on a theme. An even larger issue is working within the constraint of a limited supply of funds, as optical components, to put it bluntly, are expensive. It is therefore imperative that the experimental physicist to develop machining skills in order to custom fabricate parts or to subtly modify existing ones to suit his or her needs at his or her whim. The experimental physicist should also possess basic electronics and programming skills to quickly whip up control schemes for instruments without spending the huge sums of money often required to purchase software or custom hardware that someone else built, often for profit - and which, moreover, are unsuitable to the exact needs of the experiment[1]. The acquisition of such skills and judicious deployment of them provides a level of satisfaction that is absent from the exclusive use of manufactured products and instills a certain confidence in the scientist that carries through

[1]For instance, we built a field inversion gel electrophoresis (FIGE) apparatus out of spare parts, the total cost of which was not more than $20. A commercially purchased FIGE apparatus would be in excess of $1000. We also built an automated filter wheel for multi-color microscopy out of servo motors and spare parts for a cost of $200; the cost for a commercial automated filter wheel would also be in excess of $1000. Of course, the polish of our home-built devices is, perhaps, lacking. And they might break more easily.

into daily life and renders seemingly insurmountable problems into mere trivialities.

Remember the key about performing experiments: one should make perturbations that produce consistent and reproducible results. Science demands reproducibility because there **is** an underlying logic to things. Because experiments are reproducible, it is simply up to the scientist to uncover what that logic is, for it is certainly there.

A.2 Phage Lambda

A.2.1 Optical Trapping for phage ejections

Note that all buffer abbreviations are explained in Section A.2.14. Phages are too small (∼100 nm) to be optically trapped, so we bind them to larger particles (polystyrene beads 2 μm in diameter) via biotin-streptavidin chemistry. After purification of phage via plate lysis, phages were dialyzed with 100 mM sodium bicarbonate, pH 8.2, for 48 hours with 1 buffer exchange after 24 hours. The dialysis volume ratio was 300:1. Phages were then incubated with 10 μM of sulfo-LC-biotin for 30 minutes at room temperature on a nutating platform. Then 0.5 g of CsCl was added to each milliliter of phages, which was subsequently loaded onto a CsCl gradient, composed of 1.45, 1.5, and 1.7 g/mL CsCl in SM media. The gradient was spun at 87,000 g for 2 hours at 4 C, and recovered with a syringe. Phages were then stored at 4^oC, where their activity is expected to last for years. The titer of the biotinylated phages was $\sim 10^{10}$.

The 2 μm streptavidin coated polystyrene spheres (27 μl) were washed and resuspended in TM 3 times (3 minutes at 10,000 g, room temperature) to the original volume. Biotinylated phages (3 μl) were then incubated with the beads for a few hours at room temperature on a rotating rack. The phage ejection solution (see Section A.2.4) was injected into one port, and the phages conjugated to streptavidin spheres, diluted by a factor of 10 in TM, were injected into the other port (Fig. 3.2) at a total flow rate of 10 μL/min, with the help of a dual-syringe syringe pump. A 1064 nm laser at 100 mW was used to trap phage-coated spheres and the sample was translated so that the trapped bead was now in the phage ejection solution. Using fluorescence, it is quite easy to see where the solutions meet; under brightfield microscopy, one can visualize the boundary layer, since one solution has lots of beads, and the other side has none. As the bead is moved into the phage ejection solution, recording under fluorescence illumination begins, and eventually ejections are seen, as

demonstrated in Figure 3.3, B.

The microscope was homebuilt around a 60X IR corrected water immersion objective adapted with a 200 mm focal length tube lens, and imaged with an Andor Ixon EMCCD camera, as drawn in Figure 3.23. Instead of acousto-optic deflectors, mirrors are used to steer the laser beams; the mirrors are placed at the location the AODs would be placed at. The schematic of the flow chamber in Figure 3.2, was adapted from Brewer et al., [121].

A.2.2 Phage purification

Purification of lambda phage strain λcI60 (genome length, 48.5 kbp) was purified according to Sambrook [189]. To recapitulate:

Plate lysis and purification by precipitation:

1. Grow strain C600 E. Coli in LB until it reaches exponential phase $\sim$ OD 0.5.
2. Spin down cells (5,000 g, 3 min, RT) and resuspend in TM.
3. Incubate 10^5 plaque forming units (pfu) phages with 800 μL cells per aliquot for 15 minutes at 37^oC.
4. Add 8 mL melted top (0.7% LB agar), at $< 50^o$C and quickly spread on a large (15 cm) LB or NZY plate.
5. Let grow overnight, plates facing up, until clear lysis areas are confluent.
6. Add $\sim$ 10 mL SM onto each plate and shake on orbit shaker for 8 hours for phage to diffuse into SM.
7. Tilt plates and pipette off buffer with phages.
8. Add an additional 3 mL SM, swirl plate, and let sit at an angle for 15 minutes to collect remaining phages.
9. Add to 5% volume chloroform and vortex briefly. Let sit for 15 minutes at room temperature to lyse cells.
10. Spin down cells (1,000 g, 15 min, at room temperature) and put the aqueous fraction containing phages in new tube. Add a drop of chloroform and store at 4 ^{o}C.

11. Titer phages according to standard protocols (see Paul Grayson's thesis).

12. Prepare 4 x 500 mL NZYCM in 2 L flasks.

13. From an overnight culture of C600 in 100 ml of NZYCM, grab 4x10^{10} cells (0.1 OD $\approx 10^9$ cells).

14. Spin down each aliquot of cells (4,000g, 10 minutes, room temperature) and add 3 mL SM to each, resuspending.

15. Add 5x10^7 pfu phages to each aliquot of cells and let incubate at 37 C for 15 minutes.

16. To each 500 mL NZYCM prepared earlier (prewarmed to 37^{o}C), add the mixture of phages and cells. Incubate with shaking at 37^{o}C for 8-12 hours. In my experience, if the culture hasn't lysed (for instance, if the initial inoculum of phages was less than usual), then waiting longer will produce even more phages.

17. Add 10 mL of chloroform to each flask and shake for 10 minutes. Bacterial debris indicating lysis should be apparent (i.e., clumps of dead matter, in contrast to the silky appearance of a dense culture).

18. After letting the cultures cool to room temperature, spin it down and add DNAse and RNAse to a concentration of 1 μg/ml. Incubate at room temperature for 30 minutes. It is thought that phages are entangled in the web of cellular DNA and RNA.

19. To each 500 mL culture, ad 29.2 g NaCl (final concentration, 1 M). Swirl the cultures until the salt dissolves and store on ice for 1 hour.

20. Remove debris by centrifugation at 11,000g for 10 minutes at 4 C. Measure and combine the total volume volume of supernatant.

21. Add and dissolve 10% w/v PEG 8000, stirring gently.

22. Let the mixture sit on ice for more than one hour to precipitate phages.

23. Recover the phages by spinning down the mixture at 11,000 g for 10 minutes at 4 C. Discard the supernatants, and drain off any remaining fluid standing the bottle upside down for 5 minutes.

24. Resuspend the phages by gently dissolving the pellet in 8 ml SM per 500 mL culture. Place the bottle on the side and let SM soak the pellet for 1 hour at room temperature.

25. Extract the PEG by adding an equal volume of chloroform to each bottle. Vortex the mixture gently and centrifuge at 3,000 g for 15 minutes at 4 C. Recover the aqueous phase which contains the phage particles.

26. Add 0.5 g of solid CsCl to each ml of bacteriophage particles.

27. Make gradients by underlaying 16 ml of bacteriophages, 7.6 ml of 1.45 g/ml CsCl in SM, 1.5 g/ml CsCl in SM, and 1.7 g/ml CsCl in SM.

28. Centrifuge the gradients in a swing bucket rotor at 87,000 g for 2 hours at 4 C. There should be 4 unique bands after the spin. There is a top layer of gunk, a yellow band of stuff in the 1.45 g/ml layer, a bluish band in the 1.5 g/ml layer (these are the phages), and debris at the bottom of the tube. Recover the blue band using a syringe, 21 gauge or larger diameter.

29. Load the recovered band into 1.5 g/mL CsCl in SM and spin for 24 hours at 160,000 g at 4 C. Recover the bright blue band in same way. In this manner, I was able to obtain titers at $\sim 10^{12}$ pfu.

30. Store the phages at 4 C; they should last for years.

A.2.3 LamB purification

The membrane protein LamB was purified using a modified version of a protocol by Keller et al., [89]. The E. coli strain pop154 was grown overnight in LB + 0.2% maltose at 37^{o}C. The cells were pelleted at 3,000 g at 4^{o}C for 30 minutes and re-suspended in 50 mM sodium phosphate, pH 7.8, 100 mM NaCl, 2 mM EDTA, and 5% sucrose. The re-suspended cells were subsequently lysed in a French press. The lysate was again centrifuged at 5,000 g at room temperature for 10 minutes. The supernatant was collected and outer membrane fraction was pelleted by ultracentrifugation at 30,000 rpm, 18^{o}C, for 40 minutes. The pellet containing the membranes was resuspended in 20 mM sodium phosphate, pH 7.4, and 0.5% octylpolyoxyethylene (oPOE) in order to extract non-specific membrane proteins. The solution was incubated in a heat bath at 40^{o}C for 50 minutes and then again pelleted

by ultracentrifugation. LamB was extracted by resuspending the pellet in 20 mM sodium phosphate, pH 7.4, and 3% oPOE (to extract all the membrane proteins), incubating at 37^{o}C for 40 minutes, and pelleting the resulting mixture by ultracentrifugation. The supernatant was dialyzed or diluted to 20 mM sodium phosphate, pH 7.4, and 1% oPOE, and then loaded onto a maltose column and eluted with 20 mM sodium phosphate, pH 7.4, 1% oPOE, and 20 mM maltose after washing two times with the same solution but without maltose. The LamB solution was then dialyzed with 50 mM Tris, pH 7.4, 10 mM $MgSO_4$ and 1% oPOE. The resulting solution was typically 2 mg/ml LamB, verified by spectrophotometry at 280 nm, and its size verified by SDS-PAGE.

A.2.4 Single phage ejection assay

We follow a protocol adapted from Grayson et al., [45]. Microscope coverslips were cleaned by sonication in 1M KOH for 10 minutes followed by sonication in water for 10 minutes. Glass slides were drilled using a diamond covered drill bit and 5 inches of tubing was attached to the glass slide using epoxy. The flow chamber was assembled using laser cut double sided adhesive tape [121]. A solution of 10^8 - 10^{11} pfu/ml lambda phage, previously dialyzed into the appropriate buffer, and 20 nm fluorescent polystyrene beads was incubated in the assembled flow chambers for 10 minutes. The fluorescent beads were used as focusing aids. Once focused, the chamber was washed with 200 μl of buffer + 1% oPOE. A phage ejection solution consisting of buffer (see Figure 3.7, 3.8, and 3.9 captions for precise formulation), 1% oPOE, 1% glucose oxidase/catalase (GODCAT), 10^6 diluted SYBR gold, and 1% LamB. Occasionally, 2 mg/ml bovine serum albumin and 2 mg/ml casein was added to the buffer to block the glass surface to see if looping ejections disappeared.

Note that it is extremely important to not let air flow across the surface of the glass once phages have adhered to it. We found that air will spontaneously cause the phages to eject and therefore to be destroyed immediately. This relates to what was predicted by simulation (and verified by atomic force microscopy) [32] where they found that dessication of phages caused DNA to spill out of capsids.

Microscopy samples were imaged at 60X and 100X using a Nikon perfect focus system and either a SYBR gold or FITC filter set. The exposure time was 75 ms and the frame rate was 4 fps.

A custom segmentation algorithm was developed using MATLAB. Ejection events were

identified in each movie by applying locally adaptive thresholds on each frame and summing the results of each frame. Each identified ejection was then segmented using an adaptive low pass filter for de-noising followed by a custom canny filter for edge finding. The long axis length, total intensity, and background (the mean intensity of non-DNA related pixels) was extracted for each ejection. Trajectories were subjected to a 3 bin median filter for de-noising. The length of each ejection, in each buffer condition, was calibrated by defined lengths of DNA generated by restriction digest, under the same flow conditions as the experiment, as shown in Figure 3.4.

A.2.5 Osmotic suppression assay.

We follow a protocol adapted from Evilevitch et al., [47]. Phages were quickly swirled in a solution of 1% oPOE, 1% LamB, 1% DNAse and appropriate buffer containing PEG at 37^oC and incubated for 1 hour at 37^oC. The solution was then incubated in a 65^oC water bath for 50 minutes to break open capsids and inactivate DNAse. DNA in capsids was then extracted by a 1:1 phenol:chloroform extraction followed by chloroform extraction and finally ethanol precipitation. The precipitated DNA was pelleted and washed twice with 70% ethanol. After discarding the supernatant and letting the pellets dry, 10 μl TE was added to each sample. DNA lengths were assayed using field inversion gel electrophoresis (100 V forward 0.8 sec, 60 volts backwards 0.8 sec, for 4-10 hours). Migration distance was quantified using MATLAB.

A.2.6 Minicells purification

There's an excellent review of the different methods of purifying minicells [103]. There are 3 different protocols for purifying minicells, two of which we tried. We tried the sucrose gradient method and the antibiotic method. Details of the sucrose gradient method can be found in [110]. The alternative strategy is to separate minicells from regular cells by increasing the difference in weight by filamenting cells at low concentrations of antibiotics [190]. The concentration is low enough such that cells don't explode but that they will grow long. The last step is again differential centrifugation and may involve probe sonication to destroy everything. However, we follow the filamentation with a gradient centrifugation and remove minicells in layers and assess their nucleic acid quantity using microscopy and nucleic acid staining dyes. Sonication tends to retain small portions of cell membranes

which bind up errant phage. The third and untried method was purification through glycerol gradients, instead of sucrose. The following was our standard procedure, a hybrid of gradient purification followed by filamentation and differential centrifugation.

1. Grow overnight 1 L MinC- cells from Keio collection in LB with 0.2% maltose (to increase LamB expression) and required appropriate antibiotics (here, 30 μg/ml kanamycin).
2. Centrifuge at 4^{o}C, 8,200 g for 10 min; resuspend in 20 mL of supernatant.
3. Vigorously mix at 4^{o}C for 10 min to break up any clumps.
4. Load onto 4 sucrose gradients (see below) 5 ml each and spin in SW Ti32 rotor 5,700 rpm for 20 min.
5. Recover entire minicell band by puncturing tube. The volume is roughly 10 mL.
6. Centrifuge 13,700 g for 10 min in 50 mL conical tube at 4^{o}C.
7. Resuspend the pellet in 5 mL LB and let shake at 37^{o}C for 30 min to allow any cells to recover.
8. Add 10 U/mL penicillin G and let incubate at 37^{o}C with shaking for 2 hours.
9. Load onto 2 gradients and centrifuge as above.
10. Recover by withdrawing many fractions and assess the DNA content via microscopy.

Making gradients, following the work of Reeve [110]:

1. Freeze 22% w/v sucrose solution with appropriate salts (we used M9).
2. Let defrost overnight at 4^{o}C; this will form a 10-30% gradient naturally.

A.2.7 Phage temperature jump

Minicells and phages, in TM buffer, were kept at $<$ than 4^{o}C (on ice). Flow chambers were coated with poly-L-lysine (see Section A.2.11), and minicells flowed on and allowed to settle for 10 minutes at room temperature. The flow chambers were then washed with a SYBR gold (1:500,000 dilution) or DAPI (0.5 μg/ml) containing solution of TM. At the same time, phages were diluted into TM with an equivalent dilution of SYBR gold or DAPI.

The flow chamber was mounted on a Nikon microscope with a thermoelectric cooled sample stage, cooled to $< 4^oC$, and allowed to thermally equilibrate for 30 minutes. Phages were then pumped in with a syringe pump and allowed to bind for 10 minutes. The expected multiplicity of infection was 10:1. The sample was then washed with a continuous flow of TM and SYBR gold or DAPI while imaging commenced. After 5 minutes, the temperature was raised to 37^oC in order to monitor ejections.

The opposite preparation was also attempted, wherein phages were first bound to the surface, cooled to $< 4^oC$, before minicells were flowed on in a DNA staining dye containing solution, and the temperature raised.

A.2.8 Chloramphenicol compaction of *E. coli* chromosomes

The method follows that of Zimmerman [124]. Cells growing in minimal media, at OD 0.25, were treated with 30 μg/ml of chloramphenicol for 1 hour at 37^oC. Phages were added at the relevant ratio before the sample was applied to a poly-L-lysine coated flow chamber. After allowing the sample to settle, the sample was washed with minimal media containing chloramphenicol.

A.2.9 Glass washing

Protocol adapted from [191]

1. Sonication for 30 minutes in 100% ethanol.
2. Rinse vigorously in ddH_2O.
3. Sonication in 1 M KOH for 30 minutes.
4. Rinse vigorously in ddH_2O.
5. Sonication in ddH_2O for 30 minutes.
6. Dry glass by baking on hot plate 140^oC for > 2 hours to evaporate all traces of water

A.2.10 Functionalization of glass with antibody

We used the following protocols in our attempts to visualize *in vivo* phage ejections.

1. Clean glass vigorously, and dry to remove all traces of water.
2. Rinse glass with acetone.
3. Immerse glass in 2% 3-aminotriethoxypropylsilane (APTES) in acetone.
4. Let sit for $\sim$ 10 minutes.
5. Quench reaction by adding water.
6. Dry on hot plate at 140^{o}C for 2 hours.
7. Immerse in solution of sulfo-SMCC (2mg/ml) for 30 minutes, in 100 mM sodium bicarbonate buffer, pH 8.2. Thus solution should be used immediately, as water hydrolyzes sulfo-SMCC and renders it useless. Note that amine containing buffers (such as Tris) should not be used.
8. Wash with buffer of choice.
9. Dissolve 4 mg antibody in 450 μl of coupling buffer.
10. Dissolve 6 mg of 2-mercaptoethylamine (2-MEA) in 100 μl coupling buffer.
11. Add 50 μl of 2-MEA solution to the antibody soulution.
12. Incubate for 90 min. at 37^{o}C.
13. using a high molecular weight filter, rinse the antibody solution with coupling buffer a few times to get rid of exces 2-MEA.
14. Incubate the antibody solution with the functionalized cover glass for 2-4 hours at room temperature. The protein solution should be greater than 10 μg/ml for good results.
15. Rinse the surface with appropriate buffer. Note that thus procedure can take place in side a flow chamber to reduce sample waste.

A.2.11 Functionalization of glass with poly-L-lysine

High molecular weight poly-L-lysine was dissolved in water at a concentration of 1% w/v. The mixture was diluted to 0.05% before use. Cleaned coverslips were covered in the poly-L-lysine solution for 30 minutes before being baked at 140^{o}C or washed with appropriate buffer.

A.2.12 Functionalization of glass with biotin

Glass was cleaned, as specified in Section A.2.9. After complete drying, the glass was rinsed in acetone and immersed in a solution of 2% APTES in acetone with sonication for 10 minutes. The glass was then dried of acetone and rinsed with freshly made 100 mM sodium bicarbonate, pH 8.2. A solution of 1 mg/ml sulfo-LC-biotin in sodium bicarbonate was applied to the surface of the coverslip, and the solution was incubated for 30 minutes at room temperature. After reacting, the surfaces were rinsed with PBS.

A.2.13 Quantum dot labeling of phages

Phages were first biotinylated (Section A.2.1), before incubating with *E. coli* in minimal media, on ice for 10 minutes. 1 μl of streptavidin-coated quantum dots were then added to the mixture for an additional 5 minutes. The sample was centrifuged at 3,000g for 3 minutes and resuspended in minimal media 3 times before application to proper visualization substrate. See Edgar et al., [118], for additional details.

A.2.14 Buffer definitions

A.2.14.1 SM

Per liter: 5.8 g NaCl, 2 g $MgSO_4$·7 H_2O, 50 ml 1 M Tris-Cl, pH 7.5, 2 % w/v gelatin, H_2O to 1 L.

A.2.14.2 TM

50 mM Tris, pH 7.4, 10 mM $MgSO_4$

A.2.14.3 LB

10 g tryptone, 5 g yeast extract, 10 g NaCl, water to 1 L. Adjust pH to 7.0 with NaOH.

A.2.14.4 NZY

10 g NZ amine, 5g NaCl, 5 g yeast extract, water to 1 L. Adjust pH to 7.0 with NaOH.

A.2.14.5 NZYCM

10 g NZ amine, 5g NaCl, 5 g yeast extract, 1g casamino acids, 2 g hydrated magnesium sulfate, water to 1 L. Adjust pH to 7.0 with NaOH.

A.2.14.6 TE

10 mM Tris-Cl, pH 7.4, 1 mM EDTA.

A.2.14.7 M9

Per liter: 200 ml 5x M9 salts, 2 mL 1 M $MgSO_4$, 20% of appropriate carbon source, water to 1 L. 5x M9 salts: 64 g hydrated disodium phosphate, 15g monopotassium phosphate, 2.5g NaCl, 5g ammonium chloride, in 1 L of water.

A.3 Zebrafish methods

A.3.1 Experimental methods

A.3.1.1 Fast imaging

All bright-field imaging was accomplished on a home built microscope incorporating a 60x 1.2 NA Olympus IR corrected water immersion objective, coupled with a 200 mm focal length tube lens, producing an effective magnification of 66x. We used a Basler A602f CMOS camera (pixel size, 10 μm) which has a native frame rate of 100 fps, at 656x493 pixels. Choosing smaller regions of interest results in much higher frame rates, up to 1000 fps for a 64x64 pixel area. Acquisition was completed via an acquisition program written in MATLAB scripting language by yours truly. Occasionally, we would use a Prosilica GC1380H camera (6.4 um pixel size) that has sensitivity equivalent to that of standard fluorescence microscopes (the Basler has very bad sensitivity), but with noisier electronics and no cooling to reduce noise. The Prosilica camera has a native frame rate of 30 fps, and has also increased frame rates at reduced areas of interest. It is more difficult to program

for, however. Data taken with the Prosilica camera was also acquired via home written MATLAB scripts.

A.3.1.2 Optical trapping

The microscope configuration was extremely simple. It is similar to Figure 2.1, except with a 1064 nm laser (B & W Tek), and the laser is no longer scanned, but simply shuttered by the acousto-optic deflectors (AODs, Intraaction Corp.). The frequencies necessary to operate the AODs were generated by a custom written Labview program (adapted from Intraaction provided software). The laser was switched on and off, at a frequency of 10 Hz, by adjusting the power delivered to the AODs, for the Blinking Optical Trap experiment. The laser output power (after the AODs) was 100 mW. Imaging frame rate was 492 fps. Note that we used an AOD optimized for 532 nm light, so there was significant loss inside the AODs. Additionally, the beam quality of the laser was extremely horrible, and tended to fluctuate depending on the day.

For the trap and delivery experiment, by shining the laser light (1064 nm) a few seconds, enough particles are trapped to perform particle image velocimetry (PIV). PIV was performed over 8x8 sub-samples of the movies. The frame rate of acquisition was 30 Hz.

A.3.1.3 Laser ablation of cilia

A 532 nm solid state laser (Verdi, Coherent) at 1 W was focused into a diffraction limited spot and aimed at motile cilia in 30 second increments. We determined if the cilia had been inactivated using brightfield microscopy. Otolith shapes were checked 1, 2 or 5 hours, and 17 hours post ablation. This corresponds to 19, 20, 23, and 35 hours post fertilization.

A.3.2 Analytical and theoretical methods

A.3.2.1 Analysis of BOTs

Using MATLAB, one-dimensional Brownian dynamics simulations of a particle released by a trapping laser and subjected to a sinusoidal external force, in addition to a random force, were performed, according to Equation 4.12 in Section 4.3.3, via a finite difference method as outlined by Gillespie in [22]; sample trajectories are shown in Figure 4.14. The resulting mean squared displacement was compared to the analytical result and demonstrates near

exact agreement, as shown in Figure 4.15. Since the tracked cilia tips also move according to an approximate sinusoidal motion, as shown in Figure 4.13, we fit the BOTs movies to the result, Equation 4.16, and extract the parameters.

Here, we derive Equation 4.16, the mean-squared displacement, from Equation 4.12, the Langevin equation which governs the dynamics of the local fluid motion. A particle is being dragged through the fluid at some velocity due to a viscous force. There is also a noise term due to the collisions the particle gets from the environment and a force due to the cilium that is oscillatory in nature, resulting in the force balance:

$$F_{net} = F_{drag} + F_{random} + F_{cilium} \tag{A.5}$$

which is the same as Equation 4.12, written here again as:

$$m\dot{v_d} = -\gamma v_d + 2\gamma k_B T \Gamma\left(t\right) + \gamma v_e(t) \tag{A.6}$$

where $\Gamma\left(t\right)$ is the random force from temperature-induced fluctuations in the solution and v_e is the cilium induced local fluid velocity. It turns out, according to Risken [192], that

$$< \Delta \mathrm{x}^2 >= \int_0^t \int_0^t < v\left(t_1\right) v\left(t_2\right) > \mathrm{dt_1 dt_1} \tag{A.7}$$

and so we first calculate the velocity correlation function before performing integration. Integrating once (v_e is given by Eqn. 4.13), we have

$$v(t) = v_0 e^{-\frac{\gamma}{m}t} + \frac{1}{m} e^{-\frac{\gamma}{m}t} \int_0^t e^{\frac{\gamma}{m}t'} \left(2\gamma k_B T \Gamma\left(t'\right) + \gamma v_e\left(t'\right)\right) \mathrm{dt'} \tag{A.8}$$

which we will separate into the random and the deterministic part

$$v(t) = v_0 e^{-\frac{\gamma}{m}t} + \frac{1}{m} e^{-\frac{\gamma}{m}t} \left(\int_0^t e^{\frac{\gamma}{m}t'} 2\gamma k_B T \Gamma(t') \mathrm{dt'} + \gamma \int_0^t e^{\frac{\gamma}{m}t'} v_e(t') \mathrm{dt'} \right). \tag{A.9}$$

Let $v_e(t) = a_0 \sin\left(\omega_t + \phi\right) + b$. Then the external velocity integral is

$$\gamma \int_0^t \left(e^{\frac{\gamma}{m}t} \left(a_0 \sin[\omega t + \phi] + b\right) \right) dt \tag{A.10}$$

which when evaluated is

$$mb\left(e^{\frac{t\gamma}{m}}-1\right) \tag{A.11}$$
$$+\frac{a_0 m\gamma\left(m\omega\cos\phi-\gamma\sin\phi+e^{\frac{t\gamma}{m}}\left(-m\omega\cos\left[\phi+t\omega\right]+\gamma\sin\left[\phi+t\omega\right]\right)\right)}{\gamma^2+m^2\omega^2}.$$

Ignoring the random term, and letting $\gamma a_0 \rightarrow a_0^{'}$, we have:

$$\begin{aligned} v^{'}(t) &= v_0 e^{-\frac{\gamma}{m}t_1}+e^{-\frac{\gamma}{m}t_1}\left(b\left(e^{\frac{\gamma}{m}t_1}-1\right)\right. \\ &+ \left.\frac{a_0^{'}\left(m\omega\cos[\phi]-\gamma\mathrm{Sin}[\phi]+e^{\frac{\gamma}{m}t_1}\left(\gamma\sin\left[\omega t_1+\phi\right]-m\omega\cos\left[\omega t_1+\phi\right]\right)\right)}{\gamma^2+m^2\omega^2}\right). \end{aligned} \tag{A.12}$$

We now square this term in order to compute the velocity autocorrelation, and gather terms, resulting in:

$$\begin{aligned} & v\left(t_1\right)v\left(t_2\right)= \\ & e^{-\frac{\gamma t_1}{m}-\frac{\gamma t_2}{m}}\left(\frac{\left(a_0^{'}(\gamma\sin\phi-m\omega\cos\phi)+\left(\gamma^2+m^2\omega^2\right)\left(b-v_0\right)\right)^2}{\left(\gamma^2+m^2\omega^2\right)^2}\right) \\ - & \frac{e^{-\frac{\gamma t_1}{m}}}{\left(\gamma^2+m^2\omega^2\right)^2}\left(\left(b\left(\gamma^2+m^2\omega^2\right)+a_0^{'}\left(\gamma\sin\left[\phi+\omega t_2\right]-m\omega\cos\left[\phi+\omega t_2\right]\right)\right)\right. \\ \times & \left.\left(a_0^{'}(\gamma\sin\phi-m\omega\cos\phi)+\left(\gamma^2+m^2\omega^2\right)\left(b-v_0\right)\right)\right) \\ - & \frac{e^{-\frac{\gamma t_2}{m}}}{\left(\gamma^2+m^2\omega^2\right)^2}\left(\left(b\left(\gamma^2+m^2\omega^2\right)+a_0^{'}\left(\gamma\sin\left[\phi+\omega t_1\right]-m\omega\cos\left[\phi+\omega t_1\right]\right)\right)\right. \\ \times & \left.\left((-m\omega\cos[\phi]+\gamma\sin\phi)a_0^{'}+\left(\gamma^2+m^2\omega^2\right)\left(b-v_0\right)\right)\right) \\ + & \frac{1}{\left(\gamma^2+m^2\omega^2\right)^2}\left(\left(b\left(\gamma^2+m^2\omega^2\right)+a_0^{'}\left(\gamma\sin\left[\phi+\omega t_1\right]-m\omega\cos\left[\phi+\omega t_1\right]\right)\right)\right. \\ \times & \left.\left(b\left(\gamma^2+m^2\omega^2\right)+a_0^{'}\left(\gamma\sin\left[\phi+\omega t_2\right]-m\omega\cos\left[\phi+\omega t_2\right]\right)\right)\right) \end{aligned} \tag{A.13}$$

which we integrate with $\int_0^t\int_o^t v_e\left(t_1\right)v_e\left(t_2\right)dt_1dt_2$. We furthermore cancel terms that decay to zero as $t\rightarrow\infty$, as well as terms that are linear in mass in the numerator to get

$$\left\langle x^2\left(\phi\right)\right\rangle \approx \frac{\gamma^2\left(bt\gamma\omega+(\cos\phi-\cos[\phi+t\omega])a_0^{'}\right)^2}{\omega^2\left(\gamma^2+m^2\omega^2\right)^2} \tag{A.14}$$

and integrating the phase, we have

$$\begin{aligned} & \frac{1}{2\pi}\int_0^{2\pi} \frac{\gamma^2\left(bt\gamma\omega + (\cos\phi - \cos[\phi + t\omega])a_0^{'}\right)^2}{\omega^2\left(\gamma^2 + m^2\omega^2\right)^2}\, d\phi \\ = & \frac{\gamma^2\left(b^2t^2\gamma^2\omega^2 - (-1 + \cos[t\omega])a_0^{'2}\right)}{\omega^2\left(\gamma^2 + m^2\omega^2\right)^2}. \end{aligned} \tag{A.15}$$

And setting $a_0^{'} \rightarrow a_0\gamma$ yields

$$\langle x^2\rangle \approx \frac{\gamma^4\left(b^2t^2\omega^2 - (-1 + \cos[\omega t])a_0^2\right)}{\omega^2\left(\gamma^2 + m^2\omega^2\right)^2}. \tag{A.16}$$

A.3.2.2 Particle image velocimetry

Our images had a pixel resolution of 100 nm. Since the spherules, as measured optically, had a diameter of around 0.5 micron, this corresponded to about 5 pixels. Since PIV uses correlation, we chose a window size of 8 pixels by 8 pixels. Thus, our images, which were on the order of 400 x 400 pixels, were divided into 50 x 50 smaller chunks. Correlations were then computed on these smaller 8x8 chunks, using an 8 x 8 kernel image correlating against 7 x 7 windows. We then computed the correlation across entire movies and averaged the motion to achieve vector maps, such as in Figure 4.19.

A.3.2.3 Bootstrap algorithm for comparing SSRs

In order to obtain the p-values in Section 4.3.3, a bootstrap algorithm was used to compare the means of data sets. Briefly, data sets (control and experiment) were pooled together and randomly divided into two mixed data sets, equivalent in size to the original data sets. The distribution of means between these randomly partitioned sets was computed. The significance value was determined as the area under the curve of the distribution that was greater than the significance value.

A.3.2.4 Hydrodynamic simulations

We used MATLAB to compute the velocity field inside a sphere according to the Green's function solution to Stokes' equation as given by Maul et al., [177], here, modified into Equation 4.3 since our inner ear does not have unit radius. In brief, Equation 4.7 was used

to generate a cilium, and the force exerted by the cilium according to Equation 4.8. The velocity field inside the inner ear sphere was then computed by generating a 24 x 24 x 24 grid of evaluation points and computing Equation 4.1 at the point different phases of the cilia motion and averaging the result. Brownian motion was put on top of the averaged flow field as in Equation 4.11; the drag computed according to Equation 4.6. The time step was 1 ms. Since particles undergo Brownian motion in continuous space, and the flow field was computed on a grid, we performed linear interpolation between grid points to calculate the appropriate velocity according the following weighting rule:

$$\mathbf{v}_{interp} = \frac{\sum_{j=1}^{8} \mathbf{v}_j \left|\mathbf{v}_j\right|^{-1}}{\sum_{j=1}^{8} \left|\mathbf{v}_j\right|^{-1}} \tag{A.17}$$

where the interpolated velocity, $\mathbf{v}_{interp}$ is embedded in a cube of 8 nearest neighbor grid-computed velocities, $\mathbf{v}_j$.

The reason for computing on a grid, as opposed to in continuous space, is due to the nature of hydrodynamic Green's function, the Oseen tensor, Equation 4.2, in addition to Equation 4.3 - there is a singularity at the location of the force. Thus computing the velocity at the location of the force would produce diverging results. We thus set a maximum of the velocity generated by the cilium as $v_{max} = r\omega$ where r is the length of the cilium and ω is the frequency of the cilium, as dictated by the linear model of the cilium [176]. In order to scale all calculated field velocity points by v_{max}, a grid must be used to avoid violations of v_{max}, since the singularity occurs in continuous space. Computations were performed in MATLAB.